WP5 Final Report: Experiments and modelling of gas migration processes in undisturbed rocks

FORGE Report D5.15, D5.18 and D5.19 – VER.1.0

Work Package leader: Geert Volckaert (SCK•CEN)

Authored by:

Belgium	E. Jacops, G. Volckaert, N. Maes (SCK•CEN)
	R. Charlier, F. Collin, P. Gerard, S. Levasseur (ULg)
France	R. Delavaissière, J. Talandier (ANDRA)
	S. Granet (EDF)
Germany	M. Navarro (GRS)
Spain	M. Villar, F. Romero, P. Martin (CIEMAT)
	M. Zandarin, S. Olivella, E. Alonso (CIMNE-UPC)
Switzerland	P. Marschall (NAGRA)
United Kingdom	J. Harrington, R. Cuss, D. Noy (BGS)
	A. Woods (NDA)

Euratom 7th Framework Programme Project: FORGE

	Name	Organisation	Signature	Date
Edited	E. Jacops	SCK.CEN		May 2014
Verified	N. Maes	SCK.CEN		May 2014
Approved	R. Shaw	BGS		11th June 2014

Keywords

Gas, breakthrough, Boom Clay, Opalinus Clay, Callovo-Oxfordian Clay, 2-phase flow, pathway dilation, modelling, in-situ.

Bibliographical reference

JACOPS ET AL., 2014. WP5 Final Report: Experiments and modelling of gas migration processes in undisturbed rocks. FORGE Report D5.19. 146pp.

Fate of repository gases (FORGE)

The multiple barrier concept is the cornerstone of all proposed schemes for underground disposal of radioactive wastes. The concept invokes a series of barriers, both engineered and natural, between the waste and the surface. Achieving this concept is the primary objective of all disposal programmes, from site appraisal and characterisation to repository design and construction. However, the performance of the repository as a whole (waste, buffer, engineering disturbed zone, host rock), and in particular its gas transport properties, are still poorly understood. Issues still to be adequately examined that relate to understanding basic processes include: dilational versus visco-capillary flow mechanisms; long-term integrity of seals, in particular gas flow along contacts; role of the EDZ as a conduit for preferential flow; laboratory to field up-scaling. Understanding gas generation and migration is thus vital in the quantitative assessment of repositories and is the focus of the research in this integrated, multi-disciplinary project. The FORGE project is a pan-European project with links to international radioactive waste management organisations, regulators and academia, specifically designed to tackle the key research issues associated with the generation and movement of repository gasses. Of particular importance are the long-term performance of bentonite buffers, plastic clays, indurated mudrocks and crystalline formations. Further experimental data are required to reduce uncertainty relating to the quantitative treatment of gas in performance assessment. FORGE will address these issues through a series of laboratory and field-scale experiments, including the development of new methods for up-scaling allowing the optimisation of concepts through detailed scenario analysis. The FORGE partners are committed to training and CPD through a broad portfolio of training opportunities and initiatives which form a significant part of the project.

Further details on the FORGE project and its outcomes can be accessed at www.FORGEproject.org.

Contact details:

E. Jacops
SCK-CEN
Tel: +3214333222
email: ejacops@sckcen.be

N. Maes
SCK-CEN
Tel: +3214333235
email: nmaes@sckcen.be

Acknowledgements

This report is a summary of the work performed within Work Package 5 "Undisturbed host rocks" of the FORGE project.

This report was compiled based on the contributions and feedback of all participating organisations. All participants are thanked for their research efforts, their scientific input at meetings and for the delivery of their contribution to this joint report.

The European Commission is acknowledged for the funding of this pan-European project.

Contents

Acknowledgements **ii**

Contents **iii**

Introduction **11**

1. Gas transport laboratory experiments **13**

1.1 Baseline hydraulic and gas transport properties of the Callovo-Oxfordian claystone (BGS) 13

1.2 Determination of two-phase flow parameters and analysis of fracturing by gas overpressure in opalinus clay (CIEMAT) 26

1.3 Gas driven radionuclide transport in boom clay (SCK•CEN) 41

2 Gas transport in-situ experiments **50**

2.1 PGZ1: Gas migration in undisturbed indurated clay formation, Callovo-Oxfordian clay, at the URL site in Bure (ANDRA) gas transport in-situ experiments 50

2.2 The HG-C/HG-D gas injection experiment in intact Opalinus Clay at the Mont Terri URL (NAGRA) 61

3 Gas transport in undisturbed host rock: modelling **75**

3.1 Modelling of Mont Terri HG-C experiment, GP-A and GS experiments (UPC) 75

3.2 Modelling of the HG-C and HG-D in situ tests in the Opalinus Clay of the Mont Terri rock laboratory (GRS) 87

3.3 Modelling of the PGZ1 in situ test in the Callovo-Oxfordian clay in Bure (EDF) 108

3.4 Gas migration in undisturbed COx (ULg) 120

3.5 Modelling for understanding of flow physics and evaluation of uncertainty of gas transport in a wide range of sedimentary rocks and geological settings (NDA) 129

4 Final conclusions **138**

5 Summary of findings & way forward **141**

6 Publications **143**

FIGURES

Figure 1 Pressure and flow rate data collected during the gas injection test on sample COx-1. 18

Figure 2 Pressure and gas flow rate data from sample COx-1. Values in parentheses relate to stages numbers of the test described in Harrington et al., 2013. 19

Figure 3 Gas discharge from sample COx-1 following submersion and gentle heating in a glycerol bath. [1] = injection face; [2] = backpressure face. 19

Figure 4 Pressure and flow rate data collected during the gas injection test on sample COx-2. The initial outflow at the start of the tests relates to slug flow. Values in parentheses relate to stages numbers of the test described in Harrington et al., 2013. 20

Figure 5 Out flow and volumetric strain plotted against time. Plot [1] represents data during the first flow history; [2] represents data from second flow history (following repeat hydraulic testing). Volumetric strain is estimated from the pre-test volume of the sample COx-1 and the change in confining system volume. Negative strain represents dilation of the sample. 21

Figure 6 Flow and strain data from a triaxial test performed on COx (Cuss and Harrington 2011). Plot A shows the slow time dependent evolution in flux out of the core, while plot B, shows the sample dilating in response to changes in gas outflow. 22

Figure 7 Data from Angeli et al. (2009), showing a significant change in radial strain prior to and during gas breakthrough for a test performed on Draupne shale taken from the Troll East Field in the Norwegian Section of the North Sea. The change in P-wave velocity following breakthrough is symptomatic of gas penetration of the fabric due to the change in compressibility of the CO2 compared with that of the original porewater. 22

Figure 8 Schematic cross section of an oedometric membrane cell (Villar 2002) 28

Figure 9 Schematic cross section of a membrane cell (Villar 2002) 28

Figure 10 Schematic cross section of an oedometric cell with deposit for solutions (Villar 2002) 29

Figure 11 Appearance of samples prepared for the oedometer tests (left: EDS5_F1, right: EDS5_F2) 29

Figure 12 Samples used for the determination of the WRC in membrane cells and desiccators 30

Figure 13 Appearance of the setup for measurement of gas permeability and breakthrough pressure (low pressure configuration) 31

Figure 14 Appearance of an Opalinus clay sample drilled for a gas test, wrapped in the thermoretractable tube (black) and in the latex membrane (red) 32

Figure 15 Pressure paths followed in the gas breakthrough tests (tests OPA2 and OPA5 followed only Phase 1 under confining pressure 8 MPa) 32

Figure 16 Water retention curves obtained applying total suction under 8 MPa vertical stress and under no mechanical stress following wetting (left) and drying (right) paths. The value directly measured in borehole BDR-1 is included in one of the graphs 34

Figure 17 Retention curves obtained under free volume conditions in Opalinus clay samples from boreholes BHT1 and BHG-D1 35

Figure 18 Fittings to the van Genuchten expression as a function of the confinement conditions for total and matric suction (the dotted lines correspond to drying paths) 37

Figure 19 Fittings to the van Genuchten expression as a function of the kind of suction applied for different confinement conditions (the dotted lines correspond to drying paths) 37

Figure 20 Gas permeability values obtained in samples of Opalinus clay (tentative values, especially those below 10^{-22} m^2) 38

Figure 21 Basic concept of the tests to study gas driven tracer transport in disturbed Boom Clay. 42

Figure 22 Basic concept of the tests to study gas driven tracer transport in the interface Boom Clay – Bentonite. Blue = NaI saturated Boom Clay core. Yellow = half Boom Clay core. Pink = half bentonite core. 42

Figure 23 Iodine concentration in breakthrough samples (log-scale) vs. time of breakthrough for all experiments. 44

Figure 24 Role of time of sealing (1 night vs. 1 week) on the degree of desaturation (% of NaI saturated pore water that was transported during gas breakthrough – calculation based on measured concentration of I) for samples oriented parallel (left) and perpendicular (right) to the bedding plane. 45

Figure 25 Left: location of the gas pathway during breakthrough vs. degree of desaturation (% of NaI saturated pore water that was transported during gas breakthrough – calculation based on measured concentration I). Right: schematic view of interface clay fracture-cell. 45

Figure 26 Observation of gas bubbles during the dismantling of experiments 2011/1-1 (left) and experiment 2011/3-1(right). 46

Figure 27 Role of orientation wrt. bedding plane for disturbed clay samples sealed 1 week (left) and 1 night (right) (desaturation is % of NaI saturated pore water that was transported during gas breakthrough – calculation based on measured concentration I). 46

Figure 28 Desaturation (% of NaI saturated pore water that was transported during gas breakthrough – calculation based on measured concentration I) in combined Boom Clay/Bentonite cores (4 different samples). 47

Figure 29 3-D view of the boreholes and drifts for the PGZ tests 51

Figure 30 Details of the gas injection zone in PGZ1, position of each borehole 51

Figure 31 View of the gas module and temperature and humidity sensor in the drift 52

Figure 32 Water content profile in borehole PGZ1201 53

Figure 33 Pore pressure measurements before GAS1 in PGZ1201 and PGZ1202 53

Figure 34 Pressure measurements, gas flowrate and gas quantity injected in PGZ1201 from January 2010 to January 2011 55

Figure 35 Pressure measurements in PGZ1202 from January 2010 to April 2011 56

Figure 36 Pressure variation in interval 2 of PGZ1201 during the six pressure recovery steps (GRIS1 to GRIS6). 57

Figure 37 Comparison of the pressure difference as measured and as calculated at constant volume for the six steps GRI1 to GRI6 57

Figure 38 Successive sequences of hydraulic test and gas injection test in PGZ1 59

Figure 39 Location and layout of HG-C/HG-D site - right: location at the Mont Terri Laboratory; left: Schematic drawing of the borehole configuration and the site instrumentation. 62

Figure 40 Pressure responses in the injection borehole (BGS2-2) and observation borehole (BGS1-1, BGS1-2, BGS1-3) during the HG-C multi-step water injection (a), measured flow rates (b) and axial displacements (c). 64

Figure 41 Simulated response of the entire test sequence based on the best-fit parameters from the HI5 optimization for injection flow rates 65

Figure 42 Computed 95% confidence regions of parameter estimates based on the optimization of the log-log flow rates for HI1 through HI6. 66

Figure 43 Pressure responses in the injection borehole (BGS2-2) and observation borehole (BGS1-1, BGS1-2, BGS1-3) during the HG-C multi-step gas injection (a), measured flow rates (b) and axial displacements (c). 67

Figure 44 Simulated pressure responses in the injection borehole (BGS2-1) and observation borehole (BGS1-2) during the HG-C Experimental Phases 2, based on individual fits of Sequences GHI1–3, GHI4, and GHI5. 69

Figure 45 Simulated pressure responses in the injection borehole (BGS2-1) and observation borehole (BGS1-2) during the HG-C Experimental Phases 2, based on individual fits of Sequences GHI1–3, GHI4, and GHI5, whereby GHI5 includes the simulated results assuming pressure-dependent permeability. 70

Figure 46 HG-D testing: a) flow and pressure response; b) FIM response 72

Figure 47 HG-D testing gas injection flow and pressure response. 73

Figure 48a Schematic view of borehole location and bedding plane. 48b: Schematic view of boreholes BGS2, BGS3 and BGS4 including the position of the extensometers. 76

Figure 49a: Geometry of the model and finite element mesh. 49 b: Materials used in the model. 77

Figure 50 Elastic constitutive law of the joint element. Normal stiffness depends on joint opening. 78

Figure 51 Comparison between numerical and experimental pressures at injection borehole BGS2 and at measurement borehole BGS1 for phase “Hydro2” 81

Figure 52 Displacement measured at BGS3 (left) and displacement calculated (right) for phase “Hydro2” 81

Figure 53 Displacement measured at BGS4 (left) and displacement calculated (right) for phase “Hydro2” 81

Figure 54 Contour plot of liquid pressure at time 3380 hours 82

Figure 55 Comparison between numerical and experimental pressures at injection borehole BGS2 and at measurement borehole BGS1 for phase “Gas 2” 82

Figure 56 Displacement measured at BGS3 (left) and calculated (right) for phase “Gas2” 82

Figure 57 Displacement measured at BGS4 (left) and calculated (right) for phase “Gas2” 82

Figure 58 Contour plot of gas pressure at time 4964 hours 83

Figure 59 Comparison between numerical and experimental pressures at injection borehole BGS2 and at measurement borehole BGS1 for phase “Gas 3” 83

Figure 60 Displacement measured at BGS3 (left) and calculated (right) for phase “Gas 3” 83

Figure 61 Displacement measured at BGS4 (left) and calculated (right) for phase “Gas 3” 84

Figure 62 Contour plot of gas pressure at time 5029 hours 84

Figure 63 Comparison between numerical and experimental pressures at injection borehole BGS2 and at measurement borehole BGS1 for phase "Hydro 3" 84

Figure 64 Displacement measured at BGS3 (left) and calculated (right) for phase "Hydro 3" 85

Figure 65 Displacement measured at BGS4 (left) and calculated (right) for phase "Hydro 3" 85

Figure 66 Contour plot of liquid pressure at time 10826 hours 85

Figure 67 Comparison between numerical and experimental pressures at injection borehole BGS2 and at measurement borehole BGS1 for phase "Gas 4" 85

Figure 68 Displacement measured at BGS3 (left) and calculated (right) for phase "Gas 4" 86

Figure 69 Displacement measured at BGS4 (left) and calculated (right) for phase "Gas 4" 86

Figure 70 Contour plot of gas pressure at time 13936 hours (left) and at time 14611hours (right) 86

Figure 71 Degree of saturation of the Fracture at different distance from the injection borehole 87

Figure 72 TOUGH2 modelling grid for the simulation of the HG-C experiment. – Key explanation: Letters T, C, and B appended to the borehole names stand for "top", "center", and "bottom", respectively. Thus, BGS2B stands for interval 1 of BGS2. 89

Figure 73 Same view as in the previous figure but without the clay rock. 89

Figure 74 Measured injection pressures and injection flows (phase 2 of HG-C) 91

Figure 75 Conceptual model of the dilation process 92

Figure 76 Sketch of the tube-chamber model for gas flow. 94

Figure 77 Injection pressures in the water injection phase of the HG C experiment 98

Figure 78 Injection flows in the water injection phase of the HG C experiment 98

Figure 79 Measured and simulated injection flows (parameter set 1) 99

Figure 80 Measured and simulated injection flows (parameter set 2) 99

Figure 81 Measured flows and flows simulated with the tube-chamber model 99

Figure 82 Calculated and measured flow for the gas injection phase of the HG D experiment 99

Figure 83 2D axisymmetrical geometry 111

Figure 84 Plastic deformation on Lh 113

Figure 85 Liquid pressure and Saturation evolution on PRE02 113

Figure 86 Total radial stresses at several times along L 113

Figure 87 injection chamber Interval 2 (or PRE02) 114

Figure 88 Liquid pressure evolution in interval 2 : goal of initial saturation 115

Figure 89 $\chi_l^{N_2}$ (Gas pressure or concentration) at several times along L 115

Figure 90 Liquid Saturation at several times along L 116

Figure 91 Gas-liquid ration of Nitrogen at several times along L 116

Figure 92 Configuration and hypothesis of BDZ 117

Figure 93 Gas pressure evolution in interval 2 : goal of BDZ 117

Figure 94 Gas pressure evolution in interval 2 : goal of relative permeability in host rock 118

Figure 95 Schematic position of the pore pressure sensors (distances are measured from the gallery wall) 121

Figure 96 Gas flow injected experimentally at one face of the injection interval 122

Figure 97 Gas and water pressures evolution in the injection interval: comparison with pore pressures measurements and (b) evolution of the degree of saturation in claystone and in the injection interval for the 1st modelling 124

Figure 98 Influence (a) of the interval volume and of the initial degree of saturation in the injection interval and (b) evolution of the degree of saturation in claystone and in the injection interval for the new modelling 124

Figure 99 Influence of the introduction of an excavated damaged zone on the time evolution of pore pressures in the injection interval 125

Figure 100 (a) Influence of the gas relative permeability of the undisturbed claystone on the time evolution of pore pressures in the injection interval – (b) Gas permeability against degree of saturation- Comparisons with experimental data coming from Charlier et al. (2012) 126

Figure 101 Time evolution of pore pressures in the injection interval – Comparisons between experimental and numerical results 127

Figure 102 Time evolution of pore pressures in (a) the two intervals of the injection borehole and (b) in the three intervals of the measuring borehole – Comparisons between experimental and numerical results 127

Figure 103 Gas flows profiles at different gas injection peak – 1D modelling 128

Figure 104 Cartoon of an Anticline 129

Figure 105 Volume of gas in anticline with time (green) and effective radius (blue) as the gas dissolves 130

Figure 106 a. Illustration of the deepening of the mixed zone of red and blue fluid as a function of time and b. analysis of the histogram of red and blue fluid, illustrating the delineation between the red and blue zones, and the remaining pixels represent the mixed zone in the centre of the cell. 131

Figure 107 Evolution of the thickness of the mixing zone with time, scaled by $a(wt)^{1/2}$ illustrating the convergence of the mixing to a simple diffusion process. 131

Figure 108 a Illustration of the deepening of the mixed layer in a heterogeneous system consisting of two layers of different permeability. B. Variation of the depth of the mixed layer in the high (red) and low(blue) permeability layers as a function of time, over many oscillation cycles. The depth of the mixed zones have been scaled by $a(wt)^{1/2}$. 132

Figure 109 Illustration of the different flow patterns of a buoyancy driven gas flow in a mutply layered and single layered formation. 133

Figure 110 Experiment of the buoyancy driven dispersal of fluid in a HeleShaw cell, with a white line superposed on this image illustrating the prediction of the theoretical model we have developed. 134

Figure 111 a. Dispersal of a finite pulse of dye injected with the gas at the source for a finite time into a reseroir with 5 layers. The red green and blue series of lines denote the position

of the dye pulse at three progressively later times. b. variation of the tracer concentration which would be received at a test observation well as a function of time. The structure of the signal depends on the number of layers in the formation, and may be used to interpret the structure of the formation and hence the dispersal pattern of the gas. 134

Figure 112 Schematic of the flow configuration which leads to exchange of fluids between different aquifers. 135

Figure 113 a,b. Illustration of the experiment to test the model of exchange flow between two aquifers following development of a fracture between the layers. B. Measurement of the exchange flow rate for a series of experiments using different density differences between the upper ad lower reservoir, and also using different size ballotini which produce different permeability structures in the tube. 136

Figure 114 Series of images showing the steady state flow regimes becoming established. 136

Figure 115 Evolution of the mass with time for a single tube exchange flow experiment. 137

Figure 116 Illustration of the mass flow rate dependence on pipe length and diameter. 137

TABLES

Table 1 Summary of results from consolidation tests. Values for Young's modulus are based on a Poisson's ratio of 0.3 (Wileveau and Bernier, 2008). # Void ratio and volumetric strain values are based on pre-test moisture content off-cut data as both tests currently on-going. 15

Table 2 Summary of results of finite element modelling of consolidation tests. Values for COx-3 are provision awaiting full 3D analysis. 15

Table 3 Summary of results from hydraulic tests. COx-1 and COx-2 were orientated perpendicular to bedding, while COx-3 was parallel to the bedding. 16

Table 4 Parameters for the van Genuchten expression (Eq. 1) 36

Table 5 Parameters for the rock around Interval 2 of PGZ1201 (HYDRO1) 54

Table 6 Estimated hydraulic parameters before and after the gas injection test 58

Table 7 Overview of HG-C and HG-D experimental phases. 63

Table 8 Summary of parameter estimates from nSights optimization of HI1 through HI6. 65

Table 9 Summary of parameter estimates from ITOUGH optimization of GHI13-GHI5. 68

Table 10 Phases of the test. In blue are remarked the phases simulated. 75

Table 11 Initial conditions and parameters of the materials. 80

Table 12 Summary of figures with results corresponding to test stages 80

Table 13 Parameters used 97

Table 14 Parameter set 1 and 2 98

Table 15: parameters for HG-D experiment 99

Table 16: parameters for tube-chamber model 2 100

Table 17 Steps of modeling 111

Table 18 Hydro-mechanical parameters for Argilite and Chamber 112

Table 19 Hydraulic parameters for COx 123

Introduction

Gas generation and migration may have an impact on the hydraulic and the mechanical properties of the host rock. Consequently, these processes could affect the safety function of the host rock to retard and spread in time the release of radionuclides.

Earlier studies have shown that the ratio between the gas generation rate and the diffusive gas flux through the undisturbed host rock determines the development of a separate gas phase as well as the rate of increase of gas pressure. The two-phase flow properties of the host rock will determine the gas pressure at which gas flow will start as well as the quantity of water that will be displaced. The latter is particularly important in case of MLW disposal where gas generation and radionuclide release in the near-field can occur at the same time. There is now a general consensus that in the case of plastic clay-rich clays and in particular bentonite, classic concepts of porous medium two-phase flow are inappropriate and continuum approaches to modelling gas flow may be questionable depending on the scale of the processes and resolution of the numerical model. The mechanisms controlling gas entry, flow and pathway sealing in general clay-rich media are not yet fully understood. In order to get a better understanding of the processes and conditions by which gases are transported in porous media like clays, dedicated research is performed within WP5. Where other WP's focussed on the engineered barriers and seals (WP3) or on the disturbed host rock (WP4), this WP focusses on the undisturbed host rock.

This WP is split into 3 main research areas: gas transport laboratory experiments, gas transport in-situ experiments and modelling of gas transport in the undisturbed host rock. All three currently studied potential clay host rocks within Europe have been included i.e. the Swiss Opalinus clay, the French Callovo-Oxfordian clay and the Belgian Boom clay.

The gas transport laboratory experiments have been performed by BGS, CIEMAT and SCK•CEN. The experimental programme included a series of well focussed experiments to determine: two-phase flow parameters (e.g. water retention curves and relative permeabilities), basic gas flow mechanisms & geomechanical couplings (e.g. gas-pressure-induced pathways) and gas-driven radionuclide transport (SCK-CEN).

In-situ experiments have been performed by ANDRA in the Callovo-Oxfordian clay at the BURE URL site and by NAGRA in the Mont-Terri URL.

Andra performed a new gas borehole experiment (named PGZ-1) at the Bure site (Andra's URL) in order to evaluate gas migration properties of the saturated undisturbed indurated clay formation, following a new experimental protocol. The objectives of the test were to ameliorate the understanding of the gas transfer processes in clay porous media with low permeability, to evaluate the value of the gas threshold pressure, to estimate the dependencies between gas injection rate and gas flow into the formation and to measure gas fracture pressure.

NAGRA did set-up the HG-C/HG-D experiment at Mont Terri URL in order to investigate gas migration mechanisms at different gas pressures ranging from below pore water pressure to high pressures leading to dilatancy-controlled gas flow.

Different modelling teams used different codes and approaches to model the results obtained within the in-situ experiments performed within WP5. The PGZ-1 in situ experiment was modelled by ULg (code LAGAMINE) and EDF (code_ASTER) and the HG-C/HG-D in situ experiment was modelled by UPC (code_BRIGHT) and GRS (using the code TOUGH2/EOS7 and "tube chamber models"). Besides this direct application of models, NDA worked on models that allow

understanding of flow physics and evaluation of uncertainty of gas transport in a wide range of sedimentary rocks and geological settings.

A summary of all laboratory, in-situ and modelling activities performed within WP5 is given in this summary report. A detailed description of all laboratory, in-situ and modelling activities can be found in the reports that have been delivered within the framework of WP5 and which are available on the FORGE website (http://www.bgs.ac.uk/forge/home.html)

1. Gas transport laboratory experiments

1.1 Baseline hydraulic and gas transport properties of the Callovo-Oxfordian claystone (BGS)

1.1.1 Introduction and objectives

In a repository for radioactive waste, corrosion of ferrous materials under anoxic conditions combined with the radioactive decay of the waste and the radiolysis of water, will lead to the formation of hydrogen. If the rate of gas production exceeds the rate of gas diffusion within the pores of the barrier or host rock, a discrete gas phase will form (Weetjens and Sillen, 2006; Ortiz et al. 2002; Wikramaratna et al, 1993). Under these conditions, gas will continue to accumulate until its pressure becomes sufficiently large for it to enter the surrounding material. In a clay-based geological disposal facility (GDF), four primary phenomenological models describing gas flow can be defined: (i) gas movement by diffusion and/or solution within interstitial fluids along prevailing hydraulic gradients; (ii) gas flow in the original porosity of the fabric, commonly referred to visco-capillary (or 2-phase) flow; (iii) gas flow along localised dilatant pathways which may or may not interact with the continuum stress field; (iv) gas fracturing of the rock similar to that performed during hydrocarbon stimulation exercises. There is now a growing body of evidence (Angeli et al. 2009; Harrington and Horseman, 1999; Horseman et al. 1996, 2004; Harrington et al. 2009) that in the case of plastic clays and in particular bentonite, classic concepts of porous medium two-phase flow are inappropriate and continuum approaches to modelling gas flow may be questionable, depending on the scale of the processes and resolution of the numerical model. However, the exact mechanisms controlling gas entry, flow and pathway sealing in general clay-rich media are not fully understood and the “memory” of such pathways could impair barrier performance.

This study set out to measure the two-phase flow behaviour of the Callovo-Oxfordian claystone from the Bure underground research laboratory (URL) in France. Funding for this study has been provided by the French radioactive waste management operator, Andra, the European Union (FORGE Project) and the British Geological Survey through its well-founded laboratory programme and the Geosphere Containment project (part of the BGS core strategic programme).

The primary objectives of the study are to measure: (i) the hydraulic conductivity and intrinsic (absolute) permeability; (ii) the (threshold) capillary displacement pressure; (iii) the effective gas permeability and relative permeability to gas for a range of conditions; and (iv) the post-test gas saturation. Hydraulic testing was undertaken using a synthetic interstitial fluid. Helium was used in gas testing.

1.1.2 Experimental system and procedure

The basic permeameter consists of five main components: (1) a specimen assembly, (2) a 70 MPa rated pressure vessel and associated confining pressure system, (3) a fluid injection system, (4) a backpressure system, and (5) a PC-based data acquisition system. The specimen is subject to an isotropic confining stress, with injection platen mounted on the base of the specimen. A novel feature of the apparatus is the use of porous annular guard-ring filters around the inflow and outflow filters. The pressures in these two guard-rings can be independently monitored. The advantages of the guard-ring approach are: (a) pore pressure evolution can be studied, (b) hydraulic anisotropy can be quantified in a single test, (c) a check can be made of flow symmetry in the specimen, (d) excess gas pressure at gas entry can be determined, and (e) uncertainties associated with possible sheath leakage can be eliminated from data interpretation.

Permeants (gas and water) are injected at the base of the specimen to minimise the chance of slug flow during gas testing. In order to limit osmotic swelling of the specimen, a synthetic porewater solution was prepared for use as the backpressuring fluid and permeant during hydraulic test stages. Details of the hydrochemistry of the interstitial fluid were provided by Andra. This fluid was saturated with fluorescein prior to testing. Helium gas (selected as a safe substitute for hydrogen) was used to measure the gas transport properties of the claystone. In situ (isotropic) confining stress data was provided by Andra with the initial confining stress nominally set to 12.5 MPa with a backpressure of 4.5 MPa.

Three test plugs were obtained from a supplied core sample of Callovo-Oxfordian claystone. The first two, designated COx-1 and COx-2, were oriented with the plugs' cylindrical axies perpendicular to the bedding while the third, COx-3, was oriented parallel to the bedding.

An individual test history comprises a sequence of test stages. A consolidation (CO) stage involves incrementally raising confining pressure and measuring the volume of fluid displaced while backpressure (and injection pressure) are held constant. Constant pressure hydraulic (CPH) and gas (CPG) stages are used to evaluate the intrinsic permeability, specific storage, gas entry and breakthrough pressure, apparent threshold capillary pressure and gas permeability. At the end of hydraulic testing a pressure recovery stage (PRH) allows excess porewater pressures to dissipate. Synthetic groundwater solution is used as the backpressuring fluid in all test stages.

Sample COx-1 has been run through the most complex test sequence. Starting with initial consolidation and hydraulic tests, the sample was then run through a multi-stage gas injection test followed by a second hydraulic test and a second gas injection test. Sample COx-2 has had a consolidation test, an hydraulic test and a seven step pressure build-up gas injection test while sample COx-3 has so far just had consolidation and hydraulic tests.

1.1.3 Results

1.1.3.1 CONSOLIDATION TESTS

Each sample was first subjected to a consolidation test consisting of an initial equilibration period, with confining pressure at 9.5 MPa and porewater pressure at 4.5 MPa, followed by two steps up in confining pressure, to 11 MPa and then 12.5 MPa for samples COx-1 and COx-2 and to 11.5 MPa and 12.6 MPa for sample COx-3. Instantaneous flow rate and net cumulative flow volume data were collected, with the latter equating to volumetric strain. The data show well defined transient responses for the backpressure system for each increment in confining stress.

Analysis of the consolidation data based on the total volume of fluid expelled from the
at the end of each step is presented in

Table 1. Values for drained bulk modulus are therefore reasonably high, ranging from 1490 MPa to 2262 MPa. These values suggest that the specimen has not been subject to significant damage from de-stressing during sampling, transportation or specimen preparation. Young's modulus values were found to range from 1764 MPa to 2629 MPa.

Additional analysis of the consolidation tests was carried out using a finite element coupled deformation and porewater flow model of the experimental configuration. For these calculations the anisotropy of the permeability obtained from the hydraulic tests below was used for each sample and a value of 0.3 for the Poisson's ratio was assumed. Then, for each sample, the value of Young's modulus was adjusted to fit the magnitude of the net flow volume in each step whilst the permeability was adjusted to fit the transients. Since the code handles only 2D and axi-

symmetric configurations the test of sample COx-3 could not be analysed in this way. Table 2 shows the results of these calculations.

Table 1 Summary of results from consolidation tests. Values for Young's modulus are based on a Poisson's ratio of 0.3 (Wileveau and Bernier, 2008). # Void ratio and volumetric strain values are based on pre-test moisture content off-cut data as both tests currently on-going.

Stage no.	Ave. effective stress (MPa)	Void ratio (at end of stage)	Volumetric strain (%)	Drained compressibility $\beta/10^{10}$ (Pa^{-1})	Drained bulk modulus (MPa)	Young's modulus (MPa)
Data for CoX-1						
1	5.0	0.175	-	-	-	-
2	6.5	0.174	0.07	4.4	2262	2629
3	8.0	0.173	0.16	6.4	1574	1870
Data for CoX-2#						
1	5.0	0.193	-	-	-	-
2	6.5	0.192	0.09	5.6	1759	2092
3	8.0	0.191	0.19	6.7	1490	1764
Data for CoX-3#						
1	5.0	0.171	-	-	-	-
2	7.0	0.170	0.11	5.3	1902	2340
3	8.1	0.169	0.16	4.7	2133	2381

Table 2 Summary of results of finite element modelling of consolidation tests. Values for COx-3 are provision awaiting full 3D analysis.

Sample	Stage	k_r (m^2)	k_z (m^2)	E (MPa)	S_s (m^{-1})
COx-1	2	10.6×10^{-21}	4.0×10^{-21}	1825	7.2×10^{-6}
	3	9.0×10^{-21}	3.4×10^{-21}	1700	7.7×10^{-6}
COx-2	2	6.6×10^{-21}	2.5×10^{-21}	1600	8.1×10^{-6}
	3	6.6×10^{-21}	2.5×10^{-21}	1450	8.9×10^{-6}

1.1.3.2 HYDRAULIC TESTS

Following the consolidation tests each sample was subjected to a constant pressure hydraulic test with two steps to the injection pressure, the back pressure and confining pressure being constant. In each case the backpressure was held at 4.5 MPa while the injection pressure was stepped up to 7.5 MPa and then back down to 4.5 MPa. The data from these tests were fitted using a finite element porewater flow model and the results are collected in

Table 3. In all three samples pressure data from the guard rings show some anomalies that might indicate a measure of flow over the injection and/or backpressure surfaces which could give rise to anomalous estimates of the hydraulic anisotropy. For this reason data from the guard rings have not been used to estimate the anisotropy of this formation and only the estimated value for the axial component of permeability is reported. An estimate of hydraulic anisotropy may be obtained from the average of the axial permeabilities from samples COx-1 and COx-2 as a value for the cross-bed permeability and the axial permeability from sample COx-3 as a value for the permeability in the plane of bedding. This gives an anisotropy of 2.5.

Table 3 Summary of results from hydraulic tests. COx-1 and COx-2 were orientated perpendicular to bedding, while COx-3 was parallel to the bedding.

Sample	**k_z (m^2)**	**S_s (m^{-1})**
COx-1	1.8×10^{-21}	5.4×10^{-6}
COx-2	1.6×10^{-21}	6.0×10^{-6}
COx-3	4.5×10^{-21}	6.0×10^{-6}

1.1.3.3 GAS INJECTION TESTS

The gas injection test of sample COx-1 comprises a gradual 7 step increase in pressure gradient followed by a 2 step reduction and a shut-in period. Throughout the test the confining pressure and backpressure were maintained constant at 12.5 MPa and 4.5 MPa respectively. Figure 1 shows the pressure and flow data collected during this test.

The data from the backpressure guard-ring is notable for the fact that it differs significantly from that of the backpressure filter only for a short period around 200 days into the test. The data from the injection guard-ring after about 180 days track the pressures at the injection filter very closely with an offset of only about 100 kPa.

The gas outflow data show a small emergent flux until about 170 days when there is a gradually rising flow rate until an abrupt step at 200 days. Flow rate reduces again slightly at about 220 days and then follows a generally rising trend until about 430 days when the injection pressure is raised to 9 MPa. After an initial sharp rise in flow rate during this step there is a rapid decline at about 460 days and then recovery during the rest of the step. Flow rates then roughly double at the first of the 1.5 MPa steps in the injection pressure and a similarly substantial increase occurs in response to the final step at 600 days. Flows then decline in response to the two pressure reduction steps and then more slowly during the shut-in period.

Detailed examination of various features of the data suggests unstable gas flow is occurring through a network of pathways that varies with time. Gas breakthrough pressure is estimated to be about 2MPa. Estimates of the change of saturation at each of the pressure increase steps suggest high gas saturations at relatively small excess pressures which would appear to support the idea that dilatancy plays an important role in the passage of gas through the claystone.

Models of the gas injection experiment were constructed using the TOUGH2 porous medium multiphase flow code with the EOS3 equation of state module (Pruess et al, 1999). It was found that it was not possible to reproduce many of the important features of the data using these models. In particular the relationship between the onset of gas flow and the magnitude of subsequent flows could not be matched. Thus a model that had an onset of flow at about 180 days as seen in the data generated flow rates that were typically a quarter of those seen, whilst a model that generated flow rates comparable to those measured has an onset of flow at about 40 days.

Following completion of the initial gas injection cycle a second hydraulic test was performed to assess if the baseline hydraulic behaviour had changed. Attempts to model this data assuming a saturated initial state give rather poor fits, possibly due to the effects of residual gas in the system. However, a steady-state fit to the data was achieved with an axial permeability of 1.65×10^{-21} m^2 and a specific storage set to 4.5×10^{-5} m^{-1}. Comparison to the data in

Table 3 indicates there have been small changes to the permeability, but the specific storage appears to have increased by about an order of magnitude. This is probably due to the effect of residual gas within the sample pore space.

To examine the self-sealing capacity of the COx, it was decided to perform a second gas injection test following a simplified pressure history compared to that observed during the first gas injection cycle. Analysis of the data (presented in full in Harrington and Noy, 2013), provided clear evidence for the spatio and temporal evolution of dynamic and highly unstable gas pathways. However, a cross-plot of flux vs. excess gas pressure at steady-state, Figure 2, indicates little change in behaviour between test cycles, suggesting that the hysteresis observed between ascending and descending flow rates has been almost nullified by the reinjection of water. Under these conditions, this observation suggests the gas has little permanent impact on the structure and fabric of the clay.

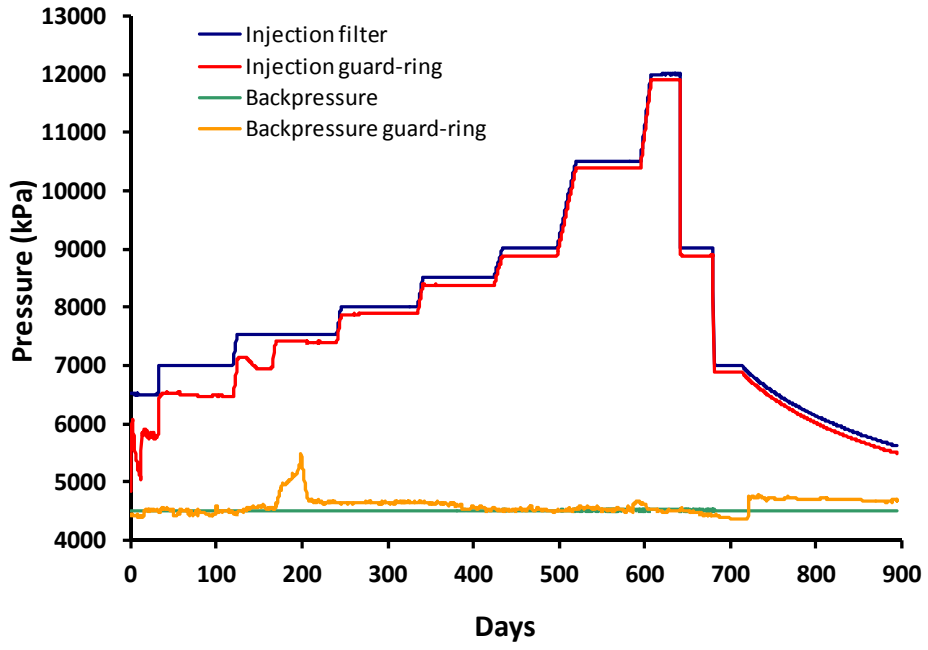

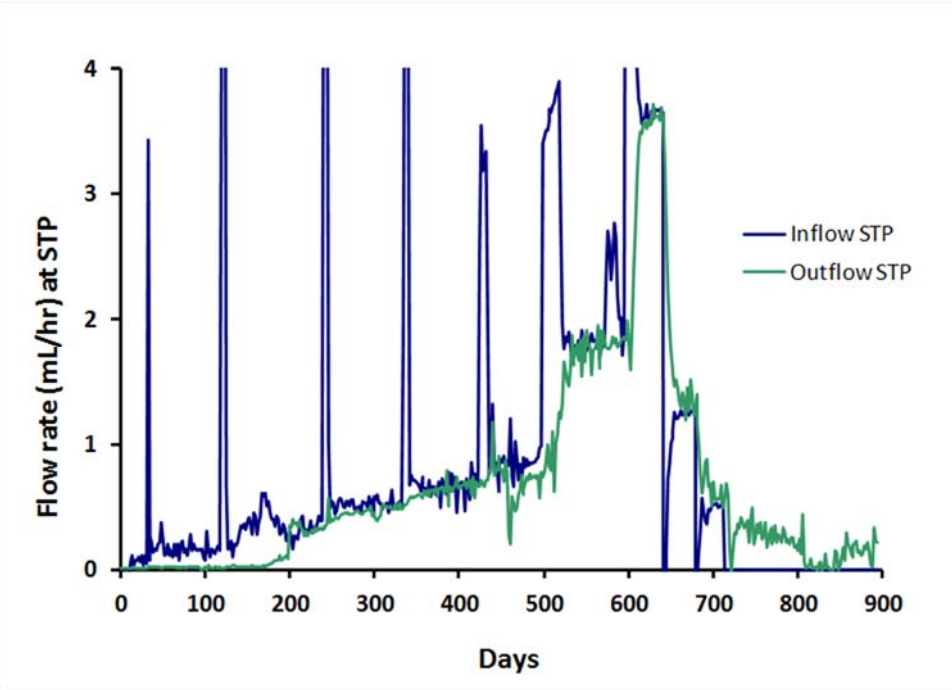

Figure 1 Pressure and flow rate data collected during the gas injection test on sample COx-1.

Following completion of test COx-1, the sample was submerged in glycerol and gently heated to promote the release of gas. Figure 3 shows two images of gas evolved from the injection and backpressure faces of the sample. Visual inspection clearly indicates a lower density of gas pathways on the inject face compared to that of the backpressure end. Intuitively, this is to be expected and is symptomatic of an expanding network of pathways which fan out as they propagate through the core. While this method of observation is not fully quantitative, it strongly suggests gas flow is very localised within the clay. This observation supports the early results describing the evolution of guard ring pressures and time dependent and non-uniform distribution of flow.

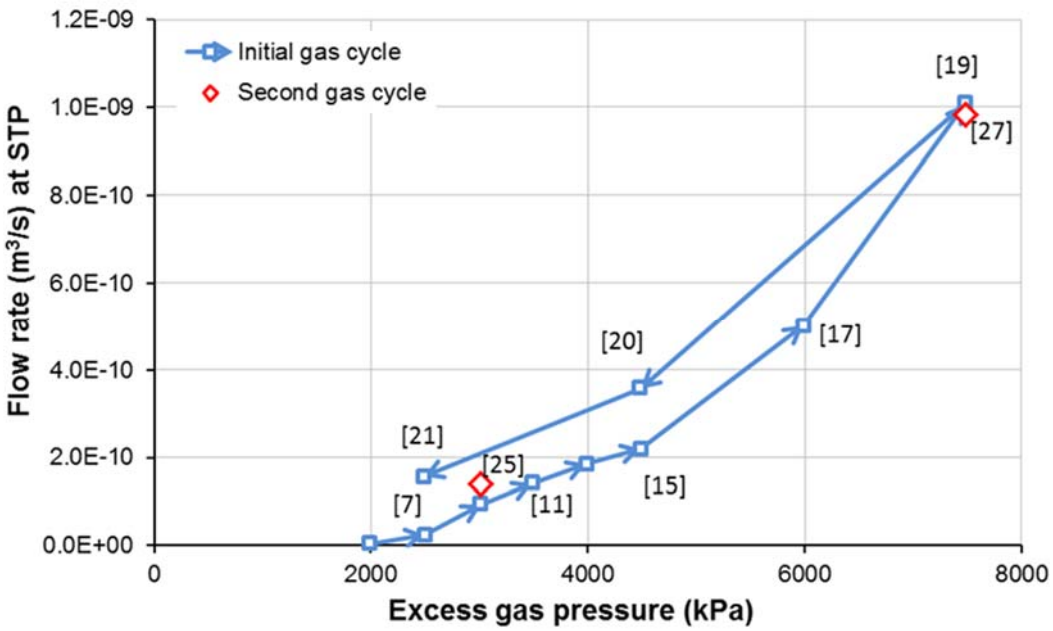

Figure 2 Pressure and gas flow rate data from sample COx-1. Values in parentheses relate to stages numbers of the test described in Harrington et al., 2013.

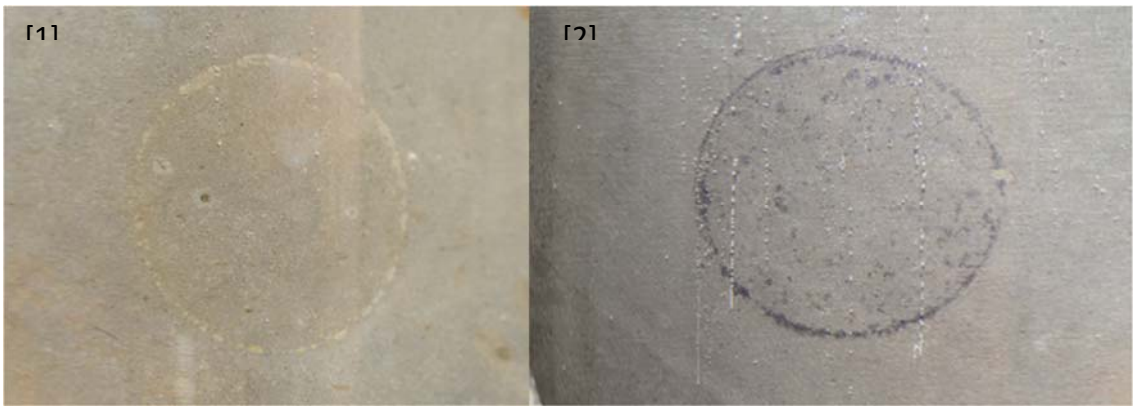

Figure 3 Gas discharge from sample COx-1 following submersion and gentle heating in a glycerol bath. [1] = injection face; [2] = backpressure face.

The gas injection test on sample COx-2 is currently incomplete with the pressure reduction and shut-in phases yet to be carried out. Figure 4 shows the pressure and flow data collected during this test. It is notable that it takes more than 400 days before there is a response at the injection guard-ring and less than a further 100 days before a response is seen at the backpressure guard-ring. Significant flow from the backpressure filter also first occurs after about 500 days.

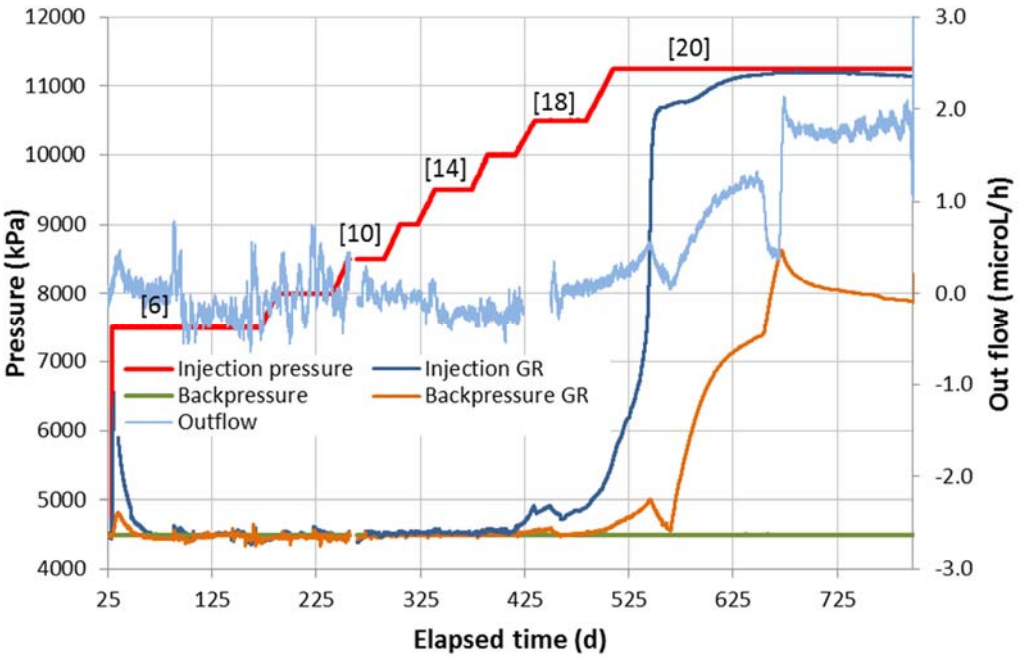

Figure 4 Pressure and flow rate data collected during the gas injection test on sample COx-2. The initial outflow at the start of the tests relates to slug flow. Values in parentheses relate to stages numbers of the test described in Harrington et al., 2013.

Modelling of the gas injection test on sample COx-2 with TOUGH2 gave similar problems to those found when looking at sample COx-1. Setting the model parameters to match the observed response time of the injection guard ring resulted in a delay to the onset of gas outflow from the backpressure filter until about 1300 days into the experiment compared to the 600 days seen. Also, gas flow rates were then about one tenth of the rates seen in the test. Conversely, setting the parameters to give a gas outflow onset at the time obtained in the test caused the model to show pressure changes at the injection guard ring much earlier than seen in the test data. However, the gas outflow rates from this model were comparable to those obtained in the test. The short time delay between pressure responses at the injection and backpressure guard rings suggests that some form of direct pathway flow is occurring rather than porous medium flow.

1.1.3.4 EVIDENCE FOR DILATANCY

Analysis of volumetric data from the confining pressure pump for test COx-1 provides an estimate for the change in sample volume during gas flow (Figure 5). The negative strain response is symptomatic of an increase in sample volume i.e. dilation. As outflow asymptotically approaches steady state, volumetric strains plateau, and the system enters a quasi-steady state. While both correlations are rather crude, they indicate a general dilatant response during gas flow within the COx. This is further supported by post-test measurements of sample saturation for test COx-1 which demonstrate no measureable desaturation of the sample following hundreds of days of gas testing.

Data from a triaxial test (Figure 6) performed within WP5 clearly illustrates the time-dependent nature of deformation (i.e. radial displacement) within the COx during gas breakthrough (Cuss and Harrington, 2011; Cuss et al., 2014). The change in sample volume stems from slow time-dependent deformation of the fabric as gas permeability develops. This evolution in behaviour provides an explanation for the evolution in gas flow observed across the specimen, as the gas meets and then slowly deforms its way through lower permeability or less compressible zones within the clay. Such a mechanism would introduce a time-dependency into the mechanisms

governing gas flow in the Callovo-Oxfordian clay and would help to explain the observations seen in this study.

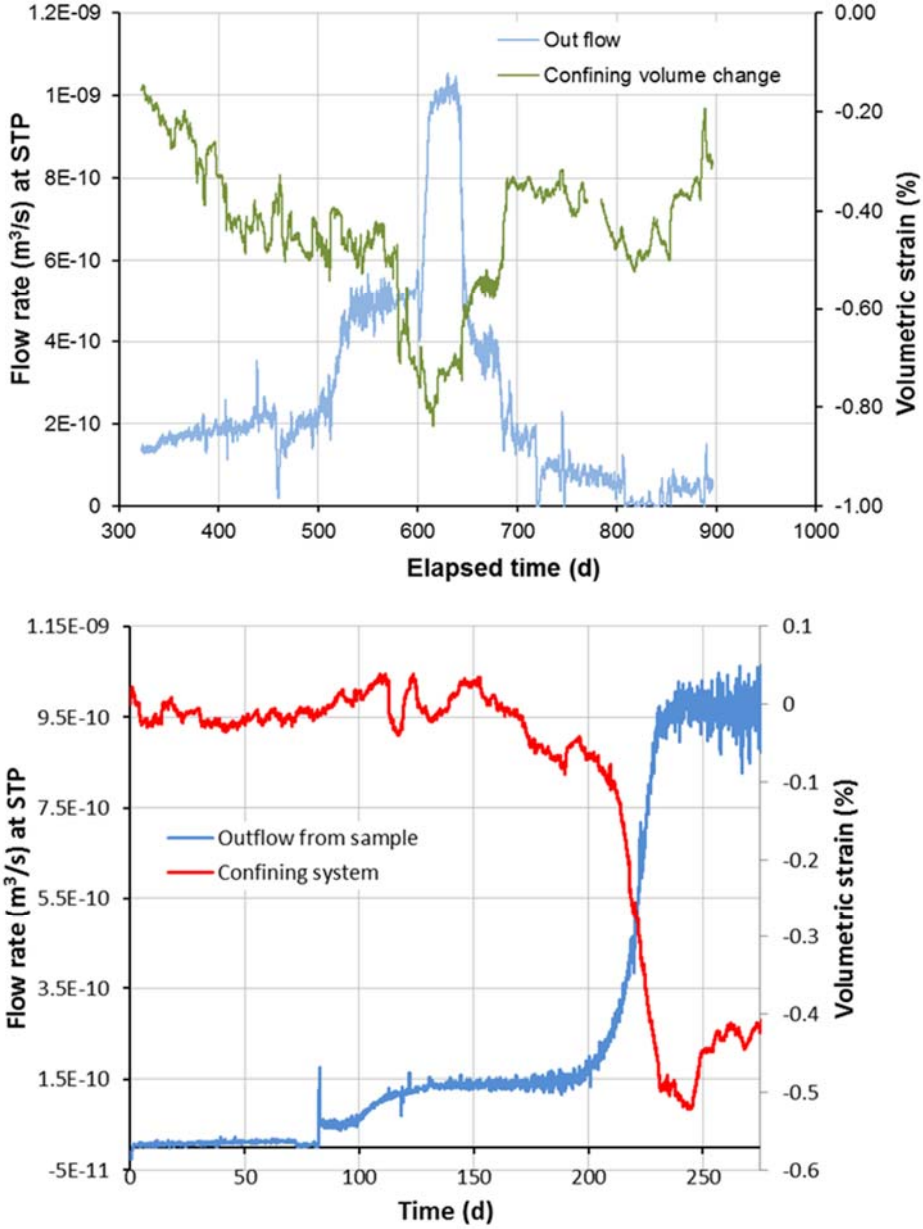

Figure 5 Out flow and volumetric strain plotted against time. Plot [1] represents data during the first flow history; [2] represents data from second flow history (following repeat hydraulic testing). Volumetric strain is estimated from the pre-test volume of the sample COx-1 and the change in confining system volume. Negative strain represents dilation of the sample.

Recent work by Angeli et al. (2009) on a sample of Draupne shale from the Troll East Field in the Norwegian Section of the North Sea, clearly demonstrates dilatancy during the onset of gas flow (Figure 7). This is accompanied by a reduction in P-wave velocity which the authors attribute to the penetration of the sample by the carbon dioxide. It is clear from the data that dilatancy and time-dependent processes are key factors in the development of gas permeability within the Draupne shale. The Draupne shale has a clay fraction (around 40% by weight) similar to that of the Callovo-Oxfordian clay but has a significantly higher porosity (around 24%).

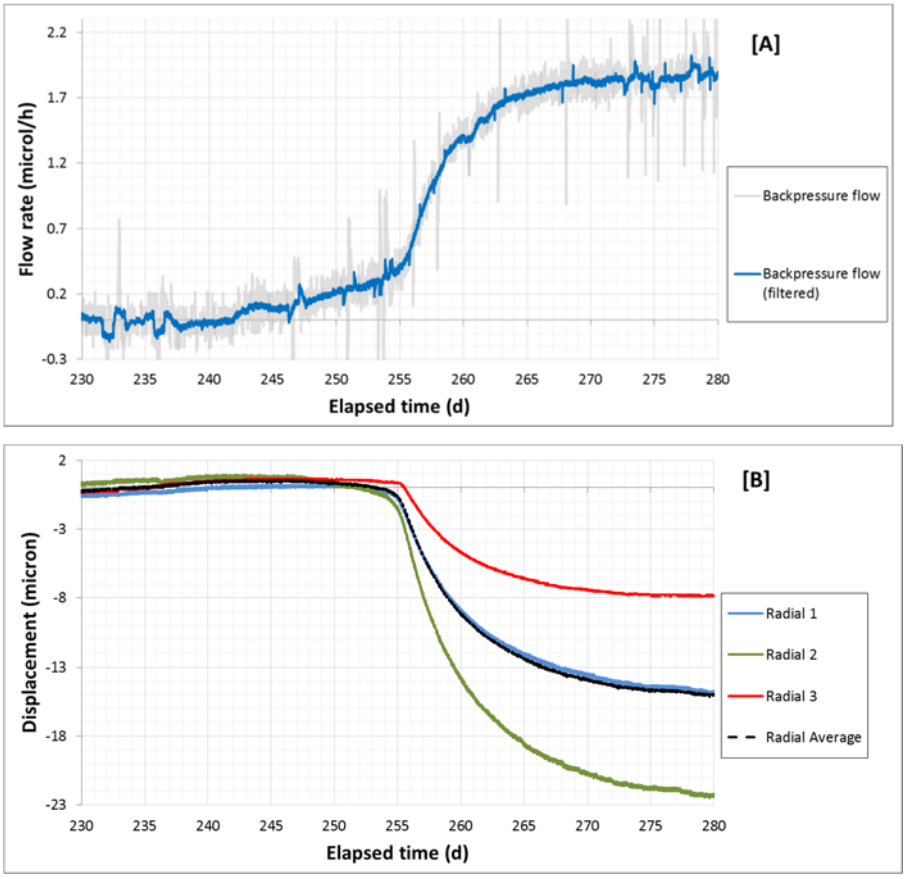

Figure 6 Flow and strain data from a triaxial test performed on COx (Cuss and Harrington 2011). Plot A shows the slow time dependent evolution in flux out of the core, while plot B, shows the sample dilating in response to changes in gas outflow.

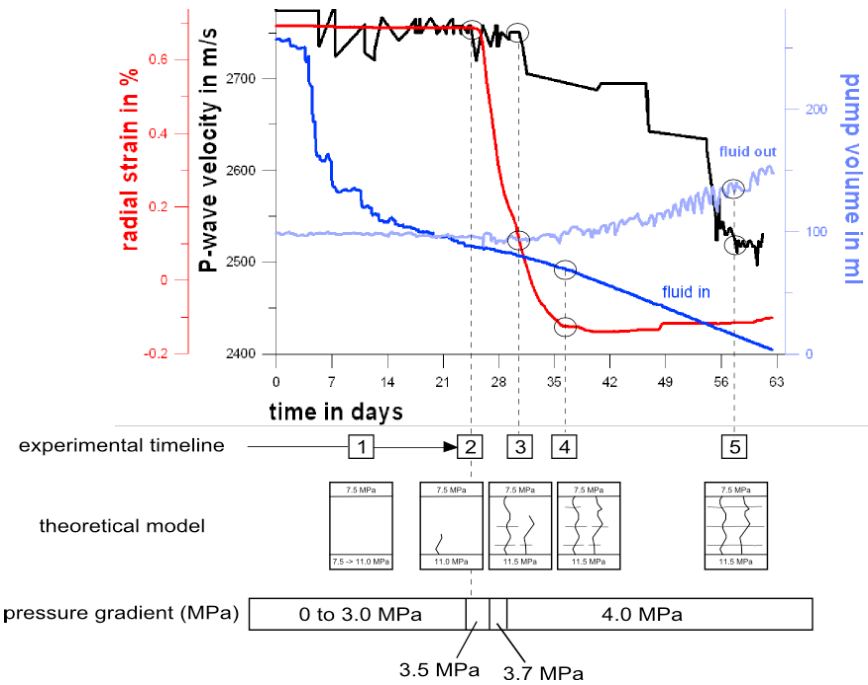

Figure 7 Data from Angeli et al. (2009), showing a significant change in radial strain prior to and during gas breakthrough for a test performed on Draupne shale taken from the Troll East Field in the Norwegian Section of the North Sea. The change in P-wave velocity following breakthrough is symptomatic of gas penetration of the fabric due to the change in compressibility of the CO2 compared with that of the original porewater.

While site specific factors will play a role in determining the multi-phase flow and hydro-mechanical behaviour of the Bure claystone, it seems highly likely that processes similar to those observed in the Draupne shale will apply. This assertion is borne out in the data and would help explain a number of observations reported during this experimental study including the apparent inability of the current modelling approach to adequately predict the system response.

When viewed in its totality, this data provides compelling evidence for the movement of gas in Callovo-Oxfordian claystone by pathway dilation.

1.1.4 Discussion/Conclusions

A series of long-term laboratory tests have been undertaken at the BGS to examine the fundamental mechanisms governing the migration of gas through COx. These measurements demonstrate the movement of gas is accompanied by dilation of the clay fabric and a slow temporal evolution of gas permeability within each specimen (Harrington et al., 2012, 2013).

Spontaneous increases/decreases in guard ring pressures and downstream flux occur throughout each test and are symptomatic of highly unstable dynamic pathways which open and close in an apparently random way. Such observations are difficult to reconcile with standard porous medium concepts.

The observed hysteresis between drainage and imbibition responses is common (Zweigel et al. 2006; Harrington et al. 2009) and signifies a non-recoverability in the system. Post-test measurements of desaturation from tests COx-1 (Harrington et al., 2013) and SPP-1 (Cuss et. al, 2014) indicate no discernible displacement of interstitial fluid from the original porosity. This and the visual observations of localised degassing strongly indicate gas flow is through localised pathway dilation.

The inability of classic porous medium models to adequately represent the data is not surprising when one looks at the response from the triaxial test SPP-1 (Figure 6) prior to and after gas breakthrough. The data clearly shows that gas flow is accompanied by a small, but well defined volume increase of the sample which cannot be explained by compressibility calculations. The data clearly exhibits time dependent strain. As dilation increases so does the volumetric discharge from the sample. This data conclusively demonstrates that permeability is a dependent variable, integrally linked to the conductive pathways aperture (in this test, manifest as volumetric strain). It is interesting to note that the observed increase in radial strain is non-uniform suggesting localised flow within the sample.

However, the existence of time-dependent discrete pathway flow coupling gas pressure gradient, porewater pressure and stress has been well documented in pure clay systems (Horseman and Harrington, 1997; Horseman et al. 1996, 1999; Harrington and Horseman, 2003; Sathar et al., 2012) and natural plastic clays (Horseman and Harrington, 1994; Ortiz et al, 1996; Sen et al., 1996; Harrington and Horseman 1999; Rodwell et al., 2000; Cuss and Harrington, 2011; Cuss et al., 2013; Gerrard et al., 2014; Harrington et al. 2009, 2012[a], 2012[b] 2013; Angeli et al., 2009).

In summary, it is clear that attempts to model these gas injection experiments have been unable to reproduce significant aspects of the data and many features are indicative of the development of discrete flow pathways. As such, these results complement a number of other studies that have shown the importance of time-dependent discrete pathway flow of gas in pure and natural plastic clays.

1.1.5 References

ANGELI, M., SOLDAL, M., SKURTVEIT, E. AND AKER, E. (2009). Experimental percolation of supercritical CO2 through a caprock. Energy Procedia 1, 3351-3358.

CUSS, R.J., HARRINTON, J., GIOT, R., and AUVRAY, C. (2014) Experimental observations of mechanical dilation at the onset of gas flow in Callovo-Oxfordian claystone. Clays in Natural and Engineered Barriers for Radioactive Waste Confinement. In: Norris, S., Bruno, J., Cathelineau, M., Delage, P., Fairhurst, C., Gaucher, E. C., Höhn, E. H., Kalinichev, A., Lalieux, P. & Sellin, P. (eds) *Clays in Natural and Engineered Barriers for Radioactive Waste Confinement*. Geological Society, London, Special Publications, **400**

CUSS, R.J., AND HARRINGTON, J.F. (2011) Update on dilatancy associated with onset of gas flow in Callovo-Oxfordian claystone; Progress report on test SPP_COx-2. British Geological Survey Commissioned Report, CR/11/110. 34pp.

GERARD, P., HARRINGTON, J., CHARLIER, R. and COLLIN, F. (2014). Modelling of localised gas preferential pathways in claystone. International Journal of Rock Mechanics & Mining Sciences, Vol. 67, pp. 104-114.

HARRINGTON, J.F., DE LA VAISSIERE, NOY, D.J., CUSS, R.J., and TALANDIER, J. (2012[a]) Gas Flow in Callovo-Oxfordian Clay (COx): Results from Laboratory and Field-Scale. *Mineralogical Magazine*. December 2012, Vol. **76(8)**, pp.3303-3318.

HARRINGTON, J.F., MILODOWSKI, A.E., GRAHAM, C.C., RUSHTON, J.C., and CUSS, R.J. (2012[b]) Evidence for gas-induced pathways in clay using a nanoparticle injection technique. *Mineralogical Magazine*. December 2012, Vol. **76(8)**, pp.3327-3336.

HARRINGTON, J.F. NOY, D.J. and Cuss, R.J. (2013). Long-term gas migration experiments in Callovo-Oxfordian Claystone. British Geological Survey, Technical Report, CR/13-088.

HARRINGTON, J.F., NOY, D.J., HORSEMAN, S.T., BIRCHALL, J.D. and CHADWICK, R.A. (2009). Laboratory study of gas and water flow in the Nordland Shale, Sleipner, North Sea. in M. Grobe, J. C. Pashin, and R. L. Dodge, eds., Carbon dioxide sequestration in geological media—State of the science: AAPG Studies in Geology 59, p. 521– 543.

HARRINGTON, J.F. AND HORSEMAN, S.T. (2003). Gas migration in KBS-3 buffer bentonite: Sensitivity of test parameters to experimental boundary conditions. Report TR-03-02. Svensk Kärbränslehantering AB (SKB), Stockholm, Sweden.

HARRINGTON, J.F. AND HORSEMAN, S.T. (1999). Gas transport properties of clays and mudrocks. In. Aplin, A.C., Fleet, A.J. and Macquaker, J.H.S. (eds) Muds and Mudstones: Physical and Fluid Flow Properties. Geol. Soc. London, Spec. Pub. 158, 107-124.

HORSEMAN, S.T., HARRINGTON, J.F. AND SELLIN, P. (1999). Gas migration in clay barriers. In: Pusch, R. and Yong, R.N. (eds) Microstructural Modelling of Natural and Artificially Prepared Clay Soils with Special Emphasis on the Use of Clays for Waste Isolation (1999 Special Edition), Engineering Geology, Vol 54, pp 139-149, Elsevier, Amsterdam.

HORSEMAN, S.T. AND HARRINGTON, J.F. (1997). Study of gas migration in Mx80 buffer bentonite. British Geological Survey, Technical Report WE/97/7.

HORSEMAN, S.T., HARRINGTON, J.F. AND SELLIN, P. (1996). GAS migration in Mx80 buffer bentonite. In: Symposium on the Scientific Basis for Nuclear Waste Management XX (Boston), Materials Research Society, Vol. 465. 1003-1010.

HORSEMAN, S.T. AND HARRINGTON, J.F., 1994. Migration of repository gases in an overconsolidated clay. British Geological Survey, British Geological Survey, Technical report WE/94/7.

ORTIZ, L., VOLCKAERT, G. and MALLANTS, D. (2002). Gas generation and migration in Boom Clay, a potential host rock formation for nuclear waste storage. Engineering Geology, 64, 287-296.

ORTIZ, L., VOLCHARET, G., DE CANNIERE, P., AERTSENS, M., HORSEMAN, S.T., HARRINGTON, J.F., IMPEY, M., AND EINCHCOMB, S. (1996). MEGAS - Modelling and Experiments on Gas Migration in Repository Host-rocks. Proc. EU PEGASUS Meeting at Rapolina-Terme, Italy, 14-15 June 1995. Nuclear Science and Technology Series, EUR 16746 EN, Luxembourg, 127-147.

PRUESS K., OLDENBURG C., MORIDIS G. (1999). TOUGH2 user's guide, version 2.0. Lawrence Berkeley National Laboratory report LBNL-43134.

RODWELL, W.R. (ED.) (2000). Research into Gas Generation and Migration in Radioactive Waste Repository Systems (PROGRESS Project). Nuclear Science and Technology EUR 19133 EN, European Commission, Luxembourg.

SATHAR, S., REEVES, H.J., CUSS, R.J., and HARRINGTON, H.J. (2012) Critical stress theory applied to repository concepts; the importance of stress tensor and stress history in fracture flow. *Mineralogical Magazine*. December 2012, Vol. **76(8)**, pp.3165-3177.

SEN, M.A., HORSEMAN, S.T. AND HARRINGTON, J.F. (1996). Further studies on the movement of gas and water in an overconsolidated clay: Contribution to MEGAS Phase 2 Report (PEGASUS Project). British Geological Survey, Technical Report WE/96/8 To: Commission of European Communities (CEC), Brussels.

WEETJENS, E. and SILLEN, X. (2006). Gas Generation and Migration in the Near Field of a Supercontainer-Based Disposal System for Vitrified High-Level Radioactive Waste, Proc. 11th Int. High-Level Radioactive Waste Management Conf. (IHLRWM), Las Vegas, Nevada, April 30–May 4, 2006.

WIKRAMARATNA, R.S., GOODFIIELD, M., RODWELL, W.R, NASH, P.J. and AGG, P.J. (1993). A preliminary assessment of gas migration from the Copper/Steel Canister. SKB Technical report TR93-31.

WILEVEAU, Y., AND BERNIER, F. (2008). Similarities in the hydromechanical response of Callovo-Oxfordian clay and Boom Clay during gallery excavation. Physics and Chemistry of the Earth, 33, S343–S349.

ZWEIGEL, P., MOEN, A., VASSENDEN, F. & ERDMANN, M. (2006). The role of hysteretic two-phase flow processes during capillary leakage. American Association of Petroleum Geologists International Conference and Exhibition, Perth, 5-8 November 2006.

1.2 Determination of two-phase flow parameters and analysis of fracturing by gas overpressure in opalinus clay (CIEMAT)

1.2.1 Scope and objectives

This report includes the work carried out by CIEMAT in FORGE WP5.1 "Gas transport laboratory experiments", which included two kinds of tests in indurated clay (the Opalinus clay), gas permeability and gas breakthrough pressure determinations and the determination of 2-phase flow parameters –one of the possible gas migration mechanisms in Opalinus clay –.

The fitting parameter P of the water retention curves is usually related to the air-entry value (AEV), which can change according to the hydraulic history of the material, its porosity and confinement conditions and even the kind of suction considered, since in some materials the osmotic suction component can be important and thus the difference between total and matric suctions large. Since the AEV is key to evaluate the two-phase flow, the water retention curves of Opalinus clay samples were determined under high confinement (vertical stress of 8 MPa) –to simulate the in situ conditions– and under free volume conditions for comparison, since this gas transport mechanism is sensitive to the stress state, in particular to porosity changes.

For the determination of the gas permeability and gas breakthrough pressure a setup was designed and fine-tuned. It allows to apply gas injection pressures of up to 18 MPa to cylindrical samples while keeping higher confining pressures and measuring the gas outflow.

The measurements of the stress state at Mont Terri indicate that σ1 is 6-7 MPa (Corkum & Martin 2007), hence the confining pressures applied in the laboratory tests were higher than this value.

1.2.2 Description of experiments

1.2.2.1 MATERIAL

The material used in the tests came from two different boreholes drilled in the Opalinus Clay Mesozoic formation in the Mont Terri Underground Research Laboratory in the Folded Jura mountains (http://www.mont-terri.ch). This formation is a mainly marly claystone with differing proportions of sand and carbonates around 180 million years old (Aalenian). At the rock laboratory, the Opalinus Clay has a layer thickness of around 140 m.

From a mineralogical point of view the Opalinus Clay consists of 40-80% clay minerals (including mixed layers of swelling illite and smectite), 10-40% quartz, 5-40% calcite and smaller proportions of siderite, pyrite and organic carbon. The dry density range is between 2.20 and 2.41 g/cm^3, the water content between 5.0 and 8.9% and the hydraulic conductivity between $2\cdot10^{-14}$ and $1\cdot10^{-12}$ m/s.

Of the three facies of Opalinus Clay that can be distinguished, the materials used in this investigation belong to the shaly one, which is a homogeneous, barely visible laminated claystone with low sand content. For the determination of the water retention curves (WRCs) the undisturbed cores from two different boreholes were used:

- BHT-1, from the Hydrogen Transfer (HT) test run by ANDRA. Core samples from metres 7.35 to 14.73 were sent to CIEMAT by ANDRA on May 2009 and they were kept since then vacuum packed at 4°C. These samples were mainly used for mineralogical and geochemical determinations in the context of the HT Project (Fernández *et al*. 2011). Their water content and dry density were between 6.6 and 8.0% and around 2.26 g/cm^3, respectively. The samples used for the water retention curve determinations belong to the depth 14.30-14.73 and 12.42-12.96, and grain densities of 2.70 and 2.72 g/cm^3, respectively, were determined.

- BHG-D1, from the Reactive Gas Transport in Opalinus Clay (HG-D) test run by NAGRA. A core sample kept in resin from metres 11.8 to 12.5 was sent to CIEMAT by NAGRA on March 2010 specifically for the tests to be performed in the context of the FORGE project. It was kept since then at 20°C. The water content and dry density determined in some samples from this core were 7.1% and 2.28 g/cm^3, respectively, and its measured grain density was 2.70 g/cm^3.

A sample from the BHG-D1 core of dry density 2.4 g/cm^3 and water content 3.4% (slightly air-dried) was lyophilised and analysed by mercury intrusion porosimetry (MIP). Most of the pore sizes were comprised in the range 2-50 nm, *i.e*. in the mesopore range, with a dominant pore mode of 11 nm. The air entry value corresponding to this dominant pore mode calculated from the Laplace's equation is 27.8 MPa.

For the gas permeability and breakthrough pressure tests a core from borehole BDR-1 was used. Additionally, the total suction of this core was measured at laboratory temperature (21°C) with two capacitive sensors inserted in a suitable perforated hole. The equilibrium value was found to be 31.3±0.1 MPa for a dry density of 2.33 g/cm^3 and water content of 6.4% (determined in samples drilled from the core). The measured grain density for this core was 2.71 g/cm^3.

1.2.2.2 WATER RETENTION CURVES

To determine the WRCs of the undisturbed material under vertical stress, suction-controlled oedometers –in which the sample was laterally confined and placed under constant vertical stress and suction– were used. The vertical stress applied during the tests was 8 MPa, the maximum that could be reached in the equipments, and the suction applied was either matric or total. The techniques applied for the determination of the WRC imposed suction instead of measuring it, that is to say, subjected the sample to a given and known suction that conditioned its water content while the other variables (stresses, strains) were modified or measured. Two different techniques were used to impose suction (Villar 2002): axis translation (matric suction, in membrane cells) and the imposition of relative humidity (total suction, in cells with deposit for solution). The WRC were also determined with the same suction control techniques in non confined samples, so that to evaluate the effect of the mechanical stress on the water retention capacity and in particular, on the air entry value.

Matric suction was applied to the samples through the axis translation technique. The principle of axis translation is the modification of the suction of a sample by increasing the pressure of the gaseous phase in its pores. The sample was placed in a cell in contact with water at atmospheric pressure through a membrane permeable to water but not to gas. The pressure in the cell was increased by injecting gas at the desired pressure, this increasing the air pressure in the pores of the sample. This situation forced the sample to exchange water through the membrane until equilibrium was reached once again. Given that the changes in capillary (matric) suction are caused by the difference between the pressure of the air in the pores (u_a) and the pressure of the water (u_w), when air pressure was applied to the sample an increase in u_a was induced, while u_w remained the same as atmospheric pressure. In this way, capillary suction varied by the same amount as gas pressure. The membrane allowed ions to pass through, as a result of which osmotic suction was not controlled by this method. The oedometer membrane cells used are shown in Figure 8 and the cells used for the determination of the WRC under no mechanical stress in Figure 9. The tests were performed at 20°C.

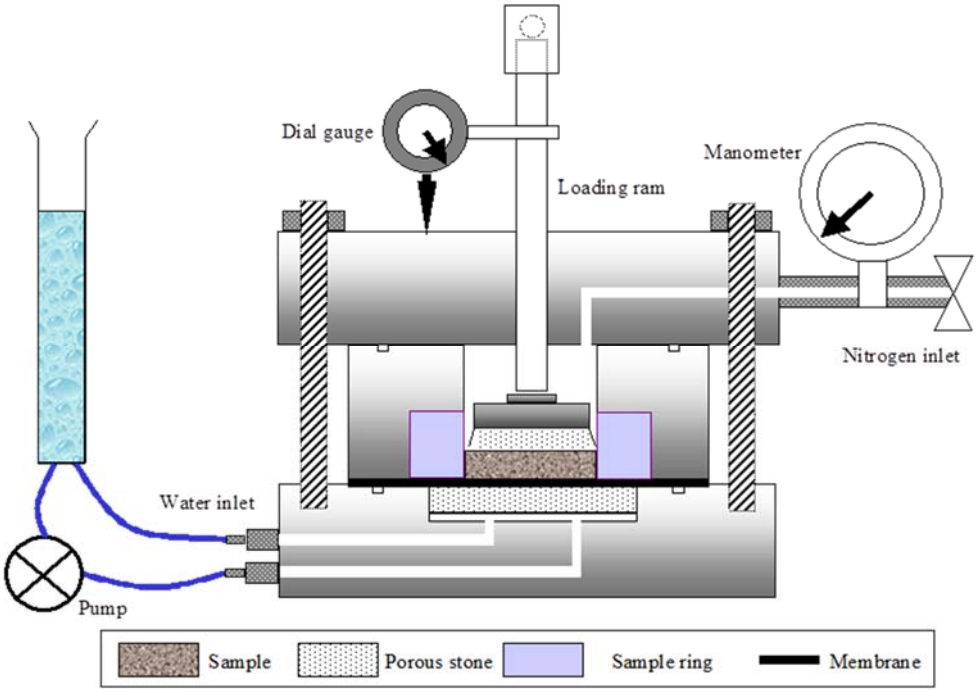

Figure 8 Schematic cross section of an oedometric membrane cell (Villar 2002)

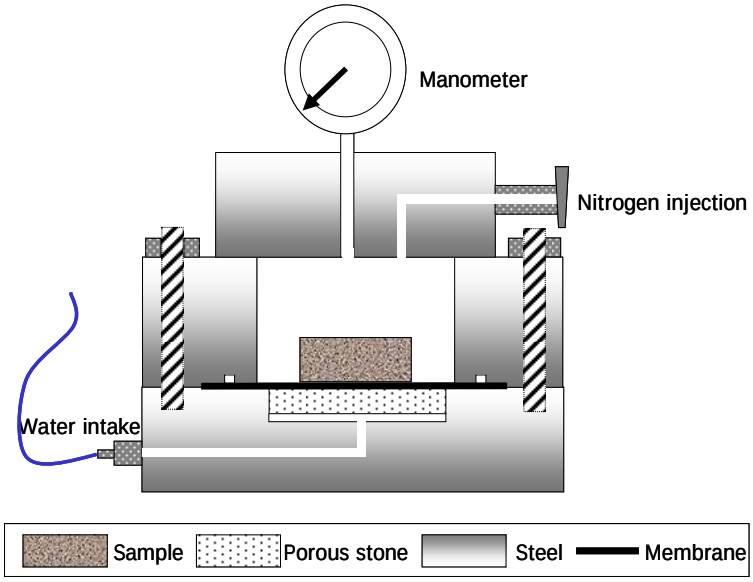

Figure 9 Schematic cross section of a membrane cell (Villar 2002)

The method to control total suction by imposing relative humidity (RH) is based on the fact that this conditions the pressure of the water and gas in the pores (u_w and u_a). This humidity may be imposed by means of solutions of sulphuric acid. The sample exchanges water with the atmosphere until thermodynamic equilibrium is reached with the vapour pressure of the solution, as a result of which total suction is modified. The temperature was kept constant at 20°C throughout the entire tests. The oedometric equipment used includes modified oedometric cells in which total suction may be applied, because they have a glass deposit in which the solution is contained (Figure 10). This technique was also applied in desiccators to determine the WRC under no mechanical stress.

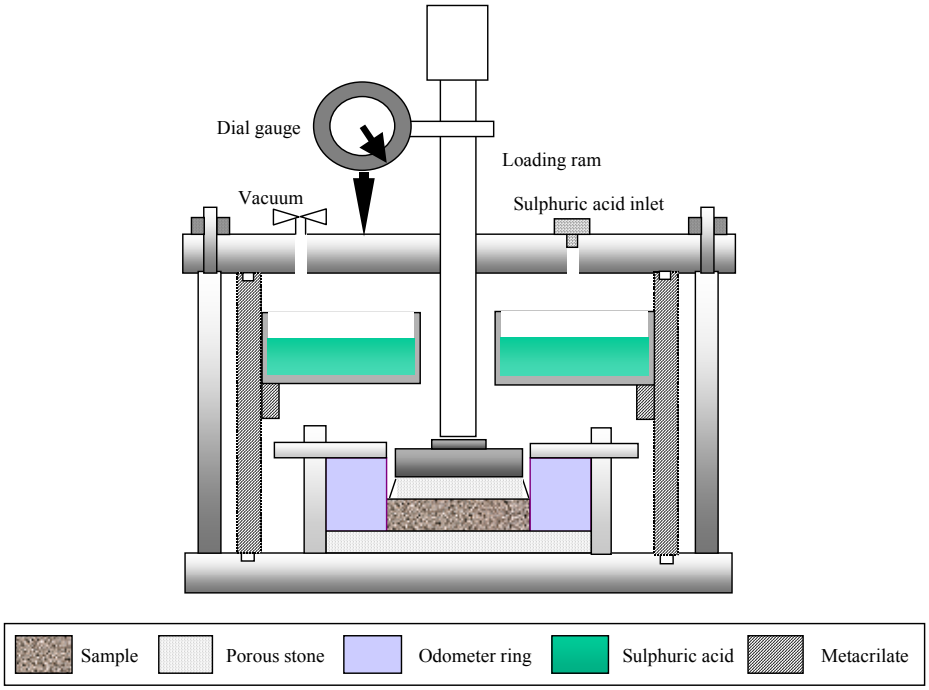

Figure 10 Schematic cross section of an oedometric cell with deposit for solutions (Villar 2002)

The undisturbed clay was trimmed in cylindrical specimens to fit the oedometer ring, i.e. 1.2-2.0 cm in length and 11.40 cm^2 in cross section. For that, an approximately 2-cm thick slice of the boreholes was cut with a band saw and a cylindrical specimen was obtained from it by trimming (Figure 11). This was a particularly difficult task due to the low consistency of the material, which easily crumbled and exfoliated. In some cases the voids between the sample and the ring were filled up with crumbled adjacent material and slightly pressed. In spite of it, the initial dry density of the samples was systematically lower than the borehole density (2.13±0.08 g/cm^3).

Figure 11 Appearance of samples prepared for the oedometer tests (left: EDS5_F1, right: EDS5_F2)

Once the oedometer ring with the sample was placed in the oedometer cell and load frame, the desired suction and vertical stress were applied simultaneously and the vertical strain recorded. Once equilibrium was reached for a given suction and stress (from previous experience it was considered that equilibrium was reached after two months or when there was no vertical strain change), the cell was released, the ring and the sample were weighed together (since the sample could not be removed from the ring without undergoing major disturbance) and the specimen height was indirectly measured. Afterwards, the oedometer ring was immediately assembled in the cell, which was placed in the oedometer frame, and the vertical stress was applied, along with the new suction.

Drying or wetting paths were followed, according to the equipment limitations. In the tests performed in oedometers with suction control by nitrogen pressure, the maximum applicable suction was 14 MPa, which was close to the in situ value of the Opalinus clay as determined in a previous research in samples from the VE test (Villar et al. 2009). In oedometers with suction controlled by solutions, the minimum suction applicable was 2 MPa.

At the end of the tests, the samples were extracted from the ring, measured, weighed and dried in the oven at 110°C for 48 h to determine their final water content.

The WRC under no mechanical stress were determined both in membrane cells (axis translation technique, matric suction) and in desiccators (control of relative humidity, total suction). The samples used were obtained by cutting slices from the boreholes and trimming from them samples (Figure 12). The samples were initially weighed and measured and subjected to the corresponding suction. The samples' weight was periodically checked and the suction was kept in the same value until no weight variation was observed. Some samples were just subjected to one suction value, and after equilibrium they were measured (and sometimes also immersed in mercury to determine their volume) and dried in the oven at 110°C for 48 h to determine their water content. Other samples were submitted to a suction path, i.e. once equilibrium was reached for a given suction the sample was weighed and measured (and sometimes also immersed in mercury) and a new suction value was imposed. Drying in the oven did not take place until the end of the suction path.

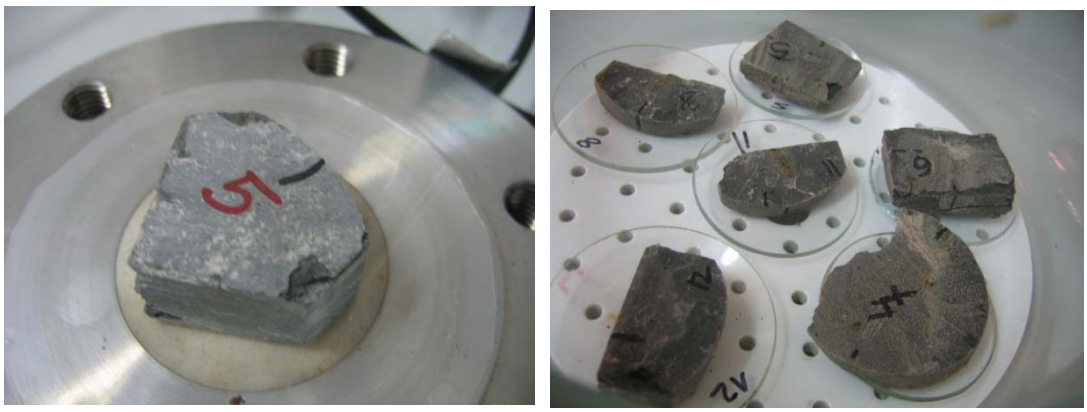

Figure 12 Samples used for the determination of the WRC in membrane cells and desiccators

1.2.2.3 GAS PERMEABILITY AND BREAKTHROUGH PRESSURES

A setup was designed to perform steady gas permeability measurements under different gas pressures (Figure 13). The cylindrical sample was confined in a triaxial cell that was pressurised to the desired confining pressure. The injection pressure could be independently varied and kept constant during the period of time necessary to get steady flow, while the backpressure was kept atmospheric and the outflow measured.

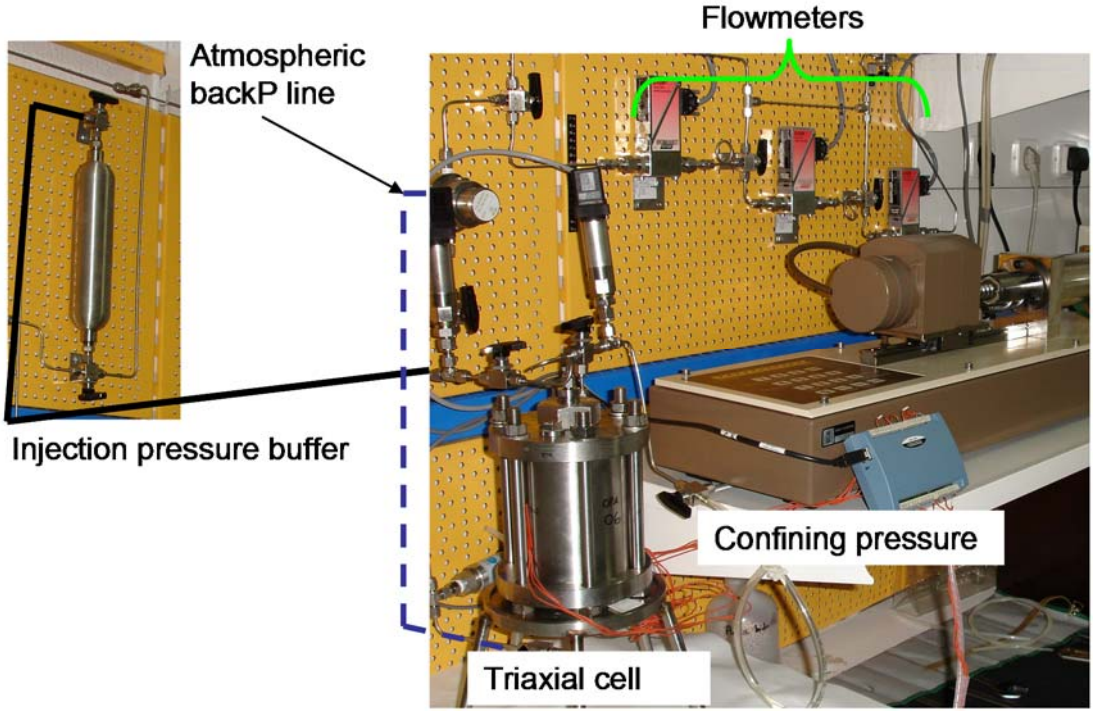

Figure 13 Appearance of the setup for measurement of gas permeability and breakthrough pressure (low pressure configuration)

The triaxial cells were made of stainless steel and able to withstand high pressures (28 MPa with a safey factor of 2.0). The confining pressure was applied with a GDS pressure/volume controller with a working capacity up to 16 MPa. To apply higher confining pressures (up to 33 MPa) the water in the cell was pressurised using the gas in an OLAER pressure bladder accumulator, which took the gas from a high-pressure deposit in which nitrogen was previously compressed by a gas-booster. Nitrogen gas was injected on top of the sample from a 300-cm^3 pressurised deposit equipped with a pressure transmitter. Injection pressures of up to 18 MPa could be applied. The oulet of the cell connected to the bottom of the sample was open to atmosphere, with a series of different-range gas mass flowmeters measuring the gas outflow. Outflow gas rates, up and downstream pressure, confining pressure and temperature were monitored online.

The samples were drilled from the BDR-1 core in a sense perpendicular to bedding and the ends were later lathed to assure their parallelism. The resulting specimens were 1.2-3.0 cm in height and 9.2 cm^2 in surface area. They were wrapped in a thermoretractable tube and then in a thick latex membrane with porous stones on top and bottom to sit the set in the triaxial cell pedestal (Figure 14).

Once the triaxial cell was filled with water it was pressurised to 8 MPa and a gas injection pressure of 0.5 MPa was applied to the top of the sample. The injection pressure was increased by 0.5 MPa every 24 h, until reaching a value of 7 MPa. Then the cell was moved to the high-pressure line (except in tests OPA2 and OPA5), in which a confining pressure of 15 MPa was applied, either in steps or suddenly. The injection pressure was also increased up to a value of 14 MPa. Then, in tests OPA1, OPA3 and OPA4, the confining pressure was increased to 19 MPa and the injection

pressure to 18 MPa, which was the maximum value allowed by the setup. All pressure values are absolute (Figure 15).

Figure 14 Appearance of an Opalinus clay sample drilled for a gas test, wrapped in the thermoretractable tube (black) and in the latex membrane (red)

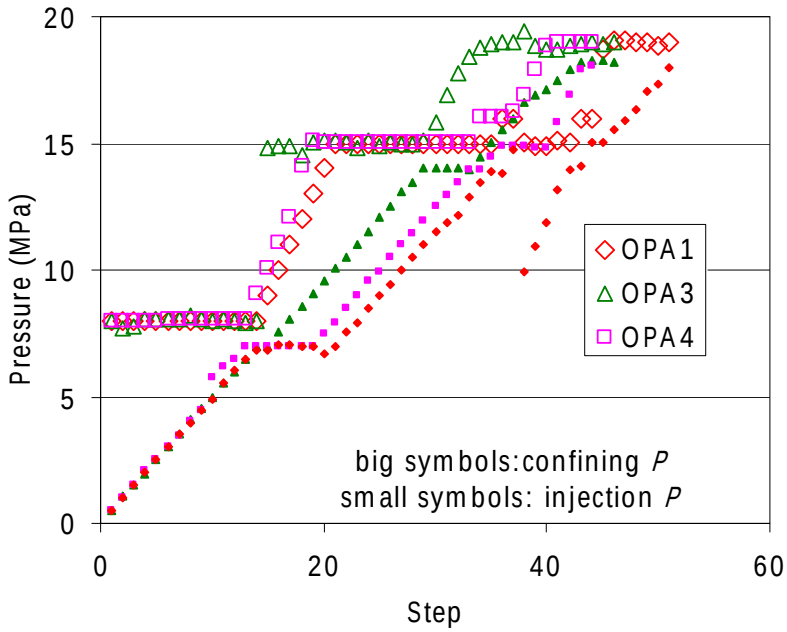

Figure 15 Pressure paths followed in the gas breakthrough tests (tests OPA2 and OPA5 followed only Phase 1 under confining pressure 8 MPa)

After the gas breakthrough tests, samples OPA3 and OPA4 were saturated with deionised water injected through the bottom surface at a pressure of 0.6 MPa (test with OPA4 still ongoing). The sample was kept in the same triaxial cell, and the confining pressure applied during saturation was 8 MPa. After full saturation the water pressure at the bottom was increased to 1.2 MPa and a backpressure of 0.6 MPa was applied on top. For that, a GDS pressure/volume controller was used, what allowed to measure the water outflow and compute the hydraulic conductivity applying Darcy's law.

1.2.3 Discussion of results

1.2.3.1 WATER RETENTION CURVES

Water retention curves were obtained with the aim of determining the effects of vertical stress, hydraulic paths and kind of suction on the water retention capacity of the Opalinus clay and on the parameters related to the two-phase flow. Figure 16 compares the water retention curves obtained under vertical stress and under no vertical stress applying total suction, both in wetting and in drying paths and in terms of water content and of degree of saturation. There is a trend to find lower water contents for the same suction in samples tested under vertical stress, particularly towards the lowest suctions. However, when expressed in terms of degree of saturation this difference disappeared or even reverted in the case of the drying paths, what is due to the fact that in the tests performed in oedometers the final dry density of the samples was higher (2.21 vs. 2.20 g/cm^3).

In the curve in terms of water content corresponding to the drying path, the value measured by capacitive sensors inserted in borehole BDR-1 was also included. This suction value agrees well with those obtained in trimmed samples, despite the fact that it was obtained in a different borehole and with a different technique.

The same comparison can be made for tests performed applying matric suction. As in the case of the tests performed under total suction, the trend is for the water contents to be lower and the degrees of saturation higher when suction was applied under vertical stress.

Figure 17 shows a summary of the results obtained under no stress conditions applying both matric and total suction. There is not a distinct difference between the results obtained under total or matric suctions. In the drying paths, both the water contents and the degrees of saturation tended to be higher when total suction was applied, however the reverse trend was observed for the water contents reached in wetting paths. As well, no clear difference was observed in the water retention curves obtained in oedometers applying total or matric suction, what points to the osmotic component of suction in Opalinus clay not being significant.

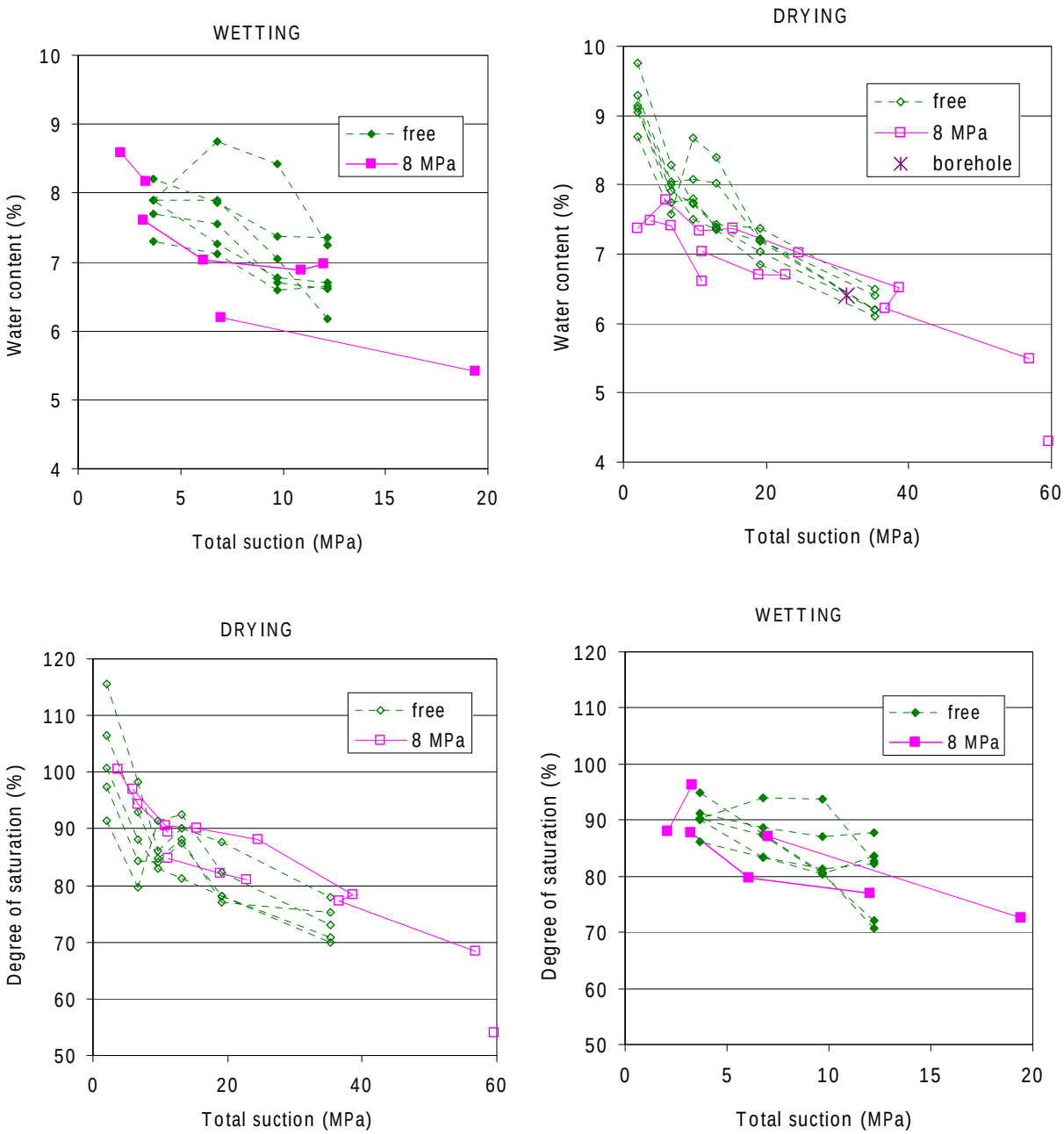

Figure 16 Water retention curves obtained applying total suction under 8 MPa vertical stress and under no mechanical stress following wetting (left) and drying (right) paths. The value directly measured in borehole BDR-1 is included in one of the graphs

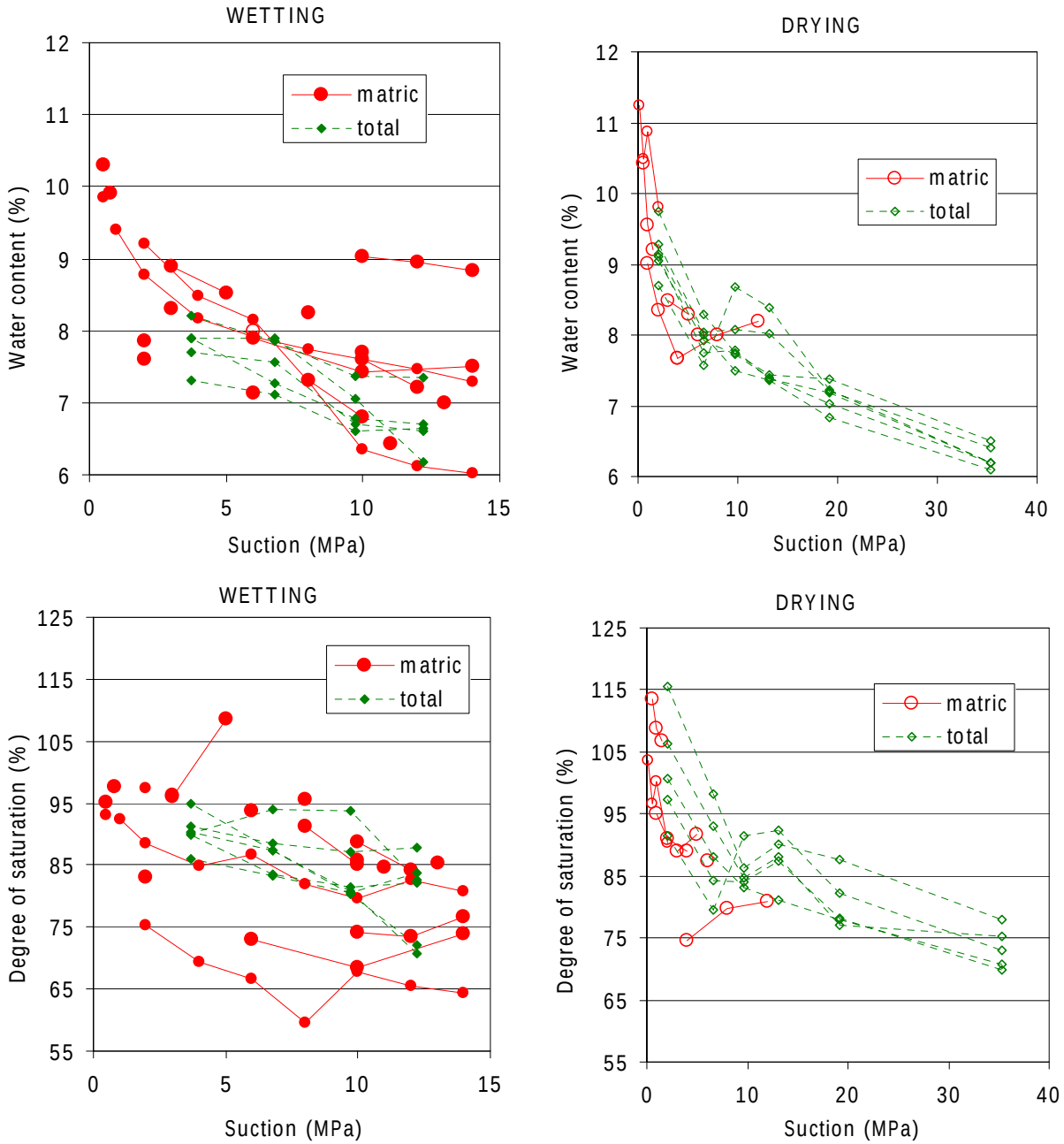

Figure 17 Retention curves obtained under free volume conditions in Opalinus clay samples from boreholes BHT1 and BHG-D1

The results obtained have been fitted to the van Genuchten expression, in order to obtain the parameters that define the water retention curves:

$$S_e = \frac{S_l - S_{rl}}{S_{ls} - S_{rl}} = \left(1 + \left(\frac{P_g - P_l}{P}\right)^{\frac{1}{1-\lambda}}\right)^{-\lambda} \quad \text{Equation 1}$$

where Se is the effective degree of saturation ($0 \leq S_e \leq 1$), P is a material parameter related to the air entry value (MPa), λ is a parameter that controls the shape of the water retention curve, P_g-P_l is suction (MPa), S_{rl} is the residual degree of saturation and S_{ls} is the maximum degree of saturation. It was considered that S_{rl}=0 and S_{ls} =1, for which reason $S_e = S_r/100$, where S_r is the degree of saturation actually measured.

It has to be taken into account that the degrees of saturation were computed from the measurements of water content and dry density. The latter were particularly difficult to achieve and in some cases the values obtained were only indicative, because the dry density was not actually measured but just assumed or estimated. For this reason the dispersion of the values obtained for each kind of test was very high and the fittings obtained have a limited value.

Eight fittings were carried out: for the tests applying matric suction under free volume conditions (membrane cells), for the tests applying total suction under free volume conditions (desiccators), for the tests applying matric suction under vertical stress 8 MPa (membrane cells oedometers) and for the tests applying total suction under vertical stress 8 MPa (deposit cells oedometers), for each of them following both wetting and drying paths. The parameters found for each fitting are shown in Table 4.

Table 4 Parameters for the van Genuchten expression (Eq. 1)

	Matric, 8 MPa		Matric, free		Total, 8 MPa		Total, free	
Parameter	Wetting	Drying	Wetting	Drying	Wetting	Drying	Wetting	Drying
P (MPa)	25.66	15.27	6.35	8.59	10.75	34.93	11.78	21.14
λ	0.51	0.45	0.25	0.45	0.35	0.42	0.37	0.33

The P parameter obtained (related to the air entry values, AEV) tended to be higher for the samples tested under stress, as well as in drying paths and when total suction was used. The AEV obtained from the mercury intrusion porosimetry was 27.8 MPa.

Figure 18 shows a comparison of the curves fitted for tests performed under free volume conditions and under vertical stress of 8 MPa. In the range of suctions tested, and when matric suction was applied, the degrees of saturation obtained for a given suction were higher for samples tested under confinement, but this trend was not so clear when total suction was applied. In the latter case and in wetting paths, the curves obtained under free or confined volume conditions were practically identical.

Drying paths recorded higher degrees of saturation than wetting paths when total suction was applied, which is the expected behaviour, but this was not the case when matric suction was applied. This is considered as due to the difficulty in fitting right curves to results showing a large dispersion.

Figure 19 shows the effect of the kind of suction on the WRC fittings. As discussed above, the effect is not clear since, although for the tests performed under free volume conditions the samples submitted to total suction tended to reach higher degrees of saturation, this was not the case for all the paths in the tests performed in oedometers.

These results have been compared with results obtained in samples taken from boreholes BVE-99 to BVE-102 (Villar et al. 2009) and BVE-1 (Muñoz et al. 2003) which were drilled in the shaly facies of the Opalinus clay in the context of the Ventilation Experiment. A good agreement was found between both sets of results, both in terms of water content and of degree of saturation (Villar & Romero 2012).

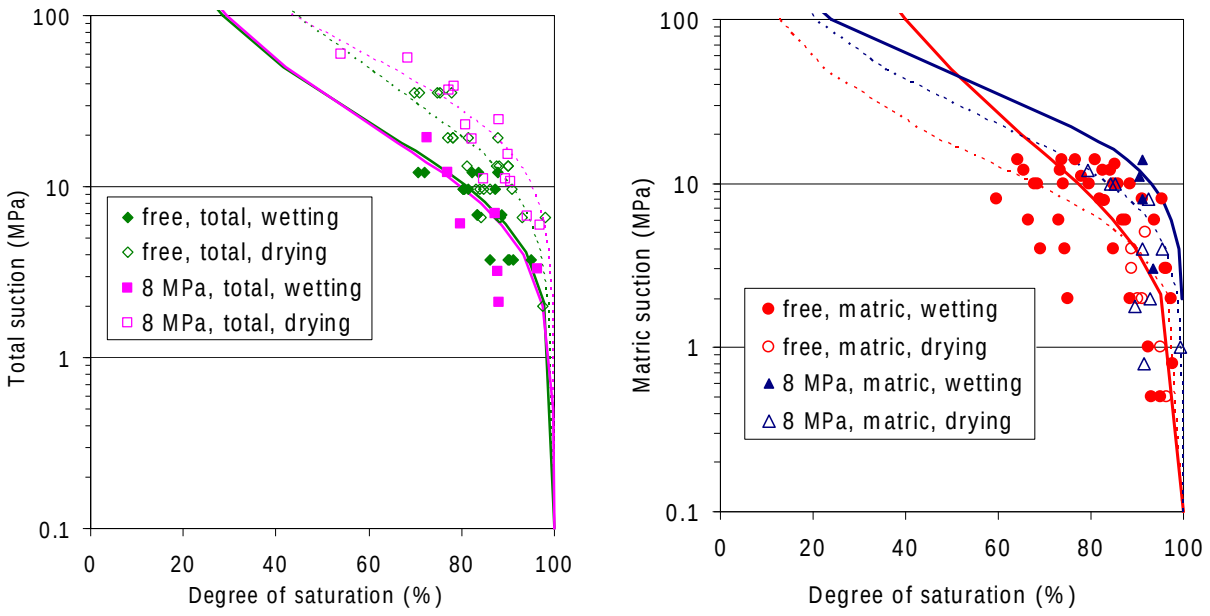

Figure 18 Fittings to the van Genuchten expression as a function of the confinement conditions for total and matric suction (the dotted lines correspond to drying paths)

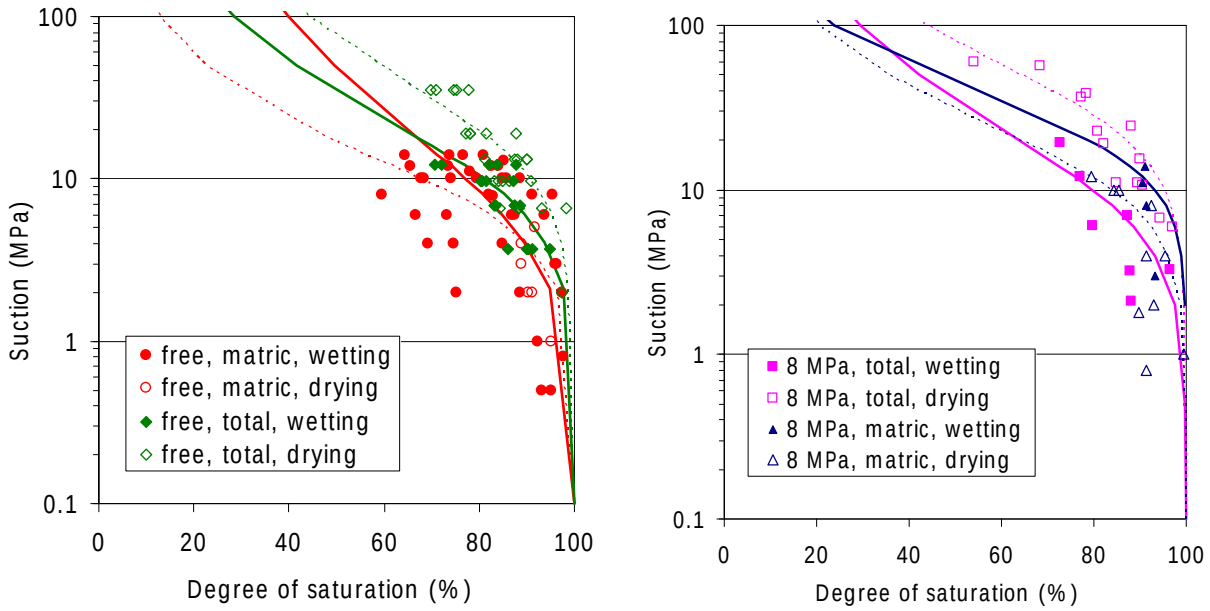

Figure 19 Fittings to the van Genuchten expression as a function of the kind of suction applied for different confinement conditions (the dotted lines correspond to drying paths)

1.2.3.2 GAS PERMEABILITY AND BREAKTHROUGH PRESSURES

Five gas permeability tests were performed in triaxial cells with Opalinus clay samples obtained by drilling from the BDR-1 core in the sense perpendicular to bedding. All of them started with a confining pressure of 8 MPa, which is slightly higher than the maximum in situ stress. The injection pressure was slowly increased until a value of 7 MPa with no significant flow been observed in any of the tests. In three of the tests the confining pressure was increased to 15 MPa and the injection pressure to 14 MPa with still no significant flow being detected. This pressure situation was prolonged for 7 days in test OPA1 and 9 days in test OPA4. Later, the pressures were increased in some tests up to values of 19 MPa for the confining pressure and 18 MPa for the injection pressure (the maximum allowed by the setup), and kept constant for 27 days in test OPA3 and 47 days in test OPA4. No significant outflow was detected in any case. This would mean that, with the devices available, it was not possible to measure gas permeability and that the gas breakthrough pressure for the Opalinus clay with a dry density of 2.29±0.05 g/cm^3 and a water content of 5.3±0.5% (S_r=80±16%) was higher than 18 MPa.

However, the flowmeters did record a value during the tests, a time-integrated value of some intermittent flow which was below their turndown value (accurate detection limit). If this flow were considered representative of the actual flow, gas permeability (k_{ig}•k_{rg}, i.e. intrinsic gas permeability times relative gas permeability) could be computed and the values shown in Figure 20 would be obtained. The values are in the range from 10^{-20} to 10^{-24} m^2 (average k_g of 8•10^{-16} m/s) and tend to decrease with the confining pressure. The minimum gas permeability values that could be calculated for the turndown value of the lowest-range flow-meter (0.04 STP cm^3/min) would range from 10^{-19} to 10^{-22} m^2 (from the lowest to the highest injection pressures). This means that all the values shown in the Figure 20 below 10^{-22} m^2 (and some under 10^{-19} m^2) cannot be considered accurate.

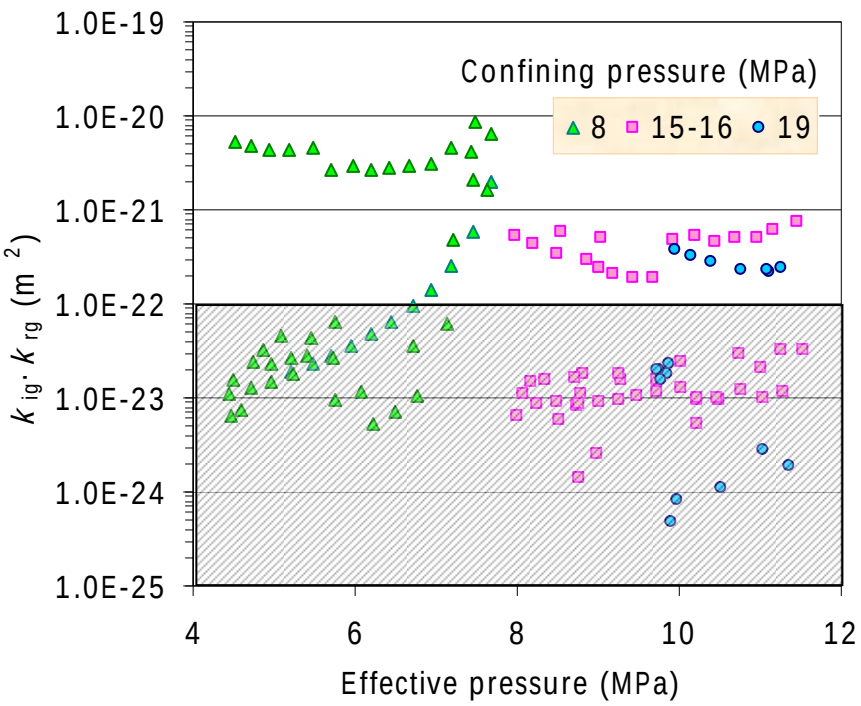

Figure 20 Gas permeability values obtained in samples of Opalinus clay (tentative values, especially those below 10^{-22} m^2)

The hydraulic conductivity (k_w) measured in one of the samples in the direction perpendicular to bedding was 2.2•10^{-11} m/s, corresponding to an intrinsic permeability (k_{iw}) of 2.3•10^{-20} m^2. Romero et al. (2012) found for similar void ratios (0.20-0.24) water permeabilities measured in

the laboratory an order of magnitude lower. The hydraulic conductivity for the sound shaly facies as determined in situ (Marschall et al. 2004) is also lower than the value determined in this work.

1.2.4 Conclusions

The water retention curve of Opalinus clay samples from boreholes BHT-1 and BHG-D1 was determined under different conditions: total and matric suction, mechanical stress or no-stress imposition, wetting and drying paths. Through the fitting of these results to expressions such as the van Genuchten one, it is possible to compute the P parameter, which is usually related to the air entry value, i.e. to the suction value above which air is able to enter the pores of the sample, and consequently, above which 2-phase flow can take place in the soil pore structure.

Because of the Opalinus clay bedding and foliation it was difficult to prepare specimens and to determine precisely the samples' dry density and degree of saturation evolution during the tests, what gave place to a large dispersion of results. The samples used in this research came from two different boreholes, BHT-1 and BHG-D1, but the behaviour of them did not depend on their location, what was confirmed by the fact that the results obtained agreed well with others obtained in samples from other boreholes analysed in previous researches, all of them drilled in the shaly facies.

There was not a distinct difference between the results under total or matric suctions. In the drying paths, both the water contents and the degrees of saturation tended to be higher when total suction was applied, however the reverse trend was observed for the water contents reached in wetting paths. As well, no clear difference was observed in the water retention curves obtained in oedometers under matric and total suctions, what points to the osmotic component of suction in Opalinus clay not being significant. Also, the samples showed hysteresis according to the expected behaviour, i.e. the water contents for a given suction were higher during a drying path than during a wetting path.

Overall, the water contents were lower and the degrees of saturation higher when suction was applied under vertical stress, what would indicate that the water retention capacity was lower under 8 MPa vertical stress than under free volume conditions. This vertical stress value is slightly higher than the maximum in situ stress.

The P parameters obtained –related to the air entry value– were between 6 and 34 MPa, and tended to be higher for the samples tested under stress, in drying paths and when total suction was used. The air entry value calculated from the mercury intrusion porosimetry tests was 28 MPa. These values correspond to degrees of saturation of between 80 and 90%, which implies that 2-phase flow (without significant deformation of the pore space) would take place only for degrees of saturation lower than about 90% (lower if confining is high). For higher degrees of saturation, macroscopic fracture formation (fracing, dependent on the stress state of the material) could be the mechanism for gas flow.

Gas injection tests currently running showed that the breakthrough pressure is higher than 18 MPa for degrees of saturation of 80±16%. Since it was not possible to determine the actual value, the relationship between the AEV and the breakthrough pressure cannot be stated.

1.2.5 References

CORKUM, A.G. AND MARTIN, C.D. 2007. Modelling a mine-by test at the Mont Terri rock laboratory, Switzerland. Int. J. Rock Mech. Min. Sci. 44(6): 846-859.

FERNÁNDEZ, A. M., MELÓN, A.M., SÁNCHEZ LEDESMA, D. M., GUTIERREZ-NEBOT. L.. 2011. Gas and water adsorption behaviour of in Opalinus Clay samples from borehole BHT-1. Mont Terri Technical Note 2009-46c, 68 pp.

MARSCHALL, P., CROISÉ, J., SCHLICKENRIEDER, L., BOISSON, J.-Y., VOGEL, P., YAMAMOTO, S. 2004. Synthesis of Hydrogeological Investigations at the Mont Terri Site (Phases 1 to 5). Heitzmann, P. ed. 2004: Mont Terri Project- Hydrogeological Synthesis, Osmotic Flow. Reports of the Federal Office for Water and Geology, FOWG, Geology Series No. 6.

MUÑOZ, J.J., LLORET, A. and ALONSO, E. 2003. VE Experiment. Laboratory Report: Characterization of hydraulic rock properties under saturated and non saturated conditions. Project Deliverable D4. EC Contract FIKW-CT2001-00126. CIMNE-UPC, Barcelona, 36 pp.

ROMERO, E., SENGER, R., MARSCHALL, P.; GÓMEZ, R. 2012. Air tests on low permeability claystone formations. Experimental results and simulations. In: Laloui, L. & Ferrari, A. (Eds.): Multiphysical Testing of Rocks and Shales. Springer Series in Geomechanics and Geoengineering, pp. 69-83. Springer, Berlin.

VAN GENUCHTEN, M.T. 1980. A Closed-Form Equation For Predicting The Hydraulic Conductivity Of Unsaturated Soils. Soil Sci. Soc. Am. J. 44: 892-898.

VILLAR, M.V., 2002. Thermo-hydro-mechanical characterisation of a bentonite from Cabo de Gata. A study applied to the use of bentonite as sealing material in high level radioactive waste repositories. Publicación Técnica ENRESA 01/2002, Madrid, 258 pp.

VILLAR, M.V. & ROMERO, F.J. 2012. Opalinus clay 2-phase flow parameters. FORGE Deliverable D5.14. Informe Técnico CIEMAT/DMA/2G207/3/12. Madrid, 31 pp.

VILLAR, M.V., A.M., FERNÁNDEZ. and MELÓN, A.M., 2009. Mont Terri Ventilation Test Phase II. Water retention curves determined on argillite samples taken before and after an in situ ventilation phase. Informes Técnicos CIEMAT 1170, Madrid.

1.3 Gas driven radionuclide transport in boom clay (SCK•CEN)

1.3.1 Scope and objectives

The main mechanisms by which gas will be generated in deep geological repositories are: anaerobic corrosion of metals in wastes and packaging; radiolysis of water and organic materials in the packages, and microbial degradation of various organic wastes. Corrosion and radiolysis yield mainly hydrogen while microbial degradation leads to among others methane and carbon dioxide.

The gas generated in the near field of a geological repository in clay will dissolve in the ground water and is transported away from the repository by diffusion as dissolved species. However if the gas generation rate is larger than the capacity for diffusive transport of dissolved gas, the pore water will get oversaturated and a free gas phase will be formed, leading to a gas pressure build-up. The gas production rate for some waste types and packages, especially LILWs, is expected to be significantly higher than the diffusive flux (although marred by large uncertainties). Hence, one of our research objectives is to improve the understanding of gas transport modes through the EBS and clay when the capacity for transport of dissolved gasses is exceeded. Indeed, the processes by which gasses are transported in porous media with a low hydraulic conductivity like clays are still poorly understood: 2-phase flow, pathway dilatation (µ-fracturing), fracturing…? Of particular importance for long-term radiological safety is the question whether the aforementioned gas transport modes are accompanied by displacement of significant amounts of pore water which could contain radionuclides depending on the timing of the "breakthrough event". (FORGE D4.17 §1.2)

The work performed within FORGE WP4 and described in D4.17 tried to answer the question "to what extent can a gas pressure build-up enhance the radionuclide and contaminants transport in a clay hostrock and the EBS". More particular, we focussed on the transfer through localised paths developing along specific discontinuities, such as fissures in the EDZ and interfaces between the EBS components and the host rock.

1.3.2 Short description/overview of executed experiments

1.3.2.1 METHOD

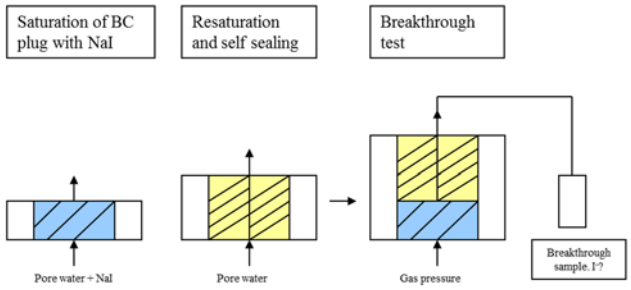

Figure 21 Basic concept of the tests to study gas driven tracer transport in disturbed Boom Clay.

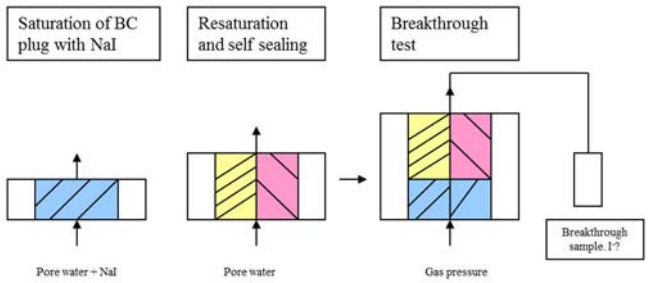

Figure 22 Basic concept of the tests to study gas driven tracer transport in the interface Boom Clay – Bentonite. Blue = NaI saturated Boom Clay core. Yellow = half Boom Clay core. Pink = half bentonite core.

To demonstrate the effect of a gas breakthrough on the transport of radionuclides, an anionic tracer is used.

So first, a small Boom Clay (BC) core (Ø 38 mm) is saturated with the anionic tracer (iodide [I^-], 0.01 mol/l NaI in Boom Clay natural pore water). Iodide (I^-) is chosen because its transport is not retarded under normal Boom Clay conditions: the sorption to clay minerals is negligible and it does not react with natural organic matter. The used iodine concentration is more than 1000x higher than the natural iodine concentration in Boom Clay pore water (~5 x 10^{-6} mol/l) (De Craen et al., 2004).

Second, for the experiments on disturbed Boom Clay (Figure 21) a larger core (38 mm high) is cut with a knife in 2 half cylinders, recombined and resaturated with natural pore water for different time periods ranging from one night to one week. During the SELFRAC project (Van Geet et al., 2008), the artificially created fracture was hardly visible after 16h, and after 20h the fracture was even no longer visible. So sealing of fractures goes very fast.

For the experiments with bentonite (Figure 22), the saturated bentonite cores (Volclay KWK, dry density 1.6 g/cm³) and the Boom Clay cores are halved, and both pieces are combined and resaturated with natural pore water during 1 week.

In the next step, the disturbed resaturated core or combined bentonite-Boom clay core is put on top of the NaI-conditioned core in a polycarbonate permeameter cell and confined (constant volume) between 2 porous stainless steel filters. The upper filter is filled with natural clay water

which has a low average background concentration of iodide ~5 x 10^{-6} mol/l (De Craen et al., 2004).

Finally a gas pressure (helium) is imposed at the bottom of the cell, and stepwise increased until gas breakthrough occurs. When gas breakthrough occurs, water can be expelled. Therefore, the water at the outflow, expelled after gas breakthrough, is analysed (with ICP-MS) for iodine enrichment. An enrichment in iodine concentration after breakthrough can be seen as an indicator for gas driven tracer transport.

The entire test is conducted in a temperature controlled room, at a constant temperature of 21°C (± 2°C).

A more detailed description of the used method can be found in FORGE D4.17 §2.1 and 2.3.

As the diffusion of iodide is unretarded it cannot be neglected when experiments last longer than 4 days. Transport calculations have shown that already after 3.5 days the concentration of diffused iodide is at the same level as the natural iodide concentration in Boom Clay water. So gas breakthrough should occur within 4 days to allow a determination of gas induced water (contaminated with tracer) displacement. In this case, a water displacement of only 0.002 ml is sufficient to double the I concentration in the pore water. So this is in fact the detection limit for gas induced water displacement of these experiments. (Jacops et al., 2013) FORGE D4.17 §2.3.3

1.3.2.2 EXPERIMENTAL CONFIGURATIONS

Experiments have been performed on undisturbed Boom Clay (no artificial fissure), disturbed Boom Clay (artificially fissured) and combined Boom Clay – bentonite cores. Disturbed Boom Clay samples were cut in 2 half cylinders and resealed for different time periods: 4 hours, 1 night or 1 week.

To investigate the effect of the artificial fissure, the NaI saturated cores were also cut in half for some experiments.To investigate the effect of the orientation of the bedding plane, we used both Boom Clay cores sampled perpendicular and parallel to the bedding plane.

An overview of all experimental configurations with only Boom Clay samples is given in FORGE D4.17 §2.3.4. Next to the experiments with Boom Clay, we also performed 4 experiments with combined Boom Clay – bentonite cores.

1.3.3 Discussion of results

1.3.3.1 GENERAL OVERVIEW OF THE RESULTS

For every experiment the I concentration in the breakthrough sample vs. time of sampling is measured and plotted in Figure 23. The background concentration accounts for the concentration of I which is naturally present in Boom Clay pore water and the concentration of I that has diffused from the 0.01 mol/l NaI saturated Boom Clay core through an undisturbed (pore water saturated) Boom Clay core of 38 mm high. The results are presented in Figure 23.

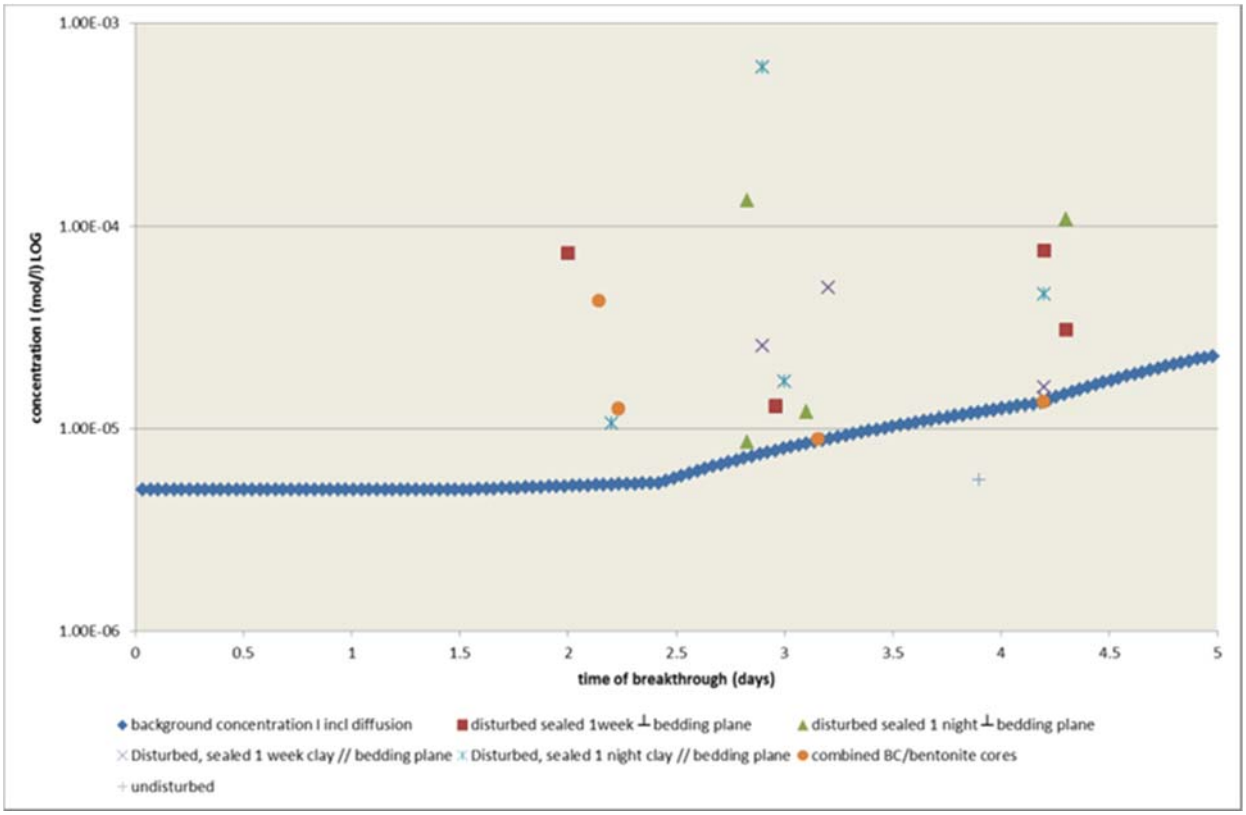

Figure 23 Iodine concentration in breakthrough samples (log-scale) vs. time of breakthrough for all experiments.

Based on the I-analyses of the pore water, and by taking into account the unretarded diffusion of I and the background concentration of I in Boom Clay pore water, we calculated the concentration of I in the water sample that is solely related to transport during gas breakthrough. Based on this value, we calculated the amount of pore water of the NaI-saturated core that was transported. This can be recalculated as a degree of desaturation of the NaI saturated plug.

In general, the measured concentration of I is rather low (< 10^{-4} mol/l I), and consequently the degree of desaturation of the bottom (NaI saturated) plug is also low (< 0.5%). A detailed table with all experimental results can be found in FORGE D4.17 §3.1

1.3.3.2 COMPARISON BETWEEN DIFFERENT EXPERIMENTAL CONFIGURATIONS

1.3.3.2.1 Role of sealing

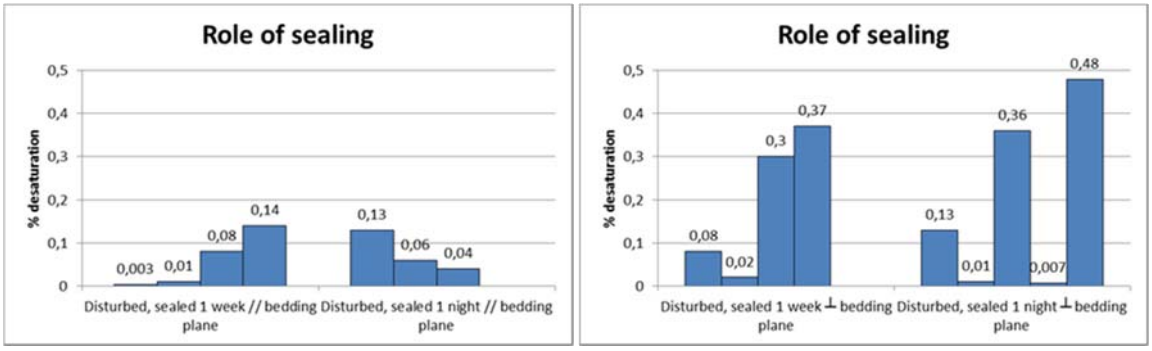

Figure 24 Role of time of sealing (1 night vs. 1 week) on the degree of desaturation (% of NaI saturated pore water that was transported during gas breakthrough – calculation based on measured concentration of I) for samples oriented parallel (left) and perpendicular (right) to the bedding plane.

From Figure 24, we observe no significant difference between sealing for 1 night or sealing for 1 week. Even after 1 night of sealing, the degree of desaturation is already low (< 0.5%). So the sealing process can be considered as a fast process.

In experiments with fissured and (re)sealed Boom Clay cores, breakthrough occurs often at the interface fissure – cell (see Figure 25, left). At this location, some "clay" material is missing (see Figure 25 right) due to the artificial fracturing (in fact cutting) and consequently it's a weak part of the core and thus a preferential path for gas.

If we want to investigate solely the role of fissures in gas-induced tracer transport, we have to use another set-up in which a confining pressure can be used to exclude gas transport along the wall. In addition, such a set-up would also allow comparing, for instance, the breakthrough and the confinement pressure. One could expect that when breakthrough occurs along the interface clay – cell, more I is transported compared to breakthrough through the clay sample. Our experimental results (see Figure 25), seem to support this hypothesis.

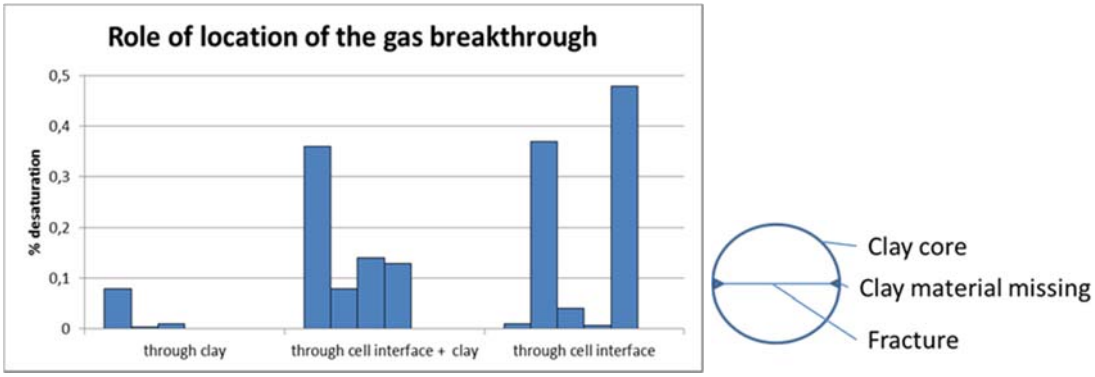

Figure 25 Left: location of the gas pathway during breakthrough vs. degree of desaturation (% of NaI saturated pore water that was transported during gas breakthrough – calculation based on measured concentration I). Right: schematic view of interface clay fracture-cell.

Based on these experiments we can state that gas moves through the weakest path which was in most cases the interface fracture – cell. In at least 10 out of 19 experiments, we observed gas breakthrough pathways at the interface clay/fracture – cell (see Figure 26 left). In only 3 experiments out of 19, we observed gas breakthrough pathways going only through the clay core. In some experiments, we observed both (see Figure 26 right).

More detailed information can be found in FORGE D4.17 §3.2.1.

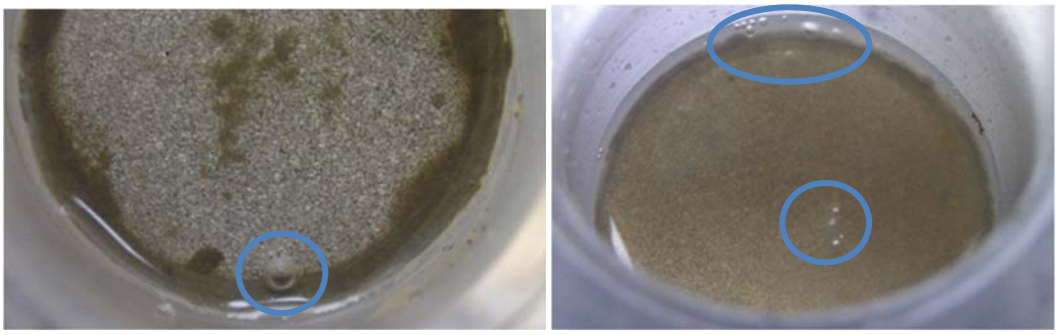

Figure 26 Observation of gas bubbles during the dismantling of experiments 2011/1-1 (left) and experiment 2011/3-1(right).

1.3.3.2.2 Role of orientation with respect to bedding plane

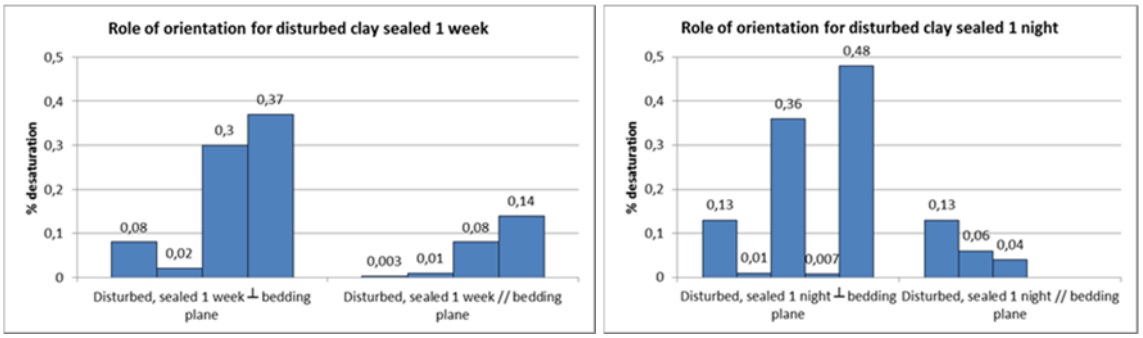

Figure 27 Role of orientation wrt. bedding plane for disturbed clay samples sealed 1 week (left) and 1 night (right) (desaturation is % of NaI saturated pore water that was transported during gas breakthrough – calculation based on measured concentration I).

When looking at the role of orientation wrt. bedding plane (Figure 27), it seems that more water is expelled from samples with an orientation perpendicular to the bedding plane. So the average degree of desaturation (hence tracer transported by gas) is less for samples // to the bedding plane. This observation could be explained by the structure of clay: clay minerals are plates oriented parallel to bedding and when swelling occurs e.g. due to unloading or after fissuring this swelling will be mainly in the direction orthogonal to bedding. Thus fissures parallel to bedding close faster and better than fissures that are orthogonal to bedding.

But we can state that if the clay core can seal properly, the amount of water transported during gas breakthrough is low. However, due to the selected experimental set-up and the selected experimental procedure, we have no objective data on the sealing status of the clay cores so it is difficult to prove a relation between orientation of the clay sample, time of sealing and degree of desaturation.

Another aspect that cannot be neglected is the reproducibility of the fractures. Fractures are created by cutting clay with a knife. This "cutting" will be a combination of shear and smearing and are totally different compared to tensile fractures. The "cutting" can "turn" the clay plates, leading to much more disturbances compared to a tensile fracture. Moreover, the cutting is not reproducible: every fracture is different, leading to other smaller fractures in the neighbourhood and different apertures of the fracture. This variability may play a larger role during the gas breakthrough process than time of sealing or orientation.

More detailed information can be found in FORGE D4.17 §3.2.2.

1.3.3.2.3 Role of materials

The presence of an interface Boom Clay / Bentonite does not lead to more tracer transport, compared to fractured (sealed and unsealed) Boom Clay (see Figure 28).

It is mainly the interface between the Boom Clay/Bentonite core and the wall of the cell which act as a preferential path. If we want to investigate solely the role of the interface Boom Clay / bentonite as a pathway in gas-inducted tracer transport, we would have to use another set-up in which a confining pressure can be used to exclude gas transport along the wall.

More detailed information can be found in FORGE D4.17 §3.2.3.

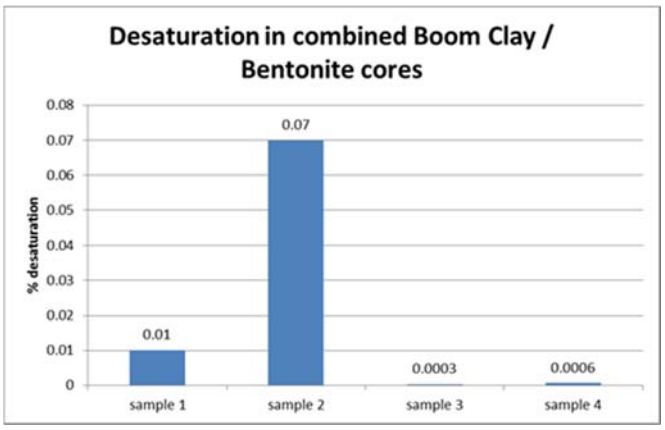

Figure 28 Desaturation (% of NaI saturated pore water that was transported during gas breakthrough – calculation based on measured concentration I) in combined Boom Clay/Bentonite cores (4 different samples).

1.3.3.3 DISCUSSION

During many of the experiments we performed, we observed that interfaces play an important role in the gas-induced tracer transport. They often act as a preferential pathway. Our most important interface was the interface between the clay sample and the wall of the permeameter cell. Especially when samples are fractured and some clay material is missing at the intersection of the fracture edge with the core cylindrical surface, then the interface Boom Clay core –cell at the level of the fracture is rather weak and acts as a gas conducting pathway. If gas starts to accumulate in a repository, this suggests that the gas might more easily escape along the interface of natural and engineered barriers than that it would escape through the host rock.

The experiments are also strongly influenced by the lack of reproducibility of the fracture. As discussed in previous paragraphs, creating fractures by cutting the clay causes much more disturbance compared to the tensile fracture that could occur in-situ and this disturbance is not reproducible.

In previous breakthrough tests performed in the 1990's on undisturbed Boom Clay, a mean decrease in saturation less than 2% was reported (MEGAS project, Volckaert et al., 1994). Based on the results of the experiments on undisturbed and disturbed Boom Clay and combined bentonite – Boom Clay cores, the amount of I that was transported and consequently the degree of desaturation due to gas breakthrough was very low (< 0.5%).

If we have a look at the amount of gas transported during breakthrough compared to the amount of tracer that was transported during this gas breakthrough, we get following results: in experiment 2010/4-1, 200.5 ml gas (STP) was blown through the clay and it transported only 0.77 µl contaminated water. In experiment 2011/3-3, 1291 ml gas (STP) was blown through the clay and it transported only 7.64 µl contaminated water. So despite the large amount of gas

transported, only very small amounts of contaminated water were transported. This points rather to "pathway dilation" and not to visco-capillary 2-phase flow.

During the experiments, we made a lot of observations on the gas flow during the gas breakthrough event and these observations allow us to draw some conclusions regarding flow mechanisms. During the breakthrough experiments, gas flow was very unstable. It could suddenly stop, start again, increase or decrease while the gas pressure was constant. Also when we observed the surface of the clay core in a dismantled cell, we could observe gas bubbles escaping at one location, and the next moment we observed gas bubbles escaping at another location or it suddenly stopped. So based on these observations, we can state that gas flow was very unstable – rather indicating another flow mechanism than visco-capillary 2-phase-flow.

1.3.4 Conclusion

The goal of this research was to answer the following question: “to what extent can a gas pressure build-up enhance the radionuclide and contaminants transport in a clay host rock?” Based on the obtained results, we can state that the transport of radionuclides and contaminants due to a gas breakthrough is indeed possible but seems very limited.

The effect of different parameters (orientation of the samples wrt. bedding plane, time of sealing of the fractures and porous medium type) on the degree of desaturation was investigated, but we did not find a clear relationship. In our opinion, other aspects like the reproducibility of the fracture, the stress-state of the sample and the presence of interfaces (Boom Clay-cell, bentonite-cell) have a stronger influence on the experimental results.

To get a better hold on the process, it could be interesting to perform some additional experiments in an adapted set-up, with control of the total stress (tri-axial cell), using a confining pressure to avoid breakthrough along the wall and making use of samples with a more realistic (shear or tensile) fracture.

Concerning the gas flow mechanisms, the observations of laboratory gas tests on BC samples indicate more and more that gas dissipation through dilation pathways is more likely than development of plane-type fractures. Of course this observation is stress and scale dependent. However, direct characterisation of the dilation pathway is with the current experiments very difficult to apply. More evidence needs to be collected to prove pathway dilation at relevant scales.

Concerning the stability of gas pathways we believe that created gas pathways are not stable in time. When we performed gas breakthrough experiments on disturbed (fissured) and undisturbed Boom Clay, the flow after breakthrough was never stable. We observed all kinds of flow patterns, even stopping and resuming of flow (Jacops et al., 2013). Probably opening and closing of pathways is related to gas pressure and stress inside the sample. Our experiments were not designed to examine this into detail as it was not our goal of the experiments. Moreover, Boom Clay is plastic and pathways can easily and quickly seal. (Van Geet et al., 2008).

Concerning interfaces, we can conclude that they played an important role in our experiments as gas mainly escaped at the interface sample – cell. However, this phenomenon is stress-related but our experiments were not equipped with for instance, strain gauges so conclusions on the stress state of the sample cannot be drawn.

Experiments performed within FORGE WP's 4 & 5 (Jacops et al., 2012) demonstrated that radionuclides can indeed be transported during gas breakthrough, but it is considered limited as the amount of displaced water is less than 0.5% of the “contaminated” water volume. The volume of water displaced is also very low (3 orders of magnitude) compared to the volume of

gas transported upon breakthrough. We do not expect that gas induced transport will have a significant effect on RN migration at repository scale.

1.3.5 references

De Craen M., Wang L., Van Geet M., Moors H. (2004) *"Geochemistry of Boom Clay pore water at the Mol site"* SCK•CEN Report (BLG 990)

Jacops E., Maes N., Maes T., Volckaert G., Weetjens E. (2012) *"Gas induced tracer transport in undisturbed & disturbed Boom Clay and Boom Clay – bentonite interfaces"* SCK•CEN Report (ER-222)

Van Geet M., Bastiaens W., Ortiz L. (2008) *"Self-sealing capacity of argillaceous rocks: Review of laboratory results obtained from the SELFRAC project."* PHYSICS AND CHEMISTRY OF THE EARTH, Volume: 33 Pages: S396-S406

Volckaert G., Ortiz L., De Cannière P., Put M., Horseman S.T., Harrington J.F., Fioravante V. Impey M. (1994) "*MEGAS Modelling and Experiments on Gas Migration in Repository Host Rocks. Final Report Phase 1*". EUR16235 EN, Luxembourg.

2 Gas transport in-situ experiments

2.1 PGZ1: Gas migration in undisturbed indurated clay formation, Callovo-Oxfordian clay, at the URL site in Bure (ANDRA) gas transport in-situ experiments

2.1.1 Scope and objectives

PGZ1 is a large scale gas injection test performed in the Meuse/Haute-Marne URL to improve the knowledge about gas migration mechanisms into Callovo-Oxfordian (COx) claystone formation. The aim of this experiment is to identify the main processes associated with gas migration, to quantify some parameters essentials to predict gas transfer in repository context and to verify the validity and the limits of the traditional biphasic model for describing gas transfer. More precisely, this experiment will be useful to estimate gas entry pressure into undisturbed host rock and in the EDZ (excavation damaged zone), to detect if pathway dilation occurs and at which gas pressure, to determine the gas fracturing pressure and to evaluate the consequence of gas injection on the integrity of the host rock, mainly in terms of water permeability.

2.1.2 Overview of executed experiments

2.1.2.1 PGZ1 SETUP

The experimental setup consists in 3 boreholes. Two of them are dedicated to gas injection and pressure monitoring (PGZ1201 and PGZ1202), the third one is for monitoring rock deformation (PGZ1031). The three boreholes have been drilled during July 2009 with air. The external diameter is 76 mm for PGZ1201 and PGZ1202 and 101.3 mm for PGZ1031. PGZ1 is located in the drift GED of the French URL (see Figure 29).

- Borehole PGZ1031 was drilled in front of the GEX drift. This hole is inclined downwards and fitted with a strain gauge with 20 measuring points. This borehole is perpendicular to borehole PGZ1201 and located about 1 m above it (cf. Figure 30).
    - Borehole PGZ1031 should enable to capture the opening of the fracture created by gas injection. Fracture location at this scale is difficult to anticipate precisely and had been identified as a risk in the design of PGZ1 experiment.
- Boreholes PGZ1201 and PGZ1202 were drilled in the GED drift at the base of the wall. These two boreholes are inclined downwards and fitted with two multi-packer completions, each with three intervals.
    - Borehole PGZ1201 is dedicated to gas and water injection. The injection interval in this borehole is the central one. It is one meter long and the other two measurement intervals, which are located on either side of Interval 2, are 0.2 m long.

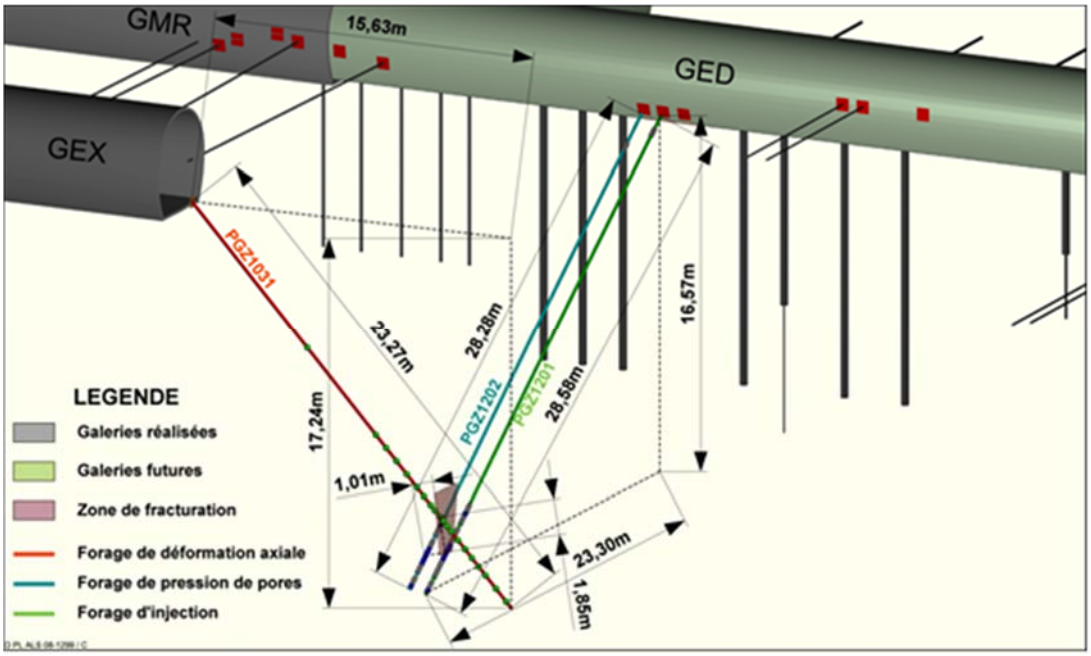

Figure 29 3-D view of the boreholes and drifts for the PGZ tests

- Borehole PGZ1202 is dedicated to monitor water and gas pressure in the host rock. The geometry is similar to PGZ1201 one with 3 chambers. The central one is one meter long and the other two measurement chambers are 0.2 m long.
- The two boreholes PGZ1201 and PGZ1202 are parallel and separated by a distance of about one meter. This design has been retained to be able to observe hydraulic, gas and hydro-mechanical interferences.

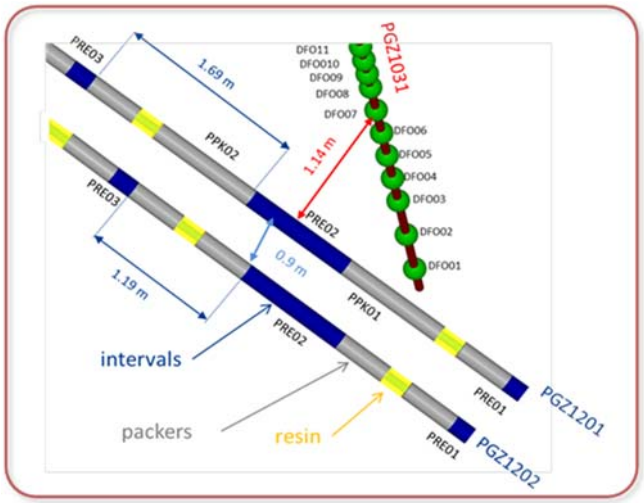

Figure 30 Details of the gas injection zone in PGZ1, position of each borehole

Several sensors have been installed in the drift (GED) to measure temperature and relative-humidity variation (see Figure 31). It has been shown that the temperature fluctuations in the drift influenced the pressure measurements in the borehole. For PGZ1 experiment, it is crucial to measure the temperature in the drift because during the gas-injection phase any variations in temperature are reflected in the gas pressure, even if thermal-insulation has been installed. The gas module is composed by 3 gas flowmeters mounted in series, one flow controller and a gas pressure sensor: (i) Flowmeter 1 (SAGD name PGZ1201_DGZ_01): 0.06 – 3 mln/min, (ii) Flowmeter 2 (SAGD name PGZ1201_DGZ_02): 2 – 100 mln/min, (iii) Flowmeter 3 (SAGD name PGZ1201_DGZ_03): 100 – 5000 mln/min, (iv) Gas pressure sensor (SAGD name PGZ1201_PGZ_01): 0 – 200 bar.

The gas used here is nitrogen and the flowrate are given in the standard reference conditions of temperature and pressure for expressing gas volumes, (0°C and 101.325 kPa).

All the details about PGZ1 set up are presented in FORGE report 5.4, de La Vaissière, 2010

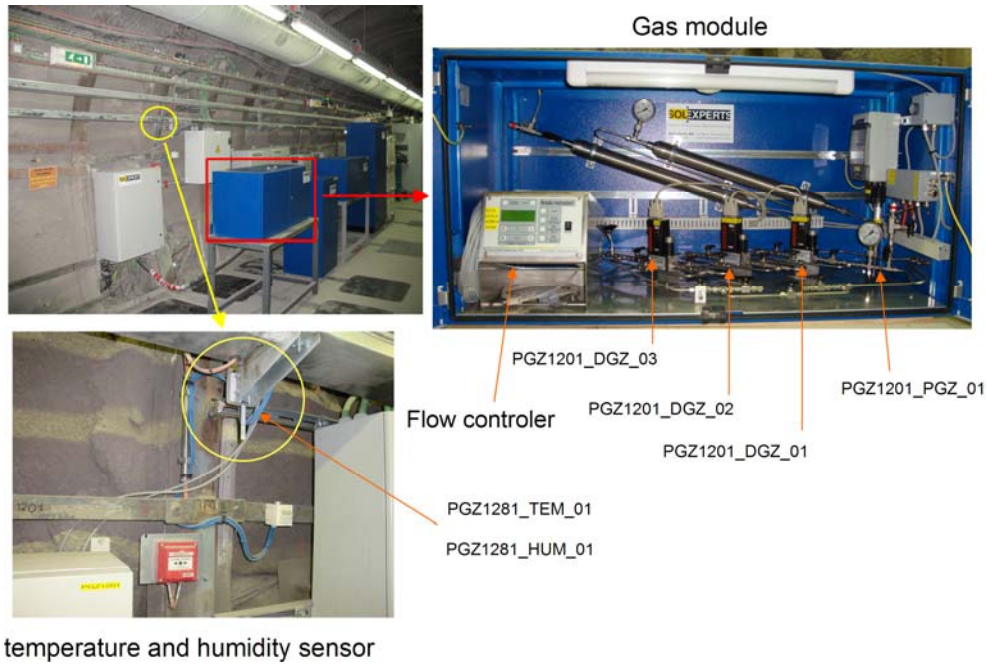

Figure 31 View of the gas module and temperature and humidity sensor in the drift

2.1.2.2 HOST ROCK CHARACTERIZATION BEFORE GAS INJECTION TEST

Initial state and preliminary observations

Geologic logging of these boreholes was carried out and the water contents have been measured in samples from these three boreholes. A first measurement was performed at 105° C for geomechanical purposes, and a second measurement at 150° C for mineralogical and geochemical purposes. After drying in an oven for 24 hours the mass water content is obtained from the following equation:

$$Water\,content = \frac{wet\,sample\,mass\,(g) - dry\,sample\,mass\,(g)}{dry\,sample\,mass\,(g)} \times 100$$

To illustrate those measures, Figure 32 shows the water-content profiles at 105 and 150° C along the PGZ1201 borehole function of the distance from the borehole mouth.

The water content varies between 6 to 8% depending on the lithology-related variations (clay content/carbonate content ratio), air flow during coring and error in the measure. The variation of clay content is accentuated by the choice of inclined boreholes in PGZ1 experiment.

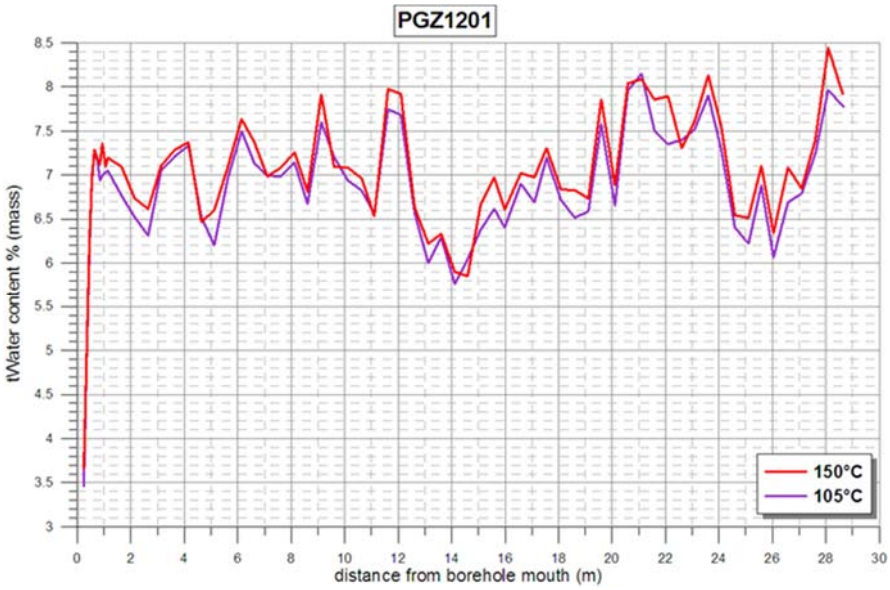

Figure 32 Water content profile in borehole PGZ1201

After 10 to 20 days, the interstitial pressures have reached a level of pseudo-stability (Figure 33). The levels are fairly well stabilised in intervals 1 to 3 of borehole PGZ1202. For the other intervals, after a stabilisation phase we see a more or less appreciable decrease in the pressure. This is clearly visible for interval 2 of borehole PGZ1201.This decrease is due to the proximity of PGZ1031 borehole which drains the rock. The equipment in it has been blocked with permeability cement about 10^{-9} m/s. Application of hydrostatic pressure within the annulus in borehole PGZ1031 causes a hydraulic disturbance equivalent to drainage.

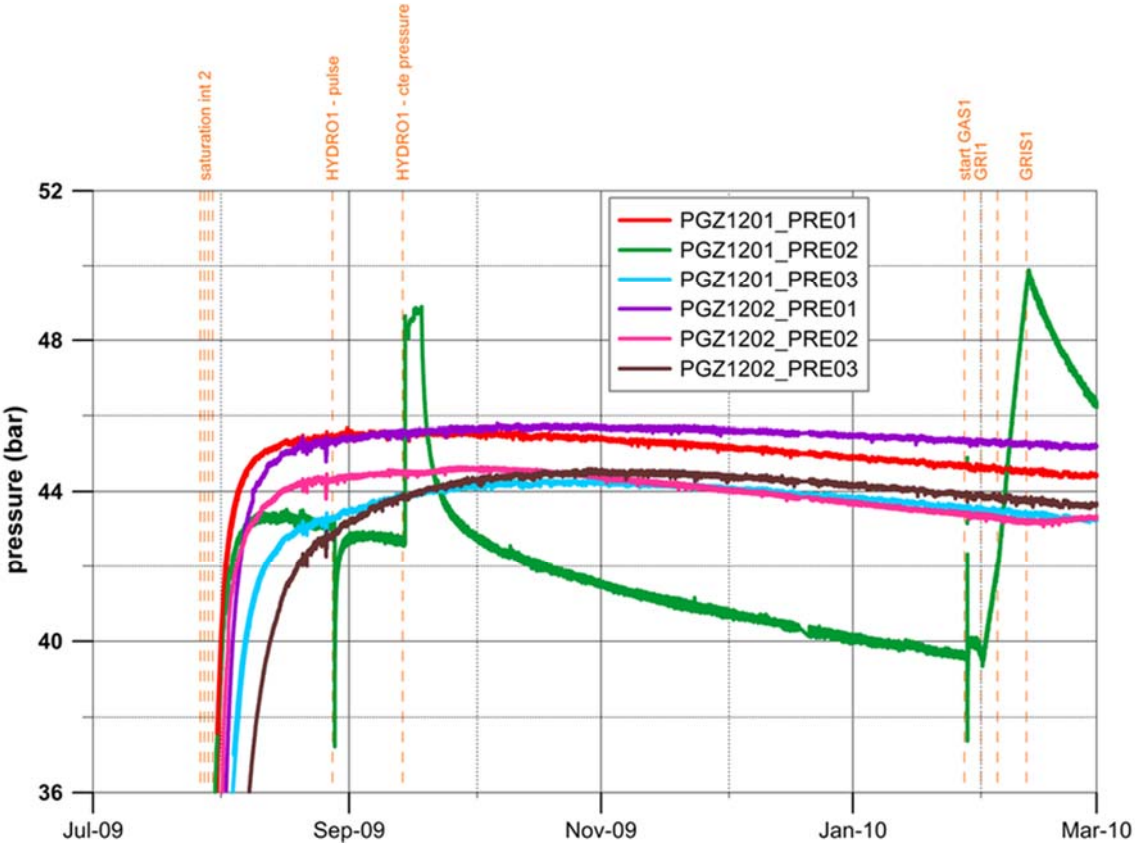

Figure 33 Pore pressure measurements before GAS1 in PGZ1201 and PGZ1202

Hydraulic tests in PGZ1201 before gas injection

A series of hydraulic tests (HYDRO1), comprising a pulse–withdrawal test and a constant overpressure test were performed in August/September 2009 in Interval 2 of PGZ1201. Numerical inverse analysis has been done to obtain the main hydraulic parameters: water permeability, specific storage coefficient and extension damaged zone around the borehole.

The flow model adopted around the test interval is a composite radial flow model with an inner zone of higher permeability than the outer zone. This inner zone represents the borehole damaged zone (BDZ) and has been estimated by the model at about 4 cm thickness around the borehole. The parameters obtained are summarized in Table 5.

Table 5 Parameters for the rock around Interval 2 of PGZ1201 (HYDRO1)

	Water permeability (m/s)	Specific storage (1/m)
Inner zone (BDZ)	6.4×10^{-11}	1.0×10^{-6}
Outer zone (sound claystone)	2.6×10^{-13}	3.0×10^{-6}

2.1.2.3 TEST SEQUENCE

The gas test sequence “GAS1” began on the 28 January 2010 with the gas-water exchange phase in Interval 2 of PGZ1201. To fill the interval with gas without excessively disturbing the interval’s near-field pressure, water was flushed from the interval by a series of gas injections.

During this phase the quantity of water extracted has been measured at about 810 cm^3. The gas pressure in the interval was raised to 40 bar, i.e. a pressure greater than the water pressure before water-gas exchange.

Six constant-flowrate gas injection steps were performed during the GAS1 phase. Each injection step was followed by a pressure recovery phase. In the rest of the document, the injection steps will be labelled “GRI”, for example GRI3 means injection step 3. Pressure recovery phases will be labelled “GRIS”. The duration, amplitudes and quantities of gas injected for the GRIx and GRISx steps are not similar.

Figure 34 shows the pressure measurements at the three measurement intervals in PGZ1201 and the gas flowrate imposed between January 2010 and January 2011.

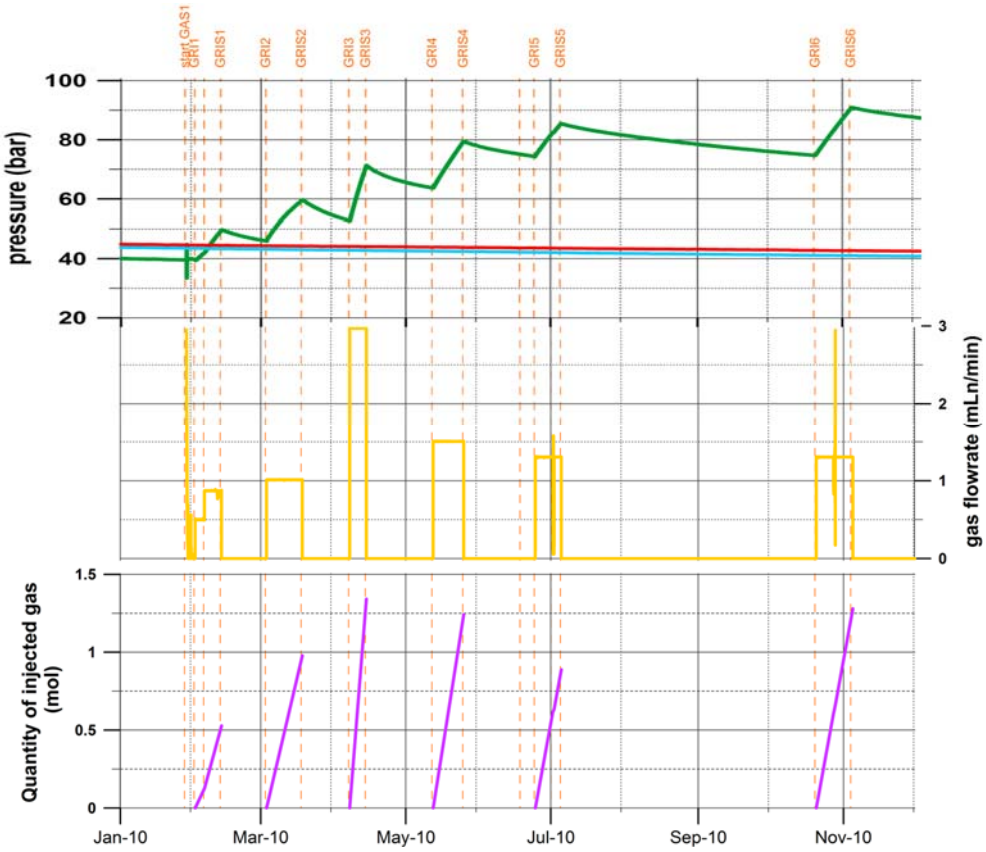

Figure 34 Pressure measurements, gas flowrate and gas quantity injected in PGZ1201 from January 2010 to January 2011

2.1.3 Discussion of results

2.1.3.1 HYDRAULIC INTERFERENCE ANALYSIS

The hydraulic interference at Intervals 1 and 3 of borehole PGZ1201, located at 1.69 m from the injection interval couldn't be detected. This is not the case for interval in PGZ1202 borehole. Figure 35 shows the pressure measurements at the three measurement intervals in PGZ1202 between January 2010 and May 2011. The dotted lines show the linear trend extrapolated from the measurements taken prior to starting gas injection. For this borehole, the hydraulic interference associated with the gas injection steps is clearly visible at Interval 2 and to a lesser extent at the other two intervals.

At Interval 2, the first three injection steps (GRI1 to GRI3) produced clear hydraulic interference in terms of amplitudes, whereas the following injection steps (GRI4 to GRI6) only produced slight interference. This observation demonstrates a change in the behaviour of the system comprised of the boreholes and the formation.

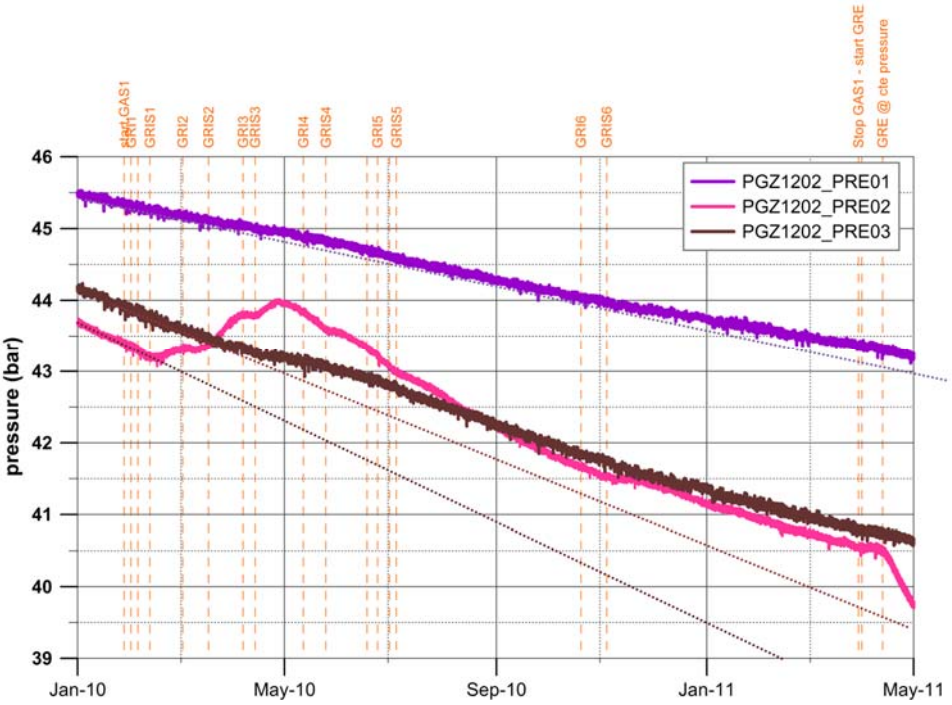

Figure 35 Pressure measurements in PGZ1202 from January 2010 to April 2011

The gas injection Interval in PGZ1201 is at a distance of 90 cm from interval 2 of PGZ1202 measured parallel to the bedding. The significant response of interval 2 in PGZ1202 rather than in other intervals highlights certainly anisotropy in permeability of clay host rock.

2.1.3.2 GAS INJECTION TEST ANALYSIS

Comparison between the six recovery pressure (Figure 36) shows a change in behavior with a faster pressure drops during GRIS1 to GRIS3 and then a slower pressure drops during the subsequent steps GRIS4 to GRIS6. The reason of behavior change has been investigated by analytical technics.

The key issue is the knowledge of the system; that is the volume of the test interval and initial gas volume at the start of GAS1. However, the exact volume of the injection interval is not known due to the presence of breakouts at the borehole wall and possible convergence of the borehole wall between drilling and the water-gas exchange phase. This volume ranges between 804 and 1540 cm3. The maximal volume corresponds to the case without any convergence and the minimal volume corresponds to the case of a full convergence around the filter of interval 2. In addition, because of the borehole angle, all the water in the test interval cannot be removed.

A volume of residual water may remain in the interval and this could be moved when the gas pressure is increased. While the exact amount of residual water is unknown, it is possible to estimate the gas volume during the initial gas injection steps using the ideal gas law.

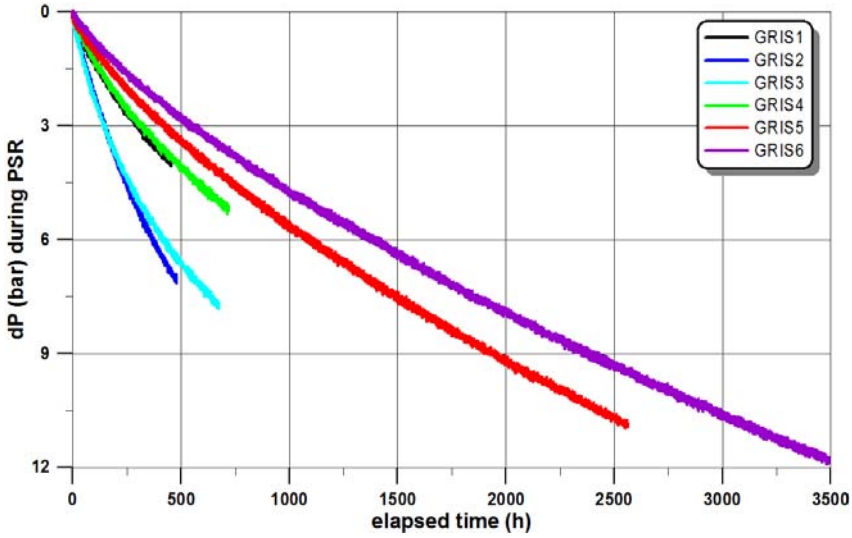

Figure 36 Pressure variation in interval 2 of PGZ1201 during the six pressure recovery steps (GRIS1 to GRIS6).

For each injection step (GRI1 to GRI6), the following are shown (Figure 37): the measured pressure difference and the calculated pressure difference assuming a constant volume for the interval for the two extreme cases 804 cm^3 and 1540 cm^3 which correspond to the theoretical minimum and maximum volumes of Interval 2 of PGZ1201. The pink curves correspond to the calculated pressure difference at the constant volume that gives the best fit to the measurements. Notice that data were not corrected for the downward trend due to the drainage effect and not for the dissolution/diffusion of nitrogen in porewater.

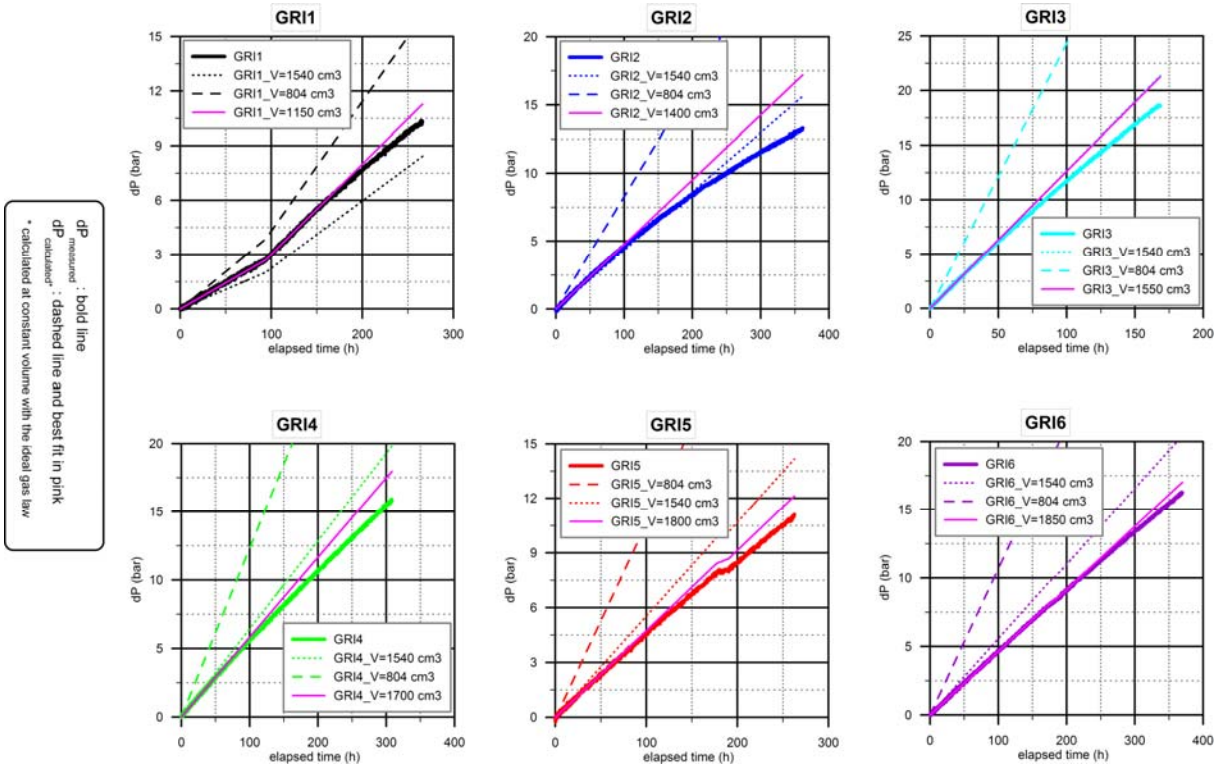

Figure 37 Comparison of the pressure difference as measured and as calculated at constant volume for the six steps GRI1 to GRI6

At the beginning, the measured pressure difference is clearly between the pressure differences calculated for the extreme volumes. At the start of the first injection step GRI1, the best fit corresponds to a volume of 1150 cm^3. The measured pressure difference only significantly deviates from the calculated best-fit pressure difference after approximately 200 hours. This means that during these first two hundred hours, the gas volume remained constant (compression effect). After that, the interval volume available for the gas increases. It is interpreted as residual water moving into the claystone pushed by gas.

Volume estimations between GRI1 to the first fifty hours of GRI3, lead to the conclusion that only the remaining residual water is expelled from the interval. After this stage, gas starts to penetrate the rock for a gas pressure of the order of 5.8 MPa, which corresponds to a gas entry pressure of approximately 2 MPa given that the water pressure is estimated at 38 bar. This value for the gas entry pressure is small compare to the knowledge about COx pore size distribution. Given the existence of a 4-cm-thick damaged zone around the borehole, it clearly represents the gas entry pressure into the borehole damaged zone. This gas entry pressure value is also a maximum value as it depends both on the volume of residual water in interval and, probably, on the injection kinetics. For example, less residual water would lead to earlier gas penetration and, thus, a lower gas entry pressure.

For these last three gas injection steps, the gas volume estimated as the best fit is always greater than the maximum theoretical volume of Interval 2. It is certain therefore that, after GRI3, there is no residual water in the injection interval. The increase in gas volume at the start of these three steps reduces from 100 cm^3 between steps GRI4 and GRI5 to 50 cm^3 between GRI5 and GRI6. Thus, gas finds it increasingly difficult to penetrate the rock as the pressure rises. This is also confirmed by considering the discrepancy between the pressure difference calculated for the best fit and the measured pressure difference. This discrepancy does indeed reduce significantly between step GRI4 and step GRI6. This interpretation fits reasonably well with the change in the behaviour seen during pressure recovery steps GRIS1 to GRIS6.

2.1.3.3 HYDRAULIC TESTS IN PGZ1201 AFTER GAS INJECTION

Hydraulic tests (HYDRO2) performed after gas injection in June 2011 highlighted the low impact of gas pressure on host rock properties. Hydraulic permeability for sound claystone and BDZ are in a same order as specific storage coefficients and BDZ extension (Table 6).

Despite the fact that gas pressure reached 9.1 MPa during the test and domain of pressure where dilatants pathways could occur, disturbance in host rock properties are not visible on hydraulic test.

Table 6 Estimated hydraulic parameters before and after the gas injection test

Parameters		HYDRO1 (September 2009)	HYDRO2 (June 2011)
Hydraulic conductivity (m/s)	Inner zone	$6.4\ 10^{-11}$	$2.7\ 10^{-11}$
	Outer zone	$2.6\ 10^{-13}$	$2.0\ 10^{-13}$
Specific storage (1/m)	Inner zone	$1\ 10^{-6}$	$1\ 10^{-6}$
	Outer zone	$3\ 10^{-6}$	$2.7\ 10^{-6}$
Radius (m)		0.04	0.04

High water constant pressure tests were performed after HYDRO2 to stimulate pressure responses in the other intervals. Test analysis confirms a small anisotropy in water permeability or in specific storage.

2.1.3.4 SECOND GAS INJECTION TEST

Following the second hydraulic test, and after a period of re-equilibrium, a second gas injection test has been started in October 2012 (Figure 38). The gas injection sequence (GAS2) consists in a constant injection test with a flowrate of 1mL/min. The objective is to reach a gas pressure of 10 MPa in the central interval of PGZ1201 borehole, below the fracturing pressure. What is expected in terms of observation is evidence of dilatant pathway into the host rock.

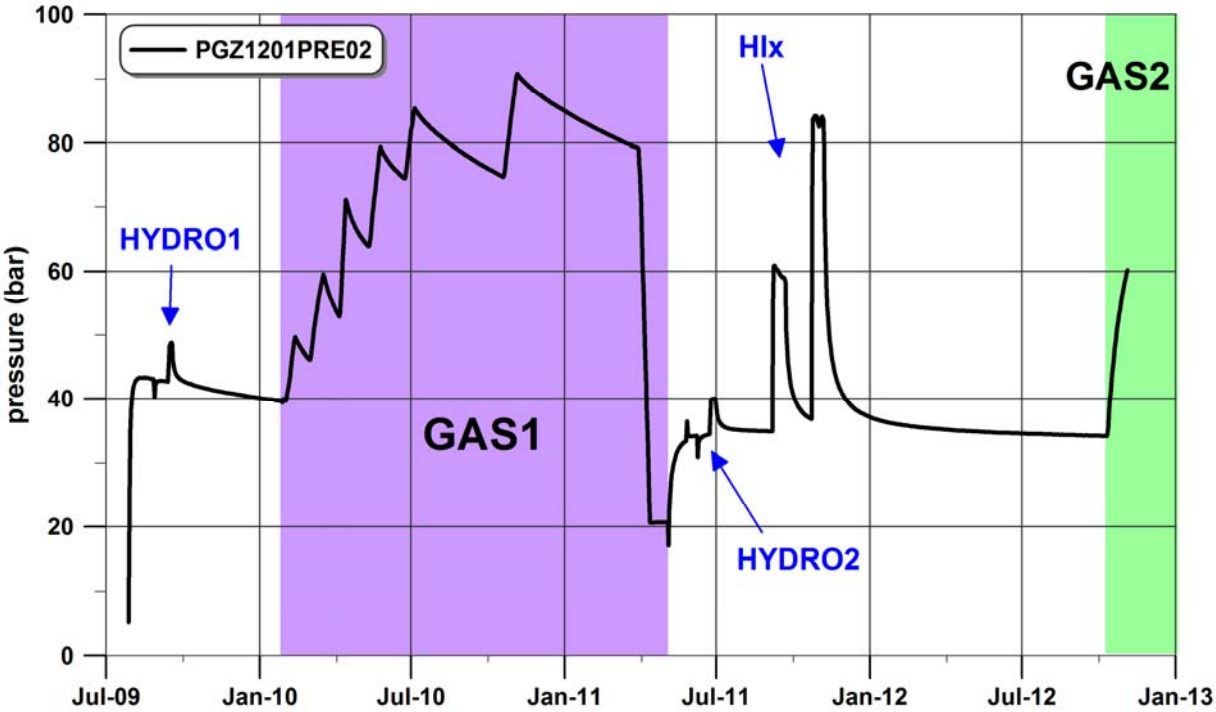

Figure 38 Successive sequences of hydraulic test and gas injection test in PGZ1

2.1.4 Conclusion

Gas injection test in Bure URL has been designed to improve knowledge about gas migration in undisturbed clay rock. In particular, the aim of the test was to observe if at large scale, the conceptual model proposed by Marschall et al. (2005) could be applied on COx claystone. Main lessons from the test are:

- Before and after the gas injection, the hydraulic properties of the host rock are unchanged. If gas pressure lead to micro-fracturing or dilatants pathway, it seems that processes are reversible due certainly to self-sealing property of the clay rock. This self-sealing ability has been observed in many experiments conducted on fractured COx samples or in the EDZ directly in the Bure URL (de La Vaissière et al., 2012c).
- At this stage, there is no evidence of dilatants pathways formation during the gas injection, even if the gas pressure reached is high (9.1 MPa) considering the gas fracturing pressure (about 12 MPa) in Bure site (Senger et al., 2006).
- All the test sequence has been modelled with continuous two phase flow (capillary flow) (see FORGE report D5.13, or de La Vaissière et al., 2012b). Those model deals with generalized Darcy law for each phase and permeability only function of the water saturation.

- Models showed also that a coupling of the flow model with mechanical behaviour is not necessary in this context to reproduce gas response. This could not be the case when gas pressure will be in the same order of the gas fracturing pressure which is one of the next objectives of the new gas injection sequence (GAS2 and GAS3[1]).
- Understanding gas migration around a tunnel supposes a good representation of the damaged zone in terms of extensions and properties. The PGZ experiment seems to demonstrate that EDZ could be a zone where gas could migrate preferentially and could be stored.
- Gas entry pressure in the undisturbed host rock has been estimated higher than 5MPa which is consistent with observations made at lab scale on COx samples.
- A maximal gas entry pressure in the EDZ generated during the drilling of the borehole has been estimated at about 2MPa.

2.1.5 References

De La Vaissière R. – 2010 - Design and Installation of the PGZ1 Experiment at Bure, Forge report D5.4.

2012 - HM modelling of PGZ and parameters studies, Forge Report D5.13

Harrington J. F., R. de La Vaissière, D.J. Noy, R.J. Cuss and J. Talandier -2012a.Gas flow in Callovo-Oxfordian Clay (COx): Results from laboratory and field-scale measurements, Mineralogical Society special publication

De La Vaissière R., P. Gerard, JP. Radu, R. Charlier, F. Colin, S. Granet, M. Piedevache, B. Helmlinger, J. Croisé, JM Lavanchy, R. Senger and J. Talandier – 2012b. Gas injection test in the Meuse/Haute-Marne Underground Research Laboratory: data and numerical approaches, Clays in Natural and Engineered Barriers for Radioactive Waste Confinement conference, Montpellier 2012.

De La Vaissière R., J. Morel, A. Noiret, P. Côte, B. Helmlinger and JM. Lavanchy – 2012c. Evolution of the excavation damaged zone during loading in claystone: in-situ CDZ experiment, Clays in Natural and Engineered Barriers for Radioactive Waste Confinement conference, Montpellier 2012.

Marschall, P., Horseman, S.T., & Gimmi, T. 2005. Characterisation of Gas Transport Properties of the Opalinus Clay, a Potential Host Rock Formation for Radioactive Waste Disposal. Oil & Gas Science Technology. 60, 1, 121-139.

Senger, R. K; C. Enachescu, T. Doe, M. Distinguin, J. Delay, B. Frieg - 2006. Design and analysis of a gas threshold pressure test in a low-permeability clay formation at Andra's Underground Research Laboratory, Bure (France), Proceedings, TOUGH2 Symposium 2006, Lawrence Berkeley National Laboratory, Berkeley, CA, 2006.

[1] GAS3 will reach the fracture pressure which is closed to 12.3 MPa

2.2 The HG-C/HG-D gas injection experiment in intact Opalinus Clay at the Mont Terri URL (NAGRA)

2.2.1 Scope and objectives

The HG-C / HG-D experiment was set up as a long-term water/gas injection experiment in a configuration of parallel boreholes in Gallery 98 of the Mont Terri URL, complemented by a laboratory programme and a modelling task. The aims of the experiment are:

- to investigate coupled hydro-mechanical processes associated with water and gas flow at different injection pressures ranging from below pore water pressure to high pressures leading to dilatancy-controlled water/gas flow and water/gas fracturing;
- to investigate the self-sealing capacity of pressure induced fractures in terms of permeability evolution and re-opening pressures
- to compare laboratory scale determinations of gas-related parameters with the results of in-situ water / gas injection experiments.

A comprehensive set of laboratory and field data has been disseminated to the FORGE project partners (Deliverable 4.16), compiling experimental evidence on phenomena and processes associated with gas transport along the excavation damage zone of a sealed tunnel section (WP 4.2.1) and through the intact host rock (WP 5.2.2). The data bases were forming the basic input for a series of benchmark exercises on gas transport processes in Opalinus Clay (see Deliverable D4.18). The data deliveries were distributed in electronic form together with a short note containing the data description (Deliverables D4.2, D4.3, D4.10, D5.2, D5.6).

2.2.2 Description of the sequence of experiments at site

The HG-C experiment consists in two sets of 4 parallel boreholes drilled perpendicular to bedding. The HG-C experiment was performed in four boreholes of the GP-A/GS site at the Mont Terri URL which had been instrumented with piezometers for pore pressure measurements and fixed installed micrometers (FIMs) for measuring axial deformation along the borehole. The boreholes were drilled inclined with respect to the tunnel floor, but perpendicular to bedding planes present in the formation.

Fig. 3.2.1 shows the layout of the tunnel and the four boreholes. Boreholes GS-1 and GS-2 had identical completions and were instrumented with triple packer systems for accurate recording of interval pressures. Boreholes GS-3 and GS-4 also had identical completions and were instrumented with a triple FIM system. The detail in Figure 39 shows a schematic of the FIM system, which measures the displacements between fixed anchors in the middle section of the borehole pipe. The spatial resolution of the micrometer systems is in the order of 1 µm at a basal distance of 1 m, resulting in a typical resolution of a microstrain.

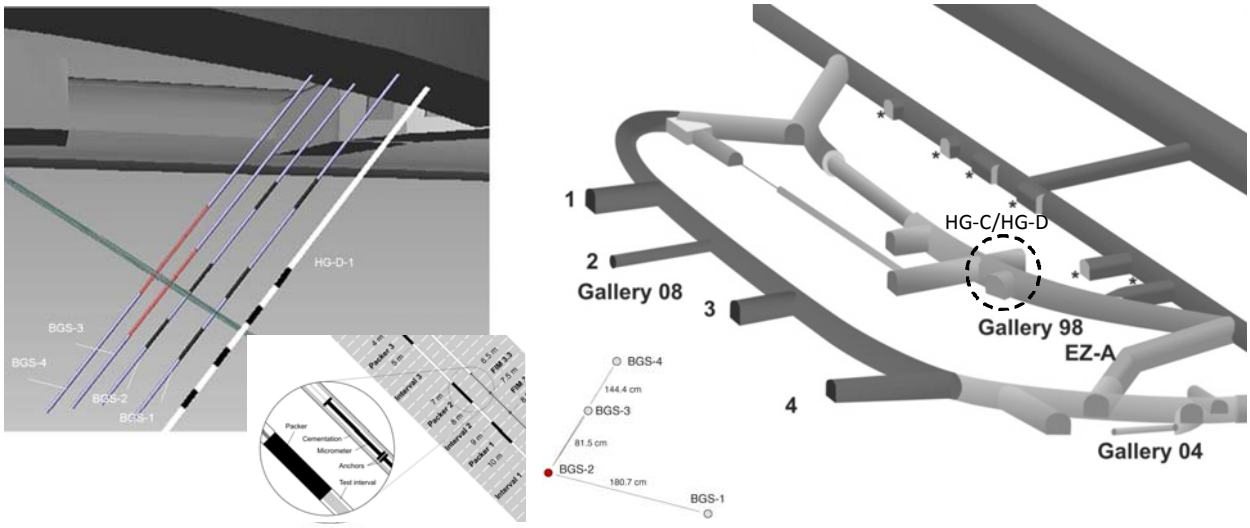

Figure 39 Location and layout of HG-C/HG-D site - right: location at the Mont Terri Laboratory; left: Schematic drawing of the borehole configuration and the site instrumentation.

In June 2009, a fifth 10m long parallel borehole has been drilled in the HG-C site as part of the newly launched project HG-D. The new borehole HG-D1 was instrumented with a hydraulic triple-packer system, which was designed to resist injection pressures up to 10 MPa. Hydraulic tests were conducted in the central packer interval HG-D1-I2 to determine interval transmissivities and to infer the hydraulic head. Pressure transducers were installed for monitoring pore pressure in the 3 pore pressure monitoring intervals. Long-term monitoring of pore pressures in the piezometers and axial displacements in the micrometer boreholes was managed via the central data acquisition system of the Mont Terri URL.

During the early stages of the Mont Terri investigation programme (1999- 2004) water and gas injection tests were conducted in zone 2 of borehole GS-2 as part of the GP-A/GS experiment. The detailed objectives of the tests were:

- Characterise formation parameters under undisturbed conditions by testing the formation with water and gas. Derive transmissivity, static formation pressure, gas threshold pressure, flow geometry.
- Starting from GS-2 Zone 2, create a hydro-frac along a bedding plane that would intersect the middle intervals (Zone 2) in GS1, 3 and eventually 4. Derive frac pressure and reopening pressure.
- Test the formation after the frac with water and gas and compare results with undisturbed formation. Conduct test phases at different pressure levels, to derive transmissivity-pressure dependency.
- Monitor and evaluate interference responses in borehole GS-1.
- Measure rock deformation using FIMs installed in boreholes GS-3 and GS-4, and correlate measurements with pressure observed in GS-2.
- Repeat water and gas tests after a long lasting re-hydration phase to characterize fracture self sealing behaviour in the Opalinus Clay.

In the context of the HG-C/HG-D experiment, complementary water and gas tests were performed in the old GS-boreholes to investigate the self-sealing capacity of the Opalinus Clay and to determine re-frac pressures after longterm pressure recovery. Pressure dependence of water and gas permeability was investigated in turn of repeat tests. After completion of the new

borehole HG-D1, a new series of water and gas tests at moderate and elevated injection pressures was conducted in an initially intact borehole section.

The experimental sequence of the HG-C / HG-D experiment is listed in Table 7.

Table 7 Overview of HG-C and HG-D experimental phases.

Test ID	Start	End	Method	Purpose
HG-C / HG-D Experiment				
HG-C Phase 12	14/12/06	27/04/07	Multi-step hydraulic test 12-58bar	Hydaulic characterisation of test interval GS2-I2; pressure dependent K
HG-C Phase 13	05/02/08	18/09/08	Gas injection varying back pressure	Gas-related characterisation of test interval GS2-I2; pressure dependent k
HG-D	24/11/09		Installation of triple packer system	
HG-D Hydrotest	29/04/10	16/08/10	Multi-step constant pressure test 10-20bar	Hydaulic characterisation of test interval HG-D1-I2; pressure dependent K
HG-D Gas test	28/10/10	09/04/11	Gas injection	Gas-related characterisation of test interval HG-D1-I2; pressure dependent k

2.2.3 Experimental results and interpretation

2.2.3.1 EXPERIMENTAL DATA BASE OF THE HG-C PHASE / HYDROTESTS

The hydrotest during the HG-C Experimental Phase 1 is described in deliverable D4.16. The measured pressures in the injection borehole BGS2 and in the observation borehole BGS1 are shown in Figure 40a. At total of six injection steps increasing in pressures from 1.2 MPa to 5.7 MPa were followed by step decreases. The measured responses in the guard intervals BGS2-3 shows a slight step increases from about 750 to 770 kPa which are probably caused by slight packer movements associated with the injection pressure steps in the injection interval BGS2-2. The pressures in the bottom interval BGS2-1 show no response to the injection test and are at 87 kPa corresponding to atmospheric pressure conditions. The measured responses in the three test intervals in the observation borehole BGS1 indicate relatively low pressures in interval BGS1-1 and BGS1-2 of less than 150 kPa, whereas the pressure in interval BGS1-3 shows a pressure of about 700 kPa, which corresponds to the expected formation pressure.

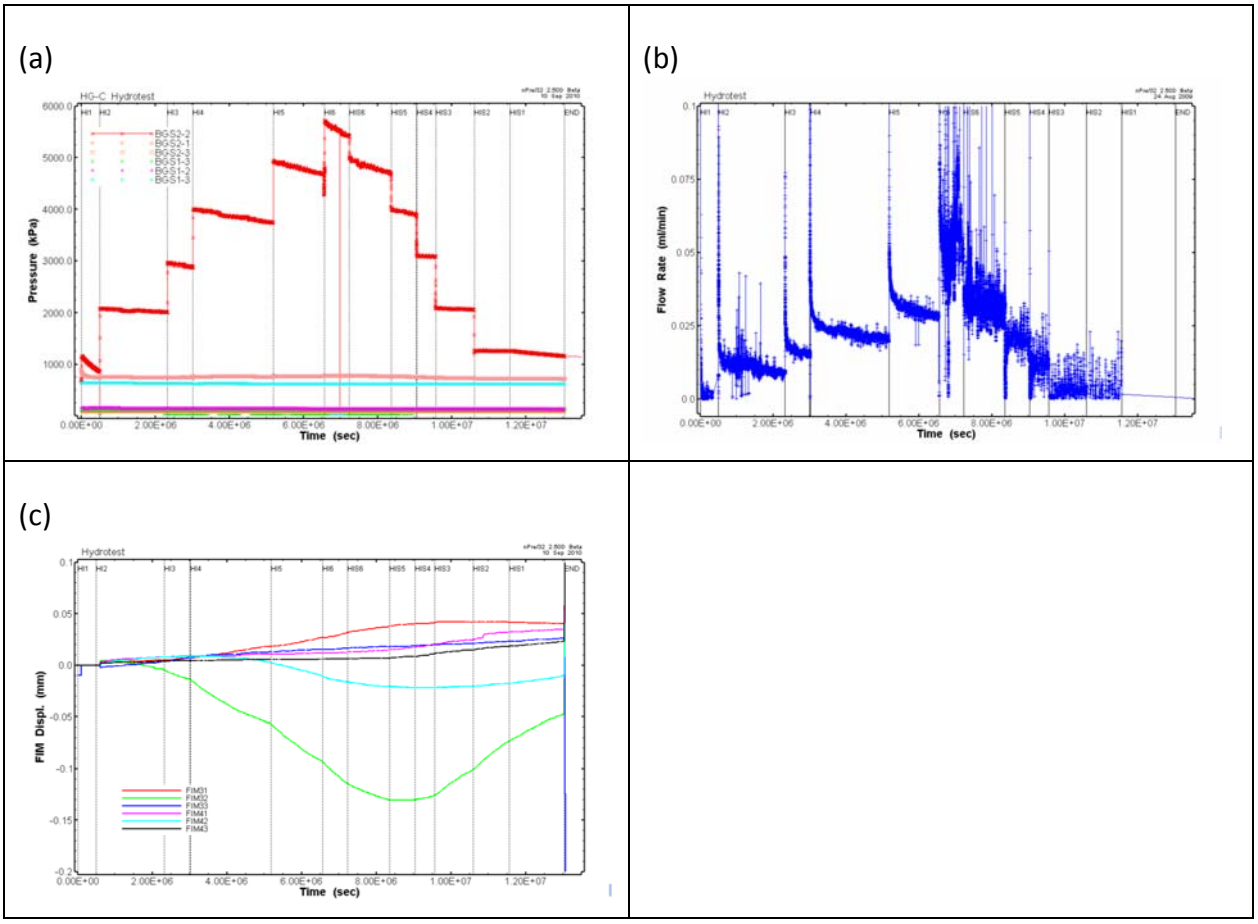

Figure 40 Pressure responses in the injection borehole (BGS2-2) and observation borehole (BGS1-1, BGS1-2, BGS1-3) during the HG-C multi-step water injection (a), measured flow rates (b) and axial displacements (c).

The measured flow rates exhibit significant fluctuations, especially during the HIS recovery periods (Figure 40b). The reasons for the fluctuations are explained in greater detail in Trick (2007). The flow data required a smoothing and filtering procedure to be suitable for further analysis (Senger 2008). The filtering and smoothing had to be done to such an extent that the variability associated with the injection pressure can still be accounted for in the variation of the flow rate data.

The mechanical observation boreholes BGS3 and BGS4 were instrumented with FIMs to measure axial deformation in the clay rock during the constant-head tests. The two boreholes are at distances of 0.7 m and 1.5 m, respectively, from the injection borehole BGS2 (Figure 39) and contain three FIMs each. The FIM measurements in response to the hydrotest are shown in Figure 40c. The FIM responses of the middle sensors indicate dilation in BGS3 and extend to BGS4, with the adjacent sensors indication compaction. The dilation occurs rather gradual indicating only slight increases in slope (Figure 40c), except for FIMGS4-1 which shows an abrupt change during the latter recovery step (HIS2).

2.2.3.2 INTERPRETATION / HYDROTESTS IN EXPERIMENT PHASE HG-C

The multi-step hydrotest sequence was subjected to detailed diagnostic analyses and numerical simulations with the borehole simulator nSights (see deliverable D4.16). The nSights analysis and optimization was performed for each test sequence to estimate the formation properties in terms of hydraulic conductivity and specific storage of the Opalinus Clay. Figure 41 displays the simulation of flow rates of the entire test sequence for the prescribed interval pressures as given

in Figure 40a. The simulation indicates that the simulated flow rates compare well with those during HI5, but are slightly higher than HI2 – HI4, and lower for HI6.

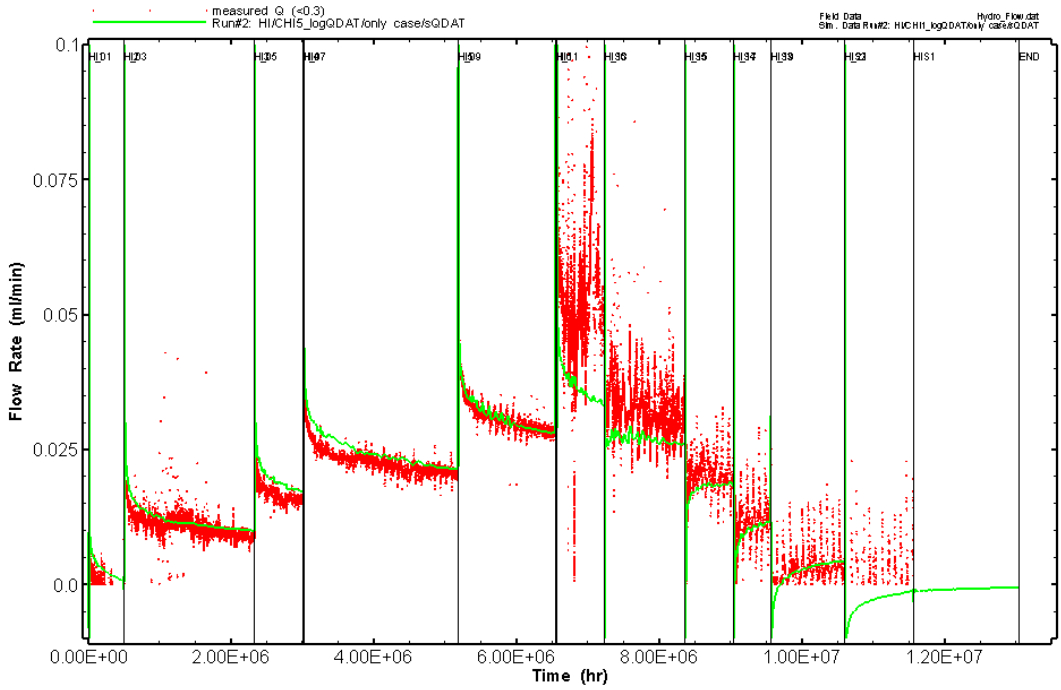

Figure 41 Simulated response of the entire test sequence based on the best-fit parameters from the HI5 optimization for injection flow rates

A summary of the estimated parameters from the different injections steps is given Table 8 and in Figure 42, showing a cross plot of formation specific storage and formation hydraulic conductivity with the associated 95% confidence regions. The results indicate a distinctly lower conductivity for HI1, whereas the conductivities for HI2 – HI5 cluster in a narrow range between 5.6E-13 and 7.1E-13 m/s. The conductivity estimate for HI6 is distinctly higher at 1.38E-12 m/s indicating a noticeably lower value for specific storage of 3.88E-7 1/m compared to those from HI1 – HI5 which yielded very similar values of between 1.3E-6 to 1.75E-6 1/m.

Table 8 Summary of parameter estimates from nSights optimization of HI1 through HI6.

	Best-Fit Parameters		$K = k\rho g/\mu$	$S_s = \rho g\,(C_p/\phi + \phi\beta)$
Seq.	**K [m/sec]**	**Ss [1/m]**	**k(m2)**	**Cp(1/Pa)**
HI1	3.09E-13	1.34E-06	3.15E-20	7.85E-10
HI2	6.19E-13	1.53E-06	6.32E-20	9.62E-10
HI3	5.66E-13	1.73E-06	5.77E-20	1.15E-09
HI4	6.51E-13	1.35E-06	6.64E-20	7.97E-10
HI5	7.06E-13	1.42E-06	7.20E-20	8.58E-10
HI6	1.38E-12	3.88E-07	1.40E-19	-8.47E-11

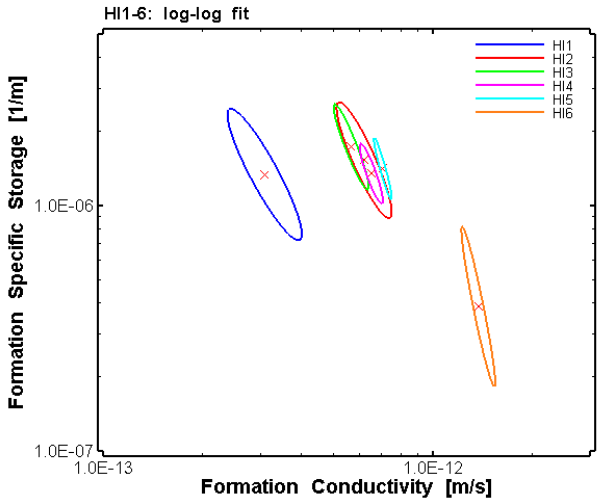

Figure 42 Computed 95% confidence regions of parameter estimates based on the optimization of the log-log flow rates for HI1 through HI6.

2.2.3.3 EXPERIMENTAL DATA BASE / GASTESTS IN EXPERIMENT PHASE HG-C

The gas tests during the HG-C Experimental Phase 2 and the corresponding references are given deliverable D4.16 and shown in Figure 43. Prior to the constant head gas injection test, the pressures were stable in all three intervals of both boreholes. The gas injection occurred in borehole BGS2 interval 2 (BGS2-I2). During the first two steps, the pressures in BGS2-I2 remained nearly constant; the third test GHI3 did indicate a slight pressure decline. The gas flow rates were calculated from the pressure changes measured in BGS2-I2, indicating a noisy pattern near zero flow during GHI1 through GHI3. During GHI4, the injection pressure showed a distinct decline, and the corresponding gas flow rate showed a slight increase.

The measured pressures in Interval 2 of the observation borehole (BGS1-I2) did show an immediate increase with a total pressure increase to 1.23 MPa at the end of GHI4. The last injection step GHI5 to 3.01 MPa resulted in an immediate pressure decline, which leveled off to about 1.5 MPa at the end of GHI5 (Figure 43a). The pressures in BGS1-I2 showed a rapid increase to as high as 1.9 MPa which was followed by the more gradual decline to about 1.2 MPa at the end of the test data. The corresponding gas flow rates similarly showed an initial peak followed by an asymptotic decline to flow rates of about 0.025 ml/min (Figure 43b).

The measured displacements (FIMs) in the observation boreholes BGS3 and BGS4, which are at 0.7 m and 1.4 m distances, respectively, from the injection borehole BGS2 are shown in Figure 43c. The data indicate a decreasing trend for FIMGS3-2 starting with the gas injection tests, whereas FIMGS3-1 and FIMGS3-3 indicate an increasing trend. Relatively large responses are associated with GHI4 and GHI5, whereby the latter indicates sudden short decreases of all the FIMs.

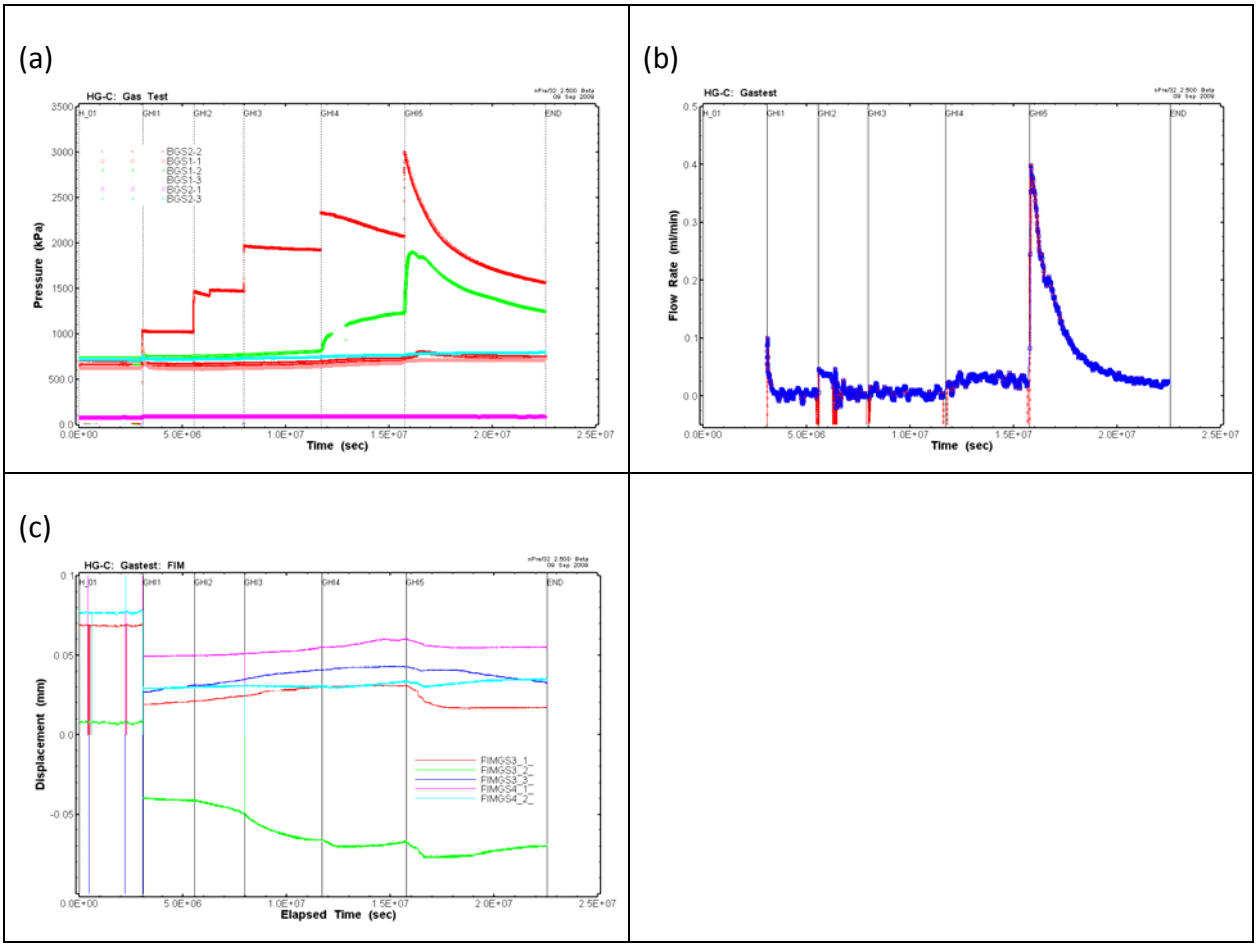

Figure 43 Pressure responses in the injection borehole (BGS2-2) and observation borehole (BGS1-1, BGS1-2, BGS1-3) during the HG-C multi-step gas injection (a), measured flow rates (b) and axial displacements (c).

2.2.3.4 INTERPRETATION / GASTESTS IN EXPERIMENT PHASE HG-C

The gas test was simulated with the two-phase flow code TOUGH2 and the inverse code ITOUGH2 was used for parameter estimation. References of the corresponding analyses and simulations is given in deliverable D4.16. For the estimation of formation properties, both the pressure responses in the injection interval (BGS2-I2) and in the observation borehole interval (BGS1 I2) were used for calibration. That is, the initial gas pressures for each injection step was prescribed based on the increased backpressure in the gas bottle, accounting for the total gas volume of the injection configuration. The subsequent pressure response in the injection interval for each step was then used for calibration, in addition to the monitored pressure in the observation borehole interval BGS1-I2. Based on the apparent difference in the observed responses, three separate optimizations were performed for (a) GHI1-3, (b) GHI4, and (c) GHI5 to estimate hydraulic and two-phase flow properties. The hydraulic properties include:

- permeability,
- pore compressibility,
- porosity

The two-phase flow properties include:

- capillary strength parameter in the van Genuchten constitutive relationship for the capillary pressure – saturation function,

- van-Genuchten 'm' parameter, and residual water saturation (S_{lr}), describing the shape of the capillary pressure and relative permeability curves

Permeability and capillary strength parameter are of particular importance to identify possible pathway dilation at increasing gas pressures. Similar to the hydrotest analyses, described above, the measured data were filtered for each interval and the number of data points for the calibration were specified to get approximately equal weighting for the inverse modeling (i.e., 50 data points for GRI1-3, 20 for GRI4, and 25 for GRI5).

The results of the inverse simulations with ITOUGH2 for the GHI1-3 steps, where the injection pressure steps increase up to 2 MPa and produced only minor pressure responses in both injection and observation intervals (Figure 43), yielded a formation permeability of 5.0E-20 m^2 which compared reasonably well with the estimate 3.9E-20 m2 from the hydrotest during HI1 (Table 8). The parameter estimates for the GHI4 indicated a noticeable increase to 1.7E-19 m^2 and reproduced well the injection pressure and observation pressure responses (Figure 44). The final injection step (GHI5) produced about a one order of magnitude increase in permeability to 1.3E-18 m^2. Moreover, the inverse modeling yielded decreasing values in the capillary strength parameter P_0 of the van Genuchten model for the capillary pressure – saturation relationship. This is consistent with the pressure-dependent pathway dilation resulting in a permeability increase and corresponding decrease in capillary pressure. The geomechanical effect of pathway dilation is also indicated by the measured displacements in the boreholes BGS3 and BGS4 (Figure 43c). The estimates for porosity and pore compressibility also decreased whereby the estimate for pore-compressibility reached a lower bound for realistic values, suggesting a localized response within the assumed total width of the test zone (1 m).

The estimated parameters and relevant statistical information from the inverse simulation are summarized in Table 9 for the different sequences.

Table 9 Summary of parameter estimates from ITOUGH optimization of GHI13-GHI5.

Parameter Estimates:

	GHI13	GHI4	GHI5
K	5.01E-20	1.35E-19	1.45E-18
Por	1.00E-01	3.48E-02	2.50E-02
Cp	3.98E-10	1.00E-10	1.00E-10
vG-n	2.50E+00	2.20E+00	3.70E+00
vG-Po	2.00E+06	7.94E+05	3.80E+05
Slr	*5.00E-01*	4.80E-01	2.30E-01

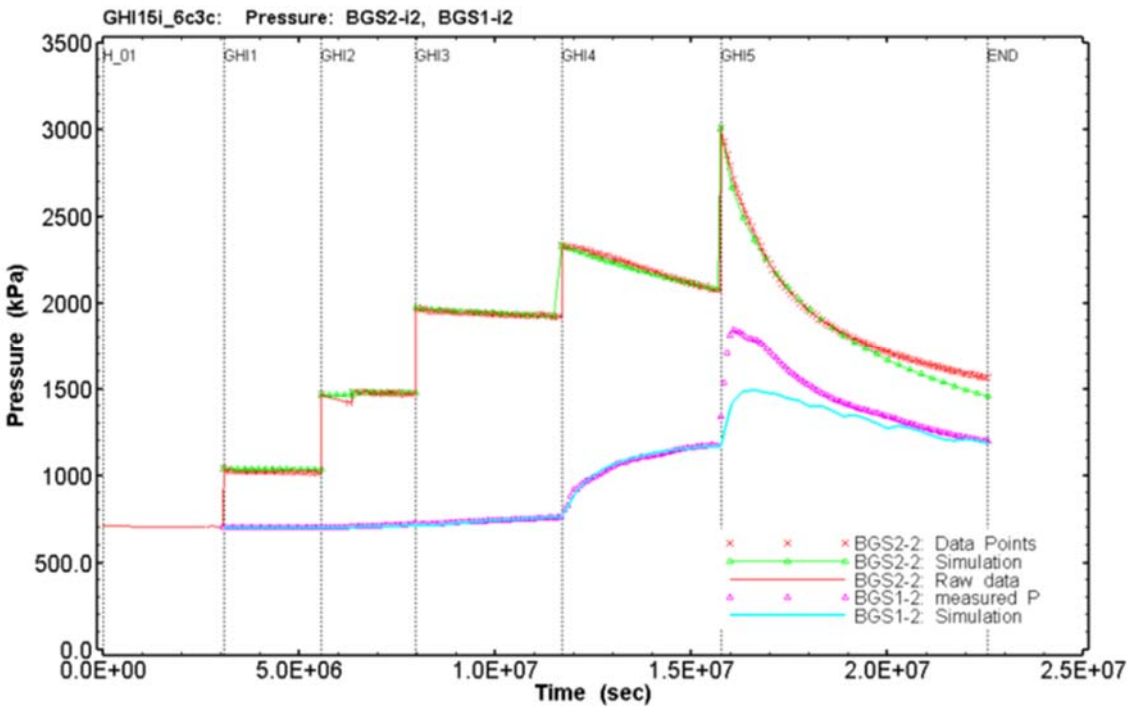

Figure 44 Simulated pressure responses in the injection borehole (BGS2-1) and observation borehole (BGS1-2) during the HG-C Experimental Phases 2, based on individual fits of Sequences GHI1–3, GHI4, and GHI5.

Overall, the simulated responses suggest potential pressure-dependency of parameters (i.e. k and vG-P_0) particularly during GHI5 because of the large pressure range. To evaluate the potential impact, a forward simulation was performed of the GHI5 sequence which involved a linear dependency of permeability. For this a special version of the TOUGH2 code was used incorporating the pressure-dependent permeability and dependency of the capillary-strength parameter P_0 in the van Genuchten model on permeability.

The pressure-dependent permeability is defined as follows:

$$k = k_0 \times (1 + (k_factor - 1) \times \frac{(P - P_1)}{(P_2 - P_1)}$$

Where k_0 is the reference permeability, k_factor is a scaling factor, P_1 is the starting pressure of dilation, and P_2 is maximum pressure corresponding to the maximum permeability. The relationship between capillary strength and permeability is typically represented by Leverett's function as:

$$P_0^{'} = P_0 \sqrt{\frac{k_0}{k}}$$

or by a cubic-law function:

$$P_0^{'} = P_0 \sqrt[3]{\frac{k_0}{k}}$$

In the following forward simulation of the GHI5 sequence, the cubic law function was used, and a linear permeability change between a pressure of P_1 = 0.75 MPa and P_2 = 3 MPa, with a value for k_factor = 15. Initial conditions for the simulation were the simulated conditions at the end of GHI4. The results of the simulation are shown in Figure 45. The simulated pressure in the injection interval shows a much improved pressure response, but are slightly lower at early time

than the measured pressures. The simulated pressures in the observation borehole (BGS1-2) shows a very good fit at early time, but tends to be noticeably higher at late time. Overall, the simulations indicate a pressure-dependency, whereby the permeability decrease with decreasing pressure. Most likely, the pressure-dependent properties are non-linear and would require a more complex functional relationship in order to improve the fits, particularly for the BGS1-2. For this, a detailed coupled modeling approach is required to relate the measured deformation in the observation boreholes to the changes in the hydraulic and two-phase flow properties of the formation.

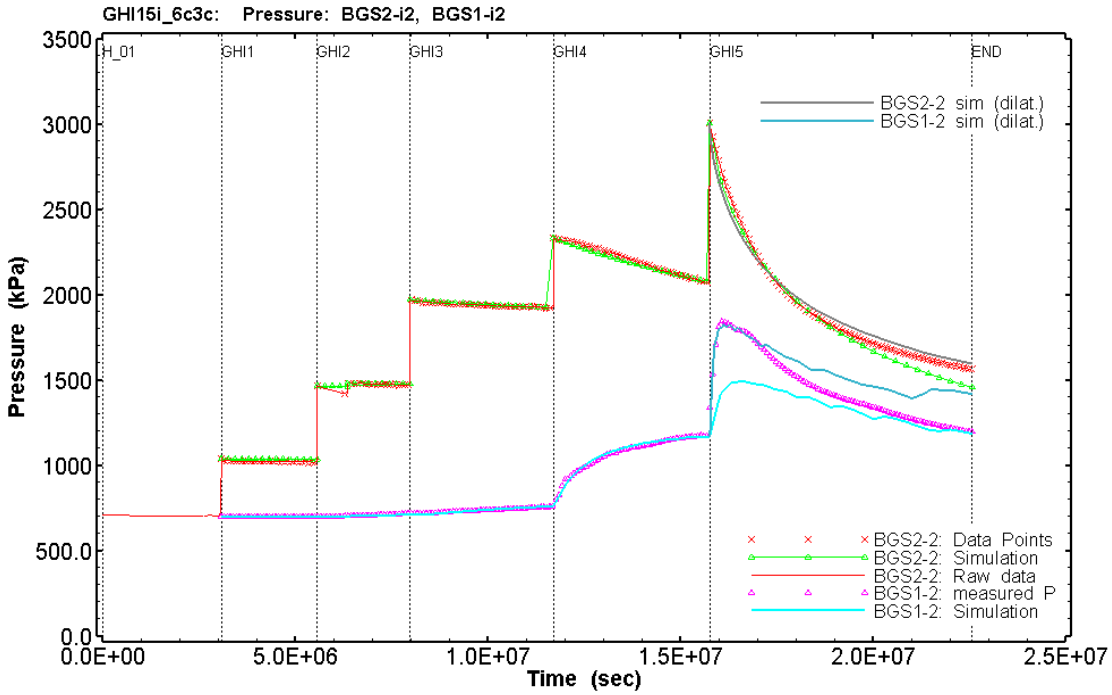

Figure 45 Simulated pressure responses in the injection borehole (BGS2-1) and observation borehole (BGS1-2) during the HG-C Experimental Phases 2, based on individual fits of Sequences GHI1–3, GHI4, and GHI5, whereby GHI5 includes the simulated results assuming pressure-dependent permeability.

2.2.3.5 WATER AND GAS TESTS AS PART OF THE HG-D EXPERIMENT

The results and the existing interpretations of the HG-C experiments (end of 2006 – 2009) were disseminated to the WP4/WP5 modelling groups for complementary analyses and simulations. In addition, data sets of the new water and gas injection tests as part of the the HG-D experiment (2011 – 2012) were distributed. The new test data are described in the subsequent paragraphs.

The new test sequence started after drilling and instrumentation of the borehole HG-D1 by the end of 2009. After an extended pressure recovery period, a multistep hydrotest was conducted in the test interval I2 of borehole HG-D1 for hydraulic characterisation of the test interval. The injection pressures were kept below 2 MPa in order to minimise the risk of hydraulic fracturing or pathway dilation. The active test phase was followed by a shut-in period of several months. After full recovery of the pore pressure in HG-D1-I2, a multistep gas injection was started. The test was aimed at determining the gas transport properties of the rock at moderate injection pressures (two-phase flow regime) and at elevated pressures (pathway dilation regime), respectively.

Figure 46a displays an overview of the available long-term monitoring data of the new HG-D experiment, starting early 2009 with an extended long-term monitoring phase and the subsequent packer installation in BHG-D1 by the end of the year. The multistep water injection

test starting in June 2010 test is marked in blue in Figure 46a. Crosshole responses on the water injection are observed in intervals I2 of borehole BGS-2 and in BGS-1-I1 and BGS-1-I3.

The corresponding transients of the FIMs are shown in Figure 46b. Unfortunately, the quality of the FIM data is rather poor. In particular BGS-3-FIM3 and BGS-4-FIM4 show strange results indicating, that the sensors might be defective. None of the sensors exhibits a significant mechanical response on the water injection test.

The subsequent gas injection test at the end of 2010 is marked in red in Figure 46a. A zoom-in of the pressure and flow transients is given in Figure 47. During the first pressure step at 1.2 MPa, the gas flow decreases quickly towards the detection limit of the flowmeter. No significant pressure responses are observed in the observation intervals BGS-1 and BGS-2. Similarly, during the second and the third pressure step (1.7 and 2.0 MPa, respectively) there is no major response observed in the adjacent monitoring boreholes. The behaviour changes when pressure is increased to a value of around 2.3 MPa: a rapid pressure response is observed in GS1-I1 and slow, but significant pressure increases are seen in BGS-2-I1 and –I3. Furthermore GS3-FIM1 displays a marked dilatation.

Even though it is evident, that the new HG-D data bases did not exhibit the same quality as the previous HG-C data, some interesting general conclusions can be drawn. Thus, gas invades the rock already at moderate gas pressures (gas threshold pressure of 1.2 MPa, corresponding to an air entry value in the order of 0.7 MPa and a static formation pressure of 0.5 MPa). Furthermore, the opening of the bedding in response to the 4th step of gas injection (at 2.3 MPa) happens at a slightly lower pressure than the previous HG-C gas test (at 2.8 MPa) and significantly lower pressure than the former GS/GP-A tests (at around 4 MPa).

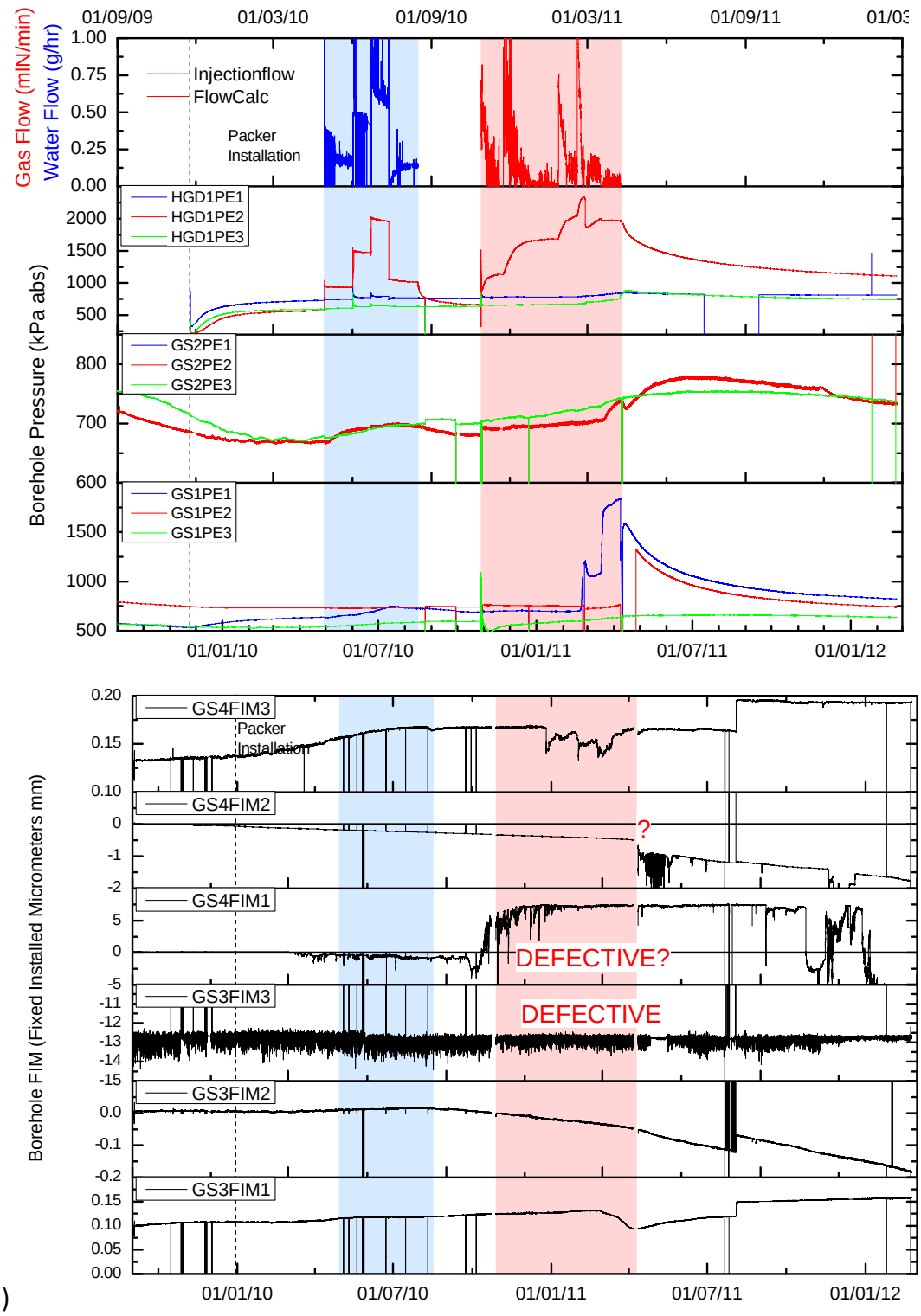

Figure 46 HG-D testing: a) flow and pressure response; b) FIM response

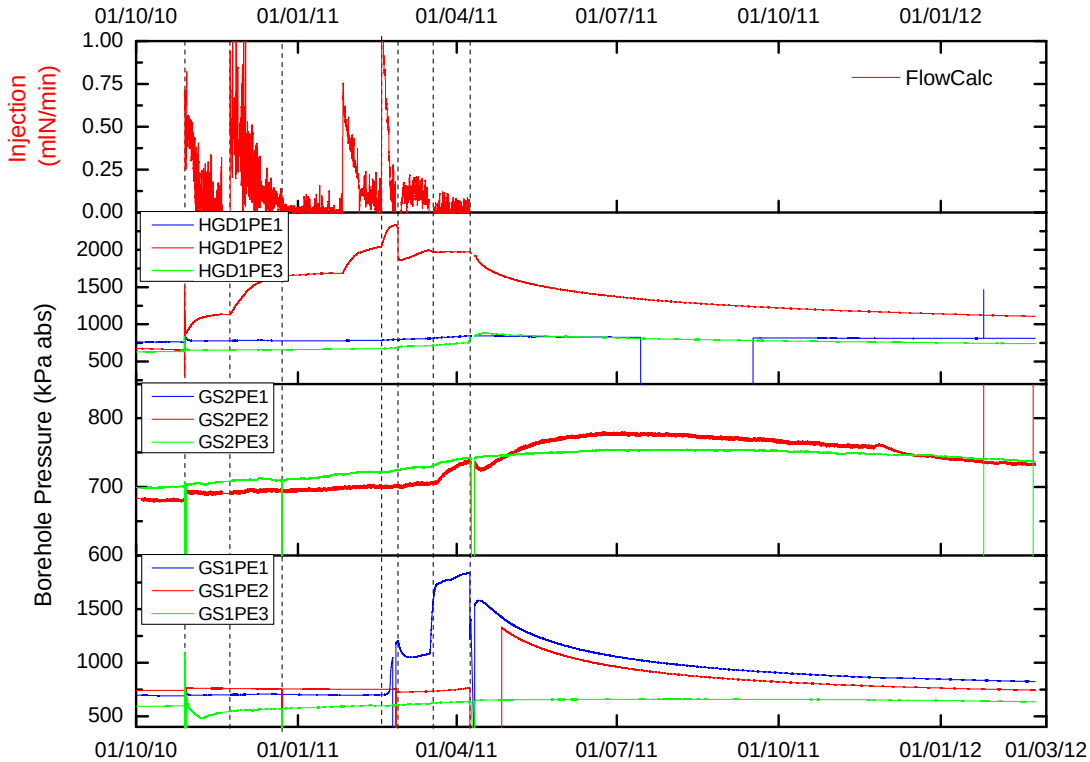

Figure 47 HG-D testing gas injection flow and pressure response.

2.2.4 Conclusions

The HG-C / HG-D in-situ experiment was aimed at investigating the coupled hydro-mechanical processes associated with water and gas flow at different injection pressures, ranging from below pore water pressure to high pressures leading to dilatancy-controlled water/gas flow and water/gas fracturing. Furthermore, scale effects were addressed by the comparison of the interpretations of the field data with laboratory scale determinations of gas-related parameters. In this context, the range of validity of two-phase flow modeling approaches was tested for the interpretation of gas transport processes on the field scale. The main conclusions achieved can be summarized as follows:

- the in-situ water injection experiments suggest an intrinsic permeability of the intact rock of about 5E-20 m^2. Evidence for moderate enhancement of water permeability by a factor of 2 is observed, when injection pressure exceeds a level of about 4 MPa. For the given test configuration, this water pressure is interpreted as the threshold pressure for the onset of dilatancy in response to pore pressure increase. Displacement measurements in nearby observation boreholes support this hypothesis.

- the in-situ gas injection experiments indicate gas entry at a gas pressure below 2 MPa, associated with an intrinsic permeability of 5E-20 m^2, which is consistent with the permeability determined from hydrotesting.

- a marked enhancement of gas permeability up to a factor of 20 is observed, when injection pressure exceeds a level of about 2 MPa. Clear crosshole responses are seen, indicating the onset of dilatancy in response to the increasing gas pressure. A distinct mechanical response in the FIM boreholes is observed during the final gas injection step (GHI5).

- The dilatancy phenomena, associated with the gas injection at elevated gas pressures were modelled using an implicit formulation for the hydro-mechanical coupling. The modelling approach was based on an extension of a classical two phase flow code (TOUGH2) to cope with

fluid flow and gas transport processes in deformable media. A convincing fit of the entire test sequence was achieved, which matched also the pressure response of the nearby observation boreholes.

- A complete set of two-phase flow parameters was obtained from the in-situ gas test, which displayed consistency with the single-phase parameters (intrinsic permeability, pore compressibility), estimated from the hydraulic test sequence.
- Moreover, the derived two phase flow parameters compare remarkably well with the analyses of gas permeability tests on core samples from the Gallery 98 (see deliverable D4.16).

Overall, the HG-C/HG-D experiments have broadened considerably the empirical and experimental evidence, required for the evaluation of the full spectrum of gas transport mechanisms in Opalinus Clay. The gas-related data packages which were disseminated to the FORGE modeling teams have proven to be most valuable for validating modeling approaches for the simulation of gas transport processes in deformable media. The progress in constitutive modeling of THM couped gas transport processes is demonstrated impressively by successful model applications, using an implicit formulation for the hydro-mechanical coupling.

Comparison of the two-phase flow parameters, derived from the analysis of laboratory-scale and field-scale experiments draws a quite optimistic picture with regards to the “upscalability” of both, gas transport mechanisms and gas related rock properties of indurated clays, such as Opalinus Clay.

3 Gas transport in undisturbed host rock: modelling

3.1 MODELLING OF MONT TERRI HG-C EXPERIMENT, GP-A AND GS EXPERIMENTS (UPC)

3.1.1 Introduction

The present report synthesizes the results of the numerical simulation of the experiments GP-A/GS. The experiments were carried out to study the two-phase flow properties of the Opalinus clay at Mont Terri. The test includes two parts; the first part of the program was the determination of the frac and reopening pressures characterization of the formation subsequent to the hydro-frac. The second part consisted in a re-hydration phase, the water and gas tests were repeated in order to characterize the fracture self sealing behaviour in the Opalinus clay (Enachescu et al., 2002). The numerical simulation is focus in the second part of the test. In Table 10 are indicated the phases of the test and in blue are remarked the phases simulated.

Table 10 Phases of the test. In blue are remarked the phases simulated.

Phase Name	Elapsed Hours		Test Phase	Test event
	Start	End		
Hyd1PRE	1	460	Hydro 1	Pretest
Hyd1PI1	460	478	Hydro 1	Pulse Test 1
Hyd1HI1	478	486	Hydro 1	Constant Head Test (1020 kPa)
Hyd1HIS1	486	503	Hydro 1	Shut-in
Hyd1HI2	503	511	Hydro 1	Constant Head Test (2070 kPa)
Hyd1HIS2	511	1631	Hydro 1	Shut-in
Gas1PI1	1631	2283	Gas 1	Gas Pulse Step 1 (1190 kPa)
Gas1PI2	2283	2355	Gas 1	Gas Pulse Step 2 (1280 kPa)
Gas1PI3	2355	2451	Gas 1	Gas Pulse Step 3 (1920 kPa)
Gas1PI4	2451	2879	Gas 1	Gas Pulse Step 4 (2780 kPa)
Gas1REL	2879	3311	Gas 1	Recovery
FracPre	3336	3338	Frac	Step pressure increase
Frac1	3338	3339	Frac	Second frac cycle -
Frac2	3339	3341	Frac	Refrac Cycle 1
Frac3	3341	3358	Frac	Refrac Cycle 2
Hyd2PI1	3359	3365	Hydro 2	Pulse Test 1 (1835 kPa)
Hyd2PI2	3365	3366	Hydro 2	Pulse Test 2 (2005 kPa)
Hyd2PI3	3366	3367	Hydro 2	Pulse Test 3 (3604 kPa)
Hyd2PI4	3367	3369	Hydro 2	Pulse Test 4 (4548 kPa)
Hyd2HI	3369	3370	Hydro 2	Constant head injection (6682 kPa)
Hyd2HIS	3370	3381	Hydro 2	Shut-in
Gas2PI	3383	4964	Gas 2	Gas pulse Nitrogen Injection
Gas3PRE	5020	5038	Gas 3	Pretest
Gas3GRI	5038	5054	Gas 3	Gas constant rate nitrogen injection (0.1 mln/min)
Gas3GRIS	5054	8689	Gas 3	Shut-in
Hyd3HI1	8689	9414	Hydro 3	Constant head water injection 1 (1845 kPa)
Hyd3HI2	9414	10852	Hydro 3	Constant head water injection 2 (2380 kPa)
Hyd3HIS2	10852	13870	Hydro 3	Shut-in
Gas4GRI	13870	13962	Gas 4	Gas constant rate nitrogen injection (20.3 mln/min
Gas4GRIS	13962	20940	Gas 4	Shut-in

3.1.1.1 DESCRIPTION OF THE TEST GEOMETRY

Four boreholes were drilled parallel, and perpendicular on the Opalinus clay bedding planes. The borehole diameter was 101mm. At borehole BGS2 was injected the water and the gas according to the test phase and at borehole BGS1 were measured the pressure transmitted through the bedding plane. The distance between BGS2 and BGS1 was 1.4 m. The displacements were measured at boreholes BGS3 and BGS4 using extensometer located at different depth. The distance between boreholes BGS2, BGS3 and BGS4 was 0.7m respectively (Figure 48a and b) (Enachescu et al., 2002).

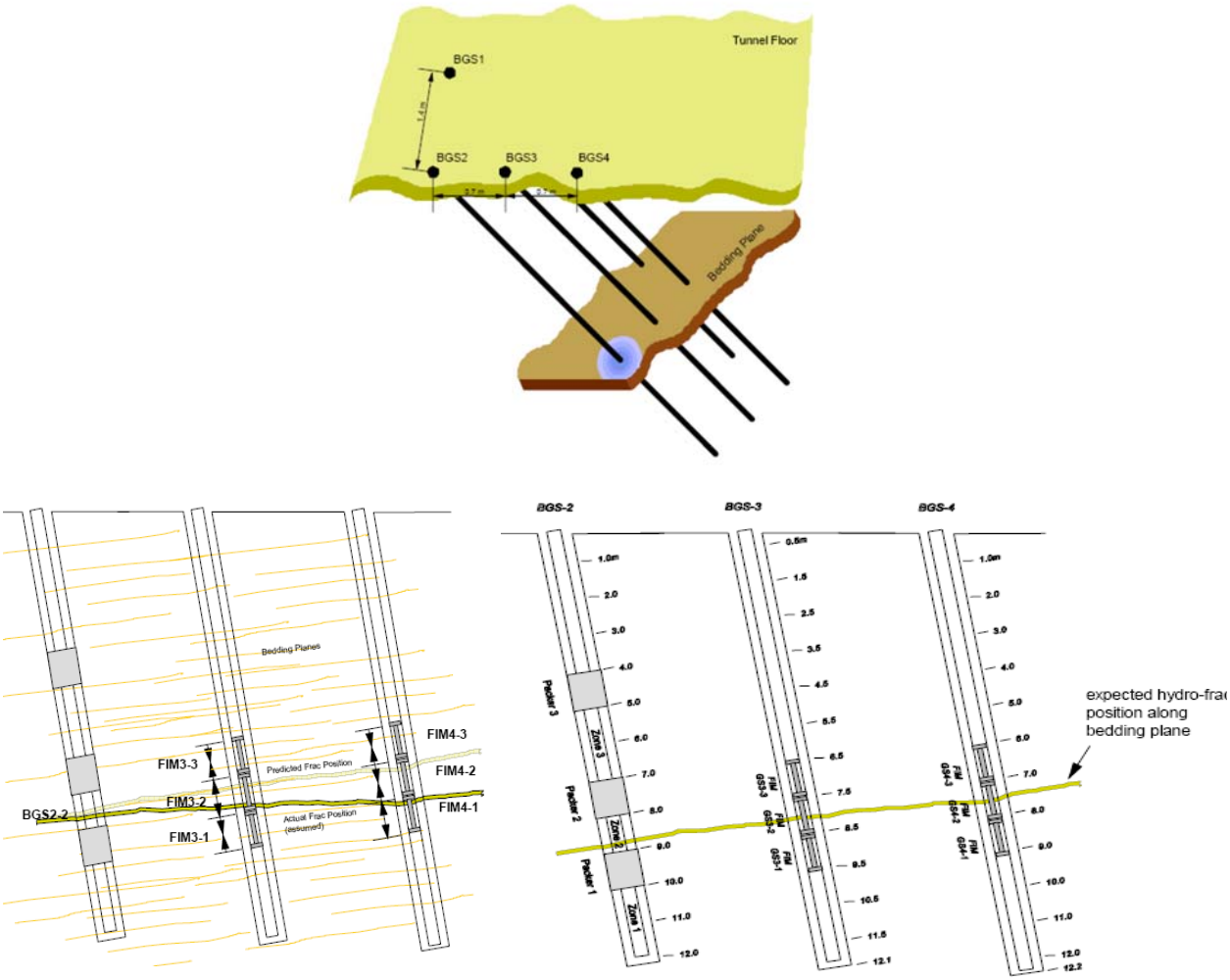

Figure 48a Schematic view of borehole location and bedding plane. 48b: Schematic view of boreholes BGS2, BGS3 and BGS4 including the position of the extensometers.

3.1.2 Geometry and materials used in the model

The geometry used in the simulation is axi-symmetric and has 15 m of length and 15 m of depth (Figure 49a). Four materials were considered in the model, the Opalinus clay, the Fracture and Water in the borehole BGS2 and Water 1 in borehole BGS1 (Figure 49 b).

The Fracture is located at a depth equal to 8.50m, according to the frac position shown in Figure 48b. The porosity of Water 1 was calculated considered the real volume of BGS1. The Opalinus clay, Water and Water 1 were discretized using 556 continuum elements, whereas, the Fracture was discretized using 19 joint elements. The constitutive laws and parameters of the materials are summarized in next section. The initial conditions are summarized in the next section as well. All the materials are considered saturated with a liquid pressure Pl = 1.4 MPa, and the injection of liquid or gas was imposed at the upper boundary of BGS2 indicated in Figure 49 b.

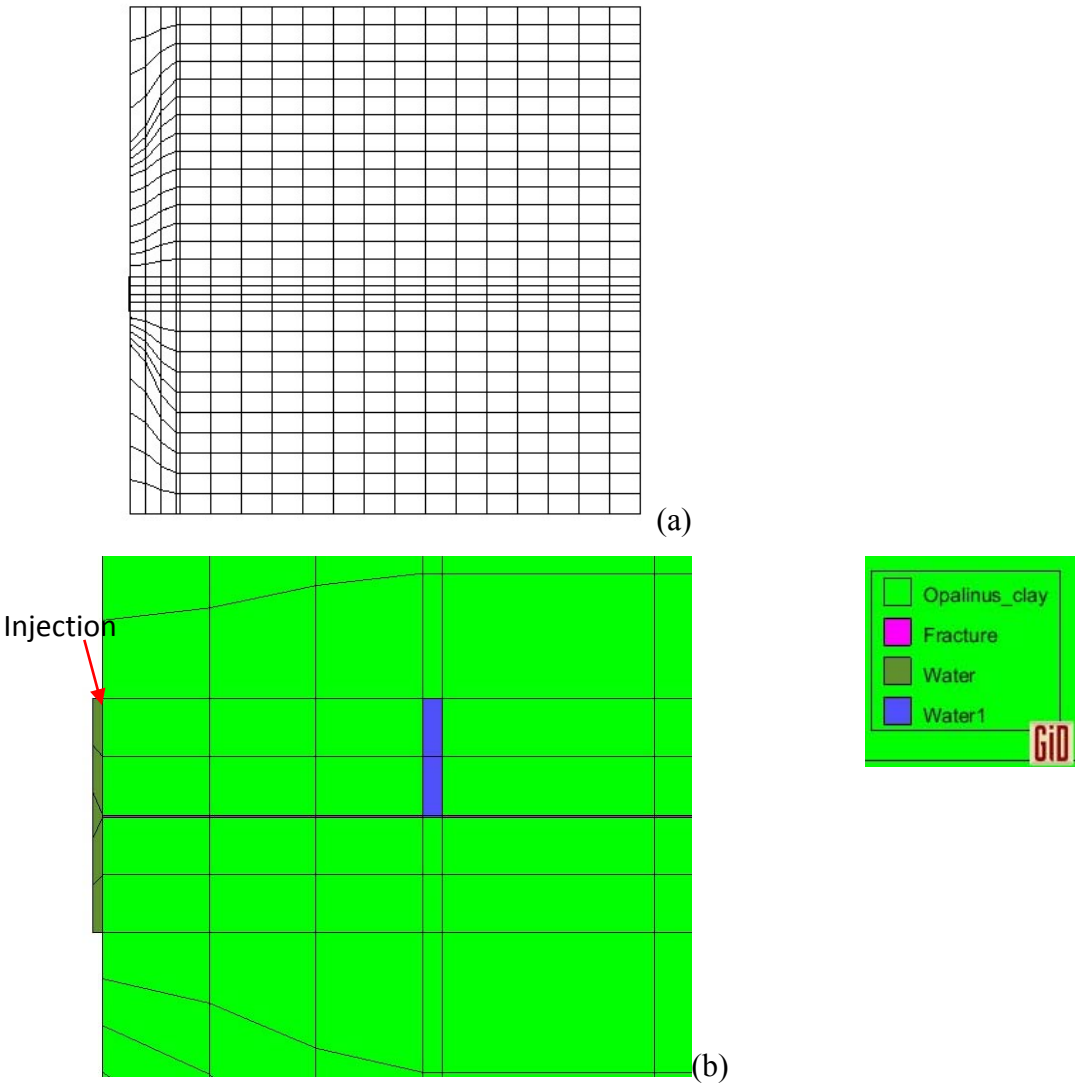

Figure 49a: Geometry of the model and finite element mesh. 49 b: Materials used in the model.

3.1.2.1 CONSTITUTIVE LAW OF MATERIALS AND PARAMETERS

For the Opalinus clay, Water and Water 1 a linear elastic law was considered in order to represent their mechanical behaviour and a constant intrinsic permeability. The water retention curve adopted for the Opalinus clay is the curve proposed by Sanchez, (2008). For Water and Water 1 it was adopted a standard Van Genutchen´s curve (1980).

However for the material Fracture it was modelled considering the recently developed joint element with a non-linear elastic law. This law calculates the normal stiffness considering the changing of the joint aperture as described in: Equation 3

$$\begin{Bmatrix} \sigma' \\ \tau \end{Bmatrix} = \begin{bmatrix} K_n & 0 \\ 0 & K_s \end{bmatrix} \begin{Bmatrix} u_n \\ u_s \end{Bmatrix} \qquad \text{Equation 2}$$

$$K_n = \frac{m}{a - a_{\min}} \qquad \text{Equation 3}$$

where σ' is normal net stress, τ is the tangential stresses, u_n and u_s are the normal tangential displacement of the joint element, K_n and K_s are the normal and tangential stiffness respectively, *m* is a parameter of the model; *a* is the opening of the element, and a_{min} is the minimum opening of the element (at this opening, the element is considered as completely closed).

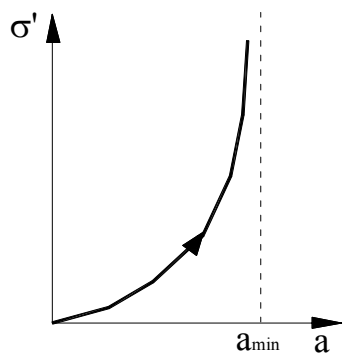

Figure 50 Elastic constitutive law of the joint element. Normal stiffness depends on joint opening.

The longitudinal fluid flow through the Fracture is considered laminar. Based on this hypothesis, the hydraulic conductivity of the joint is calculated by the following cubic law:

$$K_l = \frac{\rho g}{\mu} \frac{e^3}{12} \qquad \text{Equation 4}$$

where ρ is the fluid density; g is the gravity, and μ is the fluid viscosity and e is the aperture.

In this equation, if the water properties and gravity are not included, the intrinsic permeability is obtained:

$$k_l = \frac{e^2}{12}$$ Equation 5

In this case the hydraulic opening (e) of the Fracture is calculated adding to the initial hydraulic opening (calculated by Barton (1985)'s law) the increase or decrease of the Fracture opening calculated by the elastic law in each time period:

$$e = \frac{\mathrm{a}^2}{JRC^{2.5}} + \Delta \mathrm{a}$$ Equation 6

The transversal intrinsic permeability k_t is considered to be equal to that of the continuum media.

The degree of saturation of joints is calculated using the standard retention curve of van Genuchten (van Genuchten, 1980):

$$S_l = \left[1 + \left(\frac{\Psi}{P} \right)^{\frac{1}{1-\lambda}} \right]^{-\lambda}$$ Equation 7

where S_l is the liquid degree of saturation; $\Psi = P_g - P_l$ is the current suction; λ is a model parameter, and P is the air entry pressure necessary to desaturate joints.

The variation in the joint opening also causes changes in air entry pressure (Olivella & Alonso, 2008). The air entry pressure necessary to desaturate the joint depends on its hydraulic opening, that is:

$$P_0 = \sigma \left(\frac{1}{r_1} + \frac{1}{r_2} \right) = \frac{2\sigma}{e}$$ Equation 8

which is obtained when $(1/r_1) = 0$ and $r_2 = e/2$. In this case the wetting angle was assumed to equal zero. If Equation 8 is combined by means Equation 5, the capillary pressure necessary to start desaturation is obtained as:

$$P = P_0 \frac{\sqrt{k_{l0}}}{\sqrt{k_l}}$$ Equation 9

And the relative permeability of the materials is adopted as:

$$k_{rl} = k_{rg} = S^3$$ Equation 10

The parameters of the materials are summarized in Table 11.

Table 11 Initial conditions and parameters of the materials.

Material	Initial conditions				Hydraulic properties						Mechanical properties
	n_0	ρd [kg/m3]	Sr [%]	P_{l0} [MPa]	kx [m2]	ky [m2]	P0 [MPa]	λ	Pd [MPa]	λd	Elastic parameter
Opalinus Clay	0.137	2170	100	1.4	$9.0x10^{-21}$	$1.1x10^{-21}$	8	0.2	700	2.38	E [MPa]=4x10[illegible] υ=0.27
Joint	**-**	**-**	**100**	**1.4**	**Dependant with the aperture**	**$1.0x10^{-16}$**	**1**	**0.3**	**-**	**-**	**m[MPa] =1.0x10[illegible] Kt[MPa/m]=1.0x10[illegible] a0 [m]=0.01**
BGS2Z2 (Water)	0.99	-	100	1.4	$1.0x10^{-12}$	$1.0x10^{-12}$	$1x10^{-4}$	0.6	-	-	E [MPa]=1.0 υ=0.49
BGS1Z2 (Water 1)	0.015	-	100	1.4	$1.0x10^{-12}$	$1.0x10^{-12}$	$1x10^{-4}$	0.6	-	-	E [MPa]=1.0 υ=0.49

3.1.2.2 COMPARISON BETWEEN NUMERICAL AND EXPERIMENTAL RESULTS

In this section it is shown a comparison between numerical and experimental data (Enachescu et al., 2002) obtained for each phase. In Table 10 it is shown that water pressure used in phases Hydro 2 and Hydro 3 and the gas injection rate used in phases Gas 3 and Gas 4 are well reported. However the gas injection rate used in phase Gas 2 was not recorded and then for the simulation a gas flow equal to 1.0×10^{-5} kg/s was adopted. Table 12 shows a summary of the figures containing results for the different phases simulated.

Table 12 Summary of figures with results corresponding to test stages

Hydro 2	Figures 51 to 54
Gas 2	Figures 55 to 58
Gas 3	Figures 59 to 62
Hydro 3	Figures 63 to 66
Gas 4	Figures 67 to 70

The displacements measured by the extensometers were compared with the displacement calculated by differentiation between the displacement obtained from the model at depth 6.5, 7.5, 8.5 and 9.5m for the borehole BGS3 and at depth 6, 7, 8 and 9m for borehole BGS4.

In general it is observed that pressures are reproduced reasonable well, however the displacements are qualitatively captured. In particular, the displacements calculated for the phase Gas 2 show a great difference with the measured displacements (Figure 56 & Figure 57). This could be a consequence of the adopted larger injection rate.

Also, a contour plot of pressure is drawn for each phase. In these plots it is observed that the Fracture is a preferential path of flows due to its large transmissivity.

In Figure 71 it is drawn the evolution of the degree of saturation of the Fracture at different distance from the injection borehole (BGS2) during the tests. It is observed that the Fracture desaturate during gas injection phases and it hydrate during water injection. And these phenomena are more evident for the length of the Fracture next to the borehole.

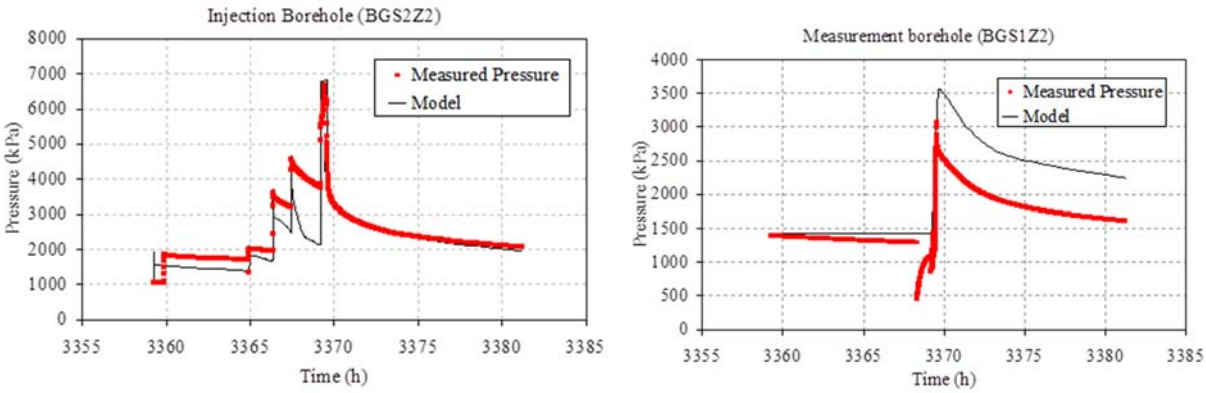

Figure 51 Comparison between numerical and experimental pressures at injection borehole BGS2 and at measurement borehole BGS1 for phase "Hydro2"

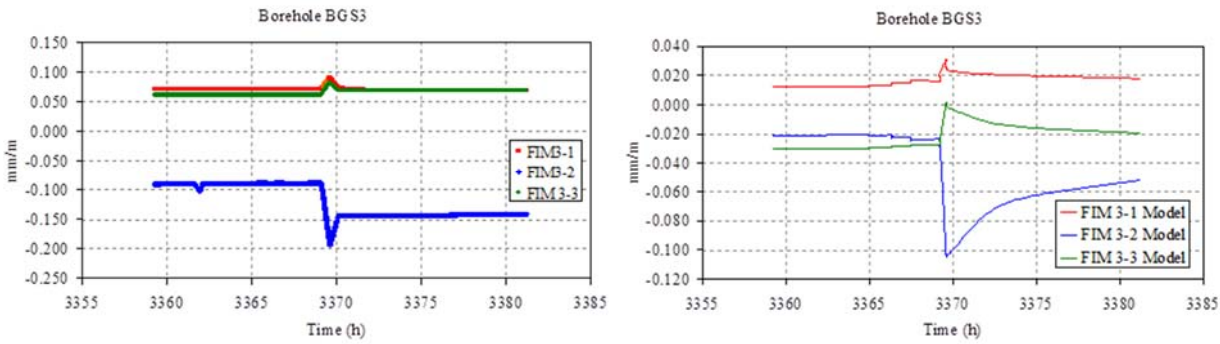

Figure 52 Displacement measured at BGS3 (left) and displacement calculated (right) for phase "Hydro2"

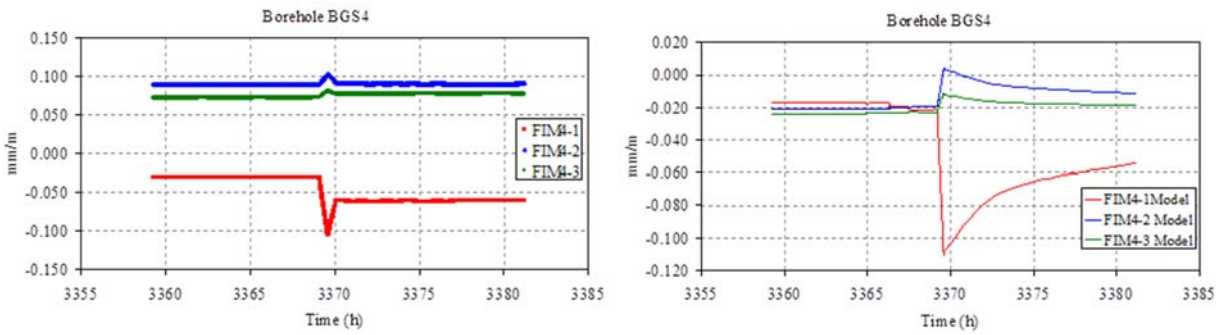

Figure 53 Displacement measured at BGS4 (left) and displacement calculated (right) for phase "Hydro2"

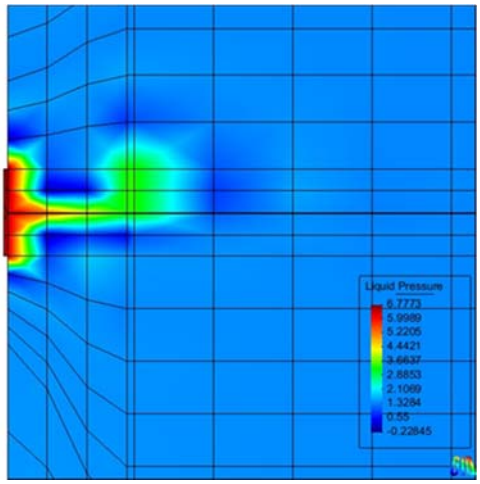

Figure 54 Contour plot of liquid pressure at time 3380 hours

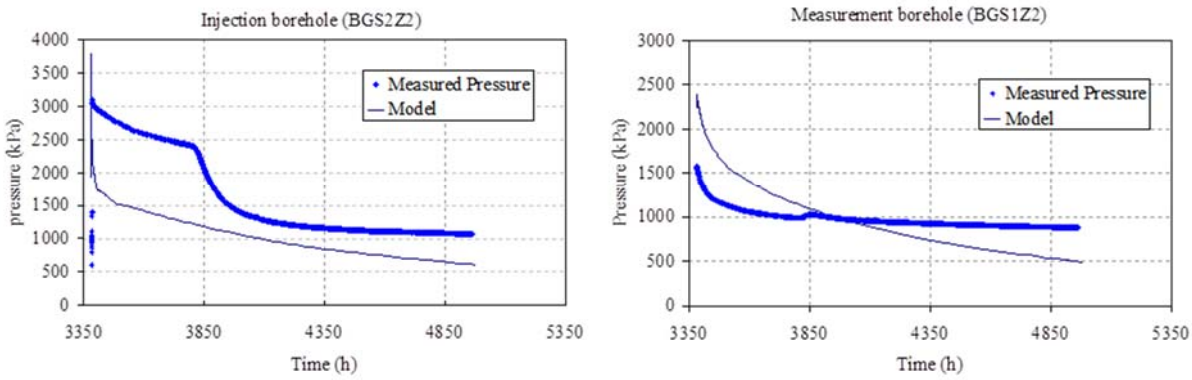

Figure 55 Comparison between numerical and experimental pressures at injection borehole BGS2 and at measurement borehole BGS1 for phase "Gas 2"

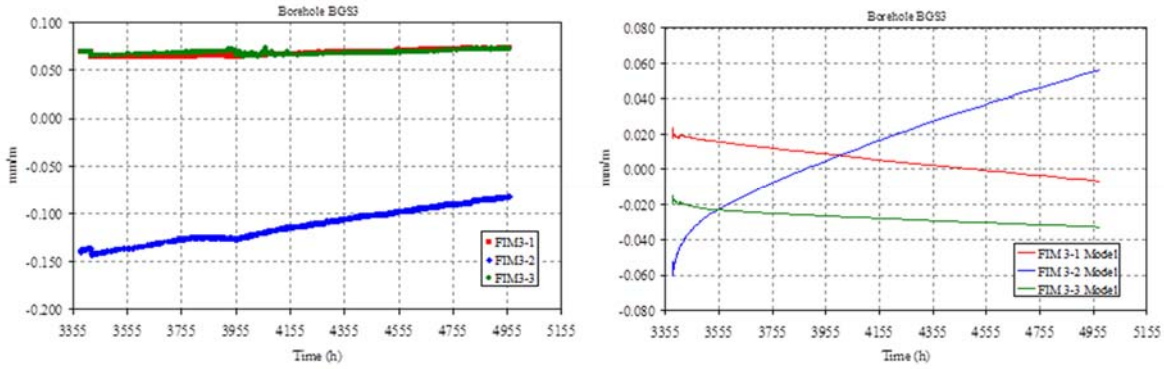

Figure 56 Displacement measured at BGS3 (left) and calculated (right) for phase "Gas2"

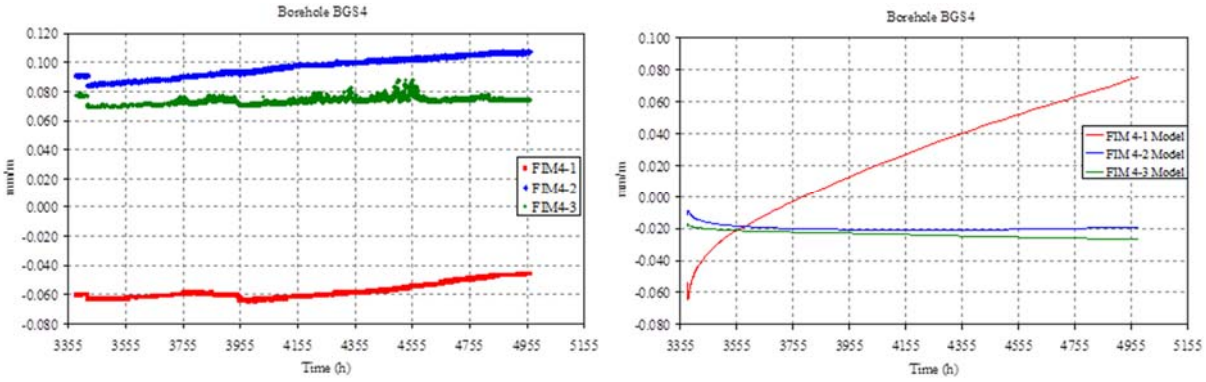

Figure 57 Displacement measured at BGS4 (left) and calculated (right) for phase "Gas2"

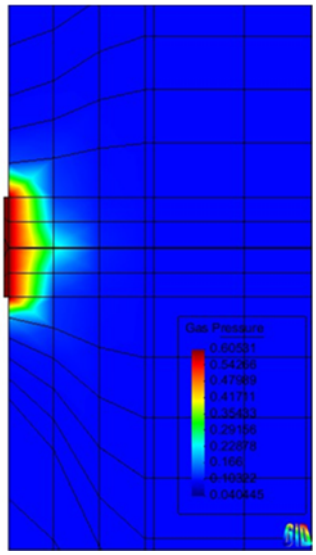

Figure 58 Contour plot of gas pressure at time 4964 hours

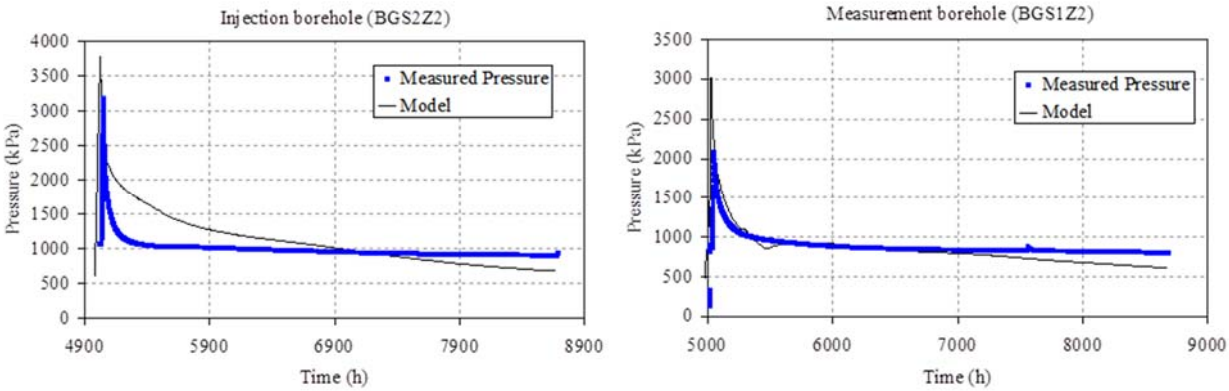

Figure 59 Comparison between numerical and experimental pressures at injection borehole BGS2 and at measurement borehole BGS1 for phase "Gas 3"

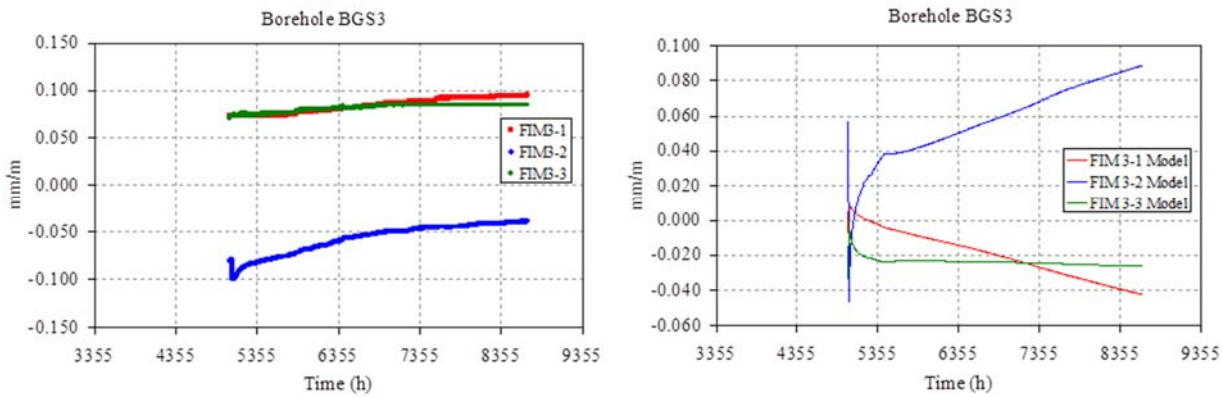

Figure 60 Displacement measured at BGS3 (left) and calculated (right) for phase "Gas 3"

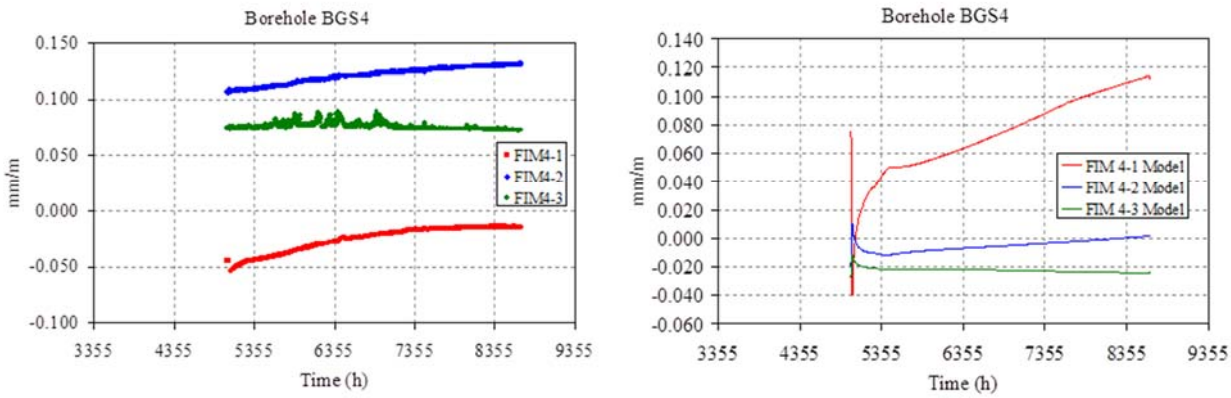

Figure 61 Displacement measured at BGS4 (left) and calculated (right) for phase “Gas 3”

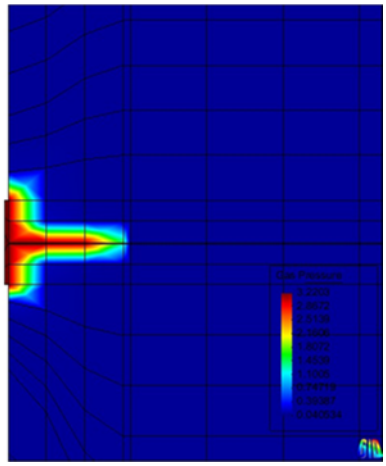

Figure 62 Contour plot of gas pressure at time 5029 hours

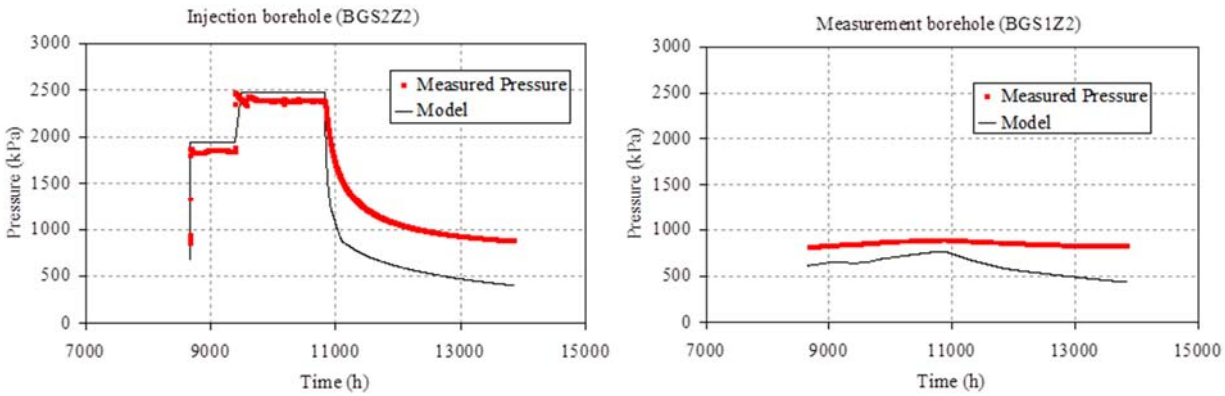

Figure 63 Comparison between numerical and experimental pressures at injection borehole BGS2 and at measurement borehole BGS1 for phase “Hydro 3”

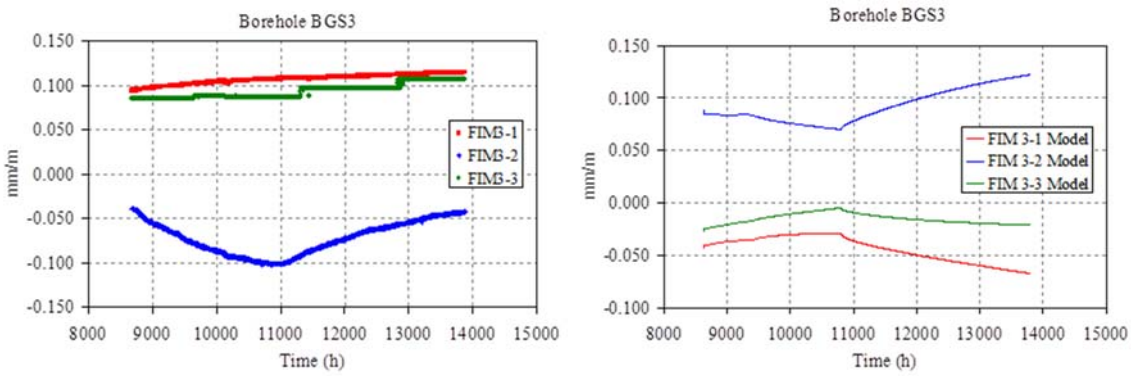

Figure 64 Displacement measured at BGS3 (left) and calculated (right) for phase "Hydro 3"

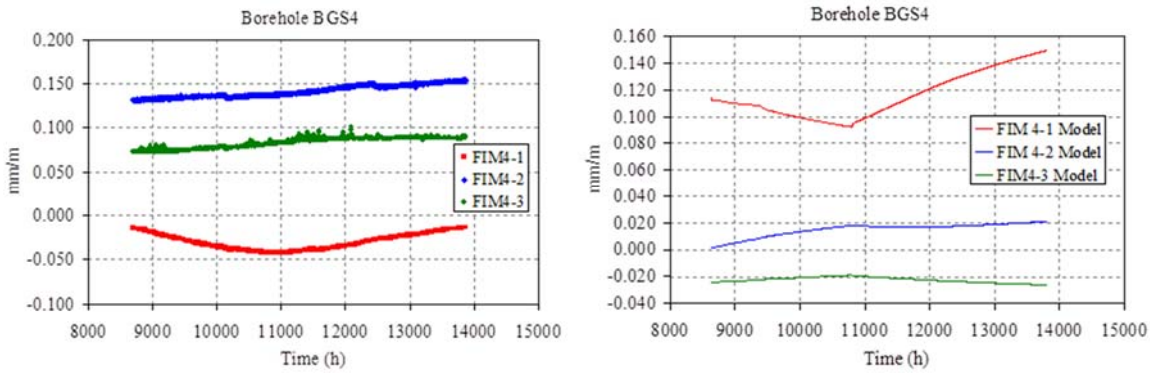

Figure 65 Displacement measured at BGS4 (left) and calculated (right) for phase "Hydro 3"

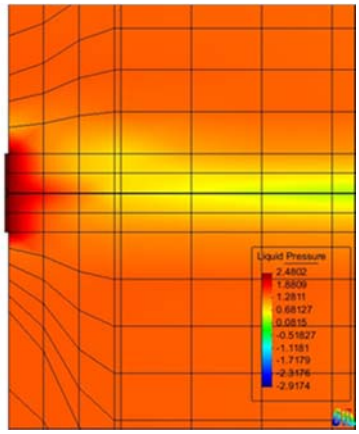

Figure 66 Contour plot of liquid pressure at time 10826 hours

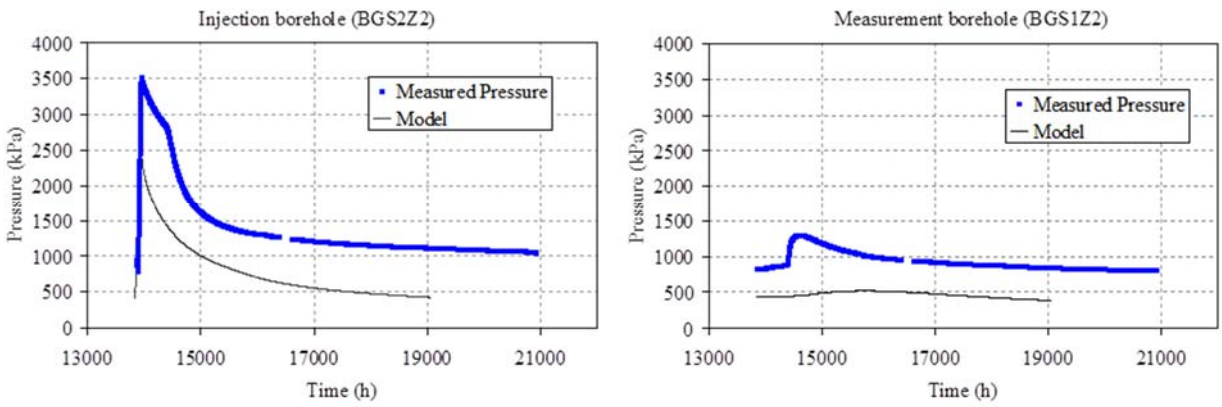

Figure 67 Comparison between numerical and experimental pressures at injection borehole BGS2 and at measurement borehole BGS1 for phase "Gas 4"

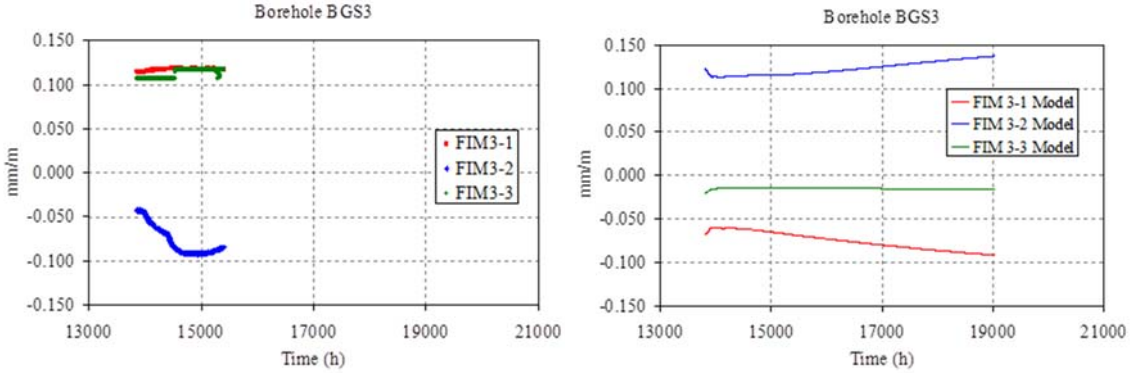

Figure 68 Displacement measured at BGS3 (left) and calculated (right) for phase "Gas 4"

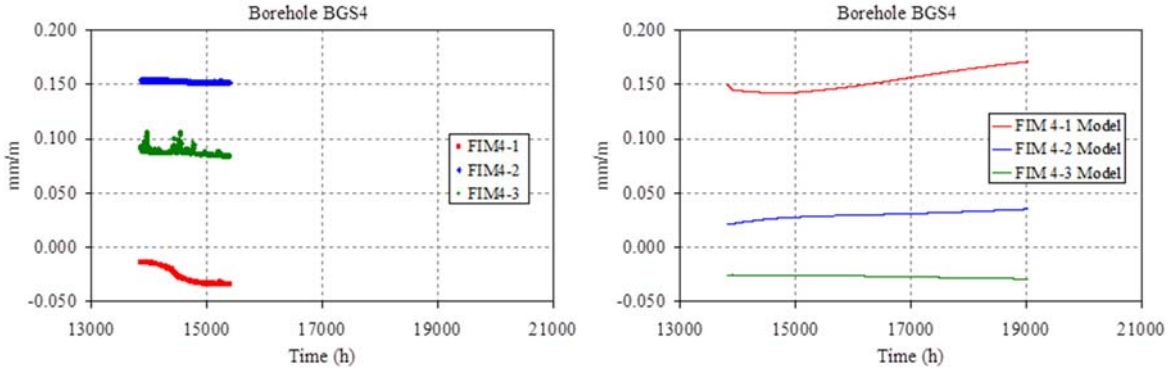

Figure 69 Displacement measured at BGS4 (left) and calculated (right) for phase "Gas 4"

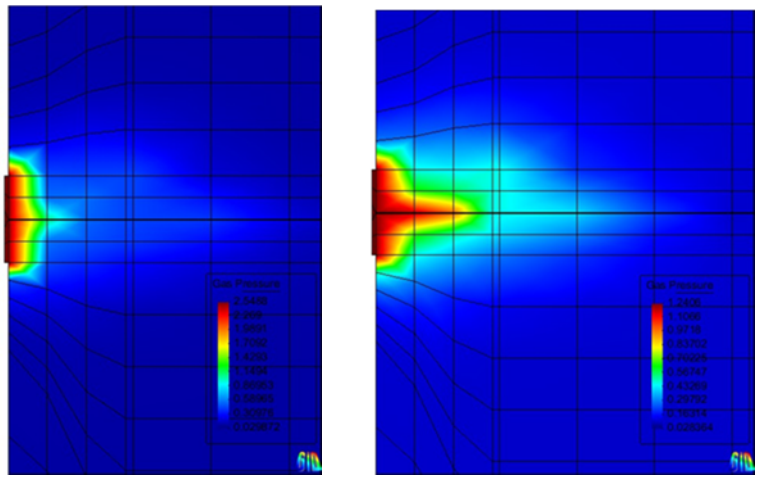

Figure 70 Contour plot of gas pressure at time 13936 hours (left) and at time 14611hours (right)

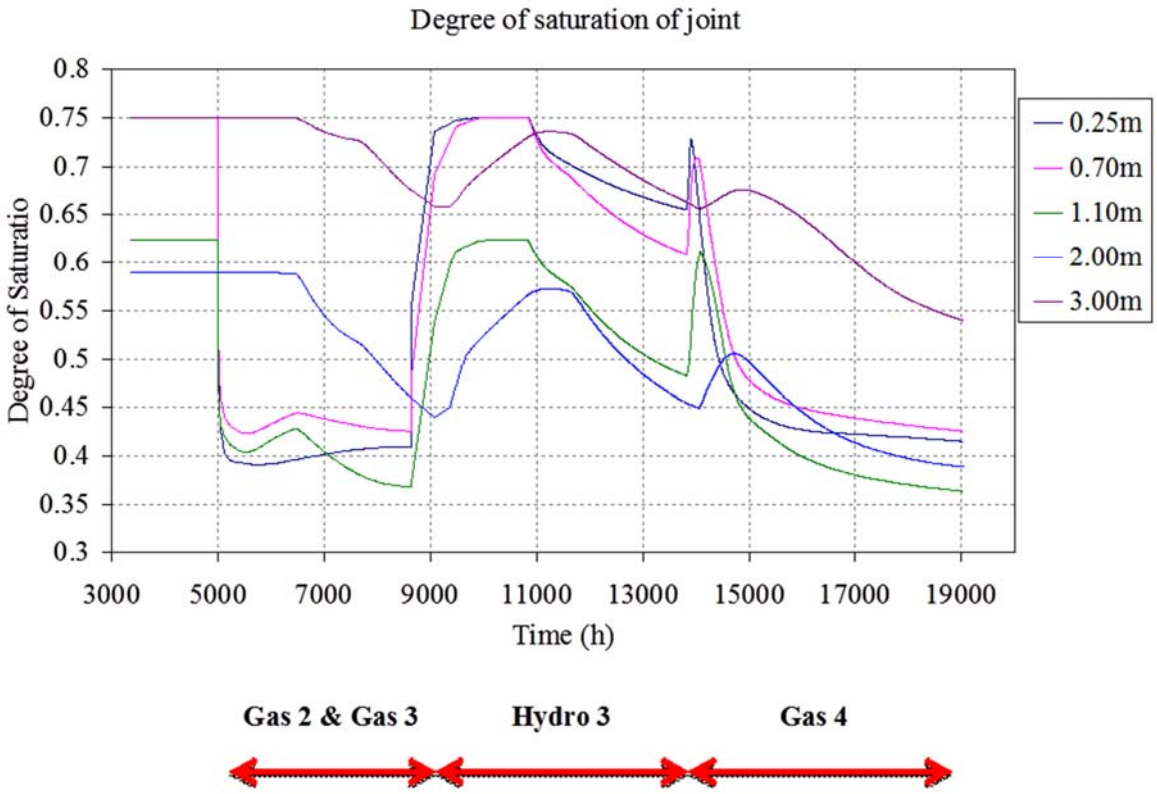

Figure 71 Degree of saturation of the Fracture at different distance from the injection borehole

3.1.2.3 CONCLUSIONS

From the comparison of the test results it is possible conclude that the evolution of pressure are well captured by the model. Displacements show an adequate tendency

It is recommended confirm the gas flow rate at phase Gas 2. Also, the variation of the permeability and compressibility of the Fracture should be analyzed during the test.

3.1.3 References

Barton N., Bandis S. & Bakhtar K. (1985), Strength, deformation and conductivity coupling of rock joints. Int. Journal of Rock Mechanics and Mining Science & Geomechanics Abst, 22(3):121–140

Enachescu C., Blüming, P., Castelao, A. & Steffen P. (2002) Mont-Terri GP-A and GS Experiments Synthesis Report, Interner Bericht 02-51.

Olivella, S. & Alonso, E. E. (2008). Gas flow through clay barrier. Geotechnique 58 No. 3, 157–176.

Sánchez, M. (2004), Thermo-hydro- mechanical coupled analysis in low permeability media. Ph.D. Thesis. Universitat Politècnica de Catalunya (UPC). 281 pp. Barcelona.

Van Genuchten, M. Th. (1980). A closed-form equation for predicting the hydraulic conductivity of unsaturated soils. Soil Sci. Soc.Am. J. 49, No. 9, 892–898.

3.2 Modelling of the HG-C and HG-D in situ tests in the Opalinus Clay of the Mont Terri rock laboratory (GRS)

3.2.1 Introduction

In order to study the process of gas migration in Opalinus Clay, Nagra has conducted several long-term in-situ tests at the Mont Terri Rock Laboratory, Switzerland. From 1999 to 2012, four

experiments have been carried out at the same site: The GP-A, GS, HG-C, and HG-D experiments, which used an array of four to five boreholes for fluid injection and monitoring.

In the GP-A experiment, a hydraulic fracture has been created. This fracture has been tested in the following GS experiment (Enachescu et al., 2002). From 2006 to 2009, after a period of possible self-sealing, the fracture has been re-tested in the HG-C experiment (Trick 2007, Rösli & Trick 2008). In order to investigate the behaviour of the undisturbed clay, a new borehole has been drilled for the HG-D experiment, approximately 1 metre below the expected location of the GP-A fracture. From 2009 to 2012, liquid and gas injection tests have been performed using the new bore hole.

In the framework of the FORGE project, GRS contributes to the analysis and interpretation of the HG-C and HG-D experiments by numerical modelling (work package 5, task 5.3.4). The main questions of this study are:

- Which models are able to reproduce the experimental observations?
- Do these models improve the understanding of gas flow in the clay host rock?

Two categories of models are used. The first category is based on the two-phase flow code TOUGH2/EOS7, which was written by the Lawrence Berkeley National Laboratory, Berkeley, USA (Pruess 1990, Pruess 1991, Pruess et al. 1999). This code was modified in order to introduce pathway dilation effects. The second category comprises simple models for gas flow, which are referred to as “tube-chamber models” in the following. These models describe the flow of gas in a tube, which is the connecting element between the injection interval and an air-filled chamber. Different properties can be attributed to the porous medium inside the tube. The tube-chamber models are used in addition to the two-phase flow code TOUGH2 to look for alternative explanations of the experimental phenomena.

A more detailed description of models and modelling results can be found in Navarro (2013).

3.2.2 Modelling

3.2.2.1 BASIS OF THE TOUGH2 SIMULATIONS

Two-phase flow simulations were only applied to the HG-C experiment because of the higher complexity of the phenomena in this experiment. All simulations using the multi-phase code TOUGH2 were based on the modelling grid displayed in Figure 72 and Figure 73. In Figure 72, the floor of the access shaft is represented by a blue horizontal rectangle on top of the picture. The boreholes are aligned perpendicular to the bedding plane. Due to the symmetry of the set-up only one half of the domain was modelled. All model boundaries are no-flow boundaries.

The pressure vessel and the piping were included in the model as a vertical column. The pressure vessel is represented by the upper part of the column, the piping by the lower part of the column. The piping was connected to interval 2 of BGS2 by an additional element connection. This connection is only present in the TOUGH2 grid description and cannot be seen in Figure 72.

Except for the injection interval (interval 2 of borehole BGS2) all packer intervals were represented by a single element (Figure 73) in order to reduce calculation time. The interval volumes visible in Figure 73 do not represent the actual volumes and were corrected in the TOUGH2 grid declaration.

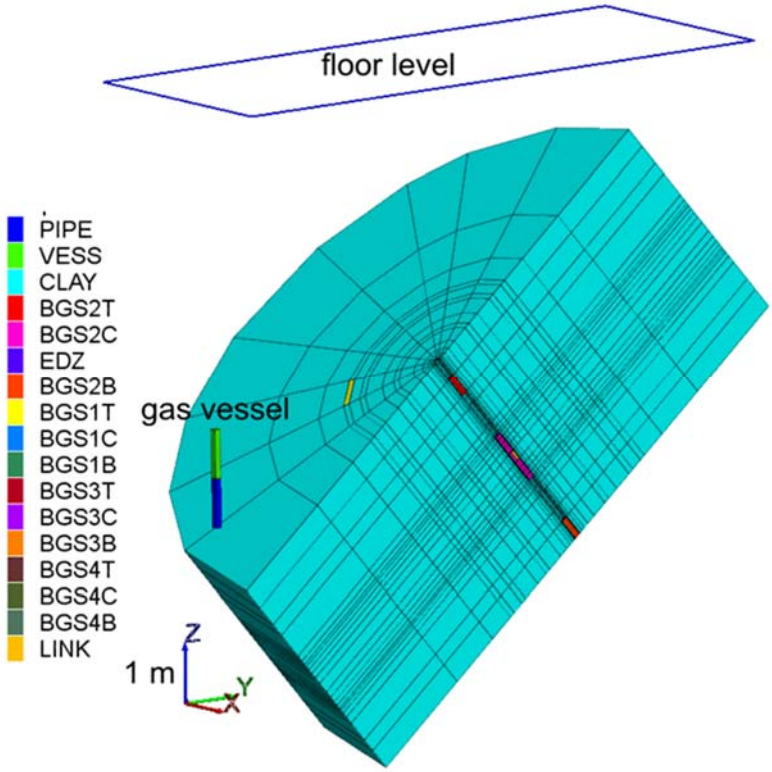

Figure 72 TOUGH2 modelling grid for the simulation of the HG-C experiment. – Key explanation: Letters T, C, and B appended to the borehole names stand for “top”, “center”, and “bottom”, respectively. Thus, BGS2B stands for interval 1 of BGS2.

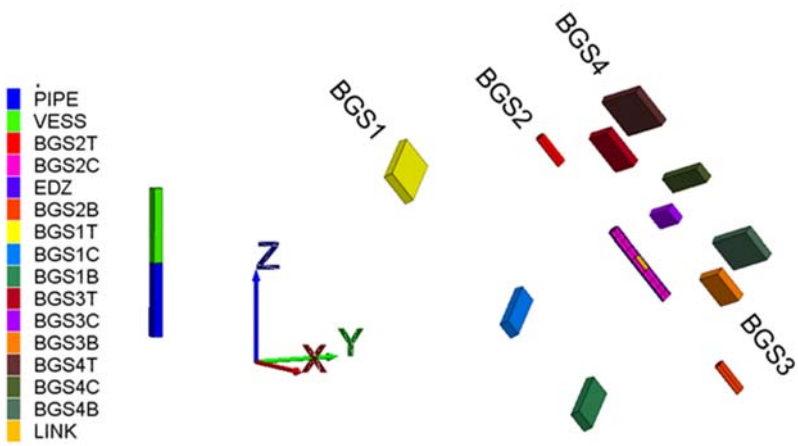

Figure 73 Same view as in the previous figure but without the clay rock.

A gas and a liquid phase were considered in the simulations (TOUGH2 was used in connection with the Equation-of-State module EOS7). The system contained the components water, vapour, and air. Gas diffusion and heat transport were neglected. A detailed description of the model parameters can be found in Navarro (2013).

We will now introduce the different models that were used to explain the phenomena of the HG-C and HG-D experiments.

3.2.2.2 VARIABLE PERMEABILITY MODEL (WATER INJECTION PHASE OF HG-C)

This model is a modified version of the TOUGH2 code. It is characterised by a pressure threshold above which permeability becomes pressure-dependent.

In TOUGH2, the flow F_β of phase β is determined by a generalised Darcy law

Equation 11:

$$F_\beta = -k \frac{k_{r,\beta}\rho_\beta}{\mu_\beta}(\nabla p_\beta - \rho_\beta g).$$

Here, k is the intrinsic and $k_{r,\beta}$ the relative permeability, ρ_β the density and μ_β the dynamic viscosity. g is the vector of gravitational acceleration and p_β the pressure of the phase. In the modified version of this equation, the relative permeability is multiplied by

Equation 12:

$$\frac{p - p_{\text{thr}}}{p_{\text{ref}} - p_{\text{thr}}}\left(\frac{k_{\text{ref}}}{k} - 1\right) + 1\,, \quad \text{with} \quad p_{\text{ref}} - p_{\text{thr}} \quad \text{and} \quad k_{\text{ref}} > k$$

if $p > p_{\text{thr}}$. (The relative permeability is modified instead of the intrinsic permeability in order to have the modification in the upstream-weighted term of the flux equation.) Mobility thus increases linearly above the pressure threshold p_{thr} so that

$$k_{\text{ref}} \frac{k_{r,\beta}}{\mu_\beta} \quad \text{at} \quad p = p_{\text{ref}}.$$

The relative permeability is only modified in the direction parallel to the bedding. It was assumed that the anisotropic fabric of the clay facilitates crack opening and propagation in this direction.

3.2.2.3 PATHWAY DILATION MODEL (GAS INJECTION PHASE OF HG-C)

In the HG-C experiment, gas injection was dominated by thresholds. According to Figure 74 the main gas entry event started on day 147 (pressure step HI5) with a precursory gas flow, which set in on day 100 (pressure step (HI4). This indicates that the initial threshold for the main gas entry ranged between 2.34 MPa and 3 MPa at the site. Since the standard TOUGH2 code failed to establish gas entry by displacement of water it seemed more likely that pressure-driven dilation of pathways was the main mechanism for gas entry.

As shown by Figure 75**Error! Reference source not found.**, gas was still injected on day 225 although the injection pressure had already dropped to 1.57 MPa, i. e. below the initial threshold for gas entry. If pathway dilation indeed was the main mechanism for gas entry then the process clearly had irreversible or at least hysteretic components.

In this study, models with pressure-dependent permeability, porosity and gas entry threshold were applied to the gas injection phase of the HG-C experiment. Yet, none of these models was capable of creating and maintaining a low pressure regime in the rock, which would allow for the observed long-lasting injection flow. This suggested the presence of an additional mechanism for pressure reduction inside the rock. These considerations gave rise to the formulation of a pathway dilation model, which introduces a pressure-dependent rate of porosity change ("dilation rate"). With a positive dilation rate, pressures are successively reduced in the rock due to an expansion of the contained gas phase. This allows the uptake of gas over long periods of time. The TOUGH2 code was extended to implement this pathway dilation model.

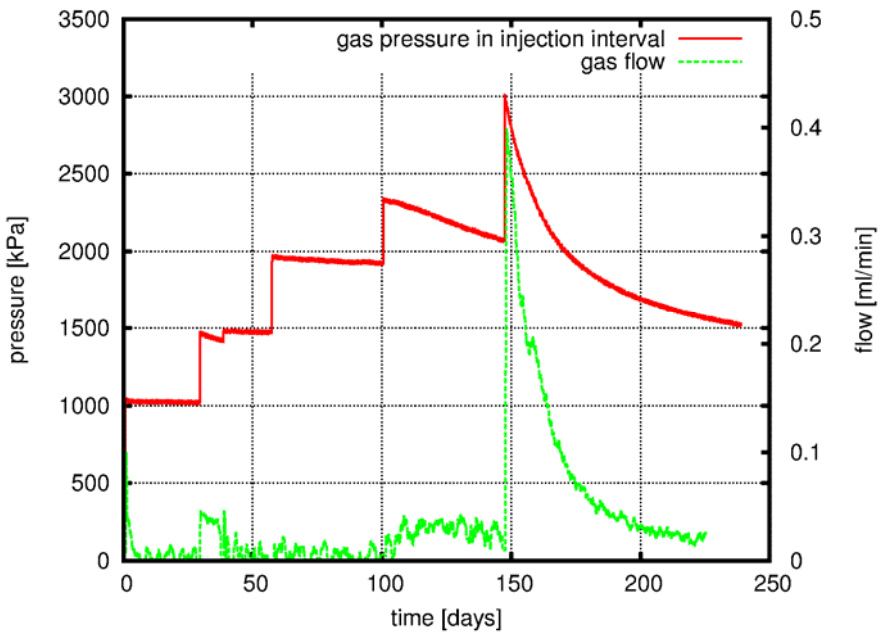

Figure 74 Measured injection pressures and injection flows (phase 2 of HG-C)

Our pathway dilation model assumes that micro cracks open in the rock if the pore pressure exceeds a certain pressure threshold while the aperture of the cracks depends on pore pressure.

The establishing crack network shall be divided into main flow paths and dead end branches (see Figure 75). The opening of dead end branches shall be a time-dependent relaxation process causing the mean porosity to increase with time. The macroscopic permeability shall be controlled by those parts of the crack network that constitute the main flow paths. Since the number of main flow paths shall not increase with time and crack apertures are in equilibrium with pressure, the macroscopic permeability is only pressure-dependent but not explicitly time-dependent. Therefore, permeability and porosity are independent in this crack network model. These considerations give rise to the following conceptual model:

- There is a threshold pressure p_{thr} below which the main flow paths are closed (but not necessarily the dead end branches). This makes the crack network impermeable.
- For a pore pressure $p > p_{\mathrm{thr}}$, the pressure threshold p_{thr} decreases from an initial value p_{thr}^{0} to a lower limit $p_{\mathrm{thr}}^{\mathrm{min}}$ with increasing pressure p (irreversible softening against microscopic tensile failure).
- Gas permeability is anisotropic and increases linearly with pressure difference $p - p_{\mathrm{thr}}$. There is no gas permeability if $p < p_{\mathrm{thr}}$.
- Porosity is variable and, in particular, time-dependent. Porosity change is governed by a "dilation rate" $d\phi_{\mathrm{dil}}/dt$, which increases linearly with $p - p_{\mathrm{thr}}$ and becomes zero for pressures below the current threshold pressure. This implies that, except for $p \leq p_{\mathrm{thr}}$, porosity grows steadily. Yet, the system equilibrates because the gas phase inside the pores expands due to the dilation of the rock causing a decrease of pore pressure. This process continues until the pore pressure reaches the threshold pressure p_{thr} so that the dilation process stops.

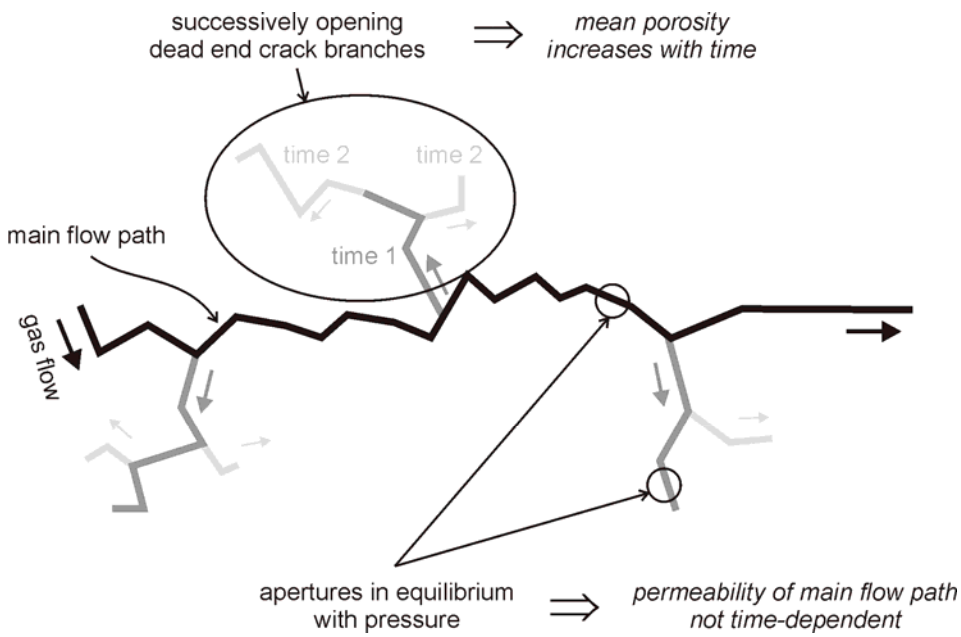

Figure 75 Conceptual model of the dilation process

The time-dependent increase of porosity reflects a time-dependent damage to the rock on the micro-scale. The model is only applicable for a low degree of damage and crack connectivity so that dead end crack branches can still exist. This should be reflected in porosities remaining well below 1 during the equilibration process.

It is likely that most of the pore water is not in direct contact with micro cracks. In order to avoid overestimation of phase interactions, the following simplifying assumptions were made: a) water is immobile, b) water is not compressible, c) no gas is dissolved in water. Also, the compressibility of the matrix was set to zero to clarify the effects of pathway dilation. With all these assumptions the system virtually is a one-phase flow system.

In the model, irreversible softening against microscopic tensile failure is achieved by reducing the threshold pressure p_{thr}. p_{thr}^{i} is the threshold pressure at time step i, with $i = 0$ at the beginning of the simulation. p_{thr}^{i} is defined by means of a pressure $\hat{p}_{\mathrm{thr}}$, which is the threshold pressure that would develop in undisturbed rock by applying pressure p:

Equation 13:

$$\hat{p}_{\mathrm{thr}} = \frac{p - p_{\mathrm{thr}}^{0}}{p_{\mathrm{soft}} - p_{\mathrm{thr}}^{0}}\left(p_{\mathrm{thr}}^{\min} - p_{\mathrm{thr}}^{0}\right) + p_{\mathrm{thr}}^{0} \quad \text{for} \quad p_{\mathrm{soft}} \geq p \geq p_{\mathrm{thr}}^{0}$$

$$\hat{p}_{\mathrm{thr}} = p_{\mathrm{thr}}^{\min} \quad \text{for} \quad p > p_{\mathrm{soft}}$$

$$\hat{p}_{\mathrm{thr}} = p_{\mathrm{thr}}^{0} \quad \text{for} \quad p < p_{\mathrm{thr}}^{0}\,.$$

$\hat{p}_{\mathrm{thr}}$ decreases from p_{thr}^{0} to $p_{\mathrm{thr}}^{\min}$ as p rises from p_{thr}^{0} to p_{soft}. An irreversible softening can now be introduced by

$$p_{\mathrm{thr}}^{i} = \min\left(p_{\mathrm{thr}}^{i-1}, \hat{p}_{\mathrm{thr}}\right).$$

The flow equation of TOUGH2 was replaced by the following equation in order to implement the effect of pathway dilation on the mobility of the gas phase:

Equation 14:

$$F_{\text{gas}} = -\left(\underbrace{\frac{\rho_{\text{gas}}}{\mu_{\text{gas}}} k\, k_{\text{r,gas}} \mathbf{I}}_{\substack{\text{determines the gas flux} \\ \text{in the original pore space}}} + \underbrace{\frac{\rho_{\text{gas}}}{\mu_{\text{gas}}} \mathbf{K}_{\text{dil}} k_{\text{dil}}}_{\substack{\text{determines the gas flux} \\ \text{in the additional pore space} \\ \text{created by pathway dilation}}} \right) (\nabla p_{\text{gas}} - \rho_{\text{gas}} g).$$

Here, k is the intrinsic and $k_{\text{r,gas}}$ the relative gas permeability, ρ_{gas} is the density, μ_{gas} the dynamic viscosity of the gas phase, and g the vector of gravitational acceleration. k_{dil} is a pressure-dependent gas permeability of dilated pathways. The tensor $\mathbf{K}_{\text{dil},i}$ introduces anisotropy. The two terms in the large brackets, which determine the gas flow in the orginal pore space and in the pore space gained by pathway dilation, can be weighted separately in the spatially discretised equation. The term for the dilated pores is always upstream-weighted.

The permeability of the pore space gained by dilation k_{dil} was defined by the relationship

Equation 15:

$$k_{\text{dil}} = (p - p^i_{\text{thr}}) C_1 \quad \text{for} \quad p \geq p^i_{\text{thr}}$$

where C_1 is a calibration parameter. If the pressure is below the threshold pressure, k_{dil} is zero.

Porosity ϕ was defined as the sum of the initial porosity ϕ_0 and the porosity gained by dilation ϕ_{dil}:

Equation 16:

$$\phi = \phi_0 + \phi_{\text{dil}} \quad \text{with} \quad \phi_{\text{dil}} = 0 \quad \text{for} \quad t = 0.$$

ϕ_{dil} is called "secondary porosity" in the following. The change of ϕ_{dil} is controlled by the equation

Equation 17:

$$\frac{d\phi_{\text{dil}}}{dt} = (p - p^i_{\text{thr}}) C_2 \quad \text{for} \quad p \geq p^i_{\text{thr}}.$$

If the pressure is below the threshold pressure, $\frac{d\phi_{\text{dil}}}{dt}$ is set to zero. The pathway dilation model is now parameterised by the six parameters $C_1, C_2, p^0_{\text{thr}}, p^{\text{min}}_{\text{thr}}, p_{\text{soft}}$, and $\mathbf{K}_{\text{dil},}$.

In order to achieve a 1-phase flow system, water was immobilised by setting the permeability of the original pore space k to zero. A flow of gas can therefore only establish itself by pathway dilation.

In order to eliminate gas storage by processes other than pathway dilation, the density of water was kept constant and the solubility of the gas component in the liquid phase was set to zero. This way, neither water compression nor gas dissolution can take place.

3.2.2.4 MODELS WITH INCREASED PHASE INTERACTION (GAS INJECTION PHASE OF HG-C)

Two model variants were derived from the pathway dilation model in order to investigate the effects of processes that provide additional gas storage inside the rock. The "water compression model" was yielded by turning on water compression in the pathway dilation model. The "gas dissolution model" was derived from the pathway dilation model by turning on gas dissolution. Dissolving gas means that gas can be stored with increasing pressure and is again released with

decreasing pressure. Both models assume that the interface between liquid and gas phase in the rock is large enough to produce considerable phase interactions like water compression or gas dissolution.

3.2.2.5 TUBE-CHAMBER MODEL 1 (GAS INJECTION PHASE OF HG-C)

In the pathway dilation model described before, a pressure-dependent injection flow can be created by introducing a pressure-dependent dilation rate of the rock. However, other ways of introducing a pressure-dependent injection flow should be possible. For example, a similar behaviour could be achieved by using a remote air-filled chamber which is charged with gas by the injection interval. The magnitude of the injection flow would then depend on the pressure difference between chamber and injection interval. These considerations provided the impulse for the development of the tube-chamber models.

The tube-chamber model is a simple representation of a preferential pathway which is connected to an air filled chamber. The connection between both is established by a tube, which contains a porous medium. The chamber might be a remote borehole or some drained part of the rock or of a fracture. Figure 76 shows the principal set-up. There is no liquid in the entire system. If the gas pressure inside the injection interval exceeds that of the chamber, gas is pressed through the tube and into the chamber. Consequently, the chamber pressure increases. The following description applies to the tube-chamber model that was used to simulate the gas injection phase of HG-C. (A modified version was used for the gas injection phase of HG-D.)

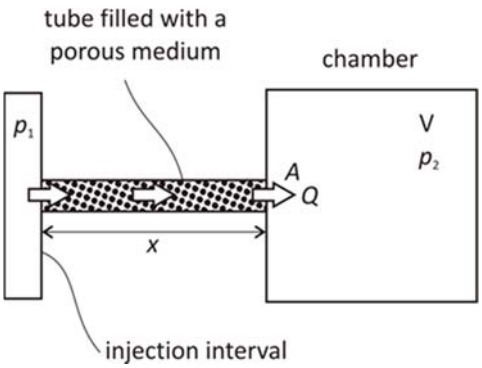

Figure 76 Sketch of the tube-chamber model for gas flow.

A pressure, density, and viscosity gradient will evolve along the tube if there is a pressure difference between the injection interval and the chamber. In order to simplify the description of the system it was assumed that the flow of gas through the tube can be described by Darcy's law using an effective pressure gradient, density and viscosity. If p_1 is the pressure of the injection interval and p_2 the chamber pressure the effective pressure gradient shall be

Equation 18:

$$\frac{p_1 - p_2}{x}.$$

The effective gas density inside the tube was assumed to be the density of an ideal gas at the mean pressure:

Equation 19:

$$\rho_{\text{eff}} = \frac{p_1 + p_2}{2}\frac{M}{RT}.$$

With this approximation and by introducing effective values also for the permeability and viscosity Darcy's law for the mass flow of gas through the chamber takes the form

Equation 20:

$$Q = \frac{k_{\text{eff}}(p, p_{\text{thr}}) A \rho_{\text{eff}}}{\mu_{\text{eff}}} \cdot \frac{p_1 \quad p_2}{x},$$

Here, k_{eff} is the pressure dependent permeability of the porous medium in the tube, A is the cross sectional area of the tube, μ_{eff} the effective dynamic viscosity of gas, and x the distance between injection interval and chamber.

A pressure threshold p_{thr}^i for gas flow was introduced. p_{thr}^i is the threshold pressure at time step i with $i = 0$ at the beginning of the simulation. The effective permeability k_{eff} of the porous medium was defined by

Equation 21:

$$k_{\text{eff}} = (p_1 - p_{\text{thr}}^i) C_1 \quad \text{for} \quad p_1 \geq p_{\text{thr}}^i \qquad \text{and} \qquad k_{\text{eff}} = 0 \quad \text{for} \quad p_1 < p_{\text{thr}}^i.$$

Using this definition, the equation for mass flow reads

Equation 22:

$$Q = (p_1 - p_{\text{thr}}^i)(p_1{}^2 - p_2{}^2) \frac{C_1 A\, M}{2\, \mu_{\text{eff}}\, x\, RT} \qquad \text{for} \qquad p_1 \geq p_{\text{thr}}^i$$

with $Q = 0$ for $p_1 < p_{\text{thr}}^i$. The volumetric flow for $p_1 \geq p_{\text{thr}}^i$ at reference pressure p_{ref} and reference temperature T_{ref} can now be calculated by

Equation 23:

$$Q_{\text{vol}} = Q \frac{RT_{\text{ref}}}{Mp_{\text{ref}}} = (p_1 - p_{\text{thr}}^i)(p_1{}^2 - p_2{}^2) \frac{C_1 A\, T_{\text{ref}}}{2\, \mu_{\text{eff}} \quad x\, Tp_{\text{ref}}}$$

With the fitting parameter

Equation 24:

$$c = \frac{C_1 A\, T_{\text{ref}}}{2\, \mu_{\text{eff}} \quad x\, Tp_{\text{ref}}}$$

the formulation of the volumetric flow simplifies to

Equation 25:

$$Q_{\text{vol}} = (p_1 - p_{\text{thr}}^i)(p_1{}^2 - p_2{}^2) c.$$

A pressure-dependent softening of the porous medium was described by reducing the threshold pressure with increasing interval pressure. A pressure $\hat{p}_{\text{thr}}$ was introduced in order to calculate the threshold pressure p_{thr}^i. p_{thr}^i is the reduced threshold pressure that would develop in undisturbed rock by applying the injection pressure p_1:

Equation 26:

$$\hat{p}_{\text{thr}} = \frac{p_1 - p_{\text{thr}}^0}{p_{\text{soft}} - p_{\text{thr}}^0} (p_{\text{thr}}^{\text{min}} - p_{\text{thr}}^0) + p_{\text{thr}}^0 \qquad \text{for} \qquad p_{\text{soft}} \geq p_1 \geq p_{\text{thr}}^0$$

$$\hat{p}_{\text{thr}} = p_{\text{thr}}^{\text{min}} \qquad \text{for} \qquad p_1 > p_{\text{soft}}$$

$$\hat{p}_{\text{thr}} = p_{\text{thr}}^0 \qquad \text{for} \qquad p_1 < p_{\text{thr}}^0 .$$

Softening was then introdruced by

Equation 27:

$$p_{\text{thr}}^i = \min(p_{\text{thr}}^{i-1}, \hat{p}_{\text{thr}}) .$$

By setting the mass flux equal to the mass increase inside the chamber, the rate of pressure change inside the chamber was calculated using the ideal gas law:

Equation 28:

$$\frac{dp_2}{dt} = Q_{\mathrm{vol}} \frac{T\, p_{\mathrm{ref}}}{T_{\mathrm{ref}} V}.$$

Here, V is the volume of the chamber. The initial condition $p_2(t = 0) = p_{2,\mathrm{ini}}$ was used.

3.2.2.6 TUBE-CHAMBER MODEL 2 (GAS INJECTION PHASE OF HG-D)

A second tube-chamber model was defined to simulate phase 2 of the HG-D experiment. The main difference to tube-chamber model 1 is the lack of pressure thresholds for gas flow. The permeability of the tube is constant.

We used the same formulation for the effective pressure and effective gas density as in tube-chamber model 1 and introduced effective values also for the permeability and viscosity. Herewith, Darcy's law for the mass flow of gas through the chamber can be calculated by

Equation 29:

$$Q = \frac{kA\rho_{\mathrm{eff}}}{\mu_{\mathrm{eff}}} \cdot \frac{p_1 - p_2}{x} = \frac{kAM}{2\mu_{\mathrm{eff}} xRT} \cdot (p_1{}^2 - p_2{}^2).$$

In this equation, k is a constant permeability of the porous medium in the tube. The volumetric flow at reference pressure p_{ref} and reference temperature T_{ref} was then calculated by

Equation 30:

$$Q_{\mathrm{vol}} = Q \frac{RT_{\mathrm{ref}}}{Mp_{\mathrm{ref}}} = \frac{kA\, T_{\mathrm{ref}}}{2\, \mu_{\mathrm{eff}}\ \ x\, Tp_{\mathrm{ref}}} (p_1{}^2 - p_2{}^2)$$

Gas flow leads to a pressure change inside the chamber which can be determined using the ideal gas law:

Equation 31:

$$dp_2 = \frac{RT}{MV} dm = \frac{RT}{MV} Qdt.$$

with $p_2(t = 0) = p_{2,\mathrm{ini}}$ as initial condition. This leads to

Equation 32:

$$\frac{dp_2}{dt} = \frac{kA}{2\mu_{\mathrm{eff}}\ xV} (p_1{}^2 - p_2{}^2)$$

By introducing the fitting parameter

Equation 33:

$$d = \frac{kA}{2\mu_{\mathrm{eff}}\ V}$$

the equations for volumetric flow and pressure change simplify to

Equation 34:

$$Q_{\mathrm{vol}} = \frac{d\, T_{\mathrm{ref}}}{Tp_{\mathrm{ref}}} (p_1{}^2 - p_2{}^2) \qquad \text{and} \qquad \frac{dp_2}{dt} = \frac{d}{V} (p_1{}^2 - p_2{}^2).$$

3.2.3 Results

3.2.3.1 RESULTS FOR THE WATER INJECTION PHASE OF HG-C

Using the variable permeability model, parameter fits were conducted with respect to injection pressures and injection flows. The gas volume in the pressure vessel was used as an additional fitting parameter. Good curve fits were found using the following parameters Table 13:

Table 13 Parameters used

intrinsic clay permeability	7.4 E-20 m² || bedding plane, 7.4 E-21 m² ⊥ bedding plane.
Initial gas volume of the pressure vessel	5 liters
$\boldsymbol{p}_{\mathrm{thr}}$	5 MPa
$\boldsymbol{p}_{\mathrm{ref}}$	6 MPa
$\boldsymbol{k}_{\mathrm{ref}}$	5 E-18 m²

The simulated injection pressures and injection flows were plotted in Figure 77 and Figure 78, respectively, together with the measured values. Both plots display a good curve fit. This especially applies to the highest pressure step, for which no calibration could be achieved in this study by using the original TOUGH2 code. The curve fits for the following two pressure steps are of minor quality which indicates the existence of irreversible or hysteretic processes.

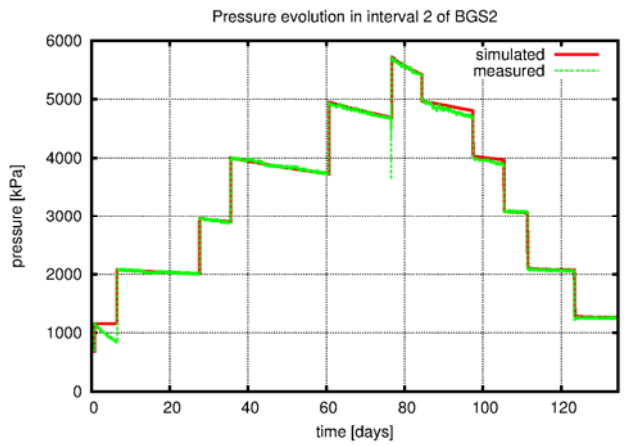

Figure 77 Injection pressures in the water injection phase of the HG C experiment

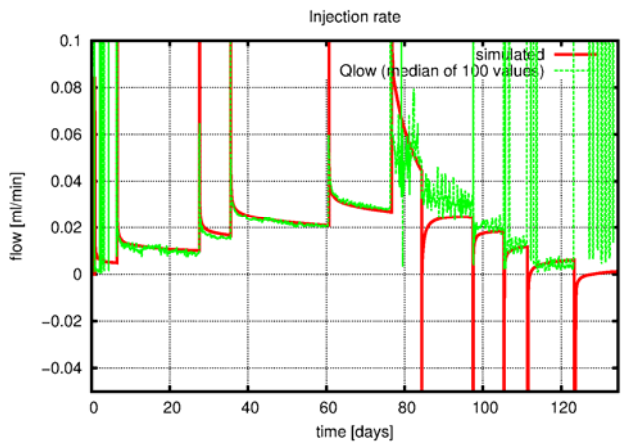

Figure 78 Injection flows in the water injection phase of the HG C experiment

3.2.3.2 RESULTS FOR THE GAS INJECTION PHASE OF HG-C

The dilation model was calibrated with the aim to fit the measured flow data. Satisfactory fits were achieved with the following two parameter sets (Table 14):

Table 14 Parameter set 1 and 2

	parameter set 1	**parameter set 2**
$\boldsymbol{C_1}$	2,1E-27 m²/Pa	1.6 E-27 m²/Pa
$\boldsymbol{C_2}$	5E-17 $sec^{-1}Pa^{-1}$	1 E-15 $sec^{-1}Pa^{-1}$
$\boldsymbol{p}^{\mathbf{0}}_{\mathrm{thr}}$	2,35 MPa	2,35 MPa
$\boldsymbol{p}^{\mathrm{min}}_{\mathrm{thr}}$	1,1 MPa	1,1 MPa
$\boldsymbol{p}_{\mathrm{soft}}$	2,4 MPa	2,4 MPa
$\mathrm{K}_{\mathrm{dil}}$	$(1, 1, k_3)$ with $k_3 = 0.1$	$(1, 1, k_3)$ with $k_3 = 0.1$

The simulated and measured flows were plotted in Figure 79 and Figure 80 for set 1 and set 2, respectively. In the experiment, a small flow of gas has been detected between day 100 and day 146, which was not reproduced by the simulations. However, there is good agreement between the measured and simulated values after day 147.

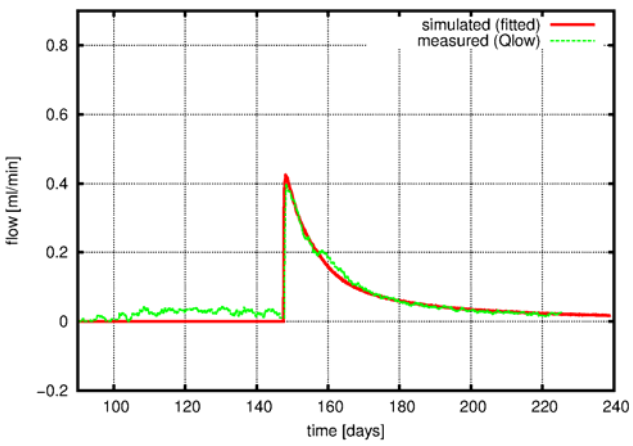

Figure 79 Measured and simulated injection flows (parameter set 1)

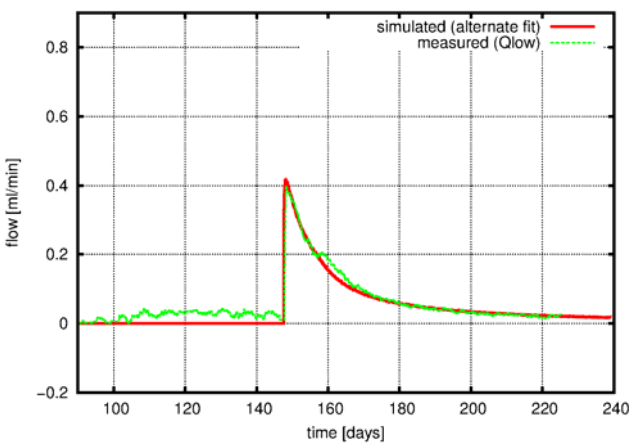

Figure 80 Measured and simulated injection flows (parameter set 2)

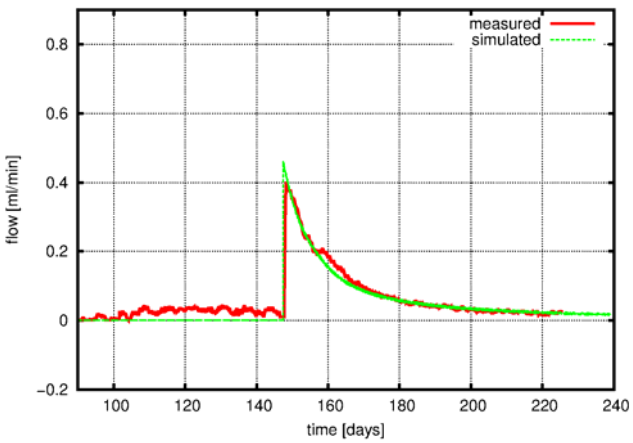

Figure 81 Measured flows and flows simulated with the tube-chamber model

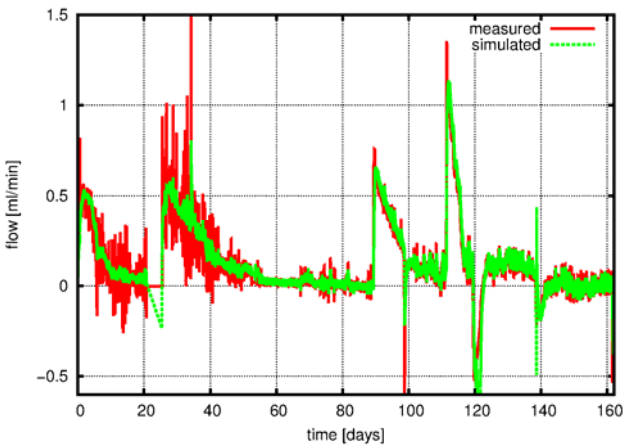

Figure 82 Calculated and measured flow for the gas injection phase of the HG D experiment

For both parameter sets, the porosity evolution indicated that the dilation zone grows to its final width in a very short time (without Figure). The width of the dilation zone was controlled by the pressure gradient in the clay. As soon as the pressure threshold was locally, the threshold was reduced (softening) and dilation commenced with a pressure dependent dilation rate. Due to dilation the gas phase expanded and the pressure decreased. As soon as the pressures reached the threshold pressure, dilation stopped and the gas phase was shut-in at the threshold pressure.

A principal difference between the two parameter sets that produced good fits was the width of the dilation zone. For set 1, the dilation zone had a width of approx. 1 m whereas for set 2 the width ranged between 10 cm and 30 cm. Both parameter sets which were able to deliver good fits of the gas flow. This implies that the flow data itself is not sufficient to determine the geometry of the dilation zone uniquely.

The gas injection phase of the HG-D experiment was also simulated using the tube-chamber model 1. Model calibration yielded the following parameter values (Table 15)

Table 15: parameters for HG-D experiment

c	5.0E-28 m^3 s Pa^{-3}
$p_{2,ini}$	0.7 MPa
p_{thr}^{0}	2.35 MPa
p_{thr}^{min}	1.1 MPa
p_{soft}	2.4 MPa
V	0.004 m^3 = 4 l
T	21 °C
T_{ref}	21 °C
p_{ref}	0.1 MPa

The simulated and measured flows are displayed in Figure 81 showing a good agreement between both curves. It was shown that the injection flow is insensitive against changes of the chamber volume" V" if the volume is larger than 4 litres (see Navarro, 2013). The chamber volume of 4 litres appeared to be minimum volume for which good fits can be achieved.

3.2.3.3 RESULTS FOR THE GAS INJECTION PHASE OF HG-D

A calibration of tube-chamber model 2 with regard to the measured injection flows yielded the following parameter values (Table 16):

Table 16: parameters for tube-chamber model 2

d	6.0E-14 m^3 s Pa
V	0.002 m^3 = 2 l
T	21 °C
T_{ref}	21 °C
p_{ref}	0.1 MPa

The simulated flows are displayed in Figure 82 together with the flow measurements. There is a remarkable agreement between both curves indicating that there is no threshold for gas flow in the HG-D experiment.

3.2.4 Discussion

3.2.4.1 Successful modelling approaches

Different numerical models were presented that were able to accurately reproduce the injection flows measured in the HG-C and HG-D experiments. The variable permeability model was able to simulate the water injection phase of HG-C. For the gas injection phase of the same experiment, the pathway dilation model provided satisfying results. Another model that was successful to simulate the gas injection phase of HG-C was the tube-chamber model, which also proved to be sufficient for the simulation of the gas injection phase of the HG-D experiment. However, the fact that different models were needed to simulate the water and gas injection phase of the HG-C experiment indicates that a universal model for water and gas injection still has to be found.

The study points out that simple modelling approaches are able to reproduce the main aspects of the water and gas injection experiments under study. The simplifications used in the models include single-phase flow, homogeneous distribution of dilating cracks and the omission of a coupled simulation of flow, stress, and strain evolution. The possibility to omit detailed hydro-mechanical coupling is surprising in view of the well-known importance of hydro-mechanical interactions for gas migration at high pressures. Gerard et al. (2012), for instance, have stated the need for a strong hydro-mechanical coupling to reproduce the development of preferential pathways in samples of Callovo-Oxfordian argillite. The applied models showed that the mechanical processes in the experiments were simple enough to be approximated by time- and pressure-dependent relations for porosity and permeability. This shows that coupled hydro-mechanical modelling is not always mandatory for processes with hydro-mechanical interactions.

3.2.4.2 Deriving system properties

The fact that two models reproduced the flow measurements of the HG-C experiment shows that there is no unique physical interpretation of the gas injection phase of the HG-C experiment. The applied tube-chamber model postulates that the injected gas finds its way to a remote air-filled space. This space might be a borehole or some part of the rock that could have been drained during the previous GS-experiment. The pathway dilation model suggests another mechanism. In this model, gas injection is caused by a certain rate of porosity increase inside the rock. A possible reason for such a time-dependent porosity increase is a gradual opening of dead-end crack branches that increases the mean porosity in the clay rock.

This clearly shows that the success of a model to reproduce experimental data does not automatically imply physical correctness and improvement of system understanding. Experimental phenomena may as well be matched by models that are physically incorrect. The two models – the pathway dilation model and the tube chamber model – that were able to provide agreeable fits for the gas injection phase of HG-C cannot both be correct at the same time.

Understanding a system by modelling is difficult if more than one model matches the experimental data. Yet, even then it may be possible to unravel the processes if there are common aspects which run through all models like a red line. The commonalities or invariants of the models likely reflect a feature of the system. The pathway dilation model and tube-chamber model 1, which were used to simulate the gas injection phase of the HG-C experiment, share the following features:

1. There was no water flow in any of the two models. Also, gas and liquid phase did not interact. (Tube-chamber model 1 does not contain any water and the pathway dilation model does not consider water flow, water compression, or gas dissolution.) It should be noted that

models that included water compression and gas dissolution did not manage to fit the experimental data in this study.

2. A threshold pressure has to be exceeded in order to trigger gas injection.

3. Once triggered, gas flow persisted even if the injection pressure fell below the initial threshold pressure for gas flow. This "softening" of the material against microscopic tensile failure was described in both models by a lowering of threshold pressures. The same mathematical formulation and the same and threshold-related parameter values were used in this respect.

4. In the pressure regime for the assumed process of pathway dilation, the injection flow was approximately proportional to the injection pressure minus the threshold pressure. The pathway dilation model generates this flow behaviour by introducing a pressure-dependent dilation rate whereas tube-chamber model 1 generates it by a Darcy flow to a distant chamber or cavity.

Assuming that these aspects indeed reflect properties of the system, the following two conclusions can be drawn for the gas injection phase of HG-C. Firstly, the system is virtually a single-phase flow system with minor interactions between the liquid and gas phases. For example, gas flow does not need to displace water as would be the case in the classical two-phase flow theory. Secondly, gas flow is dominated by pressure thresholds, which are amenable to quantification.

3.2.4.3 Interpreting thresholds

The HG-C experiment was regarded as the main resource for the investigation of the flow system. The following thresholds were observed here:

- a threshold of 5 MPa above which water injection was facilitated,
- a threshold of 2.35 MPa for initial gas injection,
- a shut-in threshold of 1.1 MPa for the gas injection phase.

Caution is advised with regard to the HG-D experiment because no flow threshold was observed here. This is unusual for clay rock and might indicate an artefact. Although no flow threshold could be detected in the gas injection phase of the HG-D experiment, a sudden pressure response was noticed in interval 1 of borehole BGS1 as the injection pressure reached a value of 2.3 MPa. This pressure corresponds to the threshold pressure for gas injection during the HG-C experiment.

It is interesting to compare the noticed threshold pressures to the threshold pressures that have been observed at the same site in the GP-A and GS experiments[2] [3]:

- In the GS experiment, the threshold for fracture re-opening by water injection was 4 MPa (phase "hydro 2"). This pressure is lower than the re-opening threshold of 5 MPa that was

[2] Enachescu et al. (2002) related these thresholds to the opening or closure of a fracture.

noticed in the water injection phase of HG-C. The higher value may indicate that mechanical healing took place in the time between the two experiments.

- In all experiments, pressures for fracture opening were higher than for fracture closing both for water and gas injection (phases “hydro 3” and “gas 3” of the GS experiment and phase 2 of the HG-C experiment). Possibly, fracture asperities have introduced a frictional resistance against fracture opening or closure.
- There is a remarkable match between the gas injection thresholds of about 2.350 MPa observed at HG-C and HG-D and the fracture opening threshold of 2.350 MPa that has been noticed in phase “gas 3” of the GS experiment during the injection of gas into the drained fracture.

All in all, there seem to be two threshold levels for the fractured rock at the site: One at 2.35 MPa for gas injection and another at about 4 MPa to 5 MPa for water injection. It is interesting to relate these thresholds to the stress state reported for the Opalinus Clay at the Mont Terri Rock Laboratory. In-situ stress measurements of Corkum and Martin (2007) have yielded values of 6.5 MPa, 4.0 MPa, and 2.2 MPa for the first, second, and third principal stress axis, respectively (positive numbers for compression). According to Martin & Lanyon (2003) the undisturbed bedding normal stress at the site falls between 4.2 MPa and 4.6 MPa.

There is a striking similarity between the re-opening pressures for water injection (4 MPa for GS and 5 MPa for HG-C) and the normal stress on the bedding plane (4.2 MPa to 4.6 MPa). This is a strong indication that the fractures that have been created in GP-A and reactivated later on in GS and HG-C are mainly aligned parallel to bedding. The assumption that fractures were opened by water injection was confirmed in phase “hydro 2” of the GS experiment. In this phase, FIM measurements of borehole 3 (interval 2) showed a sudden dilation event. This rather points towards a fracture opening process than to an elastic deformation. The very acute response measured in interval 2 of borehole BGS1 also indicates non-elastic deformation.

The observed thresholds for gas injection (2.35 MPa) agree quite well with the estimated minimum principal stress of 2.2 MPa. This suggests the opening of fractures or fissures that are aligned normal to the axis of the minimum principal stress (which does not exclude that the gas phase also employed fractures that were created parallel to bedding).

Although there is no direct evidence for the existence of dilating gas pathways in the experiments, some arguments speak in favour of pathway dilation. The mentioned correlation between the stress state and the injection pressures for gas entry suggests that there is a transition to tensile failure on the pore scale. This non-elastic process would explain the sharp onset of gas entry that was noticed in the HG-C experiment. A localised crack propagation process resulting in a high localisation of pathways would explain why gas injection could only be modelled by ruling out phase interactions in the present study.

3.2.4.4 Interpreting the characteristics of water flow

There is something curious about the pressures that were needed for water injection. Firstly, one would not expect a fracturing pressure as high as 9.027 MPa (GP-A experiment) in view of the stress normal to bedding (4.2 MPa to 4.6 MPa) and the respective tensile strength (0.5 MPa as reported by Martin and Lanyon [20]). Secondly, it is not obvious why the water did not activate fractures normal to the minimal principal stress axis. The normal stress on these fractures (2.2 MPa plus tensile strength of approx. 1 MPa)[3] is much lower than the normal stress on the bedding planes (4.2 MPa to 4.6 MPa plus tensile strength of 0.5 MPa).

It seems that water finds it more difficult than gas to enter the rock. This is probably not only caused by the higher viscosity of water. A higher viscosity would attenuate the hydraulic propagation of the pressure signal and delay the dilation process. The very sharp pressure response of borehole BGS1 in phase "hydro 2" of the GS experiment, which was correlated with a dilation event, clearly differs from such an attenuated behaviour. Also, the higher viscosity of water would not be able to raise the threshold pressure for dilation as it was observed.

The fact that the minimum principal stress was not relevant for water injection rather indicates that water was unable to activate fissures that were aligned normal to the axis of minimum principal stress. Possibly, the apertures of these fissures were so small that the thickness of the water films, which were adsorbed to charged clay minerals, became relevant. This might have reduced the effective porosity and impeded the flow of water, which was necessary for fissure creation and opening.

However, after a prolonged period of fracture drainage, it has been possible to inject water at pressures near to the minimum principal stress (phase "hydro 2" of the GS experiment). Eventually, the fissures normal to the minimum principal stress axis were altered by the previous drainage of the rock. The drying process possibly opened these fissures or destroyed the good fit of the fissure walls.

Opening fractures by water injection seems to be less difficult parallel to bedding. Studies of the three-dimensional pore space geometry of Opalinus Clay have shown a preferential orientation of pore paths parallel to the bedding plane with low tortuosity (Keller et al., 2011a and 2011b). This should indeed facilitate water flow and thus a pressure-driven dilation of pathways.

The observed difficulty to inject water may depend on the boundary conditions or on the pace of the pressure build-up. Therefore, care has to be taken when transferring the above findings to other circumstances. Future experiments should investigate the possibility to inject water at lower pressures if the pressure is raised more slowly.

3.2.4.5 Relevance of tensile strength for gas migration

The fact that similar thresholds for gas injection were observed for disturbed rock (HG-C) and undisturbed rock (HG-D) shows that tensile strength was not relevant for gas migration at the experimental site. However, there is some uncertainty whether undisturbed rock has been tested in the HG-D experiment. The relevance of tensile strength for dilation-driven gas migration in clay rock under repository conditions should therefore be confirmed by further experiments.

3.2.5 Conclusions

The present modelling study succeeded to reproduce the injection flows of the HG-C and HG-D experiments with high accuracy. A modified version of the code TOUGH2 with pressure-

[3] A tensile strength of 1 MPa to 1.5 MPa parallel to bedding and of 0.5 MPa normal to bedding was reported by Martin and Lanyon (2003).

dependent permeability was used to simulate the water injection phase of HG-C. For the gas injection phase of the same experiment, a pathway dilation model, which was also based on TOUGH2, was developed. A special feature of the pathway dilation model is the time-dependency of the porosity change, which reflects a time-dependent relaxation of the rock with networks of microscopic pathways that are not in equilibrium with pressure. Another type of model, which was developed for the simulation of the gas injection phases, is the tube-chamber model. The tube-chamber model is a simple representation of a preferential pathway (the tube) between the injection borehole and a remote air-filled chamber. The chamber may be a drained part of a borehole or a fracture inside the rock.

The fact that two models reproduced the flow measurements of the HG-C experiment shows that there is no unique physical interpretation of the gas injection phase of the HG-C experiment. The applied tube-chamber model postulates that the injected gas finds its way to a remote air-filled space. This space might be a borehole or some part of the rock that could have been drained during the previous GS-experiment. The pathway dilation model suggests another mechanism. In this model, gas injection is caused by a certain rate of porosity increase inside the rock. A possible reason for such a time-dependent porosity increase is a gradual opening of dead-end crack branches that increases the mean porosity in the clay rock.

Both models, the pathway dilation model and the tube-chamber model, are based on strong simplifications like single-phase flow. No hydro-mechanical coupled modelling has been performed although the dilation process was in fact caused by hydro-mechanical interactions. Yet, simplifying modelling approaches do have advantages because they bring out the main aspects of the system and avoid the generation of models with a lot of parameters whose individual relevance is difficult to see. The applied models showed that the mechanical processes in the experiments were simple enough to be approximated by time- and pressure-dependent relations for porosity and permeability. This shows that coupled hydro-mechanical modelling is not always mandatory for processes with hydro-mechanical interactions.

The simulations showed no evidence of phase interactions such as water displacement, water compression or gas dissolution in the gas injection experiments under study. (Models with increased phase interactions were not able to fit the measured data). This indicates that the interface between gas and liquid phase was small during the experiments, which again suggests a high localisation of gas pathways. Initial thresholds for gas injection roughly agreed with the minimum principal stress for disturbed rock. This and the non-linear character of the flow response indicate the presence of dilating pathways. Shut-in thresholds were lower than the initial thresholds for gas injection, indicating hysteretic processes.

The undisturbed rock, which was tested in the HG-D experiment, showed the same threshold for gas injection as the disturbed rock. This suggests that tensile strength was not relevant for gas migration at the experimental site. However, there is some uncertainty whether undisturbed rock has been tested in the HG-D experiment. Therefore, this finding and its transferability to other sites and conditions should be confirmed by further experiments.

In order to inject water into the saturated system, the injection pressure has to be considerably higher than the minimum principal stress. This phenomenon cannot be explained by viscosity effects alone. Water seemed to be unable to activate fissures aligned normal to the axis of minimum principal stress. Possibly, the apertures of such fissures are so small that water adsorption at mineral surfaces becomes significant and advective flow is impeded. Due to the specific pore structure of the clay it is easier to establish a water flow along the bedding planes than across the bedding planes. This may explain why water apparently prefers to open fractures parallel to the bedding planes (at pressures near to the normal stress on these planes). The difficulty to inject water might decrease if injection pressures are raised more slowly, as would

be the case in a repository. Although HG-C and HG-D are long-term experiments, pressurisation has been performed quickly. Slow pressurisation could lead to different filter characteristics of the clay with regard to water flow.

The two-phase flow theory in its pure form does not seem to be appropriate to describe the observed experimental phenomena. Especially, the noticed lack of phase interactions conflicts with this theory. In the two-phase flow theory, gas and liquid share the same pore space, which means that water has to be displaced in order to inject gas into a saturated rock. Also, phase interactions are more intense because gas flow is less localised. The concept of intrinsic permeability, which is part of the two-phase flow theory and which postulates phase-independent filter characteristics of the rock, becomes meaningless if different pore spaces are used for liquid and gas flow.

The two-phase flow theory is widely considered to be applicable if pathway dilation is absent and swelling effects remain negligible. The theory may therefore still be a reasonable starting point for the development of performance assessment models that also cover the effects of pathway dilation. This study shows that this can be done by implementing pressure- and time-dependent relations. However, two-phase flow models and derivatives usually assume homogeneity and scale-independency. It has to be investigated under which circumstances this is tolerable for highly localised flow paths. Also, the geometry and scale-dependency of gas flow paths has to be studied.

Performance assessment codes must have a certain degree of simplicity in order to cope with large spatial scales or long periods of time. The study showed that simplified assumptions, such as single-phase flow, homogeneous distribution of dilating cracks and omission of hydro-mechanical coupled simulations, can be successful in describing experimental phenomena. However, this does not imply that the models are also suitable for predicting gas migration under conditions relevant to deep geological repositories. The physical processes of gas migration have to be understood more thoroughly in order to be sure that the simplified models capture the main aspects of gas migration. Hydro-mechanical modelling might help to understand the detailed mechanisms of pathway dilation and confirm the validity of simplified modelling approaches.

The onset of pathway dilation increases the complexity of gas migration. However, the observed absence of strong phase interactions raises hope to find performance assessment models with manageable complexity in the future.

Yet, predicting gas migration in dilating pathways under repository conditions remains a complicated task. The prospects to find appropriate performance assessment models for this complex process in the future should therefore be balanced against engineering options that keep gas pressures below the threshold for pathway dilation. A pressure reduction could, for instance, be achieved by providing additional pore space for gas storage or by reducing gas production, for example, by waste conditioning, container design or reduced water access to corrodible metals. A pressure limitation would contribute to the simplicity and robustness of both the repository system and the safety assessment.

3.2.6 References

Corkum, A. G. & Martin, C. D. (2007): Modelling a Mine-by Test at the Mont Terri Rock Laboratory, Switzerland. Int. J. Rock Mech. Min. Sci., 44, 846-85.

Enachescu, C., Blümling, P., Castelao, A., Steffen, P. (2002): Mont Terri GP-A and GS Experiments, Synthesis Report. Nagra Interner Bericht 02-51, December 2002.

Gerard, P., Harrington, J., Charlier, R., Collin, F. (2012): Hydro-Mechanical Coupling of the Development of Preferential Gas Pathways in Claystone. Unsaturated Soils: Research and Applications, 2012, pp 175-180.

Keller, L. M., Holzer, L., Wepf, R., Gasser, P., Münch, B., Marschall, P. (2011): On the application of focused ion beam nanotomography in characterizing the 3D pore space geometry of Opalinus clay. In: Physics and Chemistry of the Earth, Volume 36, Issues 17–18, 2011, Pages 1539–1544.

Keller, L. , Holzer, L., Wepf, R., Gasser, P.(2011): 3D geometry and topology of pore pathways in Opalinus clay: Implications for mass transport. In: Applied Clay Science, Volume 52, Issues 1–2, April 2011, Pages 85–95.

Martin, C. D., Lanyon, G. W. (2003): Measurement of in-situ stress in weak rocks at Mont Terri Lock Laboratory, Switzerland. International Journal of Rock Mechanics and Mining Sciences, 40(7-8), 1077-1088.

Navarro, M. (2013): Modelling Gas and Water Flow through Dilating Pathways in Opalinus Clay, The HG-C and HG-D Experiments, A Study within the Euratom 7th Framework Programme Project FORGE, GRS-306, ISBN 978-3-939355-85-4, Gesellschaft für Anlagen- und Reaktorsicherheit (GRS), Germany.

Pruess, K. (1990): TOUGH2: A general purpose numerical simulator for multiphase fluid flow, Report LBL-29400, Lawrence Berkeley Nat. Lab., USA.

Pruess, K. (1991): EOS7: An equation of state module for TOUGH2, Report LBL-31114, Lawrence Berkeley Nat. Lab., USA.

Pruess, K., C. Oldenburg, and G. Moridis (1999): TOUGH2 User's Guide, Version 2.0, Report LBNL-43134, Lawrence Berkeley National Laboratory, Berkeley, California, USA.

Rösli, Ursula, Trick, Thomas (2008): Mt. Terri HG-C Experiment Phase 2, Hydraulic and gas test series in BGS-2 borehole and deformation measurements in BGS-3 and BGS-4 boreholes. – Report TN 2008-80, Mt. Terri Phase 13, October 2008.

Trick, Thomas (2007): Mt. Terri HG-C Experiment Phase 1, First hydraulic tests and deformation measurements in borehole BGS-2 (Mt. Terri Phase 12). – Report TN 2007-13, Solexperts AG, August 2007.

3.3 Modelling of the PGZ1 in situ test in the Callovo-Oxfordian clay in Bure (EDF)

3.3.1 Introduction

In order to assess feasibility of the deep geological disposal of radioactive waste, a large program of experiments, led by Andra, has been engaged at the Meuse/Haute-Marne research laboratory. PGZ1 is one of these experiments and is focused on perturbations induced by gas production in undisturbed clay.

Main goals of PGZ1 experiment are:

- Characterization of gas transfer through medium (through natural and modified clays, caps and interfaces)
- Validation of biphasic model and of its parameters (diffusion, capillary pressure, permeability)
- Estimation of micro-fracturation threshold

Further details about the experimental protocol are given in section **Error! Reference source not found.**. This experiment is still ongoing. This experiment was “a priori” dedicated to undisturbed host rock.

In this section, axisymetrical numerical simulations of PGZ1 experiment are proposed with *Code_Aster*. 3D computations have been done but are quite computationally expensive and do not bring significant novelties with respect to 2D modeling.

In a first part, digging, hydraulic phase and gas injection phase are simulated. Some comparisons with experimental observations have been done: First part of experience is well reproduced but important differences are observed for the last part. Hydromechanical coupling analysis has been done. In a second part, only gas injection phase is simulated and the initial saturation of injection chamber is well taken into account. 2D axisymmetric computations have been done under different configurations (presence or not of a borehole damage zone). More details about this work are given in FORGE deliverable D4.21. This work is part of both WP4 and WP5.

3.3.2 Description of the model

We consider an unsaturated biphasic Hydro-Mechanical model. Details of Hydro-Mechanical models available in Code_Aster are given in [5] and generally in [4]. Hereafter, we recall main equations of the model.

We consider 2 components (N_2 and H_20), denoted by upper index c existing into 2 phases (liquid and gas), denoted by lower index p. In our study, we consider that there is no vapor ; hence water does not exist in gaseous phase. Gaseous phase is composed of nitrogen, liquid phase is composed of water and dissolved nitrogen.

Mechanical unknowns are displacements $u = (u_x, u_y, u_z)$. Hydraulical unknowns are liquid pressure $p_l = p_l^{H_2O} + p_l^{N_2}$ and gas pressure $p_g = p_g^{N_2}$. They are related by capillary pressure $p_c = p_g - p_l$. Capillary pressure p_c is related to water saturation S_l by Van-Genuchten relation:

Equation 35:

$$S_{we} = \frac{1}{\left(1+\left(\frac{p_c}{p_r}\right)^n\right)^m} \quad with \quad S_{we} = \frac{S_l - S_{wr}}{1 - S_{wr}}$$

where we have introduced S_{wr} the residual saturation S_{we}, the effective saturation, p_r, n and m Van-Genuchten parameters such as: $m = 1 - 1/n$.

Liquid relative permeability is also given by Mualem Van-Genuchten model, such that :

Equation 36:

$$k_r^l = \sqrt{S_{we}}\left[1-\left(1-S_{we}^{1/m}\right)^m\right]^2$$

Gas relative permeability is given by a cubic law ponderated by a coefficient C_k:

Equation 37:

$$k_r^g = C_k\left(1-S_l\right)^3$$

Nitrogen N_2 obeys to perfect gases law:

Equation 38:

$$p_g^{N_2} = \frac{\rho_g^{N_2}}{M_{N_2}} RT$$

Where we introduce the density ρ, M_{N_2} the Nitrogen molar mass, R the perfect gas constant and T the temperature.

Water is slightly compressible, hence we have the relation

Equation 39:

$$\frac{d\rho_l}{\rho_l} = \frac{dp_l}{K_l}$$

where coefficient K_l denotes water compressibility.

Nitrogen dissolution obeys to Henry's law

Equation 40:

$$\frac{\rho_l^{H_2}}{M_{N_2}^{ol}} = \frac{p_g^{H_2}}{K_H}$$

where K_H designates Henry's constant and $M_{N_2}^{ol}$ nitrogen molar mass.

Two main equations govern system's evolution: balance momentum and fluid mass conservation. Balance momentum equation is

Equation 41:

$$\nabla \cdot \sigma\left(u, p_c, p_g\right) = 0$$

Stress tensor is decomposed in effective stress tensor σ' and pressure stress tensor σ_p

Equation 42:

$$\sigma\left(u, p_c, p_g\right) = \sigma'(u) + \sigma_p\left(p_c, p_g\right)$$

Incremental form of pressure stress tensor reads:

Equation 43:

$$d\sigma_p = -b\left(dp_g - S_l dp_c\right)$$

Where b designates Biot coefficient and S_l water saturation.

The variation of porosity $d\varphi$ is given by the classical eulerian representation

Equation 44:

$$d\varphi = (b-\varphi)\left(d\varepsilon_v + \frac{S_g dp_g + S_l dp_l}{K_S}\right)$$

With ε_v is volumic strain and K_S the compressibility of the skeleton.

Mechanical behaviour obeys to Drucker-Prager's law. Material Young modulus and Poisson ratio are respectively denoted E and ν. Plasticity surface F reads

Equation 45

$$F = \sqrt{\frac{3}{2}} II_{\hat{\sigma}} + m\left(I_\sigma - \frac{3c}{\tan\phi}\right) = 0$$

where $II_{\hat{\sigma}} = \sqrt{\hat{\sigma}_{ij}\hat{\sigma}_{ij}}$ is second deviatoric stresses invariant, $\hat{\sigma}_{ij} = \sigma_{ij} - \frac{I_\sigma}{3}\delta_{ij}$ is deviatoric stresses tensor, $I_\sigma = \sigma_{ij}\delta_{ij}$ is first stresses invariant, coefficient m is given by relation $m = \frac{2\sin\phi}{3-\sin\phi}$, is friction angle and c is cohesion. We notice that gravity effects are here neglected.

Mass conservation reads for component c:

Equation 46:

$$\dot{m}_c + \nabla\cdot\left(F_l^c + F_g^c\right) = 0$$

where m_c (resp. F_l^c , F_g^c) designates mass inflow (resp. liquid, gaseous flux) of component c. For each phase p, hydraulic fluxes obey to Darcy's law:

Equation 47:

$$F_p = -\frac{k.k_r^p(S_l)}{\mu_p}\nabla p_p$$

k stands for anisotropic intrinsic permeability $k = \left(k_x, k_y, k_z\right)$, k_r^p for relative permeability and μ_p for dynamic viscosity of phase p.

Diffusion in liquid phase obey to Fick's law:

Equation 48:

$$\frac{F_l^{H_2O}}{\rho_l^{H_2O}} + \frac{F_l^{N_2}}{\rho_l^{N_2}} = -D_l \nabla \rho_l^{N_2}$$

where D_l stands for Fick diffusion coefficient in liquid phase.

In the sequel, we will express D_l as a linear function of tortuosity τ, saturation and porosity such that:

Equation 49:

$$D_l = S_l.\tau.\varphi.D_{N2}^{w}$$

with D_{N2}^{w} the diffusion coefficient of nitrogen into water.

3.3.3 First step of hypothesis with an HM computation

Because anisotropy has no major effect in this test (3D computations have been made firstly), axisymmetrical configuration is fin

ally retained in all the computation (Figure 83). In this geometry, only injection chamber and host rock are modeled.

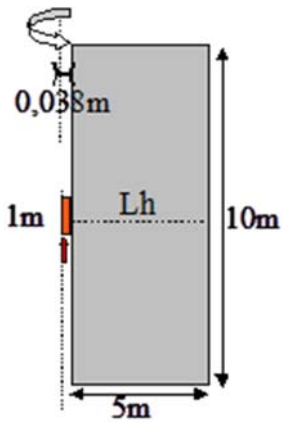

Figure 83 2D axisymmetrical geometry

The argillite is initially fully saturated, and the gravity is neglected. We consider that in the argillite the initial pressure is p_l^0 =4,5MPa. The initial total stresses are the classical values used for argillite and correspond to the rock weight: $\sigma_{xx} = \sigma_{yy} = \sigma_{zz} = -12MPa$.

We model the middle chamber by a porous media containing an empty volume of 1,1l. This interval is initially dry and its stresses are equal to zero. In this section we model the different steps of the experiment which are summarized in Table 17.

Table 17 Steps of modeling

Step	Duration	Event
1	1 h	Digging of the borehole
2	1day	Waiting
3	180 days	Installation of chamber and packers (modeled by blocked displacements along the borehole).
4	300 days	N_2 Injection in 6 steps separated by shut-in phases

The digging of the borehole is done with a classical convergence-confinement method and the gas is injected on a lateral face of the chamber (Figure 83). Material parameters are summarized in

Table 18.

Table 18 Hydro-mechanical parameters for Argilite and Chamber

	Argilite	Injection Chamber (interval 2)
Intrinsic permeability	$k_x = k_y = k_z = 2{,}2.10^{-20} m^2$	$k_x = k_y = k_z = 10^{-12} m^2$
Initial porosity	$\varphi^0 = 0{,}18$	$\varphi^0 = 0{,}25$
Van Genuchten Parameters	Pr = 15MPa ; n= 1.49 ; Swr = 0.01	Pr = 0.05 MPa ; n= 1.5 ; Swr = 0.0
Gas perm. Coef.	$C_k = 250$	1
Tortuosity	$\tau = 0{,}25$	$\tau = 1$
Young Modulus	$E = 4000\ MPA$	$E = 1\ MPA$
Poisson's ratio	$\nu = 0{,}3$	$\nu = 0{,}1$
Biot coef.	$b = 0{,}6$	$b = 1$
Friction angle	$\phi = 15°$	-
Cohesion	$c = 3\ MPA$	-

Concerning the mechanical evolution: we look at the values on the line L at several times. The radial stresses Figure 86**Error! Reference source not found.** stay in compression: no breakdown is envisaged. Figure 84 shows plastic deformation along the cross section Lh perpendicular to borehole: a small (2cm) plastic area appears after borehole digging but stays constant after that.

As expected and with such a model after (with simplified hypothesis of perfect plasticity), the gas does not affect the damage zone. The coupling with mechanic is weak here.

Figure 85 presents liquid pressure and saturation evolution on PRE02: the 3 first steps of injection (until pressure of 7Mpa) are very well reproduced. After third injection step, computation is unable to reproduce the hydraulic comportment. During first steps of injection, there is no desaturation of the interval and the nitrogen is essentially moving in a dissolved way into the water. This point is very important: due to hydraulic phase, the interval is fully saturated at the beginning of injection which is contradictory with experiment measurement (see next section).

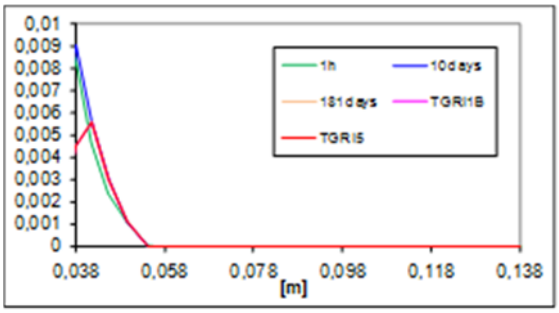

Figure 84 Plastic deformation on Lh

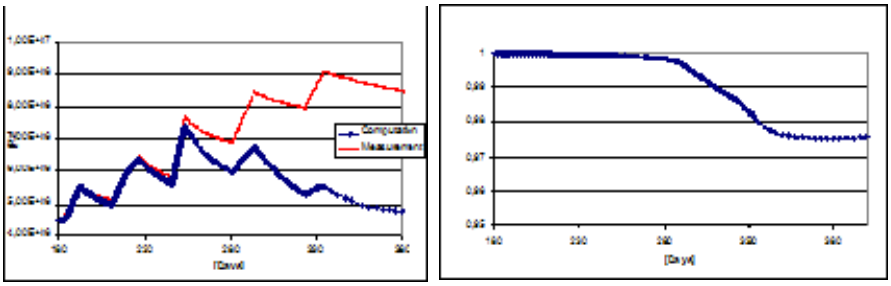

Figure 85 Liquid pressure and Saturation evolution on PRE02

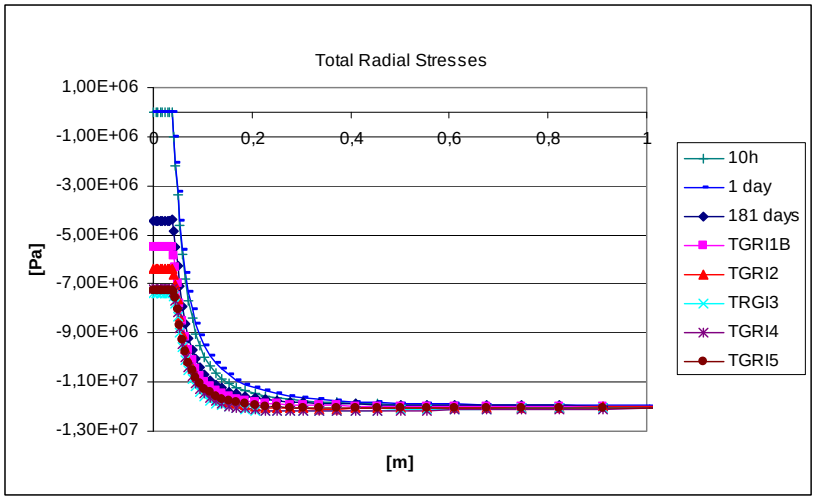

Figure 86 Total radial stresses at several times along L

3.3.4 New hypothesis of computation

3.3.4.1 SOME ELEMENTS CONCERNING THE VOLUME OF THE INJECTION'S CHAMBER

In [2] and [3] an analysis of the volume of vacuum Interval 2 (Figure 87) is provided and gives more precisions. This volume of void is composed of an "incompressible" volume (corresponding to the case of a full convergence around the filter) and of a part corresponding to a void around this filter. This void will be filled up during the convergence of the rock. Knowing that, the theoretical volume of vacuum in interval 2 ranges between two extremes:

- 804 cm^3 if the rock is fully converged
- 1540 cm^3 when there is no convergence

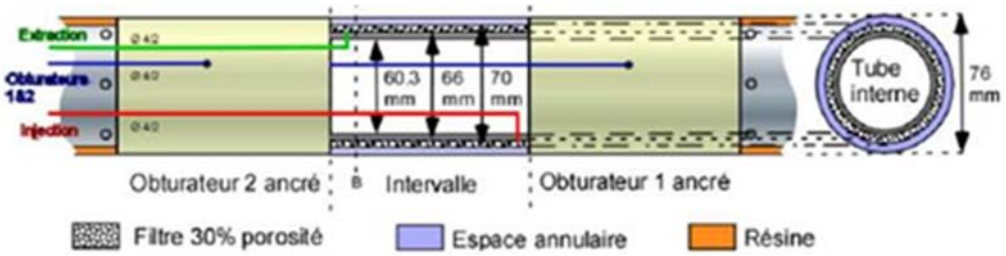

Figure 87 injection chamber Interval 2 (or PRE02)

Moreover, the volume of water rejected by flushing in the interval during the water-gas exchange before GAS1 phase is equal to 810 cm^3. This volume corresponds to the initial volume of gas in the chamber before injection.

At least, in [3] the pressure differential is fitted by an analytical solution at constant volume using a Perfect Gas law. The best fitting before GAS1 is obtained with a volume of 1040 cm^3. This gives us an indication of the volume of interval at the begining of injection. After that, the fitting is done for each injection steps: the gas volume increases and becomes more important than maximum theoretical value (1540 cm^3) of interval volume after GRI3. An interpretation of that is that residual water is first rejected, and then that gas penetrates in the rock but more and more hardly.

In the first set of hypothesis presented in section 2, the chamber is fully saturated before gas injection due to hydraulic phase. This is not consistent with the hypothesis done before. In the following, new computations are only done for Gas 1 phase considering a volume of 1040 cm^3 for the interval 2 instead of 1100 cm^3. Most of all, a precise initial saturation of gas will be taken into account.

Mesh and geometry are the same than in section 2 (axisymmetrical computation). Volume of the chamber is equal to 1040 cm^3 ($\phi^0 = 0{,}23$). Only GAS1 phase is modelled (corresponding to step 4 in Table 17).

- **Initial condition:**

As previously the argillite is initially fully saturated with an initial pressure equal to 4,5MPa. The gravity is neglected. In the interval injection, the saturation is such as:

$$S_l = 1 - \frac{810}{1040} = 0{,}22$$

According to the van-genuchten parameters indicated in

Table 18, it provides an “artificial capillary pressure” $p_c^0 = 0{,}021 MPa$

3.3.4.2 REFERENCE COMPUTATION

For this computation, in the host rock we take $k_x = k_y = k_z = 4.10^{-20} m^2$. All the other data are the same than in

Table 18.

Gas pressure evolution with these hypotheses is presented in Figure 88 with the red curve. Until second injection step (≈230 days), experimental results are well reproduced, afterwards, differences are consequents.

The blue curve represents the same computation but with a chamber initially partially saturated (0,9). Logically, the pressure is much higher (and this, as the first step of injection). Looking at the profiles on the line L_h at several times of gas pressure and liquid saturation respectively Figure 89**Error! Reference source not found.** and Figure 90, we observe that penetration of gas remains located near the injection interval: influence area is less than 20cm. The saturation stays high (more than 0,95). Looking at the ratio between gas and liquid nitrogen volume on Figure 91, we confirm that even in this case, most of nitrogen is transported by dissolution/diffusion.

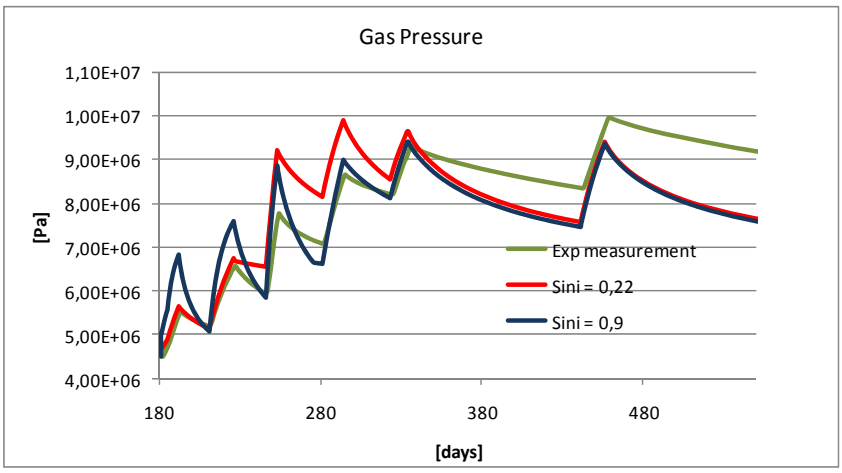

Figure 88 Liquid pressure evolution in interval 2 : goal of initial saturation

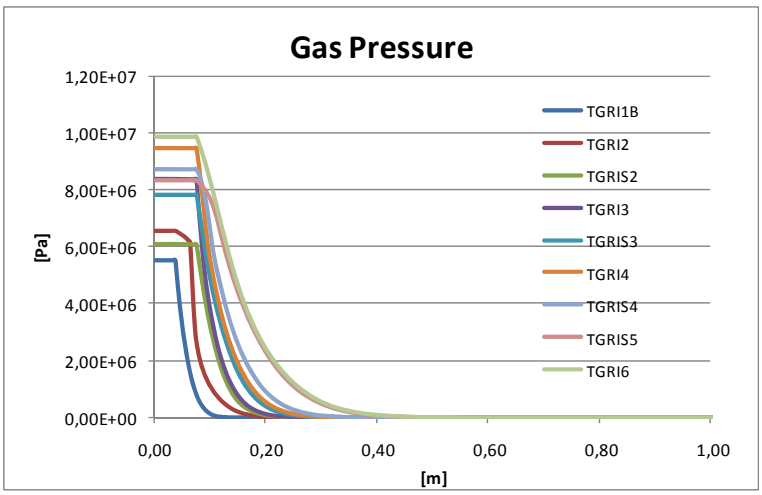

Figure 89 $\chi_l^{N_2}$ (Gas pressure or concentration) at several times along L

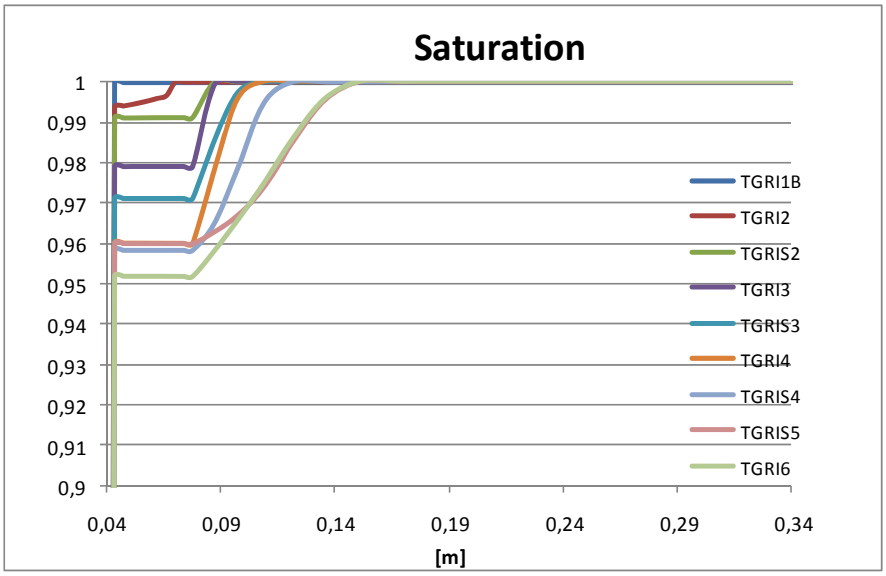

Figure 90 Liquid Saturation at several times along L

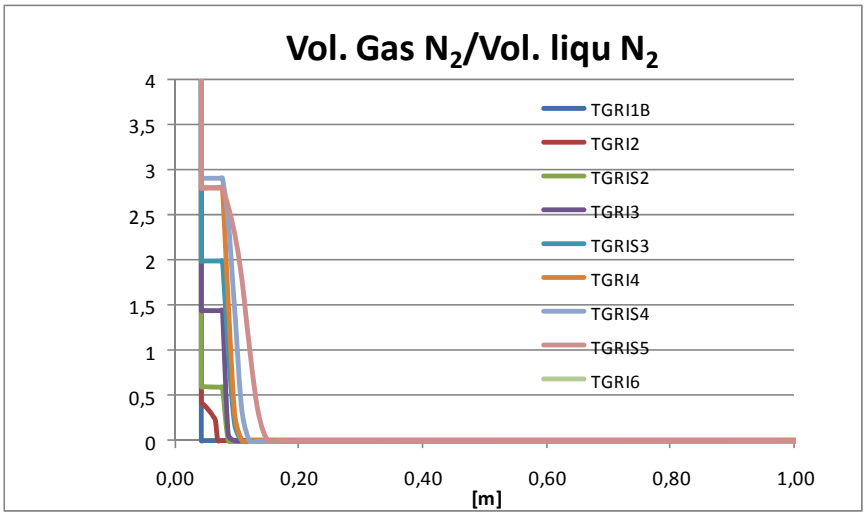

Figure 91 Gas-liquid ration of Nitrogen at several times along L

3.3.4.3 INTRODUCTION OF A BOREHOLE DAMAGE ZONE

A borehole damage zone (called BDZ) is now introduced. We take a radius equal to the radius of the hole (3,8 cm, larger than the 2cm found in Figure 84). Considering that no pressure evolution is observed in chamber PRE01 and PRE03 (Figure 84), we can imagine that this damaged zone has been closed around the packer by swelling of this one. The hypotheses we choose are summarized in Figure 92. We call this area "borehole damage zone" because we can imagine that there is an area due to drilling (Figure 84), but this area could also be a "transient zone" mixed of a damage zone and materials produced by injection gas (mud, gel, etc.).

Figure 93 shows pressure evolution in interval 2. We can observe that results with or without BDZ differ very weakly until 230 days. In this part, we can suppose that injection chamber behavior plays the main role and that water removal is the major phenomena. After 230 days, the results obtained with BDZ are better than those without: this damage zone seems to play an important role. Results are in very good agreement with experimental results until the begining of third injection step, after they differ. Nevertheless, after this, differences between results with and without BDZ seem to remain more or less constant.

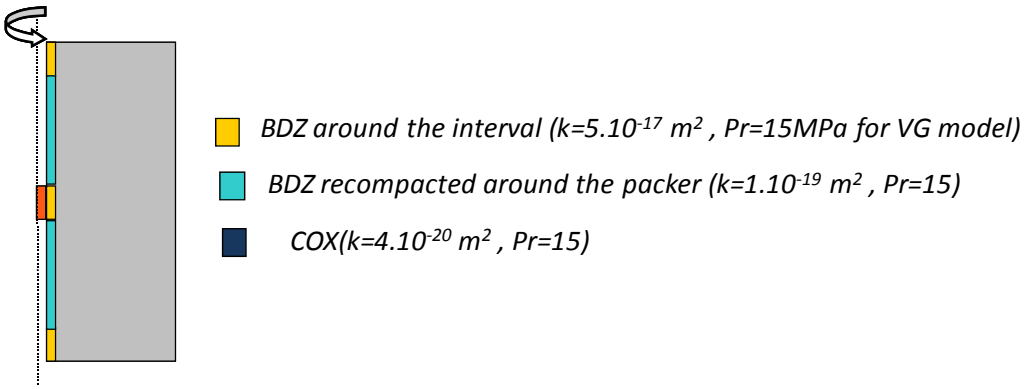

Figure 92 Configuration and hypothesis of BDZ

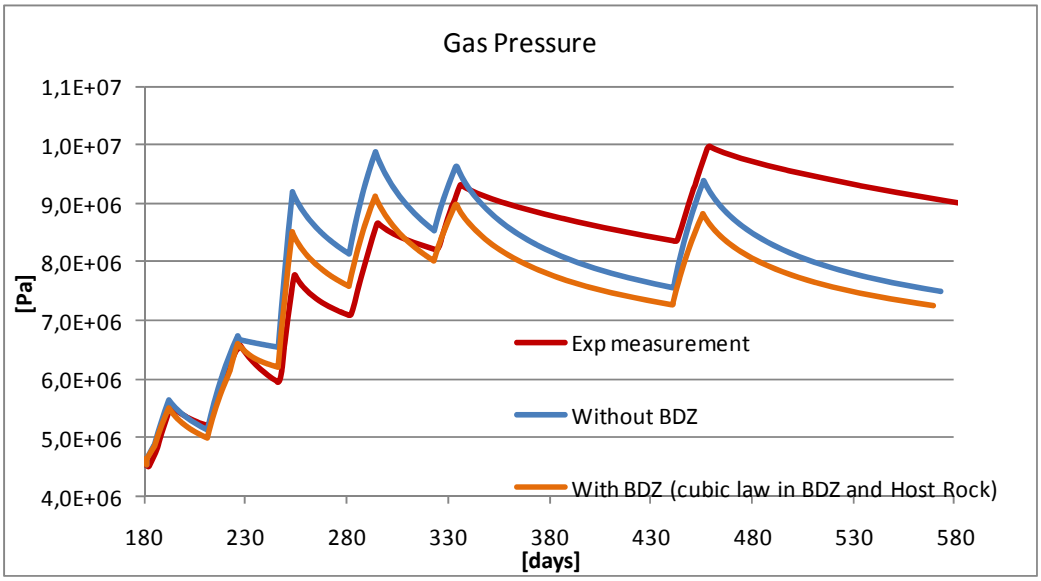

Figure 93 Gas pressure evolution in interval 2 : goal of BDZ

3.3.4.4 GOAL OF GAS PERMEABILITY

As written previously and according to several experimental results, we take for argillite a cubic law for gas permeability law. This law is not precisely known and we propose here a sensitive analysis.. For that, we change the cubic law in the undisturbed host rock by a quadratic law: $k_r^g = C_k(1-S_l)^4$.

In BDZ, the relative permeability remains a cubic law. All the other data are the same than previous.

According to Figure 94, we observe that this parameter is not influent for the 4 first steps of injection. After that, differences are significant. We can interpret that, according with time, each material is successively predominant: injection chamber, then BDZ and finally undisturbed host rock.

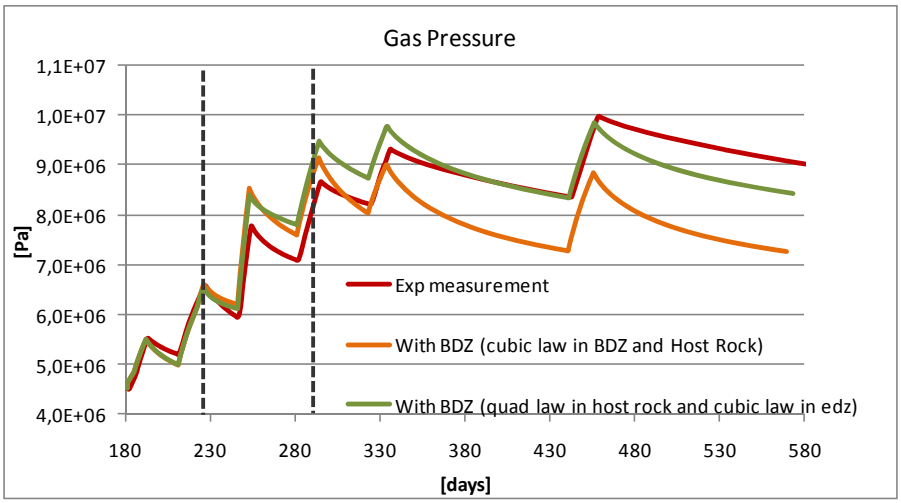

Figure 94 Gas pressure evolution in interval 2 : goal of relative permeability in host rock

3.3.5 Conclusions

This contribution proposes a numerical modeling of a field scale test with a classical coupled two-phase flow model. The major difficulty in experience modeling is finally to understand and capture what happens in the instrumentation process and not only as far as the undisturbed clay is concerned.

By the way, we can more or less reproduce experiment and provide an interpretation of involved mechanism. Indeed, we suppose that different phenomena play successively a role: First, injection chamber comportment is predominant and we observe essentially water displacement, secondly, the borehole damage zone plays a prominent part and at least undisturbed host rock seams to become the leader.

In both simulations and experimental results, we observe that the gas influence zone is very small. In undisturbed host, no désaturation is observed.

We can see that even for PGZ1 (expected as a test in a undisturbed host rock), damage zone plays an important goal. This small zone is complex to estimate a priori because not only due to digging. A better characterization of this damage zone (suction, gas permeability, etc.) seems to be necessary to obtain a better fit of experimental results and predictive computations.

3.3.6 References

[1] Tests hydrauliques dans le forage de l'unité de programme PGZ1 en galerie GED. Forage PGZ1201 et PGZ1202. Rapport d'opération. Document ANDRA D.RP-OCPE.09.0028, 10/05/04

[2] De La Vaissière, R. Talandier, J. « Gas entry pressure in Callovo-oxfordian claystone : in situ expermiment PGZ1 » Acte du colloque national Transfert 2012, ECL-LML 2012.

[3] De La Vaissière. Expérimentation PGZ Analyse de la phase d'injection de gaz GAS1. Document Andra D.NT. AMFS.11.0084

[4] P.Gerard, R.Charlier, F.Collin, R.Fernandes, S.Granet, D.Arnedo, S.Olivella, Description of initial numerical codes and conceptual model (undisturbed and disturbed host rocks). Forge Project – Deliverables 4.5 and 5.5 (February 2010).

[5] Granet, S. Meunier, S. «Numerical Modeling of in situ-experience of Gas Injection : PGZ1» Acte du colloque national Transfert 2012, ECL-LML 2012.

[6] S. Granet, Modèles de comportement THHM, doc R7.01.11, available on www.code-aster.org.

[7] Coussy O. 2004. Poromechanics. Wiley, London.

3.4 Gas migration in undisturbed COx (ULg)

3.4.1 Introduction

In a clay-based material, four primary phenomenological models describing gas flow are considered (Marschall et al., 2005): (i) gas movement by diffusion and/or solution within interstitial fluids along prevailing hydraulic gradients; (ii) gas flow in the original porosity of the fabric, commonly referred to visco-capillary (or two-phase) flow; (iii) gas flow along localised dilatant pathways which may or may not interact with the continuum stress field; (iv) gas fracturing of the rock similar to that performed during hydrocarbon stimulation exercises.

The ULg contribution in Forge project is mainly based on the hydro-mechanical modelling (with finite element code Lagamine) of laboratory and field scale experiments highlighting the first three mechanisms of gas transfers. When gas pressure increases, gas migration can be associated with the development of gas preferential paths along existing or pressure-dependent discontinuities. Such behaviour is studied in details in WP4 and presented in Deliverable D4.2.4-R.

In this workpackage (WP5), ULg is especially involved in the modelling of an in-situ gas injection experiment in Callovo-Oxfordian claystone (PGZ1 experiment in Meuse/Haute-Marne URL performed by Andra), considering an undisturbed host rock.1D and 3D hydraulic modelling of the field scale gas injection test highlight how a predictive two-phase flow model could reproduce successfully a large scale gas injection test.

3.4.2 Modellings of PGZ1 experiment

3.4.2.1 EXPERIMENT DESCRIPTION

To address the issues of gas transfer mechanisms in claystone, the French national Agency for the management of radioactive waste (Andra) has directed a field scale experiment examining the mechanisms controlling gas entry and gas migration in the Callovo-Oxfordian (COx) clay, the proposed host rock of the French deep geological repository project. This experiment, called PGZ1, studies the migration of nitrogen in the host rock. Nitrogen is injected at different flow rates from an injection interval, interrupted by shut-in phases (Figure 96). Different sensors provide the temporal evolution of pore pressures in the injection interval and in the rock mass (see Figure 95 or deliverables D5.4 and D5.9 or de La Vaissière et al., 2012 for more details about the experiment description).

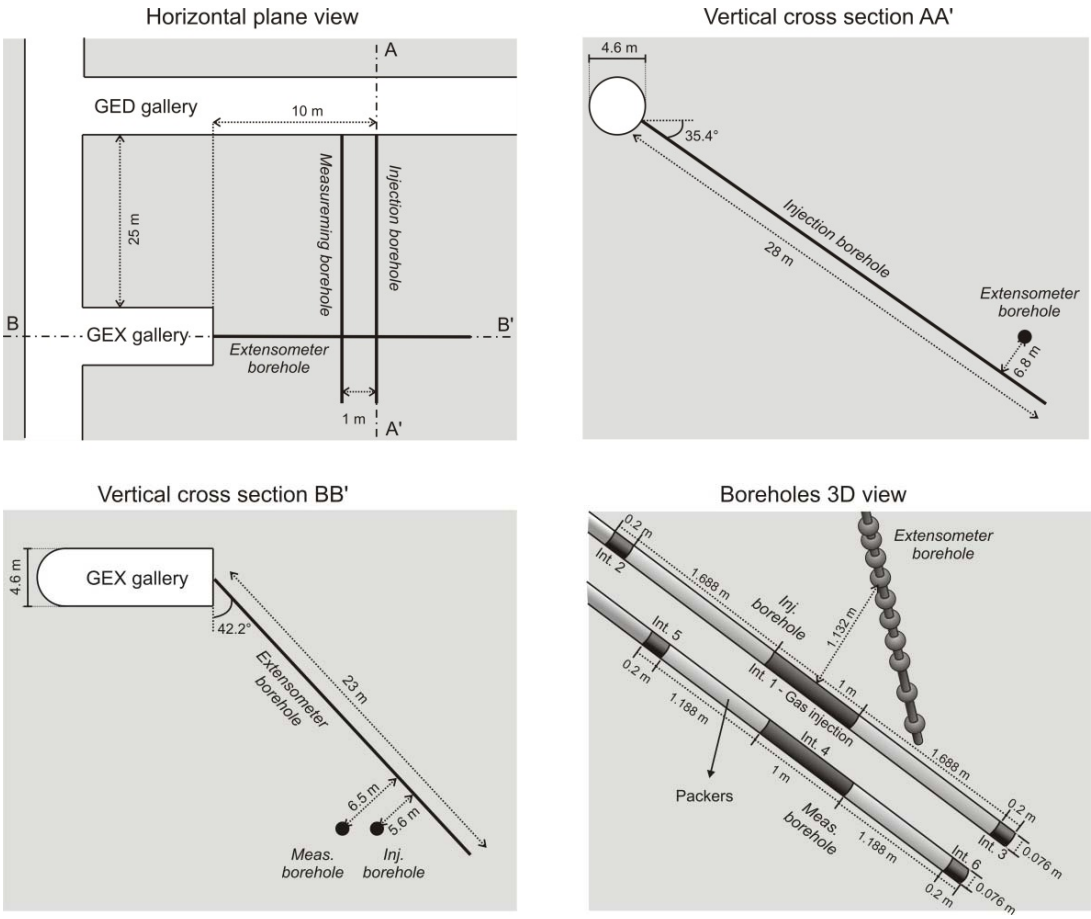

Figure 95 Schematic position of the pore pressure sensors (distances are measured from the gallery wall)

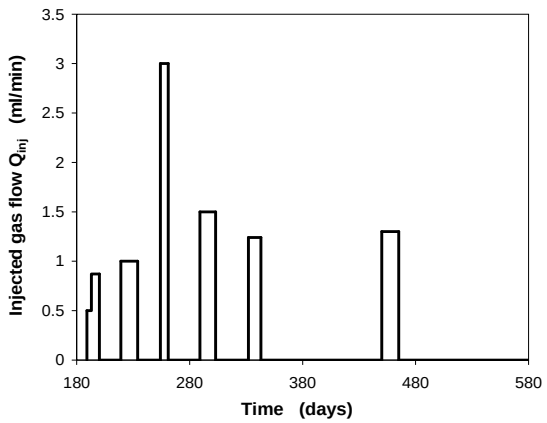

Figure 96 Gas flow injected experimentally at one face of the injection interval

A field data analysis has been first achieved by Andra, emphasizing the influence on the results of parameters for which some uncertainties remain, as the injection interval volume or the volume of remaining water in the interval (de La Vaissière et al., 2012).

3.4.2.2 BOUNDARY VALUE PROBLEM

ULg is involved in the modelling of this field scale gas injection experiment. The geometry of the problem and the permeability anisotropy lead to perform 3D modelling. But in order to highlight clearly the influence of each component of the system without time-consuming approaches, 1D modelling is first proposed. 3D modelling is then performed and provides additional information on the behaviour of the rock mass during the gas injection. A step-by-step modelling of the problem has been performed, highlighting how an accurate knowledge of the boundary conditions of the problem and a strong interaction between experimenters and modellers are necessary to obtain satisfactory numerical results.

The numerical results of the drilling phase followed by the increase of the pore pressures in the boreholes are not presented in this summary deliverable. Nevertheless a 3D modelling of these phases (not presented here) has shown that the drainage induced by the extensometer borehole could explain the decreasing trend of the pore pressures observed experimentally in the sensors located along the injection and measuring boreholes (see Deliverable D5.4 and D5.9 or de La Vaissière et al., 2012 for more details about the experimental observations).

This deliverable is thus only devoted to the hydraulic modelling of the gas injection test. We focus first on the numerical results obtained in the injection interval (interval 1), where the increase of the pore pressures is the most significant. As the drainage of the extensometer borehole is not taken into account in the modelling of the gas injection phase, a correction of the experimental data is performed in order to cancel the decreasing trend observed on the pore pressure evolutions.

1D hydraulic modelling of the problem is first achieved. An injection interval with a radius of 3.8 cm and an injection volume equal to 1540 cm³ is considered, followed by the rock mass. Such a volume corresponds to any convergence of the rock mass during and after the drilling. The injection interval is assumed almost dried at the beginning of the gas injection ($S_{r,w0}$ = 0.05), owing to the water removal at the end of the hydraulic tests. The nitrogen injection is modelled through

a controlled gas flow imposed at the injection interval face, corresponding to the experimental gas injection (Figure 96).

To reproduce gas movement by diffusion or by visco-capillary effects, a two-phase flow model is defined. This model consists of a liquid phase, composed of liquid water and dissolved gas and a gaseous phase, which is an ideal mixture of dry gas and water vapour. It takes into account the advection of each phase using the Darcy's law and the diffusion of the components within each phase (Fick's law). In the model a distinction between the water permeability in saturated conditions and the gas permeability in dried conditions is assumed, and permeability anisotropy can be defined (see Charlier et al., 2012 or Forge deliverables D4.5 and D5.5 for more details). The retention curve and the water relative permeability curve are given by the van Genuchten's model. The gas relative permeability curve is a cubic function:

Equation 50:

$$K_g = K_g^{dry}\left(1 - S_{r,w}\right)^3$$

with K_g^{dry} the gas permeabilities in dried conditions, $S_{r,w}$ the degree of saturation. Hydraulic parameters for COx are given in Table 19 and correspond to classical value for this host rock (see Charlier et al. 2012 for a review of the retention characteristics of COx).

The injection interval is modelled by considering an equivalent porous media, with high permeability, porosity equal to 1 and a low air entry pressure. No water and gas relative permeability curve is defined for this component.

Table 19 Hydraulic parameters for COx

K_w^{sat}	Water permeability in saturted conditions (m²)	4 10^{-20}
K_g^{dry}	Gas permeability in dried conditions (m²)	4 10^{-18}
ϕ	Porosity (-)	0.18
P_r	van Genuchten air entry pressure (MPa)	15
n	van Genuchten parameter of retention curve (-)	1.49
m	van Genuchten parameter of water permeability curve (-)	0.55

3.4.2.3 NUMERICAL RESULTS – 1D

Water and gas pressures evolutions in the injection interval are compared with the experimental pore pressures on Figure 97 (a). The injection interval remains dried during the gas tests, but the desaturation of claystone is very low (Figure 97 (b)). This first 1D modelling is nevertheless not satisfactory: the experimental data are not reproduced. An in-depth analysis of the hydraulic data is therefore proposed in order to emphasize the role of each component of the system and allows an improvement of our model.

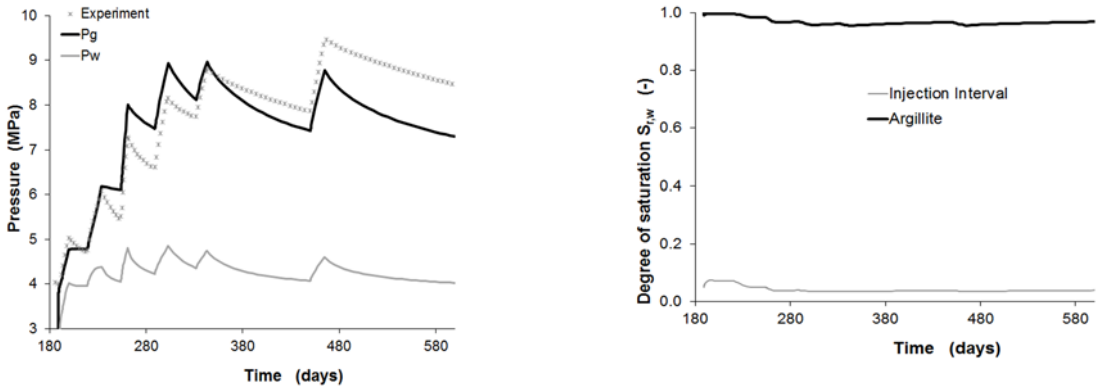

(a) (b)

Figure 97 Gas and water pressures evolution in the injection interval: comparison with pore pressures measurements and (b) evolution of the degree of saturation in claystone and in the injection interval for the 1st modelling

The field data analysis (performed by Andra) has highlighted the uncertainties on the volume of the interval and the volume of residual water in the interval before the gas injection. Obtaining the best fit of these two parameters is the first aim of 1D modeling. Considering an interval with an initial volume of 1040 cm³ and an initial degree of saturation of 0.22 seems to be satisfactory, because numerical results are strongly improved during the first two peaks (Figure 98(a)). It must be noticed here that these initial conditions do not correspond exactly to the ones deduced from the hydraulic data analysis. It could be explained by the influence of the gravity on the field behaviour. The remaining residual water is thus concentrated at the bottom of the inclined injection interval, which is not explicitly reproduced in our model. Nevertheless the numerical results highlight that all the water initially available in the interval has been expelled at the end of the third injection stage (Figure 98(b)), which confirms the hydraulic data analysis (see Deliverable D4.5 and D5.5).

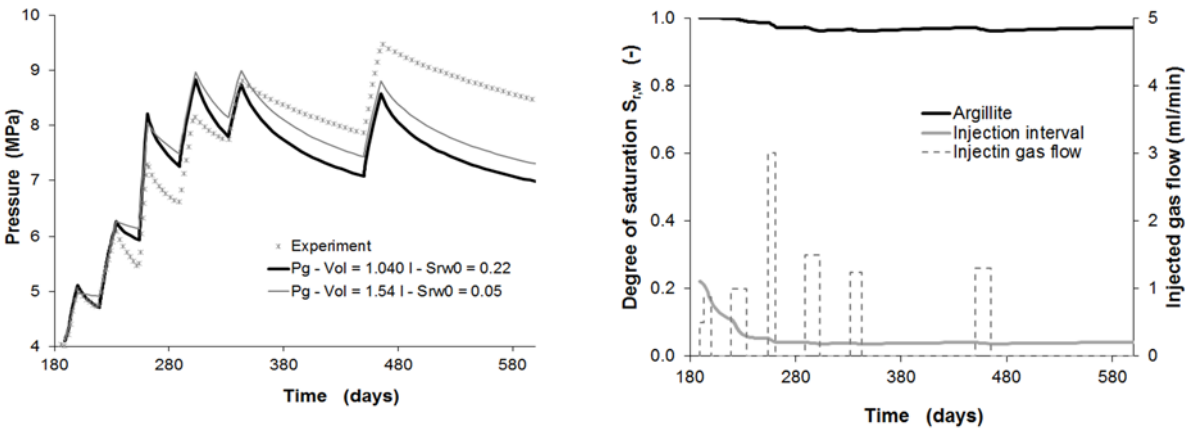

(a) (b)

Figure 98 Influence (a) of the interval volume and of the initial degree of saturation in the injection interval and (b) evolution of the degree of saturation in claystone and in the injection interval for the new modelling

Nevertheless the knowledge of the interval characteristics is not sufficient to obtain satisfactory long-term numerical predictions. The presence of a disturbed zone around the boreholes could thus be defined in our numerical problem. The extent of the EDZ is assumed close to the radius of the borehole (4 cm), which corresponds to previous experimental observations (Bossart et al.,

2002). In this damaged zone, a high permeability and a low air entry pressure are considered, which improves strongly the numerical results in the injection interval (Figure 99).

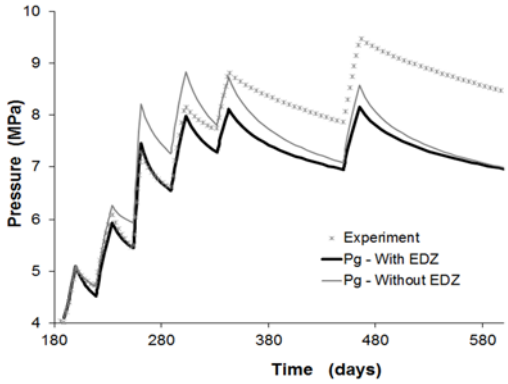

Figure 99 Influence of the introduction of an excavated damaged zone on the time evolution of pore pressures in the injection interval

Despite the improvement of the assumptions of the modelling, the long-term predictions should be better. After the fourth injection stage nitrogen reaches the undisturbed host rock. A modification of Callovo-Oxfordian claystone transfer parameters is proposed to avoid the underestimation of the pore pressures. The hydraulic characteristics of COx have been already determined in numerous laboratory or field experimental studies (Charlier et al. 2012). Nevertheless few experiments investigate the gas transfer properties of COx close to the saturation, owing to the experimental difficulties to impose accurately high degree of saturation and to detect and measure very low gas permeability. Cubic law is thus usually considered as gas relative permeability function even if we could not verify its relevance in the quasi saturated domain, but other relationships exist as the Parker's one:

Equation 51

$$K_g = K_g^{dry} k_{r,g} = K_g^{dry} \sqrt{1 - S_{r,w}} \left(1 - S_{r,w}^{1/\lambda}\right)^{2\lambda}$$

where λ is a parameter.

If the Parker's relationship (with λ = 1.6) is used to define the gas relative permeability in the undisturbed rock, but also in the excavated damaged zone, a better reproduction of the experimental pore pressures is obtained (Figure 100(a)). The Parker's function provides lower gas permeability than the cubic law (Figure 100(b)), which allows the increase of the gas pressure during the last two injection steps.

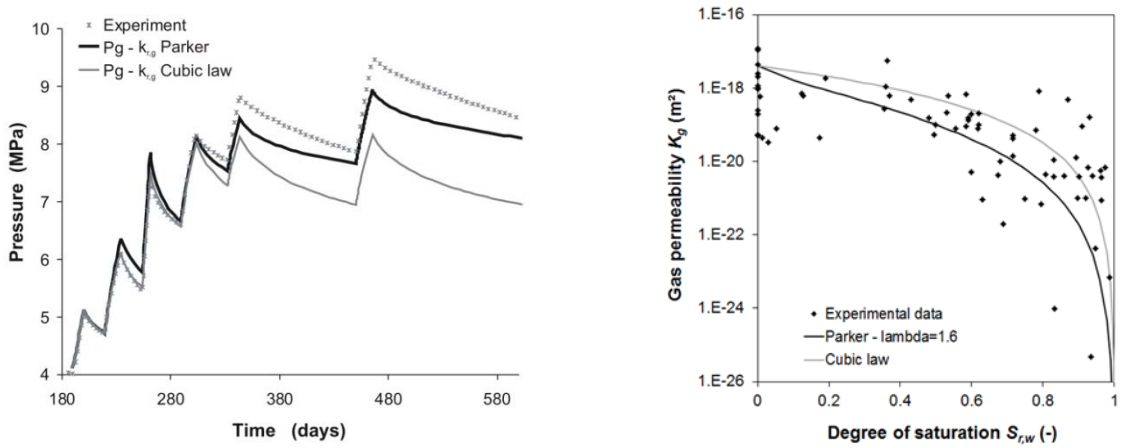

(a) (b)

Figure 100 (a) Influence of the gas relative permeability of the undisturbed claystone on the time evolution of pore pressures in the injection interval – (b) Gas permeability against degree of saturation- Comparisons with experimental data coming from Charlier et al. (2012)

3.4.2.4 NUMERICAL RESULTS – 3D

From this last satisfactory 1D hydraulic modelling, we could extract a set of parameters characterizing the behaviour of the injection interval, the excavated damaged zone and the undisturbed rock. These parameters will be used in a 3D hydraulic modelling of the problem, highlighting the role of the permeability anisotropy, the axial extent of the damaged zone along the borehole and the role of the axial flows.

Concerning the disturbed zone, it is certainly not relevant to extend this disturbed zone all around the injection borehole, because of the presence of packers between the three intervals for which the swelling pressures are higher than the gas pressures. Two domains are therefore defined in the EDZ along the injection borehole: in front of the intervals or in front of the packers. The same radial extents than in the 1D modelling are assumed for the EDZ around the borehole (4 cm), but its characteristics differ according to the domains. In front of the three intervals, the parameters coming from the 1D modelling are introduced in the two-phase flow model. On the other hand, we assume that the swelling of the packers allows recovering the initial characteristics of the sound rock in front of the packers. An anisotropic permeability ratio of 3 is introduced.

With these assumptions, the results in the interval are similar to those obtained in the 1D modelling, as shown in Figure 101. In the two other intervals located in the injection borehole on both sides of the injection interval, the modelling provides the same pore pressure evolution (Figure 102 (a)), because the intervals have been installed at the same distance from the injection interval. In this zone, the rock mass remains saturated and the variations of the pore pressures are due to water overpressures induced by the nitrogen injection. Experimentally a different behaviour is nevertheless observed in the two intervals, maybe due to different interfaces characteristics between the packers and the rock mass. Nevertheless the orders of magnitude of the pore pressure variations are very low in both intervals. The difference between experimental and numerical results is thus not significant.

Three sensors have been also installed along the parallel measuring borehole. The rock mass remains there saturated and only water overpressures are predicted by our model. The evolution of the pore pressures are well reproduced numerically, even though each injection peak is slightly overestimated (Figure 102(b)). The comparison between Figure 102 (a) and (b) emphasizes the influence of permeability anisotropy, because pore pressure variations are higher along the measuring interval, whilst it is located further from the injection interval than intervals 2 and 3.

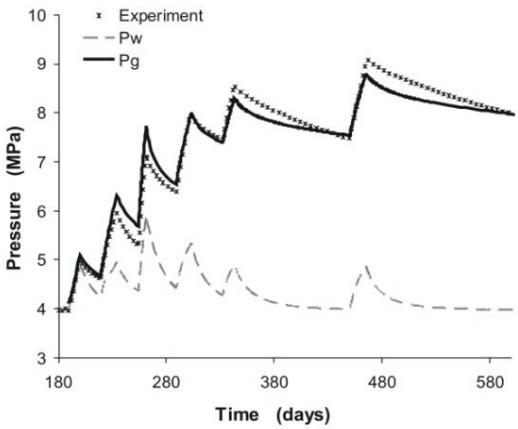

Figure 101 Time evolution of pore pressures in the injection interval – Comparisons between experimental and numerical results

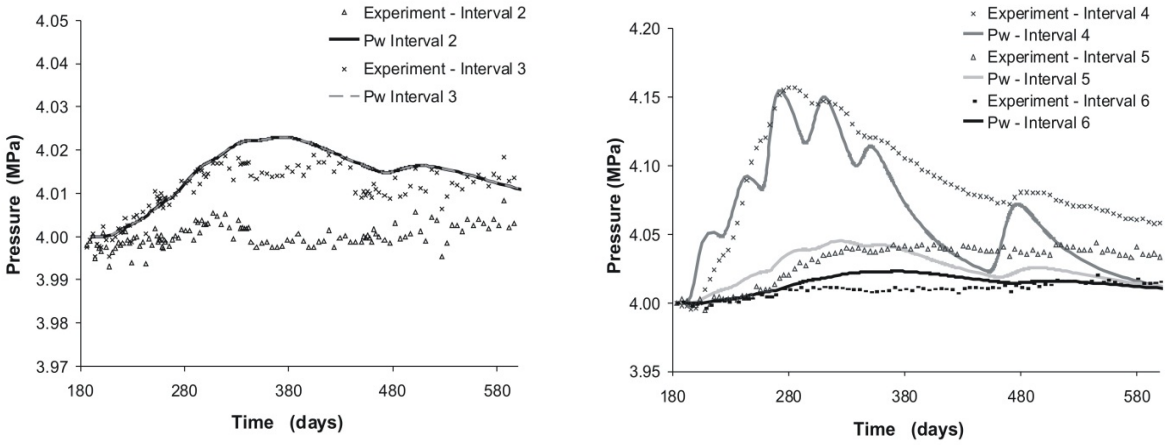

(a) (b)

Figure 102 Time evolution of pore pressures in (a) the two intervals of the injection borehole and (b) in the three intervals of the measuring borehole – Comparisons between experimental and numerical results

3.4.3 Conclusion

In conclusion, this modelling task has shown that the experimental response does not characterize the rock mass behaviour at the beginning of the nitrogen injection, even though the experiment has been initially designed in order to study the gas transfers in a potential host rock for radioactive waste disposal. As confirmed by the gas flows profiles obtained from the best 1D modelling in a domain where the gaseous transfers are predominant (Figure 103), the first injection phase tests only the behaviour of the injection interval, whilst the response of the second and the third injection stages are also influenced by the excavated damaged zone. It is only from the fourth peak that nitrogen reaches the undisturbed claystone and the pore pressures measurements characterize thus its behaviour.

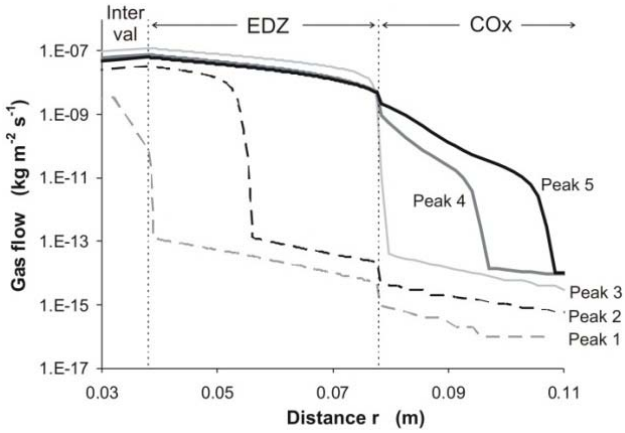

Figure 103 Gas flows profiles at different gas injection peak – 1D modelling

Finally, such results show that a predictive model as two-phase flow approach is able to reproduce experimental observations in large scale system, as far as the injection flow rate and the gas pressures remain moderate. The influence of the gas permeability close to the saturation on the numerical predictions is also emphasized. Taking into account the development of gas preferential pathways is certainly a crucial issue in the description of laboratory experiment, but seems to be neglected for this part of the test. More generally, the PGZ1 experiment has shown that gas would remain mainly confined in the borehole disturbed zone. Even though gas penetrates in the undisturbed claystone, the quantities remain low and located near the injection interval with such gas injection conditions.

3.4.4 References

Bossart P., Meier, P.M., Moeri, A., Trick, T., &Mayor, J.C. 2002.Geological and hydraulic characterisation of the excavation disturbed zone in the Opalinus Clay of the Mont Terri Rock Laboratory.Engineering Geology.66, 19–38.

Charlier R., Collin F., Pardoen B., Talandier J., Radu J.-P., Gerard P. (2012) An unsaturated hydro-mechanical modelling of two in-situ experiments in Callovo-Oxfordian argillite, Engineering Geology, submitted.

de La Vaissière R., Talandier J. (2012) Gas entry pressure in Callovo-Oxfordian claystone : in-situ experiment PGZ1. Proceedings of Transfert2012, InSkoczylas F., Davy C.A., Agostini F., Burlion F. (Eds.), pp. 360-368.

Marschall P., Horseman S.T., Gimmi T. (2005) Characterisation of Gas Transport Properties of the Opalinus Clay, a Potential Host Rock Formation for Radioactive Waste Disposal. Oil & Gas Science Technology. 60, n°1, 121-139.

3.5 Modelling for understanding of flow physics and evaluation of uncertainty of gas transport in a wide range of sedimentary rocks and geological settings (NDA)

3.5.1 Summary

During the Forge project, we have carried out a series of research investigations to explore the controls on the migration of gas through a range of different geological strata, including fractured volcanic rocks and layered sedimentary rocks. The research project has included investigation of several different flows, including (i) the competition between the transport and dissolution of the gas phase, which is envisaged to be hydrogen, with weak solubility in the ground water; (ii) the controls on the dispersion of the gas phase driven by buoyancy forces in a layered strata and (iii) the impact of exchange flows which allow for transport of groundwater between two permeable layers as a result of fracturing of the intermediate seal rock as may arise when gas leaks from a pressurized source.

3.5.2 Dissolution of a trapped pocket of gas

One problem of interest concerns the potential leakage of gas from a geological waste repository and the subsequent perching of this gas in localized anticline structures in the strata. Such perched gas may gradually dissolve into the underlying ground water leading to an extensive plume of contaminated groundwater as it migrates with the hydrogeological flow.

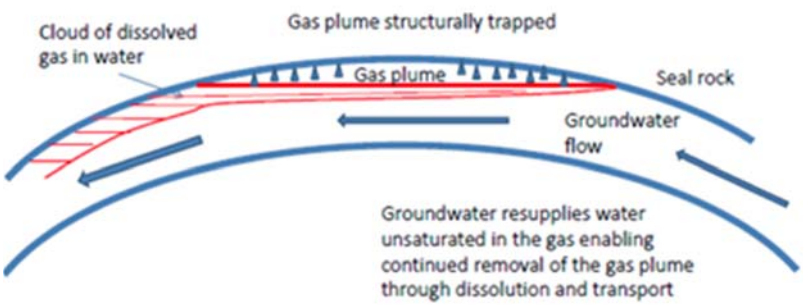

Figure 104 Cartoon of an Anticline

Important questions relate to the rate of dissolution and hence the concentration profile of the gas in the groundwater. In the case that the dissolution Is controlled by molecular transport across the gas-liquid interface, one expects a gas profile to deepen in the downstream direction at a rate proportional to $(Dt)^{1/2}$ where D is the molecular diffusivity. With typical values this produces a very slow release of the gas into the water; a layer 1m deep with gas content comparable to the saturation value requires a time of order 10-100 years to develop. Solution of the diffusion equation for the gas transport, coupled with the background hydrological flow leads to prediction of the dissolution rate of the gas trap, as measured by the decrease in the lateral extent, R, of the gas pocket shown in Figure 104, which occurs at rate

Equation 52

$$\frac{dR}{dt} == 0.9\left[\frac{2\varphi DR^3}{u}\right]^{1/2}\left[2\pi(1-s)(1-\varphi)hR^3\exp\left(-R^2/h^2\right)/w^2\right]^{-1}$$

and typical predictions from the model are shown in Figure 105, illustrating how the volume of a typical gas trap decreases with time (green line) along with the effective radius of the trap.

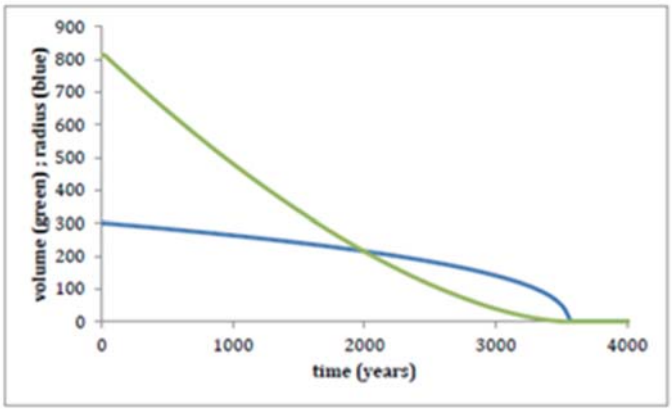

Figure 105 Volume of gas in anticline with time (green) and effective radius (blue) as the gas dissolves

In calculating the rate of dissolution in the model above, we have assumed that the dissolution is rate limited by the molecular diffusivity of the gas at the interface with the liquid. However, owing to the tidal oscillations of the earth, and the differential compressibility of the gas and the liquid, the interface between the liquid and gas oscillates enhancing the mixing and dissolution. In order to determine the controls on this mixing, we have carried out a series of experiments using small scale bead packs as an analogue model of a porous medium. By superposing a layer of low density and higher density fluid in the bead pack, and then oscillating the interface about a mean with a period of order 10-100s and an amplitude of 1-5 cm, we can study the rate of mixing of the two fluids across the interface using digital image analysis. To this end we calculate the variation with time of the area of mixed fluid in the experimental cell. Figure 106a illustrates the time evolution of the cell in a typical experiment, showing how the intermediate zone between the red and the blue dye deepens with time. By analyzing a histogram of the colors in the pixels of the digital image, thresholds can be determined to delineate the region of unmixed red and blue fluid, and the remainder represents the growing intermediate mixed zone (Figure 106b).

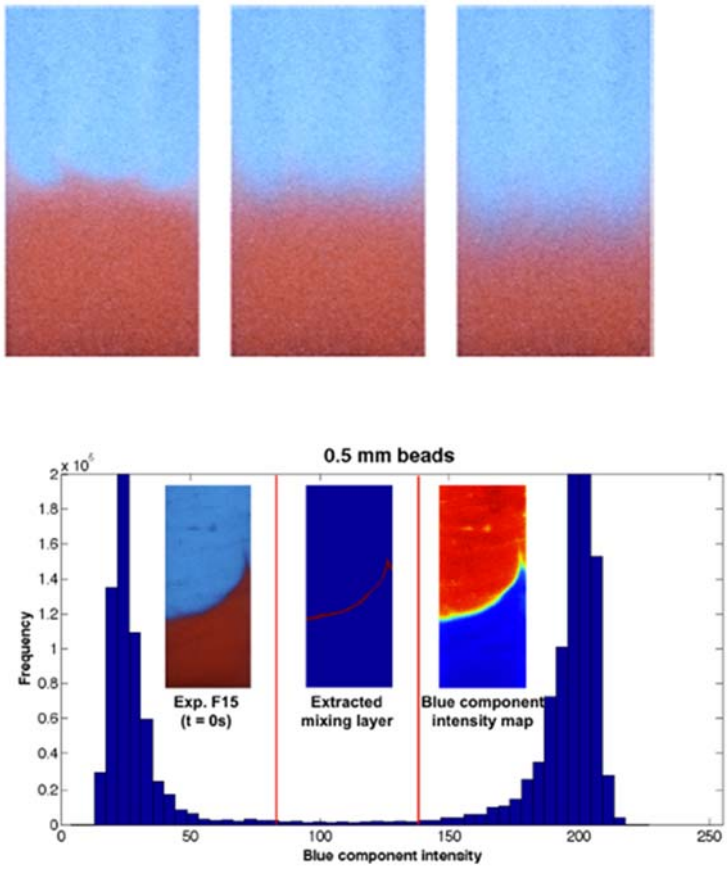

Figure 106 a. Illustration of the deepening of the mixed zone of red and blue fluid as a function of time and b. analysis of the histogram of red and blue fluid, illustrating the delineation between the red and blue zones, and the remaining pixels represent the mixed zone in the centre of the cell.

In Figure 107 we present a series of experimental results illustrating how the mixed intermediate zone grows with time. The data are shown in terms of the thickness of the intermediate zone divided by the $a(wt)^{1/2}$ where a is the amplitude of the oscillation and w is the frequency of the oscillation. This data illustrate how the effective mixing is diffusive in character, and that the effective diffusivity has value 0.01 a^2w.

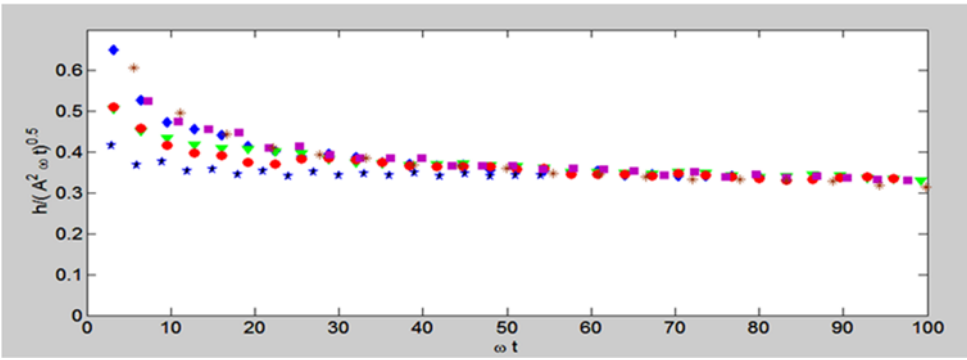

Figure 107 Evolution of the thickness of the mixing zone with time, scaled by $a(wt)^{1/2}$ illustrating the convergence of the mixing to a simple diffusion process.

In Figure 107 data are shown for a number of experiments with different amplitude, frequency and these all collapse to this same scaling. In a natural setting, if the amplitude of oscillation from the tidal stresses causes the interface to move 0.1-1.0 cm, then the effective diffusivity is 10-100 times larger than the molecular value and this may lead to dissolution of the trapped pocket of gas over times 3-10 times smaller than predicted by molecular diffusion. This will then lead to a much thicker plume of gas saturated water, and hence higher potential dose of contaminant in the groundwater.

In developing this model of the enhanced mixing, we have assumed the porous medium is homogenous. However, in many situations we may envisage there being a series of layers of different permeability or fractures which provide more rapid transport across the interface. In this case, the mixed layer will grow rapidly in the regions which are of higher permeability, and this then leads to the possibility of a gravity slumping flow developing whereby fluid migrates into the lower permeability region. As a result, the mixing ultimately becomes controlled by the sum of the displacements in the high and low permeability regions.

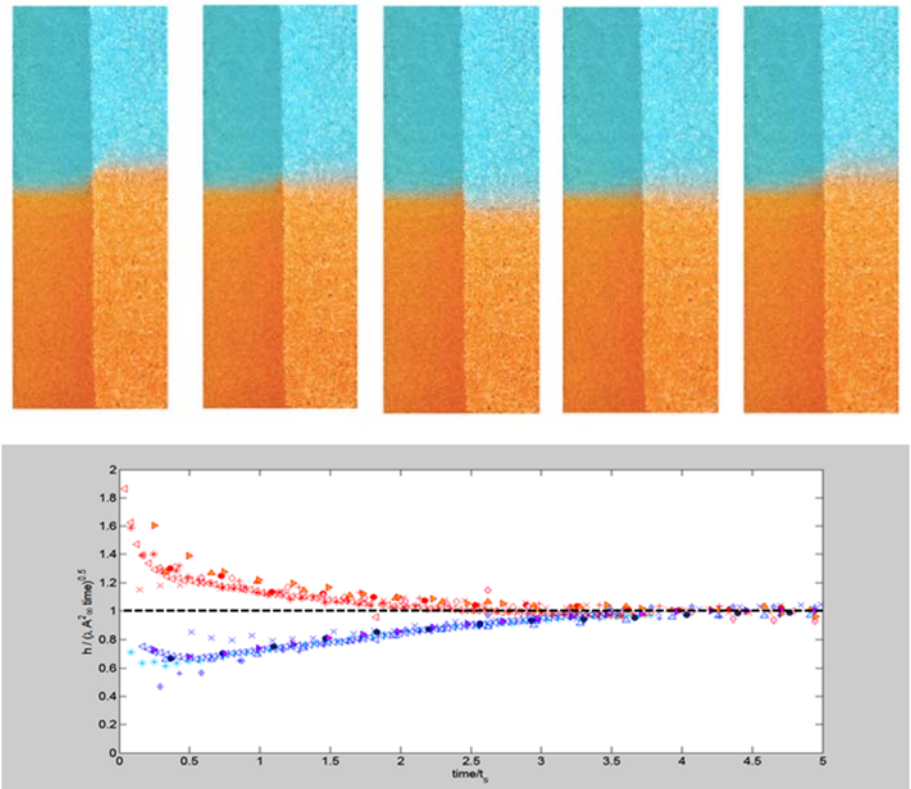

Figure 108 a Illustration of the deepening of the mixed layer in a heterogeneous system consisting of two layers of different permeability. B. Variation of the depth of the mixed layer in the high (red) and low(blue) permeability layers as a function of time, over many oscillation cycles. The depth of the mixed zones have been scaled by $a(wt)^{1/2}$.

The time to reach this asymptotic regime is given by the balance of the time for deepening in the high permeability layer or fracture and the time for gravitational slumping across the lower permeability layer. Figure 108a illustrates the mixing in a two layer permeable system in which there is a high and a low permeability region, while Figure 108b shows the data concerning the slumping of the interface from the high to the low permeability layers, and the ultimate equilbration of the the thickness of the mixed zone in both the low and high permeability regions. As a result of this equilibration, the mixing in the low permeability zone is much larger than without the high permeability regions, and this can further enhance the rate of dissolution of the gas when there is a fractured rock.

3.5.3 (B) Buoyancy Driven Dispersion.

In a second series of calculations, we have explored the dynamics of a buoyant current advancing through a layered porous medium under buoyancy forces to examine how the buoyancy forces influence the dispersal of the gas plume. Part of the objective here is to understand how the interpret possible tracer testing which might be used to monitor the flow of the gas. If the tracer is injected into a single homogeneous formation, the buoyant transport of the gas phase will be dominantly homogenous uniform flow, whereas in a layered medium the tracer will be carried at different rates in the different layers owing to the different buoyancy force associated with the source. This will lead to a buoyant dispersion of the gas plume and tracer.

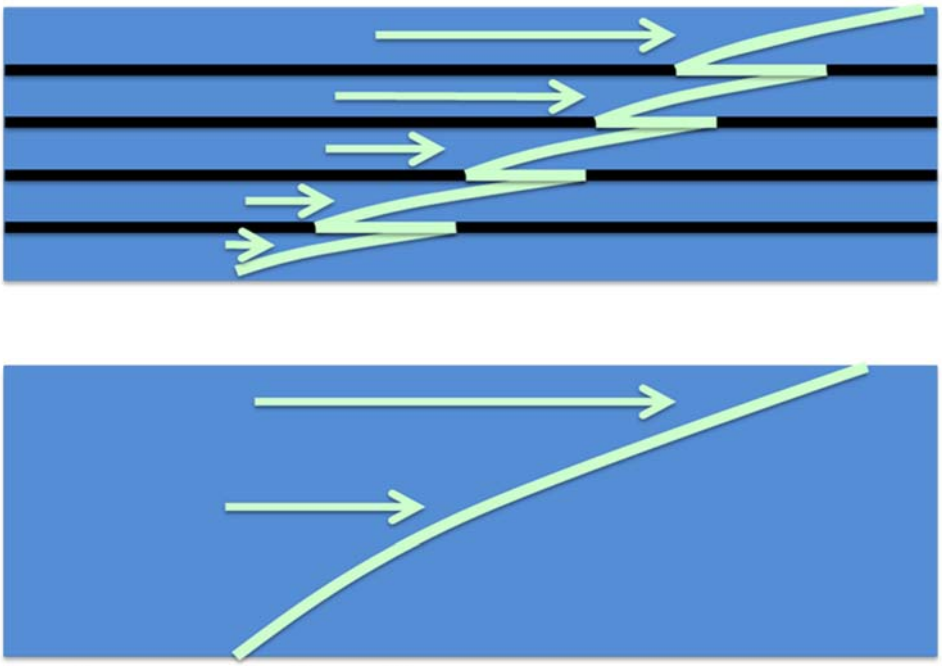

Reference – homogeneous formation

Figure 109 Illustration of the different flow patterns of a buoyancy driven gas flow in a mutply layered and single layered formation.

The flow in each layer can be described in terms of the injection pressure, which is greater higher in the formation, and the resistance to the horizontal flow associated with the intruding flow. This leads to a prediction of the shape of the gas plume in both the single and multiple layer formations. The model predictions for the flow pattern have been tested in a simple Hele Shaw cell, which includes a series of layers and a constant pressure source of fluid at one end of the tank. The pressure driving the flow in the lower layer is greater in the experiment leading to dispersion of the fluid between the different layers associated with the buoyancy.

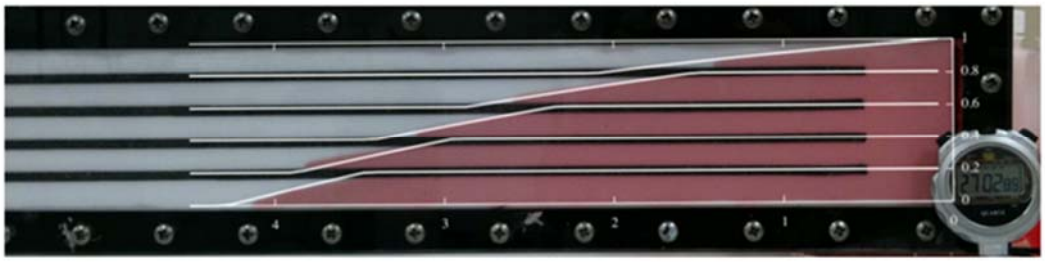

Figure 110 Experiment of the buoyancy driven dispersal of fluid in a HeleShaw cell, with a white line superposed on this image illustrating the prediction of the theoretical model we have developed.

This flow field leads to prediction of the dispersal of a finite pulse of dye injected into the system. For example, in Figure 111 we illustrate the location of a pulse of dye injected at three times after injection into a formation with 5 layers, and in Figure 111b we show a series of synthetic well tracer tests, illustrating how the concentration of a tracer would vary in time for a buoyancy driven flow in a reservoir with one (red) , two (green) , three (blue) and four layers (pink).

The result of this study has highlighted the potential dispersion which may arise in a plume of gas spreading through a layered sedimentary formation, Quantification of this dispersion is key for predicting the range of possible patterns of gas transport within the subsurface, when the buoyancy forces associated with the gas drive the flow. The modeling also illustrates the importance of quantifying the different processes which may lead to dispersion of the gas; the present model assumes a pure buoyancy driven dispersion, but in general, these effects will be complemented by the dispersion associated with variation of the permeability between the layers. The key difference between these two processes is that the contrasts in permeability tend to be randomly distributed between the layers in the vertical direction, thereby leading to a variance of the flow about a mean; in contrast the buoyancy driven dispersion leads to a well defined asymmetric trend in the dispersion as the buoyancy forces increase with height.

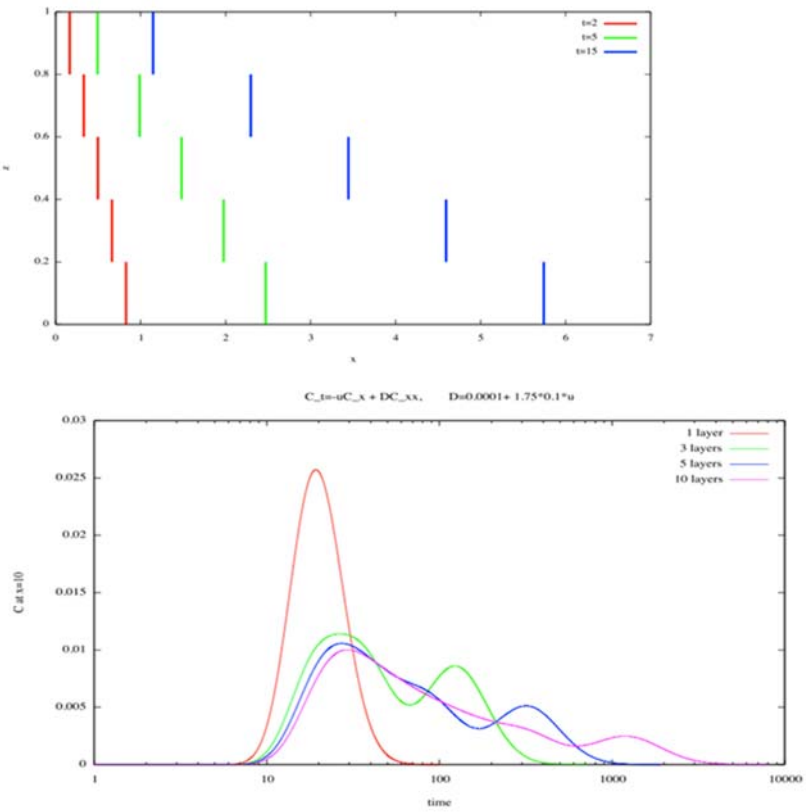

Figure 111 a. Dispersal of a finite pulse of dye injected with the gas at the source for a finite time into a reseroir with 5 layers. The red green and blue series of lines denote the position of the dye pulse at three progressively later times. b. variation of the tracer concentration which would be received at a test observation well as a function of time. The structure of the signal depends on the number of layers in the formation, and may be used to interpret the structure of the formation and hence the dispersal pattern of the gas.

3.5.4 C. Exchange flows through fractures : cross-aquifer communication

If a geological waste repository gradually builds up pressure owing to gas formation in the repository, then this pressurisation may lead to fracturing of the seal rock between vertically separated reservoirs. The development of such fractures may then enable the transfer of fluid between the different permeable layers; the groundwater in these different layers may be of different age and composition, and therefore the flow may be gravitationally stable or unstable, leading to a competition between the pressure driven flow and the buoyancy driven flow processes. Since the gas may be released into the aquifer adjacent to the repository and may dissolve into this water body, any exchange flow to different aquifers or aquitards which is enabled through the pressurization and associated fracturing can change to overall patterns of dispersal of the contaminant.

We have therefore explored the process of exchange flow between adjacent aquifers in both the buoyancy driven and buoyancy stabilized flow regimes. The basic flow configuration is illustrated in Figure 112.

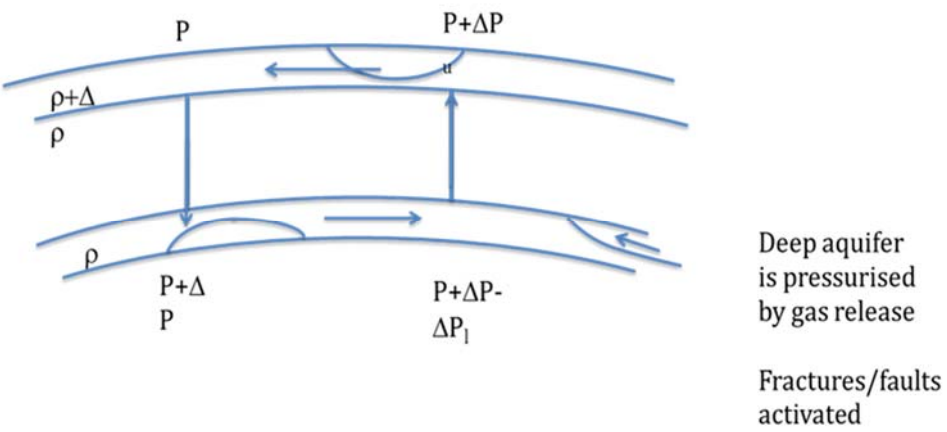

Figure 112 Schematic of the flow configuration which leads to exchange of fluids between different aquifers.

To study the exchange flow we have set up an experimental system consisting of two cylindrical pipes filled with glass ballotini; the upper end of the pipes are connected to a sealed reservoir of saline fluid and the lower end of the pipes are immersed in a vessel containing fresh water. The pipes include a valve which is opened to commence the experiment. The lower vessel is placed on a mass balance and as saline water migrates down one of the pipes into this vessel, with a corresponding return flow of fresh water in the other pipe, the mass gradually increases. As the fresh water enters the top of the upper vessel, a descending interface with the lower saline fluid in the vessel develops. A similar phenomenon occurs in the lower layer (Figure 113a). In principle the exchange flow depends on the difference in the hydrostatic head of the two columns of liquid and so effect we expect the exchange flow to vary as

$$Q = \pi r^2 \frac{k\Delta\rho g}{\mu} \qquad \text{Equation 53}$$

We have compared the predictions of this simple exchange flow model, for the tubes of radius r, permeability k with the density difference between the fresh and salt water being Δρ in terms of how the depth of the upper layer descends with time. The model results are compared with

the data in Figure 113b, It is seen that data collapse for a range of density differences, by scaling time with the time based on the above flux law. This supports the model for the exchange flow.

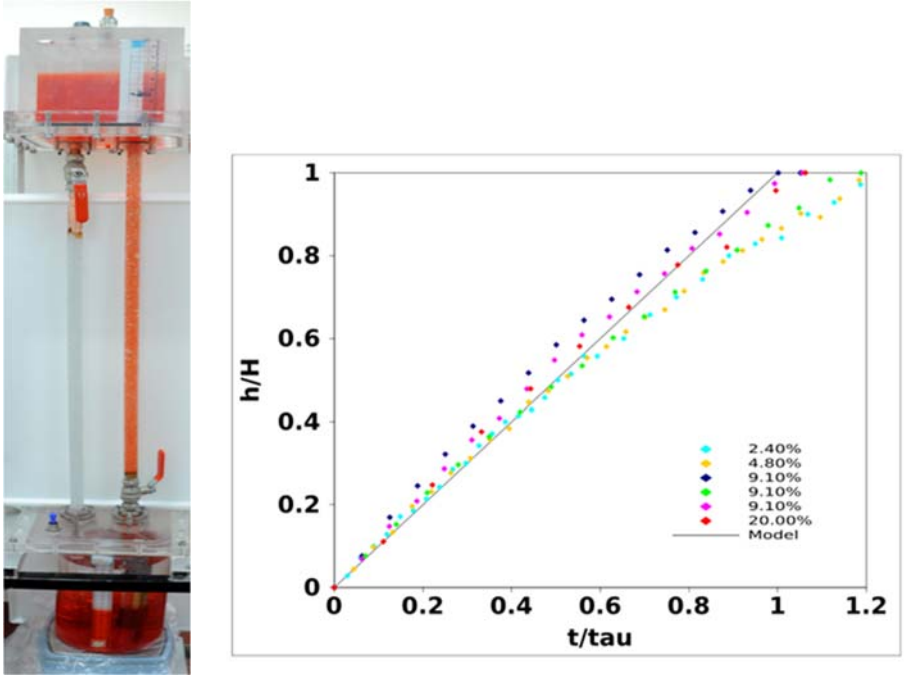

Figure 113 a,b. Illustration of the experiment to test the model of exchange flow between two aquifers following development of a fracture between the layers. B. Measurement of the exchange flow rate for a series of experiments using different density differences between the upper ad lower reservoir, and also using different size ballotini which produce different permeability structures in the tube.

One process related to the phenomenon of exchange flow driven along fractures can arise in the well casing, and in this case the exchange flow only occurs in one pipe. We have also studied this flow regime using a single pipe connecting the lower and upper reservoir. Figure 114 illustrates a series of images of a photograph showing the evolution of the mixing with time. It is seen that the red dye descends the tube as the mixing evolves until reaching a ateady state. In Figure 115 we illustrate the change of mass in the vessel at the base of the tube as a function of time. It is seen that for a range of density differences the model is again in reasonable agreement with the data.

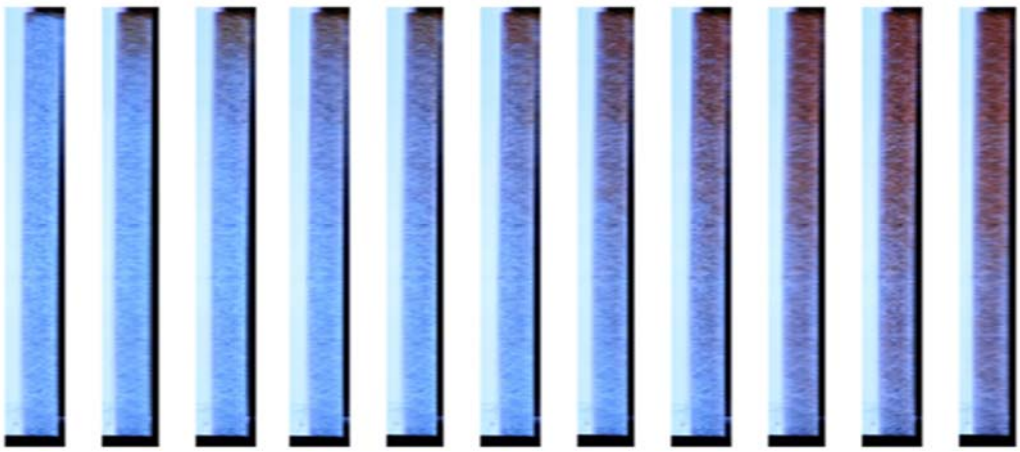

Figure 114 Series of images showing the steady state flow regimes becoming established.

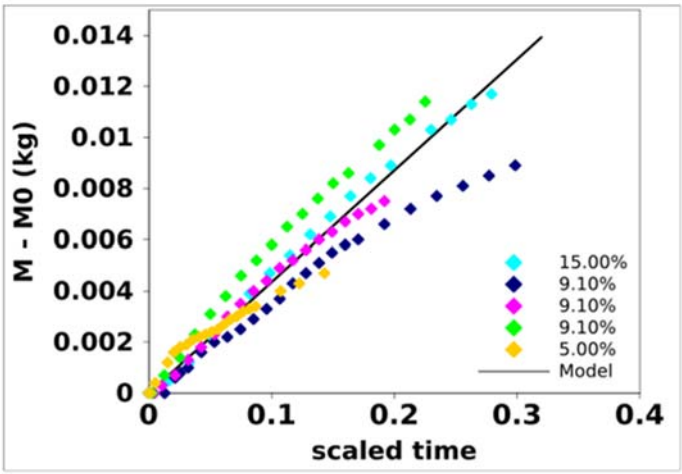

Figure 115 Evolution of the mass with time for a single tube exchange flow experiment.

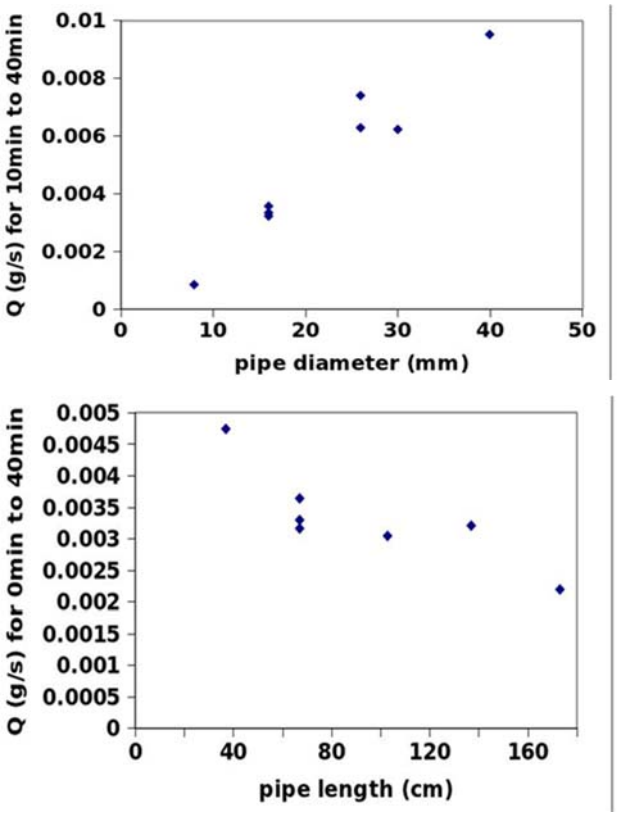

Figure 116 Illustration of the mass flow rate dependence on pipe length and diameter.

There are some systematic changes in the flux with pipe diameter and pipe length, as shown in the figures below, as expected in the scaling law for the flux (Figure 115), again providing further confirmation of the model. However, in this case, the flux depends on the fraction 0.1 of the density difference between the vessels owing to the mixing across the tube which leads to a gradual change in density as the fluids migrate up and down the tube.

3.5.5 Conclusion

In this report we have described a series of research carried out as part of the Forge project to explore the migration of gas from a pressurized geological storage facility. We have described models to quantify the rate of dissolution of the gas following ponding in a structural trap on the upper boundary of the aquifer through which it migrates. We have also shown how tidal oscillations can accelerate the rate of dissolution of the gas as the interface oscillates in time. We

then examined the impact of layering in the reservoir on the buoyancy driven dispersion of the gas, and explored how this would influence a tracer test. Finally we have examined the potential for a buoyancy driven exchange flow to develop between two aquifers in the event that the seal rock between the layers becomes fractured, for example as a result of the pressurization of the repository and the ensuing release of gas. Such an exchange may lead to mixing of different water bodies and the associated transport of dissolved gases.

3.5.6 References

The work in this report is in the process of being published in a series of articles in peer reviewed journals

Woods and Norris, 2012, Dissolution of trapped gas from an anticline

Lapotre, Otto and Woods, 2012, Oscillatory mixing in a porous kayer

Farcas and Woods, 2012, Buoyancy driven dispersak in a layered rock

Berkowitz and Woods, 2012, Exchange flows in aquifers

4 Final conclusions

One of the main goals within WP5 was to determine which gas flow mechanisms can take place when a gas phase starts to build-up within a geological repository: classical visco-capillary 2-phase flow, pathway dilation, fracturing, … ? BGS performed a series of long-term laboratory test on the Callovo-Oxfordian clay in order to examine the fundamental mechanisms governing the migration of gas through COx. The experiments demonstrated that the movement of gas is accompanied by the dilation of the clay fabric and a slow temporal evolution of gas permeability within each specimen. Pathways seemed to be highly unstable, and open and close in an apparently random way. There was no indication for the displacement of interstitial fluid from the original porosity, and combined with visual observations of localised degassing, it is concluded that gas flow occurs through localised pathway dilation.

Attempts to model these gas injection epxeriments with THOUGH-2 prous medium multiphase code were not succesful: significant aspects of the data could not be reproduced and many features are indicative of the development of discrete flow pathways. Together with a number of other complementary studies, the importance of time-dependent discrete gas flow pathways in clays has been stressed.

Experiments performed by CIEMAT on Opalinus Clay allowed to compute the P parameter which is related to the air entry value, in example to the suction value above which air is able to enter the pores of the sample and thus above which 2-phase flow can take place. The P parameters obtained were between 6 and 34 MPa. These values correspond to degrees of saturation between 80 and 90% which implies that 2-phase flow would only take place for saturation degrees lower than 90%. For higher degrees of saturation, macroscopic fracture formation could be that mechanism for gas flow. Gas injection experiments showed that for degrees of saturation 80±16%, the breakthrough pressure is higher than 18 MPa and due to experimental restrictions the relationship between AEV en breakthrough pressure could not be stated.

Experiments performed by SCK•CEN focussed on the possibility of gas-induced transport of radionuclides. Experimental results obtained within WP's 4 and 5 demonstrated that radionuclides can indeed be transported during gas breakthrough, but it is considered limited as the amount of displaced water is less than 0.5% of the "contaminated" water volume. Concerning the gas flow mechanisms, the observations of laboratory gas tests on BC samples indicated that gas dissipation through dilation pathways is more likely than development of plane-type fractures. Of course this observation is stress and scale dependent and direct characterisation of the dilation pathway was with the current experiments very difficult to apply.

Based on all laboratory experiments, no experimental observations pointed to classical visco-capillary 2-phase flow as the dominant flow mechanism. More and more evidence was obtained that gas flow within clays has to be described by time-dependent discrete gas flow pathways.

In the PGZ-1 experiment 3 boreholes were drilled: 2 for gas injection and pressure monitoring, and one for monitoring rock deformation. After a series of hydraulic tests, a gas injection experiment was performed. Based on the experimental observations, it was concluded that the hydraulic properties of the host rock are unchanged before and after gas injection. So if micro fracturing or dilatancy would occur, these processes seem to be reversible due to the self-sealing properties of the host rock. No evidence has been found of the formation of dilatant pathways during the gas injection experiment. Modelling the experiment by ANDRA was done with continuous 2-phase flow and a coupling of the flow model with mechanical behaviour was not necessary to reproduce the gas response. The EDZ, created during the drilling of the borehole seems to be a zone where gas could migrate preferentially and could be stored – the maximal gas entry pressure in the EDZ was estimated about 2 MPa.

Numerical simulations carried out by EDF (CODE-ASTER) and ULG (Lagamine) towards the PGZ-1 experiment conclude that the conventional HM coupled models based on the two-phase flow theory is capable of reproducing experimental observations in large-scale systems – as far as the injection flow rate and gas pressure remain moderate. Their simulation activities demonstrate the necessity of considering the initial condition of the gas interval and the borehole damaged zone in the modelling. Underestimation of fluid pressure after the 4th gas injection when the gas enters the intact host rock can be further improved by increasing gas permeability of intact COX when close to saturation.

The HG-C/HG-D experiment in the Mt. Terri URL consists of several parallel boreholes, equipped with packer systems and micrometers. Different water and gas injection experiments have been performed. In-situ water and gas injection tests consistently suggest an intrinsic permeability of intact host rock of about 5 E-20 m^2. The theshold pressure for the onset of dilatancy in response of water and gas increase is around 4 MPa and 2 MPa, respectively. Modelling suggests the potential capability of the classical 2-phase flow code in simulating the dilatency behaviour of soil when incorporated with pressure-dependent permeability. The second phase of the GP-A/GS experiment was modelled by UPC with CODE-BRIGHT, which incorporates a type of joint element with aperture-dependent permeability to simulate fluid flow along the fracture. The developed model captured well the evolution of pressure and an adequate tendency of displacements. GRS fitted successfully the HG-C/ HG-D experiment using various models (Tough2 with pathway dilation model, "tube chamber" model). Both models are based on strong simplifications (like single-phase flow) and did not account for hydro-mechanical coupling. The applied models showed that the mechanical processes in the experiments were simple enough to be approximated by time- and pressure dependent relations for porosity and permeability, showing that it is not always necessary to apply hydro-mechanical coupled modelling for processes with hydro-mechanical interactions. The simulations showed no evidence for phase interactions (water displacement, water compression or gas dissolution).

5 Summary of findings & way forward

The aims of WP5 were to establish the conditions under which the different gas migration processes are dominant, to identify how those processes can be modeled and to determine the values of the main parameters and finally to establish whether an impact on the long-term safety as a consequence of enhanced radionuclide transport through the host rock could be expected.

When one wants to perform experiments on undisturbed clay host rock, some major experimental challenges need to be taken into account i.e.

- In laboratory experiments, it is quite difficult to obtain and prepare samples that are representative for undisturbed conditions and it is very difficult to obtain reliable two-phase flow parameters at very low degree of desaturation which is the most representative of what is expected in-situ;
- In in-situ experiments, one needs to be aware that drilling boreholes causes a damaged zone (EDZ) at the borehole wall. Although self-sealing will occur, this borehole EDZ will have a strong influence on the pressure evolution of test intervals. This effect might be stronger in stiffer clays. In in-situ experiments it can also be quite difficult to have exact measurements of the initial gas filled volume in a gas injection interval.

Measuring the water retention curves of an indurated clay like the Opalinus clay remains a challenge especially at high water saturation where the spread in results remain high. No difference was noted between applying matric or total suction and the expected hysteresis behavior was observed. Increasing mechanical stress seems to further increase the air entry value which is in any case high (6 to 34 MPa)

It is quite difficult to create a gas flow into an intact clay host rock as the gas entry pressure and water retention is very high. Both laboratory and in-situ experiments show that when a gas phase flows through an undisturbed clay, that very little water is displaced. Very carefully performed laboratory experiments in which all mechanical and hydraulic boundary conditions are well controlled point to hydro-mechanical coupling and pathway dilatancy as gas transport mechanism.

It is still a debate whether hydro-mechanical coupling is required to model the actual gas flow and pressure transients. In some cases one was successful to model experimental outcomes using standard two-phase flow however modifications for permeability, porosity and water retention were always required. In other cases only through hydro-mechanical coupling one was able to grasp the main features of the experimental results. From the modeling exercises it was also very clear that it is essential to correctly represent the details of the experimental set-up, its in-situ installation and experimental history to have a correct representation of e.g. the gas injection boundary condition and its evolution. In general one needs to take into account a borehole EDZ what causes additional uncertainty in the modeling.

As very little water can be displaced by a gas phase through an undisturbed clay host rock, there is little risk for advective transport of contaminated water from a repository through the clay

host rock. As the gas will take the easiest way the disturbed host rock around excavations (galleries or disposal cells) and the access ways to repository will most probably act as preferential pathways for the gas to escape. Large scale simulations for simulated geologies show that gas flow is very sensitive to local variations in gas transport properties with the gas taking always the path with the lowest resistance with also the inclination of layers (or pathways) having an impact due to buoyance. As the gas generation rate and local variations in gas transport properties (thresholds for gas entry) determine the dynamics of the pressure buildup, the gas generation rate will have an impact on in which pathways the gas flows and thus how the gas spreads over the repository and geology.

6 Publications

Charlier, R., Collin, F., Pardoen, B., Talandier, J., Radu, J.-P., Gerard P. (2012) An unsaturated hydro-mechanical modelling of two in-situ experiments in Callovo-Oxfordian argillite, Engineering Geology, submitted.

Cuss, R.J., Harrington, J., Giot, R., and Auvray, C. (2014) Experimental observations of mechanical dilation at the onset of gas flow in Callovo-Oxfordian claystone. Clays in Natural and Engineered Barriers for Radioactive Waste Confinement. In: Norris, S., Bruno, J., Cathelineau, M., Delage, P., Fairhurst, C., Gaucher, E. C., Höhn, E. H., Kalinichev, A., Lalieux, P. & Sellin, P. (eds) Clays in Natural and Engineered Barriers for Radioactive Waste Confinement. Geological Society, London, Special Publications, 400.

Cuss, R.J., Harrington, J., Graham, C.C., and Noy, D.J. (2014) Observations of stable high-pressure gradients in clay-rich materials; implications for the concept of effective stress applied to unconventional hydrocarbons. Geophysical Research Abstracts. Vol. 16, EGU2014-14071, 2014. EGU General Assembly 2014.

Cuss, R.J., Harrington, J.F., and Graham, C.C. (2013) Fundamentals of gas flow in shale; What the unconventional reservoir industry can learn from the radioactive waste industry. European Geosciences Union General Assembly. Vienna, Austria, 7th – 12th April 2013. EGU2013-9341.

Cuss, R.J., and Harrington, J.F. (2011) Update on dilatancy associated with onset of gas flow in Callovo-Oxfordian claystone; Progress report on test SPP_COx-2. British Geological Survey Commissioned Report, CR/11/110. 34pp.

de La Vaissière, R., Gerard, P., Radu, J.-P., Charlier, R., Collin, F., Granet, S., Piedevache, M., Helmlinger, B., Croisé, J., Lavanchy, J.-M., Senger, R., Talandier, J. (2013) A large-scale gas injection test in the Meuse/Haute-Marne research laboratory : data analysis and numerical approach. Geological Society special publication, submitted.

Gerard, P., Radu, J.-P., Talandier, J., de La Vaissière, R., Charlier, R., Collin, F. (2012) Gas migration through clay barriers in the context of radioactive waste disposal: numerical modelling of an in-situ gas injection test. Geomechanics in CO2 storage facilities. In G. Pijaudier-Cabot & J.-M. Pereira (Eds.), Wiley, in press.

Harrington, J.F., de La Vaissiere, Noy, D.J., Cuss, R.J., and Talandier, J. (2012) Gas Flow in Callovo-Oxfordian Clay (COx): Results from Laboratory and Field-Scale. Mineralogical Magazine. December 2012, Vol. 76(8), pp.3303-3318.

Harrington, J.F., Noy, D.J. and Cuss, R.J. (2013). Long-term gas migration experiments in Callovo-Oxfordian Claystone. British Geological Survey, Technical Report, CR/13-088.

Harrington, J.F., Cuss, R.J., Noy, D.J. and Talandier, J. (2014) Processes Governing Advective Gas Flow in the Callovo Oxfordian Claystone (COx). Fourth EAGE Shale Workshop. 6th-9th April, Porto, Portugal. Extended abstract.

Harrington, J.F., Cuss, R.J., and Noy, D.J. (2013) Dilatancy driven gas flow in the Callovo-Oxfordian Claystone (COx). Gas Generation and Migration. International Symposium and Workshop. Luxembourg, 5th – 7th February, 2013. Extended abstract.

Jacops, E., Maes, T., Maes, N. Volckaert, G., Weetjens, E., Sillen, X. (2013) Gas-driven radio nuclide tranport in disturbed and undisturbed Boom Clay. Geological Society special publication, submitted.

Navarro, M. (2013) Modelling Gas and Water Flow through Dilating Pathways in Opalinus Clay, The HG-C and HG-D Experiments, A Study within the Euratom 7th Framework Programme Project FORGE, GRS-306, ISBN 978-3-939355-85-4, Gesellschaft für Anlagen- und Reaktorsicherheit (GRS), Germany.

Villar, M.V. & Romero, F.J. (2012) Water retention curves of Opalinus clay. Informes Técnicos CIEMAT 1262. Octubre 2012. CIEMAT, Madrid, 33 pp.

Villar, M.V. & Romero, F.J. (2012) Opalinus clay 2-phase flow parameters. FORGE Deliverable D5.14. Informe Técnico CIEMAT/DMA/2G207/3/12. Madrid, 31 pp.

Villar, M.V., Romero, F.J. & Martín, P.L. (2012) Opalinus clay gas induced fracturing. FORGE Deliverable 5.11. Informe Técnico CIEMAT/DMA/2G207/5/12. November 2012. CIEMAT, Madrid, 24 pp.